Solid-State Nuclear Magnetic Resonance Studies of Hydrogen Storage Materials

Gregory Stephen Bernard Martin, MSci.

Thesis submitted to the University of Nottingham for the

Degree of Doctor of Philosophy

- March 2014 -

Abstract

Currently, solid-state nuclear magnetic resonance (NMR) methodology is still evolving. However, this thesis focuses on the application of NMR methods to improving the understanding of solid-state hydrogen storage materials. In particular, this thesis demonstrates how NMR can provide a unique perspective on materials from a molecular level, complementary to other analytical techniques. All of this work has been done in collaboration with other research groups, so effort has been made to interpret the NMR results recorded here in the context of the synthetic methods used and results obtained from other analytical techniques.

Firstly, chapter 1 contains a review on the necessity and challenges of storing hydrogen. Then a complete review of the relevant NMR theory and methodology will be given in chapter 2, before turning attention to its application to specific hydrogen storage systems in subsequent chapters. Chapter 3 studies the metal organic frameworks (MOF): NOTT-207, NOTT-201 and NOTT-209 as potential storage systems. Static ^{7}Li studies elucidated the change in the lithium co-ordination environment upon desolvation, necessarily unblocking the pores for gas sorption.

Chapter 4 contains a multi-nuclear study on the $LiBH_4/MgH_2$ system. In the first part, static ^{7}Li NMR reveals the effects of ball milling (particle grain size reduction) on lithium ion diffusion; for the hexagonal (high temperature) structure of $LiBH_4$. Evidence is also found for significant lithium ion diffusion in the orthorhombic (low temperature) structure. Then in the second part of chapter 4, ^{1}H, ^{6}Li, ^{7}Li, ^{11}B and ^{25}Mg *ex situ* magic angle spinning experiments were used to follow the route of decomposition, analysing the effects of varying reaction temperature, pressure and sample stoichiometry. The different phases present at different stages in the amorphous intermediates and products were elucidated, in

particular it was possible to show the necessary thermodynamic conditions for the $[B_{12}H_{12}]^{2-}$ intermediate formation.

Chapter 5 uses static ^{7}Li NMR to study the Li-N-H system. Firstly, Li_3N nanowires are characterised in terms of lithium ion diffusion, with an improvement to diffusion being found upon nano-structuring. Then bulk Li_2NH and dual phase $Li_2NH/LiNH_2$ are also characterised with respect to lithium ion diffusion, and analysis suggests hopping occurs between tetrahedral sites. Since the three systems studied in this thesis are different, each chapter will contain all the background scientific information and conclusions relevant to the NMR results of the system under consideration. Finally, chapter 6 will summarise and conclude as a whole in the context of the technological importance of this work.

Acknowledgments

First and foremost, I owe sincere gratitude to my supervisor Dr. Jeremy Titman, who has supported my studies with a combination of brilliant ideas, technical expertise and encouragement. Thank you for your patience with a multitude of questions and for your vigilance with proof-reading my work. For that, among innumerable other factors, I owe my huge appreciation.

Thank you to everyone in the solid-state NMR group I have had the pleasure of working with: Dr. Andrew Jurd, Dr. Andrew Powell, Dr. Yanqi Wu, Dr. Daniel Lee, Dr. David Bennett, Habeeba Miah, Francesca Martini and Lyndsey Knight. Thank you for your stimulating conversations, bright ideas, entertainment and general camaraderie throughout the course of my studies. Thank you also to all the technical staff who have supported the experimental work.

Thank you to all the collaborators from different research groups I have worked with for your inspiring discussions, invaluable information and patience whilst this work matured. Specifically, for the metal organic frameworks: Prof. Martin Schröder and Dr. Sihai Yang; for the $LiBH_4/MgH_2$ work: Prof. Gavin Walker, Dr. Tobias Price and Dr. Mariem Meggouh; for the Li - N - H work: Prof. Duncan Gregory and Dr. Nuria Tapia-Ruiz.

I would like to thank the EPSRC for funding this work, making it possible.

I would like to acknowledge all the teachers and individuals who have inspired and enabled me to pursue my path through higher education. This includes the teachers at Northfield Manor Primary School and King's Norton Boys' Secondary School and 6^{th} form College. In particular, thank you to my A-level chemistry teacher Jacqui Davis who introduced me to the concepts around NMR, which have fascinated me ever since and led to this PhD thesis. Also thank you to

my tutors who supported and enabled academic study during my undergraduate degree at The University of Nottingham. I am indebted to all your efforts and expertise.

On a personal note, I would like to say a massive thank you to all my friends and comrades who have supported me during this work. Thank you to all my housemates, church friends, walking, running and climbing comrades, and other acquaintances who have enabled the necessary escapes and distractions from studying.

Thank you to my whole family for being there through thick and thin, and for unwavering love and support. A particularly special mention to my father Dr. Brian Martin, for empathy from personal experience on the highs and lows I went through whilst completing this work. Also, thank you Dad for being generous enough to give this work an entire proof read to help iron out literacy errors. Finally, thank you to both my parents for all the years of tireless efforts and countless sacrifices, for which I am ever indebted.

Contents

Abstract i

Acknowledgements iii

Contents v

Abbreviations xi

1 Context and Motivation: Hydrogen Storage 1

1.1 Towards a Hydrogen Powered Future 2

1.2 The Hydrogen Storage Challenge 4

1.3 Storage of Hydrogen in the Gas Phase 7

1.3.1 Compressed Gas 7

1.3.2 Hollow Glass Micro-spheres 8

1.3.3 Clathrate Hydrates 8

1.4 Storage of Hydrogen in the Liquid Phase 9

1.5 Liquid-State Chemical Storage 9

1.6 Solid-State Chemical Storage 12

1.6.1 Metallic/Intermetallic Hydrides 13

1.6.2 Ionic Metal Hydrides 15

1.6.3 Complex Metal Hydrides 16

1.6.4 Ammonia Borane 18

1.7 Solid-State Porous Media 18

1.7.1 Zeolites 19

1.7.2 Carbon-Based Materials 20

1.7.3 Metal Organic Frameworks 21

1.8 Summary: Hydrogen Storage Systems Studied in this Thesis 22

2 NMR Theory and Practice **26**

2.1 Basic Nuclear Magnetism 27

2.2 Classical Representation of Macroscopic Magnetization 27

2.2.1 Static Magnetic Field Case 27

2.2.2 Time-Dependent Magnetic Field Case 28

2.3 Quantum Mechanical Representation of Nuclear Magnetism 29

2.3.1 Density Matrix 29

2.3.2 Liouville-von Neumann Equation 30

2.3.3 Simulating NMR Spectra Using SIMPSON 31

2.3.4 The Nuclear Spin Hamiltonian 32

2.4 The Zeeman Interaction 33

2.4.1 Thermal Equlibrium 34

2.5 The Radio-Frequency Interaction 35

2.6 Quadrupolar Coupling 37

2.6.1 Pake Pattern (Powder) Line Shapes 38

2.6.2 Second Order Quadrupole Coupling 40

2.7 Dipolar Coupling 42

2.8 Shift Interactions 44

2.8.1 Chemical Shift 44

2.8.2 Knight Shift 46

2.9 Relaxation 48

2.9.1 Spin Temperature 48

2.9.2 The Bloch Equations 49

2.9.3 Autocorrelation 50

2.9.4 The Master Equation and Spectral Density 51

2.9.5 Non-Exponential Correlation of Motional Processes 52

2.9.6 Relaxation by a Time Dependent Magnetic Field $\mathbf{B}_\mathbf{t}'$ 53

2.9.7 Common Relaxation Models 55

2.10 Static Line Shapes and Narrowing due to Ionic Diffusion 57
2.10.1 Origin of the Line Width 57
2.10.2 Dipolar Line Broadening 57
2.10.3 Ionic Diffusion in the Solid-State 59
2.10.4 Motional Narrowing caused by Diffusion 60
2.10.5 Exchange Broadening of the Quadrupolar Satellites 61
2.10.6 Studying Dynamics on Different Time-Scales 61
2.11 Experimental Techniques 62
2.11.1 Sample Preparation and Handling 62
2.11.2 Overview of the NMR Experiment 62
2.11.3 Temperature Control 63
2.11.4 Magic Angle Spinning (MAS) 64
2.11.5 Continuous Wave Decoupling 66
2.11.6 Spin Echoes 67
2.11.7 Cross-Polarization 68
2.11.8 High Resolution of Quadrupolar Nuclei: The MQMAS Experiment 69
2.12 Experimental Strategy 77

3 Metal Organic Frameworks: NOTT-MOF 81

3.1 Introduction: Progress on the Design of Metal Organic Frameworks for Hydrogen Storage 82
3.2 Synthesis and Characterisation: The structure of NOTT-MOF . . . 84
3.3 Lithium-7 Static NMR: Characterisation of Lithium Binding Sites . 88
3.4 Discussion: H_2 Sorption Properties 90
3.5 Conclusion 94

4 The Lithium Borohydride / Magnesium Hydride System 95

4.1 Introduction: Hydrogen Storage using the Lithium Borohydride - Magnesium Hydride System 96
4.2 Mechanically Milled Mixtures of Lithium Borohydride with Magnesium Hydride 99
4.2.1 Literature Review: Structure of and Dynamics in Lithium Borohydride 99
4.2.2 Literature Review: Correlated Ion Hopping Studied by Spin-Lattice Relaxation 101
4.2.3 Synthesis and Characterisation: Ball Milling Lithium Borohydride with Magnesium Hydride 102
4.2.4 Lithium-7 Static NMR: General Line Shape Analysis 103
4.2.5 Lithium-7 Static NMR: Comparison of Samples 1 to 6 107
4.2.6 Discussion: Lithium-7 Line Shape Analysis in both Low and High Temperature Phases 110
4.2.7 Lithium-7 Static NMR: Spin-Lattice Relaxation Measurements 111
4.2.8 Discussion: The Effects of Ball Milling on Lithium Ion Diffusion. Lithium-7 Spin-Lattice Relaxation Measurements. . . 115
4.2.9 Other Useful Experiments: Methods of Quantifying Grain Sizes 116
4.2.10 Other Useful Experiments: Spin Diffusion Measurements to Determine the Average Grain Size 118
4.2.11 Other Useful Experiments: $T_{1\rho}$ Relaxation Measurements . . 122
4.3 *Ex situ* NMR Study on the Decomposition of the Lithium Borohydride/Magnesium Hydride System 123
4.3.1 Literature Review: Decomposition of the Lithium Borohydride/Magnesium Hydride System 123

4.3.2 Synthesis and Characterisation: Decomposition of Lithium Borohydride/Magnesium Hydride under Different Conditions 127
4.3.3 Sample Handling and Testing for MAS Studies 131
4.3.4 ^{11}B, ^{6}Li and ^{25}Mg MAS NMR Spectroscopy: Decomposition at 400^{o}C 133
4.3.5 ^{11}B MAS NMR Spectroscopy: Varying Temperature and Stoichiometry 136
4.3.6 Discussion: Effects of Temperature and Pressure on Intermediate Formation 141
4.3.7 Discussion: Effects of Stoichiometry on Intermediate Formation 143
4.3.8 Discussion: Evidence for $Mg_{1-x}Li_{2x}B_2$ Formation 144
4.3.9 ^{7}Li NMR Spectroscopy: Detection of Alloys Under Varying Temperature and Stoichiometry 144
4.3.10 Discussion: Formation of Lithium-Magnesium Alloys 148
4.4 Conclusion 149

5 The Lithium Nitride - Imide - Amide System 151

5.1 Introduction: Progress on the design of the Li-N-H Storage System 152
5.2 Lithium Nitride Nanowires 155
5.2.1 Literature Review: Studies on Lithium Nitride 155
5.2.2 Synthesis and Characterisation: Lithium Nitride Nanowires . 157
5.2.3 Lithium-7 Static NMR: Characterisation of the Nanowires . 160
5.2.4 Lithium-7 Static NMR: Line Shape Analysis 165
5.2.5 Discussion: Lithium Ion Diffusion and Hydrogenating Rates in Lithium Nitride Nanowires 171
5.3 Bulk Lithium Imide - Amide Non-Stoichiometric Mixed Phase Materials 174

5.3.1 Literature Review: Crystal Structures and Dynamics in Lithium Amide and Lithium Imide 174
5.3.2 Synthesis and Characterisation: Ammonia Storage in the Lithium Imide - Amide System 180
5.3.3 Lithium-7 Static NMR: Variable Temperature Line Shapes of Lithium Amide and Lithium Imide 183
5.3.4 Lithium-7 Static NMR: ^{1}H Decoupling Measurements 185
5.3.5 Lithium-7 Static NMR: Line Shape Analysis on Samples (a), (b) and (c) 186
5.3.6 Lithium-7 Static NMR: Spin-Lattice Relaxation Measurements on Samples (a), (b) and (c) 190
5.3.7 Lithium-7 Static NMR: Line Shape Analysis on Samples (d), (e) and (f) 192
5.3.8 Discussion: Structure and Dynamics in Lithium Imide . . . 197
5.4 Conclusion 199

6 Final Summary and Concluding Remarks **201**

References **205**

***Appendix A:* Processing MQMAS Data** **232**

***Appendix B:* Low-Dimensional Nanostructures of Lithium Nitride (*In preparation*)** **234**

Abbreviations

BET	Brunauer Emmett Teller (isotherm for multi-layer coverage)
CS	Chemical Shift
CP	Cross Polarisation
CSA	Chemical Shift Anisotropy
CT	Central Transition
CW	Continuous Wave (decoupling)
DAS	Dynamic Angle Spinning
DFT	Density Functional Theory
DOE	Department of Energy (USA)
DOR	Double Rotation
DSC	Differential Scanning Calorimetry
DUMBO	Decoupling Under Mind Boggling Optimisation
EFG	Electric Field Gradient
fcc	face centered cubic
FID	Free Induction Decay
FWHM	Full Width Half Maximum
GUI	Graphical User Interface
HT	High Temperature
IR	Infra Red
LOHC	Liquid Organic Hydrogen Carriers
LT	Low Temperature
MAS	Magic Angle Spinning
MD	Molecular Dynamics (simulations)
MOF	Metal Organic Frameworks
μSR	Muon Spin Resonance

MQMAS	Multiple Quantum Magic Angle Spinning
MW	Microwave (synthesis)
NMR	Nuclear Magnetic Resonance
PAS	Principal Axis System
PCI	Pressure Composition Isotherm
PEM	Polymer Electrolyte Membrane (fuel cell)
(P)ND	(Powder) Neutron Diffraction
PPM	Parts Per Million
(P)XRD	(Powder) X-Ray Diffraction
QIS	Quadrupolar Induced Shift
RF	Radio Frequency
RMS	Root Mean Square
RPM	Revolutions Per Minute
SAED	Selected Area Electron Diffraction
SSB	Spinning Side Bands
SEM	Scanning Electron Microscopy
SO	Solid Oxide (fuel cell)
ST	Satellite Transition
TEM	Transmission Electron Microscopy
TGA	Thermogravimetric Analysis
VLS	Vapour Liquid Solid
ZMOF	Zeolite Metal Organic Frameworks

Chapter 1

Context and Motivation: Hydrogen Storage

1.1 Towards a Hydrogen Powered Future

Environmental concerns, increasing cost of extraction and depletion of fossil fuels motivate the quest for alternative energy sources[1]. The two most promising alternative energy sources are electricity or hydrogen[2,3]. The electrical infrastructure is already highly developed, which gives electricity a head start over hydrogen. The crux of using electricity as power lies in green methods of generation. Wind, tidal, solar and nuclear power technologies, or at least carbon capture and sequestration while coal stocks last, will ultimately be amalgamated to generate electricity without production of CO_2, at least in the short term future.

For mobile applications, the electric motor exhibits a doubling in efficiency at optimum power operation levels, over the internal combustion engine[4]. However battery technology is the Achilles heel of the electric vehicle. The best efforts to date for electrical storage for on-board power use lithium ion batteries, which have the highest energy density of electrical storage methods[5]. However, the increased weight of lithium ion batteries results in a reduction in the energy density by a factor of ≈ 100 compared to gasoline. Thus vast increases in mass and volume of the storage media are required to achieve the US DOE target[6] for a vehicle range of around 300 miles between refueling. Furthermore, the fastest charging time for a 300 mile vehicular range is an impracticable 2.5 hours, even using high power charging circuits[7].

On the other hand, the hydrogen fuel cell offers an on board alternative means of producing electrical power, circumventing the disadvantages of batteries. Thomas[2] compares the merits of a vehicle powered by a polymer electrolyte membrane (PEM) fuel cell powered by hydrogen stored in a compressed cylinder, with a vehicle powered by a battery. The fuel cell with gas cylinder (at 700 bar) approach has approximately half the vehicle mass, improves the specific energy density by a factor of 3 compared to battery technology, decreasing required storage volume by

a factor ≈ 2 and specific weight by a factor ≈ 1.75. The result is improved vehicle efficiency and handling. Subsequently a similar reduction in CO_2 emissions occurs; in fact, the battery powered vehicle makes no improvement on that powered by petroleum owing to the increased overall weight of the vehicle with batteries. Furthermore, the refueling time is reduced to 10 minutes via this method. Several challenges must be overcome before the potential of hydrogen my be realised[8]; broadly speaking these are production, distribution and storage of hydrogen.

Hydrogen is the most abundant element on Earth, and therefore a potentially unlimited source of energy. Hydrogen can be produced from reforming or gasification of fossil fuels; this coupled with carbon capture may provide a short term solution. Alternatively hydrogen can be produced via electrolysis of water, a more sustainable approach, provided clean production of electricity in the first instance. More novel methods including production from wet biomass[9], thermochemical cycles[10] or photocatalytic processes[11], which are still in their birth stages. The ideal production method will either use solar energy directly or electricity from carbon neutral sources.

The distribution method of hydrogen is inextricably linked to its storage method, and ultimately will be governed by what storage methods are found to be most favourable. It is possible to envisage an infrastructure which distributes hydrogen via underground pipe lines, analogous to natural gas distribution. Storage in the static context may hold hydrogen in large, low pressure underground tanks. However, this storage solution would be inappropriate for the mobile context, since space saving is critical. The crux of the emergent hydrogen economy currently is a effective storage methods for mobile applications[12].

1.2 The Hydrogen Storage Challenge

The physical properties of the H_2 molecule make it a challenge to store efficiently. The H_2 molecule has a low molecular weight ($M_r = 2$), low boiling point (20.4 K at 1 bar) and low critical point (32 K). This results in the lowest density of 0.090 kg m^{-3} at 1 bar and 273 K of all the chemical elements in its ambient phase (gas)[13]. For hydrogen to succeed as an alternative energy vector, it must provide an overall improvement in energy efficiency throughout the entire hydrogen cycle from harvesting through to consumption, compared with using electricity. At the storage point of the cycle, this means minimising the weight and space used (gravimetric capacity and volumetric density). Thus the United States Department of Energy (US DOE) has set criteria for suitable hydrogen storage media. The ultimate targets are[14,15]:

- gravimetric H_2 capacity: 2.5 kWh/kg (7.5 $wt\%$ H_2)
- volumetric H_2 density: 70 kg H_2 m^{-3}
- min/max operating ambient temperatures: -40/60 ^oC
- cycle life ($\frac{1}{4}$ tank to full): 1500 cycles
- operating pressure min/max: 3/12 bar
- system filling time (5 kg H_2): 2.5 min
- Vehicular range: 300 miles

Optimising the gravimetric capacity, volumetric density, operating temperatures, operating pressure and cycle life will result in optimum efficiency and minimal environmental impact. The operating temperature is targeted to work in the operable range of a hydrogen fuel cell, recycling produced heat from the fuel cell. In addition, factors such as system filling time and vehicular range define reasonable operation for a first world economy.

One other key factor of effective hydrogen storage is safety and public perception. The high flammability of hydrogen, as demonstrated by the Hindenburg disaster of 1937 (explosion of the German airship which took 36 lives), has created a general fear surrounding hydrogen. However it was the flammable skin material which started the fire[16]. It is worth pointing out that in the world today usage of highly flammable materials is routine (e.g. natural gas and petroleum). Managed correctly with suitable technologies and protocols, their is no reason that hydrogen should pose any greater risk than chemicals currently used for energy. Furthermore, hydrogen has a much lower toxicity than petroleum or battery materials; any leakage would pose no environmental/health threat. Therefore, hydrogen has the potential to be a safer energy vector than batteries or hydrocarbons. For this to be realised, the design of the storage media is crucial to prevent leakage.

The following sections will discuss different technological approaches towards meeting the DOE targets (table 1.1). It should be made clear that no current existing method yet fulfills all the DOE criteria, but different methods have different attributes. Gaseous and liquid storage are conventional methods using established technologies, whereas both liquid- and solid-state chemical storage are novel. The concept of chemical storage is to utilize chemical bonds between hydrogen and other atoms as a way of stablising hydrogen. In principle, any hydrogen-containing compound which releases H_2 during chemical conversion to another species could be considered a chemical hydrogen store. In the following sections it will be shown why certain materials are preferable. The chemical storage methods may be sub-divided into those which store hydrogen by the following two phenomena: (i) by the forming and breaking of bonds between hydrogen and other atoms; (ii) by physisorption between hydrogen and a porous host material, where the host structure does not change chemically. In the following discussion, materials which operate by phenomenon (i) have been further sub-divided into liquid-state and solid-state storage methods.

Storage Method	Examples	Details
Gas H_2 storage[13]	Compressed gas	700 bar compression for 6 $wt\%$ H_2 and 30 kg H_2 m^{-3}.
	Hollow glass microspheres[17]	1 - 200 μm pores, act as microballoons.
	Clathrate Hydrate cages[18]	4 $wt\%$ H_2 at - 20 ^{o}C and 50 bar with THF guest.
Liquid H_2 storage[13]		Cooling to $<$ 32 K, expensive. Boil off rate 0.4 % daily for a 50 m^3 tank.
Liquid-state chemical storage	Phosphonium Borate[19]	Decomposition of liquids require temperatures 100 - 300 ^{o}C.
	Liquid organic hydrogen carriers (LOHC)[20]	
	Imidazolium Ionic Liquids[21]	
	Ammonia[22], Formic Acid[23], Methanol[24]	
Solid-state chemical storage: porous media	Metal organic frameworks[25]	Hydrogen physisorbed onto surface of pores. Sorption at 77 K and pressures $>$ 80 bar required.
	Carbon based materials[26]	
	Zeolites[27–29]	
Solid-state chemical storage: metal hydrides	Binary metal hydrides[30,31]	Strong chemical bonds requires temperatures $>$ 120 ^oC to decompose.
	Alloy metal hydrides[13,32]	
	Complex metal hydrides[33,34]	

Table 1.1: Summary of all hydrogen storage methods.

The storage capacities of some emerging solid-state methods are compared with conventional methods in figure 1.1.

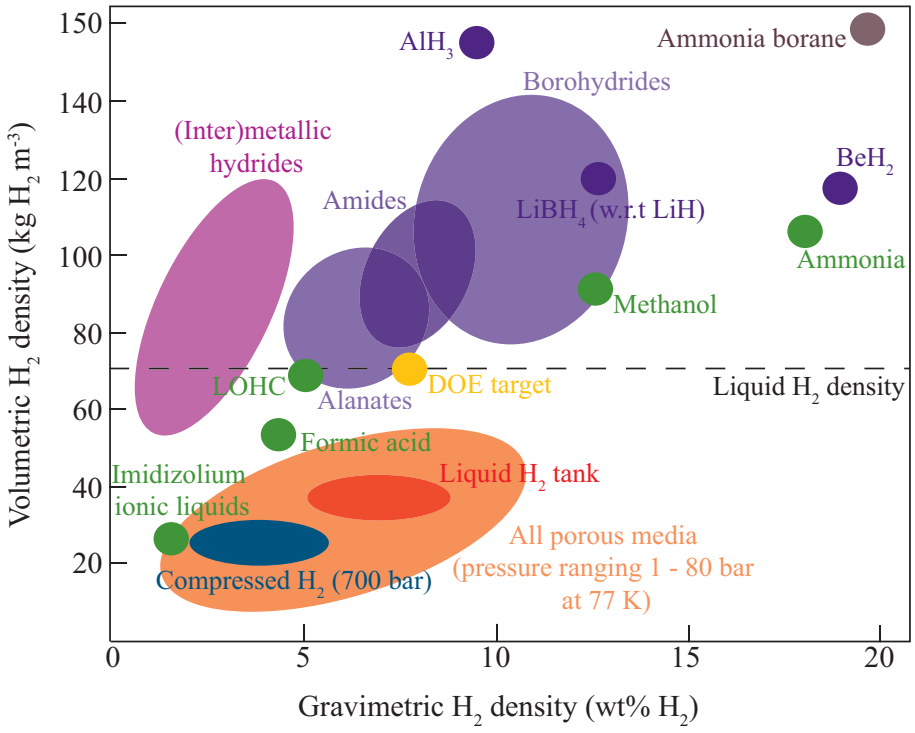


Figure 1.1: Gravimetric and volumetric densities of different hydrogen storage options. This figure is copied from Edwards *et al.*[35] and modified to show the latest designs and some key (complex) metal hydrides. The liquid state materials are marked individually since they span a broad range.

1.3 Storage of Hydrogen in the Gas Phase

1.3.1 Compressed Gas

At ambient temperatures, hydrogen may be stored as a gas. Since it has a much lower energy density by volume compared to hydrocarbon fuel, it is preferable to pressurise the storage cylinder to improve the volumetric density. The storage cylinder must therefore be reinforced to withstand such pressures; a large gravimetric penalty is paid even with the most advanced composite materials. Conven-

tional high pressure storage (700 bar) therefore requires heavy vessels, resulting in poor gravimetric capacity. The current industry standard is a 110 kg cylinder which achieves 6 $wt\%$ H_2 and 30 kg H_2 m^{-3}, falling short of the DOE targets[13]. Safety considerations limit the storage pressure to 700 bar with current materials. Structuring the inside of a storage vessel with capillary arrays may provide a safer alternative, since each capillary hold only a small amount of hydrogen and thus reduces the risk of explosion during accidents. However capillary arrays would result in an overall lower gravimetric capacity and volumetric density[30].

1.3.2 Hollow Glass Micro-spheres

Hollow glass micro-spheres with pore diameters of the range 1-200 μm may be engineered using a glass frit bonding method[36], acting like micro-balloons[17]. The interconnected micro-pores allow in- and out-gasing, however the rate was found to be too slow. The rate can not be improved significantly by heating, owing to the poor thermal conductivity of inorganic glasses.

1.3.3 Clathrate Hydrates

Alternatively, clathrate hydrate cages which encapsulate H_2 gas within $\sim$300 μm diameter micro-pores form at 2000 bar and -20 ^{o}C. The sII hydrate is attractive for hydrogen storage because it comprises all non-toxic elements. The system must be kept frozen or hydrogen will be rapidly released with safety implications. Also, 2000 bar is too high to achieve in practice[18]. The inclusion of tetrahydrofluoride as a second guest compound lowers the necessary pressure to stabilise the structure to 50 bar, at around the freezing temperature of water. The storage capacity was then reduced to ~ 4 $wt\%$ H_2, and with known clathrate structures this is unlikely to improve much[23].

1.4 Storage of Hydrogen in the Liquid Phase

H_2 in its liquid phase has a density of 70.85 kg m^{-3}; therefore a vastly superior energy density over gaseous H_2. However, the low critical temperature of hydrogen (32 K) means cooling to liquid hydrogen temperatures requires an energy intensive process. Typically, hydrogen will be pre-cooled by liquid nitrogen (77 K), and then undergoes isenthalpic Joule-Thomson expansion to produce a liquid. The technical work done is roughly 15.2 KWh kg^{-1}, almost half of the calorific value of hydrogen combustion. This process takes too much energy to be viable. Furthermore, insulated spherical containers with the lowest boil-off rates are difficult and expensive to manufacture; the daily boil-off rate is about 0.4 % for a 50 m^3 vessel, and reduces with tank size. Liquid hydrogen is only suitable for applications where the hydrogen will be used quickly, and high costs are acceptable; such as air and space applications[13].

1.5 Liquid-State Chemical Storage

Liquid-state chemical storage materials break/form chemical bonds with hydrogen upon (de-)hydriding. Apart from the phosphonium borate system, the principles of operation are categorised as follows: firstly, the cycling between saturated and unsaturated organic compounds; secondly, the decomposition of small molecules (e.g. ammonia, methanol, formic acid). Table 1.2 summarises the key liquid-state hydrogen storage materials.

Storage Method	Capacity and typical operating conditions
Phosphonium Borate[19]	0.25 $wt\%$ H_2 < 100 ^{o}C in toluene.
Liquid organic hydrogen carriers (LOHC)[20]	5.8 $wt\%$ H_2 at 50 - 200 ^{o}C; rehydrogenation under 70 bar H_2.
Imidazolium Ionic Liquids[21]	2.2 $wt\%$ H_2, 230 ^{o}C gives 60 % dehydrogenation in 50 minutes.
Ammonia[22]	17.6 $wt\%$ H_2 at 300 ^{o}C with Ru catalyst. Purity for fuel cells an issue.
Formic Acid[23]	4.4 $wt\%$ H_2 at 100 ^{o}C in 30 minutes with Ru catalyst.
Methanol[24]	12.5 $wt\%$ H_2 at 250 ^{o}C.

Table 1.2: Summary of the most popular liquid-state chemical hydrogen storage methods.

Phosphonium borate species are zwitterionic with a positive charge located at the phosphorus atom and a negative at the boron[37]. Bulky substituent groups prevent stabilisation, causing the molecule to be a frustrated Lewis pair. Loss of H_2 occurs upon warming to 100 ^{o}C in toluene, which may be reversed by exposure to 1 bar H_2 at ambient temperatures. However, only 1 molecule of H_2 is gained for every phosphonium-borate molecule, resulting in only 0.25 $wt\%$ H_2. However when reported, this was the first example of reversible H_2 activation by a nonmetallic species[19].

Liquid Organic Hydrogen Carriers (LOHC) are organic liquids which may reversibly cycle between saturated/unsaturated molecules by release/uptake of hydrogen. Without a catalyst, temperatures in excess of 800 ^{o}C would be required for hydrogen cycling[13]. Cyclic compounds which contain just carbon and hydrogen (e.g cyclohexane) have the best gravimetric/volumetric capacity, however notable success is observed with five-membered ring heterocycles which contain

nitrogen[38]. For example, N-ethyl carbazole may release 5.8 $wt\%$ H_2 at 50 - 200 ^{o}C, and re-hydrogenate at 70 bar at 160 ^{o}C, using a noble metal catalyst (Ru, Pt Pd) catalyst. Since an on-board reformer is regarded as too complex; proposals are to simply swap dehydrogenated liquid for hydrogenated liquid[20].

Imidazolium ionic liquids which contain a phenyl ring afford the opportunity for reversible hydrogenation analogous to that for LOHC. The uptake of 3 - 6 hydrogen atoms gives at best a gravimetric capacity of 2.2 $wt\%$ H_2 and volumetric density of 30 kg H_2 m^{-3} at atmospheric pressure. The best kinetics have been found with the addition of catalytic Ir^0 nano-particles, requiring 50 minutes for dehydrogenation with the liquid heated to in excess of 230 ^{o}C for a 60 % yield[21].

With impressive gravimetric capacity of 17.6 $wt\%$ H_2 and volumetric density $\sim$120 kg H_2 m^{-3}, ammonia provides a carbon-free alternative[22]. Production and distribution of ammonia is already well established; however production currently proceeds via the energy intensive Haber-Bosch process. Ammonia must be decomposed before the hydrogen can be utilised requiring temperatures around 300 ^{o}C, and is strongly endothermic (46 KJmol^{-1}) even with a Ru catalyst. Furthermore, the decomposed product would need to be purified before use with a PEM fuel cell. However, decomposition may be avoided by use of NH_3 with a Solid Oxide (SO) fuel cell. The SO fuel cell may also run on methanol. Unlike hydrogen, ammonia is not flammable, but most crucially high toxicity makes it unlikely to become accepted. This problem may circumvented by chemical storage of ammonia; an attempt has been made with porous metal amine complexes, such as $Mg(NH_3)_6Cl_2$[39]. Storage of Ammonia will be discussed again in chapter 5, using the Li-N-H system.

Organic liquids with a high percentage of hydrogen per unit weight, such as LOHC, methanol or methanoic (formic) acid may react in the presence of O_2 to give CO_2 and H_2 (steam reforming), or in the presence of H_2O to give CO and H_2 (par-

tial oxidation)[23]. For hydrocarbons, the technology would require an on-board reformer to obtain the hydrogen (at temperatures $\sim$ 600 ^{o}C). The fuel cell is poisoned with CO concentrations $>$ 10 ppm, requiring heavy and bulky purification equipment. On the other hand, methanol yields much lower CO impurity levels, and may be reformed at lower temperatures (c.a. 250 ^{o}C), reducing the amount of required purification technology on-board. Formic acid, which releases its 4.4 $wt\%$ H_2 at temperatures around 100 ^{o}C in around 30 minutes using a Ru catalyst, is promising[24]. However similar fuel cell poisoning problems exist.

1.6 Solid-State Chemical Storage

Solid-state chemical storage materials operate in a similar manner to liquid-state materials, with the forming and breaking of chemical bonds. The principles of operation are as follows: firstly, by the shuttling of hydrogen in and out of a lattice, which undergoes a phase transformation to accommodate the hydrogen (intermetallic hydrides); secondly, by decomposition of the material into elemental or simpler components (complex/ionic hydrides or phosphonium borate). A pertinent issue with solid-state storage methods is the kinetics of decomposition; various nano-engineering efforts towards reducing diffusion distances in the solid phase, in order to improve the kinetics will be also be discussed. Table 1.3 summarises the key solid-state hydrogen storage materials.

Class of material	Common examples	Capacity and typical operating conditions
Ionic metal hydrides[31]	MgH_2	7.6 $wt\%$ H_2, 360 ^{o}C.
	BeH_2	18.26 $wt\%$ H_2, 280 ^{o}C, very toxic.
	AlH_3	10.0 $wt\%$ H_2, 180 ^{o}C, irreversible.
(Inter)Metallic hydrides[13,40]	LaN_5H_6	1.37 $wt\%$ H_2 released at 2 bar, 25 ^{o}C.
	$FeTiH_2$	1.89 $wt\%$ H_2 released at 5 bar, 30 ^{o}C.
	Mg_2NiH_4	3.59 $wt\%$ H_2 released at 1 bar, 280 ^{o}C.
	$PdH_{0.6}$	0.56 $wt\%$ H_2, 0.02 bar 25 ^{o}C.
Complex metal hydrides[33,41]	Alanates	4 - 8 $wt\%$ H_2 released between 130 - 230 ^{o}C.
	Borohydrides	9 - 18 $wt\%$ H_2 released between 350 - 650 ^{o}C.
	Imides and Amides	5 - 10 $wt\%$ H_2 released between 200 - 400 ^{o}C.
Ammonia borane[42,43].	BH_3NH_3	19.6 wt% released at < 200 ^{o}C
	Amido boranes[30]	7.5 - 10 $wt\%$ H_2 released at < 120 ^{o}C.

Table 1.3: Summary of solid-state chemical hydrogen storage materials. Successful examples to date in each class have been included; note this is not exhaustive.

1.6.1 Metallic/Intermetallic Hydrides

An feature of many transition metals (particularly electropositive ones) is their ability to form metallic/intermetallic hydrides. These materials possess many

properties associated with metals, such as conduction of electricity and or a metallic/graphitic appearance. Metallics consist of a single element, whilst intermetallics are alloys of the form AB, AB_2, A_2B or AB_5. Usually element A will have a high affinity for hydrogen and B a low affinity. Ni is often used as B (e.g $MgNi_4$), since it is an excellent catalyst for H_2 dissociation[13,41].

Hydrogen uptake occurs via chemisorption at the metal surface. The H_2 molecule dissociates, shares electrons with the host metal and when the surface becomes saturated may diffuse into the bulk. It will reside at interstitial sites within the metal lattice. Whilst the hydrogen/metal concentration > 0.1, hydrogen is dissolved into the metal lattice forming a solid solution; the α phase. At higher concentrations, the β phase forms. This transformation occurs between the hydrogen/metal ratio limiting values 0.1 to 0.9, where the non-expanded α-phase and anisotropically expanded β-phase coexist[13].

Only a small pressure increase is associated with transformation between the α and β phases; therefore this region offers suitable hydrogen cycling. The entropy change is roughly the same for all systems, since it corresponds to the entropy change from molecular hydrogen gas to dissolved hydrogen. Therefore an equilibrium pressure around 1 bar at 300 k requires an enthalpy change $\sim$ 30 - 40 kJ(mol H_2)$^{-1}$. The exact enthalpy change depends upon the host metal/alloy. The $LaNi_5H_6$, $PdH_{0.6}$ and $TiFeH_2$ systems will cycle close to ambient conditions, however these materials contain relatively heavy elements and the gravimetric storage capacities usually do not exceed 3 $wt\%$ H_2[32,40].

A consequence of coexistence of the α and β phases is the formation of lattice defects and internal strain fields, which cause degradation of the brittle host metals. This often limits their lifetime[44].

Typically, inter-metallic compounds have a hydrogen/metal concentration ratio up to 2. When this value is exceeded, the tendency is for ionic or complex metal

hydride formation.

1.6.2 Ionic Metal Hydrides

Alkaline and alkaline earth metals form ionic compounds with hydrogen. High gravimetric capacities (7 - 20 $wt\%$ H_2) occur for light elements of the period 1 and 2 hydrides. In these systems, the hydrogen is released by chemical decomposition. Decomposition temperatures tend to be high, owing to the strong ionic bonds. For the alkaline metals, decomposition temperature decreases going down the group, starting with LiH at 700 ^{o}C, ruling these out. Alkaline earth metals exhibit the reverse trend of increasing decomposition temperature going down, making BeH_2 and MgH_2 favourable choices. Whilst BeH_2 offers a high gravimetric capacity and decomposition at 250 ^{o}C, it (and many other compounds containing Be) is extremely toxic[31].

The more successful metal hydride systems MgH_2 and AlH_3 offer decomposition at 360 and 180 ^{o}C respectively, which are approaching the US DOE criteria. However, the H_2 equilibrium pressure of AlH_3 at ambient temperature is 7 kbar, suggesting very high pressures are required to re-hydride this material from aluminum metal after decomposition. This feature renders AlH_3 irreversible for mobile applications. AlH_3 is commonly prepared by reacting $LiAlH_4$ with $AlCl_3$, which would require an energy input equivalent to 70 % of the energy stored in AlH_3[45].

On the other hand, MgH_2 may be cycled reversibly with 10 bar overpressure for hydrogen uptake. However, the kinetics of MgH_2 are too slow for mobile applications, to the extent that only 55 % of the available hydrogen is released in 800 minutes[46]. The sorption kinetics may be improved by milling MgH_2 to smaller particle sizes, increasing the overall sorption surface area. In particular, milling with a small amount of Pd allows the formation of catalytic Pd nano-particles, where the hydrogen spillover mechanism can enable full dehydrogenation in 50

minutes at 360 ^{o}C[47]. Alternatively, Nb_2O_5 may act as a catalyst, being shown to reduce the growth of grains by the formation of MgO as Nb_2O_5 is reduced[30,48]. The disadvantage of the catalytic additive strategy is a lowering of the gravimetric capacity; a more beneficial alternative may be to destabilise with another hydride.

1.6.3 Complex Metal Hydrides

Complex metal hydrides comprise anions which contain hydrogen covalently bound to a light atom centre, such as alanates $[AlH_4]^-$, borohydrides $[BH_4]^-$ or amides $[NH_2]^-$ stabilised by light metal cations such as Li^+, Na^+, Mg^{2+} or Al^{3+}. The usual cycle pathway is between the complex metal hydride and associated hydride, (for example $NaAlH_4 \rightarrow NaH + Al + \frac{3}{2}H_2$); this step has an associated gravimetric capacity in the range 6 - 15 $wt\%$ H_2 for all complex metal hydrides[33]. Two problems are common with complex metal hydrides. Firstly, they are usually very thermodynamically stable with decomposition enthalpies ranging from 50 - 80 kJmol^{-1} H_2 with respect to metal hydride formation; hence a large amount of energy is spent acquiring the hydrogen from the lattice. The second is poor kinetics, requiring high temperatures to progress beyond stable reaction intermediates; often in the range 100 - 400 ^{o}C, dependent on the reaction intermediate(s). Decomposition of $NaAlH_4$ proceeds via the intermetallic Na_3AlH_6 intermediate.

For both alkali metal borohydrides and alanates, the desorption temperatures are found to decrease with Pauling electronegativity of the metal atom (decreasing along the series K, Na, Li) which forms the cation[34]. In the alanate series, $LiAlH_4$ is unstable at ambient conditions, and hence the study of $NaAlH_4$ has prevailed. On the other hand, $LiBH_4$ is stable at room temperature and offers a much higher gravimetric capacity. However slow kinetics of $LiBH_4$ decomposition require high temperatures $>$ 500 ^{o}C. The Li_3N - Li_2NH - $LiNH_2$ offers a different approach,

whereby cycling between the 3 compounds allows (de-)hydrogenation. Again, the kinetics are slow and the decomposition temperatures are high.

Complex metal hydrides were realised as an effective method for hydrogen storage materials after Bogdanovic and Schwickardi[49] showed the decomposition of $NaAlH_4$ could be catalysed by doping with Ti, reducing decomposition temperatures to less that 100 ^oC. Success at improving the kinetics of $LiBH_4$ has been found with the addition of various catalysts, such as SiO_2[50] or with transition metal fluorides (NbF_5, TiF_3, LaF_3)[51].

Alternatively, efforts have been made to thermodynamically destabilise the hydrogenation state. This has been achieved using multi-component (multinary) systems such as: $Mg(BH_4)_2/CaH_2$[52]; $LiNH_2/LiAlH_4$[53]; $Mg(NH_2)_2/Ca(NH_2)_2/LiH$[54]; $(LiNH_2)_x/(LiBH_4)_{1-x}$[55]; and $LiBH_4/LiNH_2/MgH_2$[56,57]. Multi-component systems allow an alternative route of decomposition at lower enthalpy to occur in comparison to the single phase counterparts, allowing dehydrogenation in the range 100 - 200 ^oC for the best cases. For example, the $LiBH_4/MgH_2$ system leads to the formation of MgB_2 in place of elemental boron[58]. Similar decomposition has also been predicted using other multi-component light metal hydrides (e.g. CaH_2 or AlH_3)[59]; the advantage of using a light metal hydride is the minimisation of the gravimetric penalty. Dual-cation systems, such as $LiBH_4/Mg(BH_4)_2$ also exhibit lower decomposition temperatures; the role of the cation is clearly also important, and has received little attention to date[60].

Production of multi-component systems is typically done by ball milling the individual phases together, to achieve intimate mixing. The theme of particle size reduction has become an important one in association with complex metal hydrides, and various other nano-engineering approaches towards producing nanometer size particles have also been examined. For example, it has been found that confining $LiBH_4$ in a nano-porous carbon aerogel scaffold with average pore size $\sim$ 13 nm

improved dehydrogenation times by up to a factor of 50[61]. It has been shown that nano-confinement of $LiBH_4$ significantly alters the solid-state diffusion properties owing to the increase in surface and amorphous regions between grains[62], which can be linked to improvements in hydriding. Similar improvements have been observed with nano-structuring and -confinement of other solids[63]; in particular for 2 nm Mg/MgH_2 clusters[64].

1.6.4 Ammonia Borane

Ammonia borane is an adduct of NH_3 and BH_3. It is a solid at room temperature, and decomposes at temperatures $> 200\ ^oC$. The high valence of both light atoms: B and N, allows a high theoretical gravimetric content (19.6 wt%). Major drawbacks of this material are NH_3 release which poisons the fuel cell and thermodynamic irreversibility. A vast array of efforts have employed many of the usual engineering strategies outlined above, including nano-confinement[63], catalysis[65] or dissolution in ionic liquids[66] with varying degrees of success. In different cases, the reaction pathways differ leading to formation of different products, leaving this system not fully characterised[42,43].

1.7 Solid-State Porous Media

Porous media operate in the solid state, however the principle of operation here is by physisorption of hydrogen on to the high surface area of the material. The key factors in design of these materials are: pore volume, pore surface area and choice of elements. The ideal elements will provide the highest affinity for H_2, and have low atomic weight. Table 1.4 summarises the main types of porous media for hydrogen storage.

Class of material	Common examples	Capacity and typical operating conditions
Zeolites	Sodalite[27] H-SSZ-13[67] NaY[28]	< 2 - 3 $wt\%$ H_2 at 15 bar and 77 K.
Metal organic frameworks	MOF-5 MIL-101[68] NOTT-112[69] MOF-177[70]	< 3 $wt\%$ H_2 at 1 bar and 77 K. < 5 - 10 $wt\%$ H_2 at ∼80 bar and 77 K.
Carbon based materials	activated carbon carbon nanotubes carbon nanofibers Zeolite templated carbon	1 - 4 $wt\%$ H_2 at 298 K 100 bar[71,72]. 2 - 6 $wt\%$ H_2 at 298 K and ∼110 bar[73]. ~ 7 $wt\%$ H_2 at 77 K and 20 bar, pore sizes > 1.2 nm[74].

Table 1.4: Summary of porous media for hydrogen storage. Successful examples to date in each class have been included; note this is not exhaustive.

1.7.1 Zeolites

Zeolites are naturally occurring microporous hydrated aluminosilicates, which may be expressed chemically as $M_{\frac{2}{n}}(OAl_2O_3.xSiO_2.yH_2O)$ with x>2; the metal has valence n and y moles of water reside in the voids. The Al and Si tetrahedral atoms form a 3-dimensional network of AlO_4 and SiO_4 tetrahedra linked by shared oxygen atoms. The porous nature of zeolites makes them suitable hydrogen storage media; the gravimetric capacity of many has been measured[27,28,75]. The most promising zeolites include NaX (or cation exchange variants) with 1.7 - 1.9 $wt\%$ H_2 at 15 bar and 77 K[28,29]. H-SSZ-13 with the chabazite-type structure has 1.28 $wt\%$ H_2

at 0.92 bar and 77 K[67].

1.7.2 Carbon-Based Materials

Activated Carbon

Treatment of carbon with oxygen opens capillary passages with inter-connected pores exhibiting high surface area, up to 3000 $m^2 g^{-1}$. The highest isosteric heats of adsorption are $\sim$ 6.4 $KJmol^{-1}$ at 77 K and 60 bar for zero surface coverage (observed for AX-21[71]). In this regime, ~ 5 $wt\%$ H_2 was achieved. A small gravimetric capacity has also been observed (~ 0.5 $wt\%$ H_2) at ambient temperature and 60 bar. It was found that the isosteric heats of adsorption above the monolayer are very low[26]. Therefore, the best design in activated carbons for hydrogen storage have high microporous surface area to volume ratios.

Carbon Nanotubes

Optimum pore sizes for hydrogen storage are found to be no more than a few molecular diameters, allowing potentials from the walls to exhibit appreciable magnitude within the pore centres. Indeed around 50 % of the pores in many activated carbons are $>$ 4 nm, which is too high. On the other hand, carbon nanotubes offer inner diameters between 1.5 and 15 nm. The highest gravimetric capacities are found to be reproducible up to 3 - 4 $wt\%$ H_2 at 298 K or up to ~ 10 $wt\%$ H_2 at 77 K and 100 bar. Hydrogen uptake has been found to increase with tube diameter, and vary with packing arrangement[72,73].

Carbon Nanofibers

Carbon nanofibers are grown on a metal catalyst with diameters 10 - 100 nm. The insides contain platelets of carbon arranged in a herringbone fashion. This

arrangement provides a much larger BET surface area than for nanotubes; usually $\sim$ 300 m^2g^{-1}. These structures are similar, attaining up to $\sim$ 6 - 8 $wt\%$ H_2 at 298 K and $\sim$110 bar[26,73].

Carbon-Templated Zeolites

The most recent approach towards porous carbon media is to use a zeolite as a template for carbon assembly, with pores of similar shapes and dimensions to those of zeolites. Excellent gravimetric capacities up to $\sim$ 7 $wt\%$ H_2 have been achieved at 77 K and a moderate 20 bar with pore sizes as small as 1.2 nm[74]. As expected, H_2 uptake improves with BET surface area[76]. Doping porous materials with metallic nano-particles affords another strategy towards better hydrogen storage properties, by allowing the spillover mechanism to occur (e.g. doping with Pd nano-particles[77]).

1.7.3 Metal Organic Frameworks

Metal organic frameworks (MOF) comprise metal centres co-ordinated with organic linkers in an array, yielding 3D porous structures with low density and high surface area. Common classes of organic linkers include the similar carboxylate and heterocyclic azolate groups. Particular success with MOF for hydrogen storage has been found with carboxylate ligands. This was first realised for MOF5[78,79] ($Zn_4O(BDC)_3$, where BDC = 1,4-benzenedicarboxylate)[78], which has storage capacity around 2 - 4 $wt\%$ H_2[30] at cryogenic temperatures and 1 bar pressure. Following this success a variety of similar structures have been synthesised[25]. Notably, the highest storage capacities have been found for MOF-177[70] which may hold 7.5 $wt\%$ H_2 and 50.3 kg H_2 m^{-3}, and NOTT-112[69] achieved 10 $wt\%$ H_2 and 48 kg H_2 m^{-3} at pressures around 80 bar and 77 K. However both MOF-177 and NOTT-112 have similarly low capacities to most other MOF at lower pressures. In

this case, it has been found that both a large pore volume and high BET surface area are both necessary for high storage capacity.

Covalent organic frameworks (COF) comprise just organic linkers held together by covalent bonds. Calculations predict COF to have high gravimetric capacities, up to 20 $wt\%$ H_2 for COF-108 at 100 bar and 77 K owing to lack of heavy metal atoms. However volumetric capacity is not expected to exceed 50 kg H_2 m^{-3} which is low considering the density of such materials[80]. The progression of this type of storage material awaits a synthetic route towards optimal pore sizes ~ 10 $\mathring{A}$.

1.8 Summary: Hydrogen Storage Systems Studied in this Thesis

In this chapter, the most common approaches towards solving the hydrogen storage problem have been introduced. All the methods presented fall short of different aspects of the DOE criteria. The physical methods (compressed gas, liquefaction, clathrate hydrates and glass micro-spheres) generally fail on storage capacity, and liquefaction also requires operating temperatures which are too low. The same is the case for liquid-state chemical storage. In addition, the storage methods employing ammonia, methanol and formic acid are currently too technologically complicated to implement. Intermetallic hydrides (e.g. $LaNi_5H_6$) may operate close to ambient conditions, however the storage capacity is again too low. Ionic and complex metal hydrides are both thermodynamically stable, and kinetics are also too slow. However, complex metal hydrides have very high storage capacities, and therefore afford the potential for destabilisation. On the other hand, porous media suffer because high pressures and low temperatures are required in order to retain enough hydrogen.

If complex metal hydrides are going to be effective hydrogen stores, then the cycling temperatures and times must be reduced, whist gravimetric capacity is retained. The best techniques for achieving this are: to use light elements; catalyse the decomposition; lower the crystallinity (by either nano-confinement or ball milling); and/or destabilise the decomposition by use of additives. The aim of destabilisation is to lower the temperature of decomposition to within the operable range by providing a more favourable thermodynamic route, thereby improving the kinetics.

In this thesis, the $LiBH_4/MgH_2$ and Li-N-H systems were both studied (chapters 4 and 5 respectively). A comparison with the US DOE criteria of these systems is made in table 1.1. Understanding the decomposition of these systems is important for the future design of similar improved versions of these materials. However, this can be challenging for the following reasons. Firstly, multi-component/destabilised systems usually undergo complicated multistage routes of decomposition, where the route may depend upon reaction conditions at different stages. Secondly, nano-structuring lowers the crystallinity; this may cause poor resolution when using many diffraction- and scattering- based methods.

The opposite is the case for porous media. For use as hydrogen stores, the operating temperatures must be increased and pressures decreased, both towards ambient operating conditions. Again, the gravimetric penalty should be minimised. The way to achieve this is to increase the isosteric heats of adsorption between hydrogen and the host. This may be done by: optimising the pore volume; maximising the pore surface area; increasing the electrostatic potentials within the pores; and/or optimising the pore texture. The pore volume must be chosen to optimise the electrostatic potentials for physisorption in the pore centres, and provide maximum space for H_2. Exposure of metal centres, or doping with metal particles/ions may also increase the electrostatic potentials within the pores.

In this thesis, NOTT-MOF were studied (chapter 3). A comparison of NOTT-MOF with the US DOE criteria is presented in table 1.1. Whilst MOF do not meet the required gravimetric/volumetric capacities, they present distinct advantages over complex metal hydrides in that kinetics are easily controlled by system overpressure. Also, NOTT-MOF do not collapse upon dehydrogenation, as some porous frameworks do. In fact, all the systems in this thesis have demonstrated operation over multiple cycles.

In conclusion, the reaction mechanisms in complex metal hydrides may be difficult to elucidate, due to low crystallinity. In this thesis, the power of NMR as a spectroscopic tool will be demonstrated on the $LiBH_4$ / MgH_2 system. The potential NMR offers for making deductions about the fundamental ionic diffusion, which may be linked to kinetics, will be demonstrated on both the $LiBH_4$ / MgH_2 and Li-N-H systems. MOF are also complicated systems, and spectra obtained from diffraction- or scattering- based methods are difficult to interpret. NMR offers the opportunity to examine just one nucleus at a time; an example of NMR spectroscopy used in this way will also be demonstrated.

Criteria	Chapter 3: NOTT-MOF	Chapter 4: $LiBH_4$/ MgH_2	Chapter 5: Li-N-H
Gravimetric H_2 capacity	×	✓	✓
Volumetric H_2 capacity	×	✓	✓
min/max operating temperatures	×	×	×
cycle life	✓	✓	✓
operating pressure min/max	×	×	×
System filling time	✓	×	×
Vehicular range	×	✓	✓

Table 1.5: Comparison of storage systems studied in this thesis with the DOE criteria. ✓ indicates the criterion is met, or × implies not met.

Chapter 2

NMR Theory and Practice

2.1 Basic Nuclear Magnetism

Many atomic nuclei possess quanta of intrinsic angular momentum, usually referred to by the term *spin*, **I**. Spin has magnitude $|\mathbf{I}|$ where I is the nuclear spin quantum number.

$$|\mathbf{I}| = \hbar\sqrt{(I(I+1))} \tag{2.1}$$

The magnetic properties of a nucleus may be satisfactorily described by a magnetic dipole moment $\boldsymbol{\mu}$, which is collinear to and related to the spin vector **I** by:

$$\boldsymbol{\mu} = \gamma\mathbf{I} \tag{2.2}$$

where γ is the gyromagnetic ratio of a nucleus defined here in units of rad s^{-1} T^{-1}. The study of the response of the nuclear magnetic dipole moment to experimental input forms the basis of nuclear magnetic resonance. The rest of this section will describe relevant theory on the nuclear magnetic resonance phenomena utilized in this thesis.

2.2 Classical Representation of Macroscopic Magnetization

2.2.1 Static Magnetic Field Case

The classical vector model affords an intuitive picture for understanding the behavior of isolated spin $I = \frac{1}{2}$ nuclei.

In the absence of a magnetic field at thermal equilibrium, an ensemble of spins possess magnetic moments oriented in random directions. In the presence of an

applied magnetic field conventionally along the z-axis $\mathbf{B_0}$, nuclei will preferentially align with the field to give a net magnetization vector $\mathbf{M}$:

$$\mathbf{M} = \sum_{\mathbf{i}} \mu_{\mathbf{i}} \tag{2.3}$$

For $\mathbf{M}$ not parallel to $\mathbf{B_0}$, $\mathbf{M}$ undergoes precessional motion about the z-axis on the surface of a cone with constant angle to the field, according to[81]:

$$\frac{d\mathbf{M}}{dt} = \gamma \mathbf{M} \times \mathbf{B} \tag{2.4}$$

Precession has a characteristic angular frequency $\boldsymbol{\omega_0}$, known as the Larmor frequency, defined in the laboratory frame of reference as:

$$\boldsymbol{\omega_0} = -\gamma \mathbf{B_0} \tag{2.5}$$

2.2.2 Time-Dependent Magnetic Field Case

Radio frequency (RF) waves provide a time-dependent magnetic field $\mathbf{B_1}$ oscillating at a frequency ω_0. The effect of an RF field upon $\mathbf{M}$ is usually considered in a frame of reference where $\mathbf{B_1}$ is static. This is called the *rotating frame*; which rotates about the z-axis at frequency ω_{RF}. Upon application of an RF pulse, $\mathbf{M}$ will precess about $\mathbf{B_1}$ in the rotating frame, in addition to precession about $\mathbf{B_0}$. Therefore a nutation frequency $\boldsymbol{\omega_1}$ may be defined in the laboratory frame as:

$$\boldsymbol{\omega_1} = -\gamma \mathbf{B_1} \tag{2.6}$$

When the frequency of the RF $\omega_{RF} = \omega_0$, the pulse is on resonance; however in practice this resonance condition is seldom met exactly. A resonance offset Ω is

therefore useful:

$$\Omega = \omega - \omega_{RF} \tag{2.7}$$

where ω is the actual frequency of the spin under nuclear spin interactions. The RF pulse is usually applied in the plane perpendicular to the z-axis; the xy-plane. The phase of the RF pulse is defined as the angle ϕ between $\mathbf{B_1}$ and the x-axis. The application of an RF pulse with duration τ_{RF} causes $\mathbf{M}$ to nutate through a flip angle θ_{RF}, defined between the z-axis and $\mathbf{M}$ at any instance in time as:

$$\theta_{RF} = \omega_1 \tau_{RF} \tag{2.8}$$

2.3 Quantum Mechanical Representation of Nuclear Magnetism

2.3.1 Density Matrix

A more useful picture of nuclear magnetic resonance emerges using quantum mechanics[82,83]. The wavefunction ψ is employed to characterise a spin state. If ψ can be expressed in the basis set of eigenvectors $\phi_1, \phi_2 ... \phi_n$, the expectation value for an observable A is given by the sum of all elements of a square matrix $i \times j$:

$$\left\langle \hat{A} \right\rangle = \sum_{ij} c_i^* c_j \left\langle \phi_i \right| \hat{A} \left| \phi_j \right\rangle \tag{2.9}$$

where c_i is the weight of ϕ_i, in ψ. The coefficients c_i may be extracted by taking scalar products with ψ, such that:

$$\langle \phi_i | \psi \rangle \langle \psi | \phi_j \rangle = c_i^* c_j \tag{2.10}$$

where the operator $|\psi\rangle\langle\psi|$ may be defined as the density operator $\hat{\rho} = |\psi\rangle\langle\psi|$. An overbar may be introduced to denote the density operator for an ensemble average ($\overline{|\psi\rangle\langle\psi|}$). The sum of the diagonal elements (or the trace) of $\rho\boldsymbol{A}$ corresponds to the expectation value $\overline{\left\langle \hat{A} \right\rangle}$. Expressed mathematically:

$$\overline{\left\langle \hat{A} \right\rangle} = Tr(\rho\mathbf{A}) \tag{2.11}$$

Diagonal elements of the density matrix for $i = j$ imply spins are in the same eigenstate so correspond to *populations* of the basis functions ϕ_i. Off-diagonal elements for $i \neq j$ exist if there is correlation between the basis functions creating *coherence* between the states.

2.3.2 Liouville-von Neumann Equation

The time-dependent Schrödinger equation calculates the evolution of a single spin state. For an ensemble of spins, the evolution of the density matrix may be calculated in a similar manner using the Liouville von-Neumann equation:

$$\frac{d\hat{\rho}(t)}{dt} = -i\big[\hat{H}_{spin}, \hat{\rho}\big] \tag{2.12}$$

where $\big[\hat{H}_{spin}, \hat{\rho}\big] = \big(\hat{H}_{spin}\hat{\rho} - \hat{\rho}\hat{H}_{spin}\big)$ is the commutator of the operators $\hat{\rho}$ and $\hat{H}_{spin}$. $\hat{H}_{spin}$ is the complete Hamiltonian for the spin system. The solution to equation 2.12 for a time-independent Hamiltonian is:

$$\hat{\rho}(t) = e^{-i\hat{H}_{spin}t}\hat{\rho}(0)e^{i\hat{H}_{spin}t} \tag{2.13}$$

where t is the time period over which $\hat{H}_{spin}$ operates and the exponential is a propagator responsible for the evolution of the spin system. The propagators

may be adapted by a frame transformation to the rotating frame, to describe the rotation of the magnetization vector **M** under RF irradiation.

However, in circumstances where the Hamiltonian is not time-independent (e.g. under magic angle spinning) the solution to 2.12 is:

$$\begin{aligned} \hat{\rho}(t) &= U(t)\hat{\rho}(0)U^{\dagger}(t) \\ U(t) &= \hat{T}e^{-i\int_0^t \hat{H}(t')_{spin}dt'} \end{aligned} \tag{2.14}$$

where $\hat{T}$ is the Dyson time-ordering operator, necessary when $\hat{H}(t')_{spin}$ does not commute with itself at different times t'.

2.3.3 Simulating NMR Spectra Using SIMPSON

SIMPSON software[84] provides a highly flexible command line controlled interface for the numerical evaluation of the Liouville-von Neumann equation (2.12). The propagator $e^{-i\int_0^t \hat{H}(t')_{spin}dt'}$ which describes how the spin system will evolve under the Hamiltonian $\hat{H}(t')_{spin}$ is approximated by a time-ordered product of propagators:

$$U(t) = \prod_{n=0}^{n=t/\Delta t} e^{i\hat{H}(t_n)_{spin}\Delta t} \tag{2.15}$$

where n is the number of time intervals, of short enough length Δt for the Hamiltonian to be considered time independent. SIMPSON calculates the value of the propagator successively at times $t_n + \Delta t$ by diagonalizing the matrix representation of the Hamiltonian, kept strictly in chronological order by $\hat{T}$ for application to $\hat{\rho}(t_n)$. Hence numerical values for $\hat{\rho}(t_n)$ (equation 2.14) are then found at successive time increments Δt allowing successive calculation of the expectation value of the magnetization average over the ensemble $\overline{\langle\hat{\mu}\rangle}$ using equation 2.11.

Simulations may be computationally demanding. The symmetric time dependence of the Hamiltonian may be exploited by systematically reusing propagators for pulses or experimental time delays where appropriate.

The evolution of $\overline{\langle\hat{\mu}(t')\rangle}$ is usually dependent on the orientation dependence of nuclear spin interactions with respect to $\mathbf{B_0}$. Here, all simulations were for uniformly distributed powders, where all orientations are sampled.

2.3.4 The Nuclear Spin Hamiltonian

The nuclear spin Hamiltonian represents the sum of all nuclear spin interactions. It is conveniently split into external and internal parts:

$$\hat{H}(t)_{spin} = \hat{H}(t)_{ext} + \hat{H}(t)_{int} \tag{2.16}$$

The external Hamiltonian comprises two parts, the Zeeman interaction $\hat{H}_z$ and the radio-frequency interaction $\hat{H}(t)_{RF}$. These interactions are under experimental control.

$$\hat{H}(t)_{ext} = \hat{H}_z + \hat{H}(t)_{RF} \tag{2.17}$$

The internal Hamiltonian comprises many nuclear spin interactions, but the parts relevant to this thesis are the chemical shift interaction $\hat{H}_{cs}$, the dipolar coupling $\hat{H}_{dd}$, the quadrupolar coupling $\hat{H}_Q$ and the Knight shift $\hat{H}_K$.

$$\hat{H}_{int} = \hat{H}_{cs} + \hat{H}_{dd} + \hat{H}_Q + \hat{H}_K \tag{2.18}$$

The internal Hamiltonian depends entirely on the spin system. The mechanisms of all the interactions will be discussed in subsequent sections, for now we are content with a few generalities.

Usually in NMR, the Zeeman interaction is the dominant interaction and therefore $\hat{H}_{int}$ can be treated as a perturbation to $\hat{H}(t)_{ext}$. It follows that only the parts of any interaction Hamiltonian which commute with $\hat{H}_z$ are required for a first order correction to the Zeeman energy levels. These terms are the *secular* parts of any Hamiltonian.

2.4 The Zeeman Interaction

The Zeeman interaction occurs between a nuclear magnetic moment μ and a static magnetic field. Since the z-axis is defined as the direction in which B_0 is applied, the Hamiltonian for these energy levels, may be written in terms of $\hat{\mathbf{I}}_\mathbf{z}$:

$$\hat{H}_z = -\gamma \hat{\mathbf{I}}_\mathbf{z}.\mathbf{B_0} \tag{2.19}$$

The Zeeman interaction splits the nuclear spin **I** energy levels into (2I+1) non-degenerate eigenstates. Each eigenstate, or spin state, is labeled as m_I, which defines the spatial orientation of the magnetic moment. For all I, m_I has values:

$$m_I = I, (I-1), (I-2), ...(-I+2), (-I+1) - I \tag{2.20}$$

Spin states which are aligned parallel with B_0 are lower in energy than those which are anti-parallel. Application of the Zeeman Hamiltonian to a spin state via the time-independent Schrödinger equation gives the energy levels (in Joules):

$$E = -\gamma \hbar m_I \mathbf{B_0} \tag{2.21}$$

2.4.1 Thermal Equlibrium

In thermal equilibrium, the population p of spins in an energy level with energy E is given by a Boltzmann distribution:

$$p = \frac{e^{\left(\frac{-E}{k_B T}\right)}}{\sum_{\psi} e^{\left(\frac{-E_{\psi}}{k_B T}\right)}} \tag{2.22}$$

where k_B is the Boltzmann constant. The Boltzmann factor $\frac{\gamma \hbar B_0}{k_B T}$ predicts that when temperature T is near ambient, the Zeeman energy splitting is of the order of 10^{-21} J (at typical B_0 values for a laboratory magnet). Therefore, the difference between the populations of two energy states relatively is small, of the order 10^{-4} of the total. Since the Zeeman energy increases with magnetic field (equation 2.21), high field NMR (20 T) has been used in this thesis to increase the sensitivity of low γ nuclei such as ^{25}Mg.

The expectation value of z-magnetization for an ensemble of spins $\overline{\langle \hat{\mu}_{\mathbf{z}} \rangle}$ is equivalent to $\boldsymbol{M_z}$, the z-component of $\boldsymbol{M}$. For a spin $I = \frac{1}{2}$ nucleus it may be shown that $\overline{\langle \hat{\mu}_{\mathbf{z}} \rangle}$ corresponds to the difference in populations between energy levels:

$$\overline{\langle \hat{\mu}_{\mathbf{z}} \rangle} = \frac{1}{2}\gamma\hbar\left(p_{\frac{1}{2}} - p_{-\frac{1}{2}}\right) \tag{2.23}$$

From the density matrix representation, it may be shown that the density operator for a spin system in thermal equilibrium (i.e. obeying the Boltzmann distribution) is given by:

$$\hat{\boldsymbol{\rho}}_{\boldsymbol{eq}} = \frac{e^{\left(\frac{-\hat{H}}{k_B T}\right)}}{Tr\left(e^{\left(\frac{-\hat{H}}{k_B T}\right)}\right)} \tag{2.24}$$

In the high temperature approximation, $e^{\left(\frac{-\hat{H}}{k_B T}\right)}$ can be expanded to give:

$$e^{\left(\frac{-\hat{H}}{k_B T}\right)} \approx 1 + \left(\frac{-\hat{H}}{k_B T}\right) \tag{2.25}$$

Only the term $\frac{-\hat{H}}{k_B T}$, called the reduced density matrix, which represents the difference in the occupancy of the energy levels, can be manipulated in the high temperature approximation. Thus at thermal equilibrium, the reduced density matrix is diagonal and $\propto \mathbf{I_z}$.

2.5 The Radio-Frequency Interaction

The application of a time-dependent magnetic field $\mathbf{B_1}$ oscillating at radio-frequency ω_{RF}, mixes the Zeeman spin states by inducing transitions between the Zeeman energy levels, if the resonance condition is close or exactly met.

The radio-frequency Hamiltonian describes the evolution of a magnetic moment in a time varying magnetic field, $\mathbf{B_1}$. Assuming $\mathbf{B_1}$ along the x-axis:

$$\hat{H}(t)_{RF} = -\hat{\mu}.\mathbf{B_1}(\mathbf{cos}(\omega_{\mathbf{Rf}}\mathbf{t})) \tag{2.26}$$

A $\frac{\pi}{2}$ RF pulse is defined using equation 2.8 as one of length τ_{RF} and power ω_{RF} which results in the magnetization vector $\mathbf{M}$ being tilted into the (transverse) xy-plane. Likewise a π pulse aligns the magnetization vector in the -z direction. For spin-$\frac{1}{2}$ nuclei, the populations of the $|\pm\frac{1}{2}\rangle$ energy levels are equal after a $\frac{\pi}{2}$ pulse and inverted after a π pulse.

If the RF pulse is applied along the x-axis, then nutation of the magnetization under $\hat{H}_{RF}$ causes magnetization oriented along the y-axis to be generated. The expectation value of y-magnetization $\overline{\langle\hat{\mu}_{\mathbf{y}}\rangle}$ in the rotating frame is:

$$\overline{\langle \hat{\mu}_{\mathbf{y}} \rangle} = -\frac{1}{2}\gamma\hbar\left(p(0)_{\frac{1}{2}} - p(0)_{-\frac{1}{2}}\right)\sin(\omega_{RF}t) \tag{2.27}$$

It is noted that this has the same form as equation 2.23 but multiplied by $-\sin(\omega_{RF}t)$, and equation 2.27 can be derived from both the Boltzmann population and the density matrix formulation for ensembles of spins[81].

2.6 Quadrupolar Coupling

Nuclei with spin quantum number $I > 1/2$ possess an electric quadrupole moment eQ, which interacts with an electric field gradient (EFG).[85,86] An EFG is generated by an asymmetric electron charge distribution in the vicinity of the nucleus. It can be represented in a principal axis system (PAS) with the orthogonal components $\mid V_Z \mid \geq \mid V_Y \mid \geq \mid V_X \mid$, with the electric field gradient tensor V being diagonal in the PAS frame of reference. The anisotropy eq and asymmetry η_Q which characterise an EFG are defined as:

$$eq = V_Z \tag{2.28}$$

$$\eta_Q = (V_X - V_Y)/V_Z \tag{2.29}$$

where η_Q ranges between ± 1, is 0 for a uniaxially symmetric EFG, and either ± 1 for a completely asymmetric EFG. When the quadrupole moment of the spin interacts with an EFG, the EFG perturbs the nuclear spin energy levels m_I, which leads to a perturbation in the resonance frequency of a nucleus (2.5). This is illustrated by figure 2.2. The Hamiltonian for the quadrupolar interaction in the PAS frame of reference is[87]:

$$\hat{H}_Q^{(PAS)} = \frac{C_Q}{4I(2I-1)}\left[3\hat{I}_{z\,PAS}^2 - \hat{I}^2 + \frac{1}{2}\eta_Q(\hat{I}_{x\,PAS}^2 - \hat{I}_{y\,PAS}^2)\right] \tag{2.30}$$

where C_Q is the quadrupole coupling constant, defined in rads^{-1} as:

$$C_Q = \frac{(eq)(eQ)}{\hbar} \tag{2.31}$$

C_Q quantifies the strength of the quadrupolar coupling, which depends upon $e \times Q$

from the nucleus and $e \times q$ from the EFG, decreasing as the symmetry of the EFG increases. It is thus a sensitive probe of local nuclear environment.

The magnitude of the quadrupolar interaction is usually greater than the chemical shift or dipolar coupling, but less than the Zeeman interaction; typically in the range 100kHz to 10MHz. The quadrupolar hamiltonian may therefore be treated as a perturbation to the Zeeman interaction. Under this limit the secular approximation can be applied to obtain a first order approximation to the quadrupolar Hamiltonian $\hat{H}_Q^{(1)}$. The first order quadrupolar coupling frequency splitting $\nu_Q^{(1)}$ (in Hz) is easily derived from $\hat{H}_Q^{(1)}$[87]:

$$\nu_Q^{(1)} = \frac{3C_Q}{4I(2I-1)} \times (m^2 - \frac{1}{3}I(I+1)) \times \frac{1}{2}\left[(3cos^2\theta - 1) + \eta_Q \cos 2\phi \sin^2\theta\right] \quad (2.32)$$

With $\mathbf{B_0}$ aligned along the *z-axis* of the laboratory (lab) frame of reference, the polar angles (θ, ϕ) map $\mathbf{B_0}$ to the interaction tensor in the PAS. The orientation dependence of $\nu_Q^{(1)}$ with respect to $\mathbf{B_0}$ may be observed in the case of a single crystal. For nuclei with small quadrupole moments, such as ^7Li, $\hat{H}_Q^{(1)}$ is a sufficient description of the quadrupolar interaction in the high $\mathbf{B_0}$ field limit (c.a. $>$ 3 T).

2.6.1 Pake Pattern (Powder) Line Shapes

A powder sample contains crystallites of all orientations. Therefore according to equation 2.32 a distribution of resonance frequencies occurs giving rise to a Pake pattern line shape[88], shown in figure 2.1. The complete width of the Pake pattern is C_Q. It is convenient to define the first order quadrupolar splitting frequency:

$$\nu_Q^{(1),sat} = \frac{3C_Q}{2I(2I-1)} \quad (2.33)$$

It is noted here that the definition of $\nu_Q^{(1),sat}$ differs between authors by a factor of 2, here the convention given by Abragam[87] is adhered to. For a $I = \frac{3}{2}$ nucleus such as ^7Li, it is easily shown that $\nu_Q^{(1),sat}$ becomes:

$$\nu_{Q\frac{3}{2}}^{(1),sat} = \frac{C_Q}{2} \tag{2.34}$$

Under this definition, $\nu_{Q\frac{3}{2}}^{(1),sat}$ is the frequency splitting between the satellite maxima, as marked on figure 2.1. This provides a simple tool for estimating C_Q.

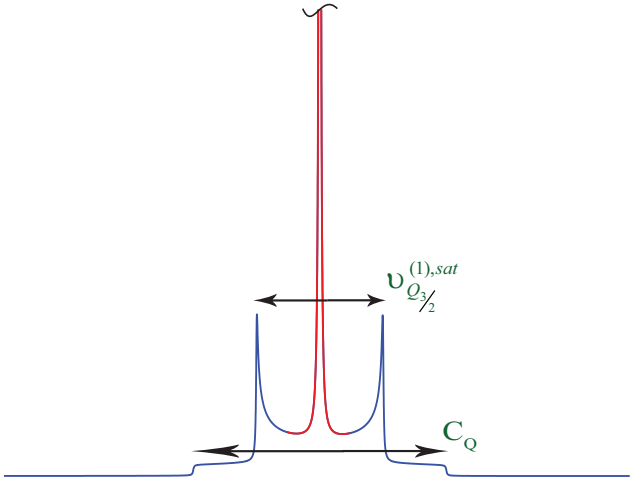


Figure 2.1: Powder pattern line shape for a $I = \frac{3}{2}$ nucleus, generated using SIMPSON. Red = central transition; blue = satellite transitions.

The origin of the quadrupolar satellites may be understood by examining the energy level diagram for a $I = \frac{3}{2}$ nucleus, given in figure 2.2. The perturbation to the energy levels under the first order quadrupole coupling increases the energy gap of the $m_I = -\frac{1}{2} \rightarrow -\frac{3}{2}$ transition and decreases that of the $m_I = +\frac{3}{2} \rightarrow +\frac{1}{2}$ by $\nu_Q^{(1),sat}$. The energy gap of the central transition ($m_I = +\frac{1}{2} \rightarrow -\frac{1}{2}$) is unaffected by the first order quadrupole coupling.

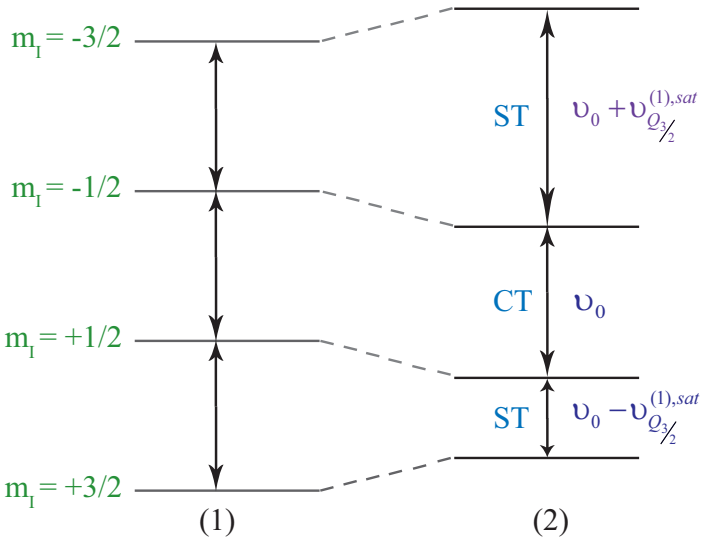


Figure 2.2: (1) Zeeman splitting of energy levels for $I = \frac{3}{2}$, (2) perturbation due to first order quadrupolar coupling. CT=central transition and ST=satellite transition.

2.6.2 Second Order Quadrupole Coupling

Larger quadrupole moments, such as ^{11}B, cause a more significant perturbation to the Zeeman energy levels even at moderate $\mathbf{B_0} \sim 7$ T. Such nuclei therefore require the quadrupolar Hamiltonian to be corrected to higher order approximations for accurate description of the quadrupole coupling. A second order correction $\hat{H}_Q^{(2)}$ is sufficient for nearly all quadrupolar nuclei. The second order quadrupolar frequency in the PAS is:

$$\begin{aligned}\nu_Q^{(2)} = &-\left(\frac{C_Q}{4I(2I-1)}\right)^2 \frac{m_I}{\nu_0} \times \Bigg(C_0 A_{00} \\ &+\frac{1}{2}C_2\left[A_{02}(3\cos^2\theta - 1) + \frac{3}{7}\eta_Q^2 \sin^2\theta \cos 2\phi\right] \\ &+\frac{1}{8}C_4\Bigg[A_{04}(35\cos^4 - 30\cos^2\theta + 3) \\ &+\frac{3}{7}\eta_Q \sin^2\theta(7\cos^2\theta - 1)\cos 2\phi + \frac{1}{4}\eta_Q^2 \sin^4\theta \cos 4\phi\Bigg]\Bigg)\end{aligned} \tag{2.35}$$

The $C_{(k)}$ parameters contain information about the evolving coherence:

$$\begin{aligned}C_0 &= [I(I+1) - 3m_I^2] \\ C_2 &= [8I(I+1) - 12m_I^2 - 3] \\ C_4 &= [18I(I+1) - 34m_I^2 - 5]\end{aligned} \tag{2.36}$$

The A_{k0} values express the contribution of the asymmetry of the electric field gradient:

$$\begin{aligned}A_{00} &= -\frac{1}{5}(3 + \eta_Q^2) \\ A_{02} &= \frac{1}{14}(\eta_Q^2 - 3) \\ A_{04} &= \frac{1}{140}(18 + \eta_Q^2)\end{aligned} \tag{2.37}$$

The relevance of the above parameters shall become clear when examining the effects of magic angle spinning in section 2.11.4 and describing high resolution methods on quadrupolar nuclei 2.11.8.

2.7 Dipolar Coupling

Nuclei with a non-zero value of I possess a dipole moment. This gives rise a small local magnetic field, which couples through space with neighboring nuclei. The local field possessed by nuclei is typically several orders of magnitude less than B_0. Therefore the Hamiltonian for this interaction may be truncated under the secular approximation, to remove single and double quantum contributions. The secular dipolar Hamiltonian for a pair of homonuclear coupled spins $\hat{\mathbf{I}}$ and $\hat{\mathbf{S}}$ is given by[89]:

$$\hat{H}_{dd}^{homo} = \frac{d_{jk}}{2}(3cos^2\theta_{jk} - 1)(3\hat{I}_z\hat{S}_z - \hat{\mathbf{I}}.\hat{\mathbf{S}}) \tag{2.38}$$

where d_{jk} is the dipole-dipole coupling constant. The polar angles (θ_{jk}, ϕ_{jk}) describe the orientation of the inter-nuclear vector to $\mathbf{B_0}$. Under the secular approximation, terms which contain ϕ_{jk} are truncated. The dipole coupling is greatest when $\theta_{jk} = 0$. The term $\hat{I}_z\hat{S}_z$ couples spins I and S, splitting the energy levels of the system according to the orientation of the spins (parallel or anti-parallel to B_0). $\hat{\mathbf{I}}.\hat{\mathbf{S}}$ allows simultaneous reversal of spins in opposite directions, often called the 'flip-flop' term.

In the case of a heteronuclear spin pair the term $\hat{\mathbf{I}}.\hat{\mathbf{S}}$ is truncated; the secular dipolar Hamiltonian is then given by:

$$\hat{H}_{dd}^{hetero} = d_{jk}(3cos^2\theta_{jk} - 1)(\hat{I}_z\hat{S}_z) \tag{2.39}$$

For a powder sample, all angles θ_{jk} are present which gives rise to the Pake powder pattern (analogous to that shown in figure 2.1).

The strength of the dipolar coupling is dependent on the size of the gyromagnetic ratio of both nuclei. It diminishes according to the cube of the internuclear

distance r_{jk}^3 and in units of rads^{-1} is given by:

$$d_{jk} = -\frac{\mu_0}{4\pi}\frac{\gamma_j\gamma_k\hbar}{r_{jk}^3} \tag{2.40}$$

2.8 Shift Interactions

2.8.1 Chemical Shift

The external magnetic field B_0 causes electrons surrounding a nucleus to circulate and induce a small magnetic field B_{ind} which adds to or subtracts from the external field. This perturbs the resonant frequency of a nucleus ν_0, by shielding it from B_0. The extent of this effect is dependent on the surrounding electronic structure and the orientation of the crystallite, and is quantified by the chemical shielding tensor σ. With B_0 aligned along the z-axis the induced magnetic field can be defined:

$$\mathbf{B_{ind}} = \sigma.\mathbf{B_0} \tag{2.41}$$

Under the secular approximation only the component of the shielding tensor parallel to $\mathbf{B_0}$ is retained. Since $\mathbf{B_0}$ is oriented along the z-axis, the chemical shift Hamiltonian can be written as:

$$\hat{H}_{CS} = -\gamma\sigma_{zz}\hat{\mathbf{I}}_\mathbf{z}.\mathbf{B_0} \tag{2.42}$$

where σ_{zz} is the z-component of the shielding tensor which interacts with the external magnetic field.

The chemical shielding tensor is often described in a principal axis frame of reference, where it is diagonal. The polar angles (θ, ϕ) translate the shielding tensor in the principal axis frame of reference σ^{pas} to the laboratory frame. The frequency shift which results for a non-spinning sample due to $\hat{H}_{CS}$ operating on a spin system is:

$$\nu_{CS} = -\nu_0\sigma_{iso} - \frac{1}{2}\nu_0\zeta\left[3\cos^2\theta - 1 + \eta\sin^2\theta\cos 2\phi\right] \tag{2.43}$$

where ν_0 in the Larmor frequency in units of (Hz), ν_{CS} is the perturbation to the Larmor frequency by the chemical shielding effect, σ_{iso} is the isotropic chemical shielding, ζ the chemical shielding anisotropy (CSA) and η the asymmetry. They are defined as:

$$\sigma_{iso} = \frac{1}{3}\left[\sigma_{xx}^{pas} + \sigma_{yy}^{pas} + \sigma_{zz}^{pas}\right] \tag{2.44}$$

$$\zeta = \sigma_{zz}^{pas} - \sigma_{iso} \tag{2.45}$$

$$\eta = \frac{\sigma_{xx}^{pas} - \sigma_{yy}^{pas}}{\zeta} \tag{2.46}$$

where σ_{xx}^{pas}, σ_{yy}^{pas} and σ_{zz}^{pas} are the x, y an z components of σ^{pas}.

If B_{ind} is equal along the three principal axes then shielding is isotropic. Otherwise, the shape of the shielding tensor is characterized by ζ and η. A finite value of ζ will give rise to an anisotropic line shape of the form given by equation 2.43, for a powder sample which contains all values of θ.

The isotropic chemical shift δ_{iso} is defined as the difference between the frequency of precession under the induced magnetic field and the frequency of a reference compound. Since the magnitude of the chemical shift is usually a very small perturbation to the Larmor frequency, it is conventionally quoted in ppm. It may also be related to the shielding parameter in the following manner:

$$\delta_{iso} = \frac{\nu_{CS} - \nu_{CS}^{ref}}{\nu_{CS}^{ref}} * 10^6 = 10^6 * \frac{\sigma_{iso}^{ref} - \sigma_{iso}}{1 - \sigma_{iso}^{ref}} \tag{2.47}$$

As a general rule the range of chemical shifts observed tends to increase with atomic number. Since the shift is dependent on electronic structure, it may be used for identifying chemical compounds. To do so, the chemical shift scale is referenced to a standard compound for every nucleus. When the chemical shift was used for analysis, ^{6}Li spectra were referenced to 1M LiCl(aq), ^{25}Mg spectra to $MgCl_2$ (aq) and ^{11}B to $BF_3.OEt_3$. The same solution state compounds served as suitable samples for pulse length calibrations. It is noted that static ^{7}Li NMR spectra typically have a broad dipolar linewidth (10-50 KHz) which obscures the very small range of chemical shifts (± 10 ppm), therefore the ^{7}Li chemical shift is not used for species identification in this thesis.

2.8.2 Knight Shift

The Knight shift[90] is a form of paramagnetic interaction specifically observed in metals. In the presence of an external magnetic field B_0, unpaired delocalised conduction electrons within the energy range k_BT of the Fermi energy E_f may align their magnetic moment either parallel to B_0 or anti-parallel. The parallel orientation is favorable in energy, inducing a weak net magnetization M_K:

$$M_K \approx \frac{N\mu_e^2}{k_B T_F} B_0 \tag{2.48}$$

where N is the total number of atoms in the sample, μ_e is the magnetic moment of an electron and T_F the Fermi temperature $\frac{E_F}{k_B}$. This effect is known as *Pauli paramagnetism*[91]. The Pauli paramagnetic susceptibility of a material is defined as:

$$\chi_p = \frac{M_K}{B} \tag{2.49}$$

The Knight shift arises due to the coupling between M_K and the magnetic dipole

moment of a nucleus. The Knight shift is temperature independent because M_K is temperature independent, apparent from equation 2.48. The Hamiltonian for the Knight shift may be given by[92]:

$$\hat{H}_K = -\frac{\gamma}{2}\mathbf{I}.\chi_\mathbf{s}\mathbf{T}.\mathbf{B_0} \tag{2.50}$$

where χ_s is the Pauli paramagnetic susceptibility per unit volume, and T represents a coupling tensor between the electrons and B_0. Anisotropic contributions to the Knight shift are finite in some cases, but generally very small. It is therefore common to assume the electronic environment about a nucleus in a metallic species is cubic. The Hamiltonian may then be written in a more tractable form:

$$\hat{H}_K = -\frac{8\pi}{3}\left\langle \left| \Psi_k(0) \right|^2 \right\rangle_F \chi_p \gamma(\hat{\mathbf{I}}_\mathbf{z}.\mathbf{B_0}) \tag{2.51}$$

where $\left\langle \left| \Psi_k(0) \right|^2 \right\rangle_F$ represents the average probability density at the nucleus for all electronic states at the Fermi surface. Since $-\gamma\hbar\hat{\mathbf{I}}_\mathbf{z}.\mathbf{B_0}$ represents the Zeeman nuclear energy, the frequency shift K relative to B_0 may be defined:

$$K = \frac{\Delta\nu}{\nu_0} = \frac{\Delta B}{B_0} = \frac{8\pi}{3}\left\langle \left| \Psi_k(0) \right|^2 \right\rangle_F \chi_s \tag{2.52}$$

where K represents the isotropic Knight shift. The magnitude of the Knight shift $\frac{\Delta B}{B_0}$ is typically 2 to 3 orders of magnitude greater than the diamagnetic chemical shift. ^{7}Li metal has a relatively small Knight shift of 256 ppm and the general trend is for the Knight shift to increase with atomic number[93]. ^{7}Li and ^{25}Mg Knight shifts measured in this thesis were referenced to the same diamagnetic compounds that were used for referencing chemical shifts. It is noted that chemical shift in lithium metal is negligible compared to the Knight shift.

2.9 Relaxation

Relaxation, first reported by Bloembergen, Purcell, and Pound[94], is the restoration to thermal equilibrium of nuclear spins amongst the Zeeman energy levels. For this to occur transitions between nuclear spin energy levels m_I must occur. Relaxation of a nuclear magnetic moment μ occurs when it interacts with randomly fluctuating magnetic fields $\mathbf{B}_\mathbf{t}'$ oscillating at the Larmor frequency, inducing transitions between states with different m_I.

2.9.1 Spin Temperature

Equation 2.22 shows a system of spins which may be described by Boltzmann statistics with a characteristic *spin temperature* T, where populations of energy levels decrease exponentially. The spin temperature may be represented by the Boltzmann factor $\beta = \frac{1}{k_B T}$, determining the occupancy of energy levels. By computing the change in average energy of an ensemble of spins, the change in spin temperature with respect to time may be derived:

$$\frac{d\beta}{dt} = \frac{\beta_L - \beta}{T_1} \tag{2.53}$$

where $\beta_L = \frac{k_B}{T}$, T is the lattice temperature and T_1 is the time constant for temperature flow from the spin system to the lattice, called the spin-lattice relaxation time. Thus relaxation occurs when a temperature gradient between the Zeeman reservoir and the lattice exists. This is a suitable way of describing of relaxation in the rigid lattice limit; that is to say in the absence of molecular motion[95].

2.9.2 The Bloch Equations

When a system is perturbed by RF irradiation, the evolution of the x, y and z components of magnetization $\boldsymbol{M}$ (equivalent to $\overline{\langle\hat{\mu}\rangle}$) may be described by the phenomenological Bloch equations:

$$\frac{d\boldsymbol{M_z}}{dt} = 0 - \frac{\boldsymbol{M_z} - \boldsymbol{M_0}}{T_1} \tag{2.54}$$

$$\frac{d\boldsymbol{M_x}}{dt} = \gamma \boldsymbol{M_y} \boldsymbol{B_0} - \frac{\boldsymbol{M_x}}{T_2} \tag{2.55}$$

$$\frac{d\boldsymbol{M_y}}{dt} = \gamma \boldsymbol{M_x} \boldsymbol{B_0} - \frac{\boldsymbol{M_y}}{T_2} \tag{2.56}$$

where $\mathbf{M_0}$ is the magnetization at thermal equilibrium. The Bloch equations describe the evolution of $\mathbf{M}$ after RF excitation. Equation 2.54 may easily be solved to give:

$$\boldsymbol{M_z} = \boldsymbol{M_0}\left(1 - exp\left(-\frac{t}{T_1}\right)\right) \tag{2.57}$$

Equation 2.57 shows that the z-component of magnetization M_z (longitudinal magnetization) recovers exponentially to equilibrium value M_0 over time t. T_1 is the time constant for longitudinal relaxation, commonly referred to as the spin-lattice relaxation time. T_1 is dependent on the relaxation mechanism and temperature of the sample. For solids at ambient temperature it typically varies between ≈ 0.1 s and ≈ 15 hours.

Knowledge of T_1 is important to ensure magnetization is not saturated by scanning too quickly. Measurement of T_1 with variable temperature also provides insight into the mechanism causing relaxation, and the type of thermal motion which

drives it. Measurement of T_1 in this thesis was routinely performed using the saturation-recovery technique. First saturation is achieved by a train of around 10 to 100 $\frac{\pi}{2}$ pulses, separated by a short time of the order 10 to 100 μs. Then the system is given time τ to recover before a $\frac{\pi}{2}$ is applied to create detectable transverse magnetization. Incrementing τ produces a dataset which may be fitted by equation 2.57 to extract T_1.

Equations 2.55 and 2.56 describing the evolution of transverse magnetization are a pair of coupled differential equations, which correspond to damped circular motion. T_2 is the time constant for transverse relaxation commonly referred to as the spin-spin relaxation time. Transverse relaxation is interpreted as the exchange of energy between spins leading to precession at different frequencies, and subsequent loss of coherence in the rotating frame.

2.9.3 Autocorrelation

Hopping of particles between sites creates fluctuating magnetic fields B_t'. The time behavior of $\mathbf{B_t'}$ can be described by a correlation function, equation 2.58, where a particle position at time t generates a magnetic field B(t). The bar denotes an average taken over an ensemble of spins. It is equally valid to write the correlation function in terms of the time evolution of the density matrix elements $< m|\hat{H}'(t-\tau)|n >$ and $< m|\hat{H}'(t)|n >$ which couple transitions from spin states m to n via a time-dependent perturbation Hamiltonian $\hat{H}'$.

$$G(\tau) = \overline{B'(t).B'(t+\tau)} = \overline{< m|\hat{H}'(t-\tau)|n >< m|\hat{H}'(t)|n >} \tag{2.58}$$

When τ is short, the system has had little time to evolve so $G(\tau)$ is close to the root mean square (RMS) of the fluctuating field. Conversely when τ is large, $G(\tau)$ is small because time dependent fields have evolved significantly and can be

averaged to zero causing the system to lose correlation.

Under the BPP framework for relaxation, particle hoping is assumed to be stochastic, which generates randomly fluctuating magnetic fields. The loss of correlation may then be described by an exponential autocorrelation function[94]:

$$G(\tau) = G(0) \times e^{\left(\frac{-|\tau|}{\tau_c}\right)} \tag{2.59}$$

$G(\tau)$ is symmetric with respect to τ. The time constant τ_c is the correlation time, which characterises the decay of the RMS average random magnetic field. Therefore τ_c reflects the time scale over which a system can 'remember' its state.

Since $\mathbf{B}_\mathbf{t}^{'}$ originates from molecular motion, τ_c is directly equated with the motional correlation time for the process; for example that which describes the time taken for hopping of lithium ions between sites during diffusion. Then since molecular motion is temperature dependent, τ_c may often take the form of a simple Arrhenius law:

$$\tau_c = \tau_0 e^{\left(\frac{E_a}{k_B T}\right)} \tag{2.60}$$

where E_a is the activation energy of the motional process, and τ_0 is the Arrhenius pre-factor, which may be interpreted as the correlation time at infinite temperature.

2.9.4 The Master Equation and Spectral Density

The *master equation* for transition probability between spin states per second $\overline{W_{mn}}$ may be derived by evaluating the Liouville-von Neumann equation for a perturbation $\hat{H}'(t)$ to states m and n[96]. If it is assumed the time interval τ is long on the time scale of $\mathbf{B}_\mathbf{t}^{'}$ then $\overline{W_{mn}}$ may be written:

$$\overline{W_{mn}} = \frac{1}{\hbar^2} \int_{-\infty}^{\infty} G^{(q)}(\tau) e^{(-i\omega\tau)} \, \mathrm{d}\tau = J^{(q)}(\omega) \tag{2.61}$$

Equation 2.61 is mathematically equivalent to a Fourier transform. Fourier transformation of the correlation function yields a *spectral density function* $J^{(q)}(\omega)$, describing fluctuations in the frequency domain:

$$J^{(q)}(\omega) = G(0) \times \frac{2\tau_c}{1 + \omega^2 \tau_c^2} \tag{2.62}$$

Since $G(\tau)$ is approximated to be exponential, $J(\omega)$ is a Lorentzian centered at zero frequency, with a half-width at half-amplitude equal to τ_c^{-1}. The constant $G(0)$ is related to the strength of the interaction causing relaxation. It is noted that the component of the spectral density where $\omega = \omega_0$ is that which causes relaxation.

2.9.5 Non-Exponential Correlation of Motional Processes

In many chemical systems ionic diffusion is not completely random. Correlated motion may result from coulombic interactions of the spin, a vacancy mediated diffusion mechanism or long range disorder (typical of nano-crystalline or amorphous materials). When particle hopping is not entirely stochastic $G(\tau)$ is not necessarily exponential[97]. The Kohlrausch-William-Watts function, colloquially known as a stretched-exponential, was derived to account for non-exponential dielectric relaxation[98,99]. The stretched-exponential may also provide an empirical correction to $G(\tau)$:

$$G^{\alpha}(\tau) = G(0) \times e^{\left(\frac{-|\tau|}{\tau_c}\right)^{\alpha}} \tag{2.63}$$

where $0 < \alpha < 1$. Strictly speaking, the Fourier transform of $G^{\alpha}(\tau)$ is the

Havriliak-Negami function[100,101].

Various other empirical models exist, which often apply to specific materials or situations[102,103]. In general, such models exhibit non-quadratic $\omega_0\tau_c$ dependence, caused by an asymmetric $J^{(q)}(\omega)$. Thus a good approximation to the spectral density is[104]:

$$J^{(q)}(\omega) = G(0) \times \frac{2\tau_c}{1 + (\omega\tau_c)^{1+\alpha}} \tag{2.64}$$

When $0 < \alpha < 1$, the $\omega_0\tau_c >> 1$ flank of $J^{(q)}(\omega)$ is stretched.

It is also worth mentioning that reduced dimensionality partially determines a diffusion pathway. In the common case of 2D diffusion, a logarithmic frequency dependence characterises $J^{(q)}(\omega)$ where $\omega_0\tau_c << 1$, and a sub-quadratic frequency dependence where $\omega_0\tau_c >> 1$[97,105,106].

2.9.6 Relaxation by a Time Dependent Magnetic Field $\mathbf{B}_\mathbf{t}^{'}$

Various attempts to describe relaxation in terms of evolution of the density matrix have been made by Wangsness and Bloch[107], Kubo and Tomita[108] but most notably by Redfield[109]. Redfield theory evaluates the time evolution of the density matrix based upon transition probabilities between quantum states and a coupling to the lattice allowing transfer of thermal energy from the spins to the lattice. Slichter[110] has shown how Redfield's theory may be applied to compute the relaxation under a fluctuating magnetic field. Such treatment leads to the Bloch equations. In this circumstance the relaxation rates $\frac{1}{T_2}$ and $\frac{1}{T_1}$ take the following form:

$$\frac{1}{T_1} = \frac{\gamma^2\left(\overline{B_x^2} + \overline{B_y^2}\right)}{2} J(\omega) \tag{2.65}$$

$$\frac{1}{T_2} = \gamma^2 \overline{B_z^2} \tau_c + \frac{1}{2T_1} \tag{2.66}$$

where $\overline{B_x^2}$, $\overline{B_y^2}$, $\overline{B_z^2}$ denote the average value $\mathbf{B_t'}$ in respective directions.

Since $\mathbf{B_0}$ is oriented along the z-axis, equation 2.65 shows it is the perpendicular component of $\mathbf{B_t'}$, $\left(\overline{B_x^2} + \overline{B_y^2}\right)$ which drives spin-lattice relaxation. Spin-lattice relaxation requires non-secular terms in the time-dependent Hamiltonian to be non-zero.

Equation 2.66 shows that spin-spin relaxation is driven by two components. The first term is a consequence of the parallel component of $\overline{B_z^2}$ which causes dephasing of spins owing to a spread in precession frequencies. This time the secular terms in the time dependent Hamiltonian are non-zero. The second term has the same $\left(\overline{B_x^2} + \overline{B_y^2}\right)$ dependency as for spin-lattice relaxation, and is interpreted as the broadening of the energy levels owing to the finite life time of a spin in an excited state resulting from spin-lattice relaxation. Both terms contribute to a finite intrinsic linewidth of the resonance line.

Equation 2.66, which governs the width of a resonance line, is valid when $\tau_c \ll \frac{1}{\omega_0}$. When $\tau_c \gg T_2$, the width of the resonance line is determined by the rigid lattice; which will be discussed in section 2.10.2.

A maximum is expected for equation 2.65 when $\tau_c = \frac{1}{\omega_0}$; where spin-lattice relaxation is most efficient. It is also noted that in solids, spin-spin relaxation is always faster than spin-lattice relaxation.

2.9.7 Common Relaxation Models

The local magnetic field in the vicinity of a nucleus is determined by the nuclear spin interactions in the sample. Therefore fluctuations in such interactions often drive relaxation, depending on their relative strength. Two common mechanisms of relaxation in solids are introduced here.

Relaxation by the Dipolar Coupling

The coupling of spin states by the magnetic dipole interaction perturbs their energy levels and introduces additional spin states[111]. The fluctuation of a magnetic dipole moment modulates the local magnetic field and hence the energy levels according to the Zeeman interaction. The spin-lattice relaxation time T_1 must reflect all possible transitions and therefore takes the following form for I = $\frac{1}{2}$, for the heteronuclear dipolar interaction:

$$\frac{1}{T_1^{hetero}} = \frac{M_2^{IS}}{2}\left[J^{(0)}(\omega_I - \omega_S) + 3J^{(1)}(\omega_I) + 6J^{(2)}(\omega_I + \omega_S)\right] \tag{2.67}$$

and the homonuclear dipolar interaction:

$$\frac{1}{T_1^{homo}} = M_2^{II}\left[J^{(1)}(\omega_I) + 4J^{(2)}(2\omega_I)\right] \tag{2.68}$$

where M_2^{II} and M_2^{IS} are the Van Vleck second moments for the homonuclear and heteronuclear dipolar interactions respectively, and are proportional to the strength of the dipolar interaction. Equation 2.68 is often called the BPP formula because the relaxation assumed by Bloembergen, Purcell, and Pound[94] was via the dipolar coupling. Under the BBP framework $J^{(0)}$, $J^{(1)}$ and $J^{(2)}$ all share the same Lorentzian form given by equation 2.62.

Relaxation by the Quadrupolar Coupling

For many quadrupolar nuclei, fluctuations in the electric field gradient (EFG) cause quadrupolar relaxation. Quadrupolar relaxation is often more rapid than other mechanisms because the quadrupole coupling is usually the strongest NMR interaction. For a $I = \frac{3}{2}$ system, if the EFG fluctuations dominate then two relaxation times R_1 and R_2 exist:

$$R_1 = \frac{1}{2W_1} \qquad R_2 = \frac{1}{2W_2} \tag{2.69}$$

where W_1 and W_2 are the transition probabilities for $\Delta m_I = 1$ and 2 respectively. W_1 and W_2 depend upon the mechanism producing EFG fluctuations. W_1 and W_2 are therefore related to the spectral density function in the following manner: $W_1 \propto J(\omega)$, $W_2 \propto J(2\omega)$. If $W_1 \neq W_2$ the occupancy of the spin energy levels is expected to deviate from the Boltzmann distribution during the relaxation process[112]. However, spin-spin transfer (via the flip-flop terms) during relaxation is capable of maintaining a common spin temperature, thus yielding a single relaxation rate[112]:

$$\frac{1}{T_1} = \frac{2I+3}{5I(2I-1)}(W_1 + 4W_2) \tag{2.70}$$

This occurs as long as the spacings between the energy levels are less than the dipolar linewidth. This situation is common for quadrupolar nuclei with small C_Q and large dipolar coupling such as ^7Li, particularly in the slow motion limit $\frac{1}{\tau_c} < \omega_0$ where the dipolar coupling has not been motionally averaged[113].

2.10 Static Line Shapes and Narrowing due to Ionic Diffusion

2.10.1 Origin of the Line Width

The NMR experiment measures the current induced in a coil by the precession of **M**. Relaxation causes the decay of the induced signal, hence the signal is usually referred to as a free induction decay (FID). In the presence of rapid molecular motion, usually found in solution, spin-spin relaxation is exponential. Then it follows that the Fourier transform of the FID yields a Lorentzian line shape with finite linewidth $\frac{1}{T_2}$, called the intrinsic linewidth[114,115]. Magnetic field inhomogeneities or crystal lattice irregularities may all perturb the resonance frequencies of nuclei causing additional dephasing T_2'. Then an effective linewidth $\frac{1}{T_2^*}$ is necessarily defined:

$$\frac{1}{T_2^*} = \frac{1}{T_2} + \frac{1}{T_2'} \tag{2.71}$$

where $\frac{1}{T_2}$ is the homogeneous part and $\frac{1}{T_2'}$ the inhomogeneous part.

2.10.2 Dipolar Line Broadening

For an ensemble of spins, the dipolar coupling Hamiltonian (equations 2.39 and 2.38) is a sum over all pairs nuclei:

$$\hat{H}_{dd}^{homo} = \frac{1}{2}\sum_{j<k}^{N} d_{jk}(3cos^2\theta_{jk} - 1)(3\hat{I}_{jz}\hat{S}_{kz} - \hat{\mathbf{I}}_\mathbf{j}.\hat{\mathbf{S}}_\mathbf{k}) \tag{2.72}$$

For heteronuclear dipolar coupling, the $\hat{\mathbf{I}}_\mathbf{j}.\hat{\mathbf{S}}_\mathbf{k}$ term is simply omitted.

Alignment of μ parallel to $\mathbf{B_0}$ is lower in energy than anti-parallel. Therefore, the dipolar energy of every spin depends upon the orientation of neighboring spins within its vicinity. For a multi-spin system, the degeneracy of the levels for a given value of m_I is approximately Gaussian. The resultant isotropic Gaussian line broadening in a NMR spectrum is nearly always far more substantial than the Lorentzian broadening caused by spin-spin relaxation.

For solids, equation 2.72 is not currently tractable. However the contribution of the dipolar interaction to the linewidth may be very well approximated by the Van-Vleck 2^{nd} moment[116] M_2. M_2 may be calculated from the dipolar Hamiltonian (equation 2.72) for homonuclear spins in a powder sample to be[117,118] ($rad^2 s^{-2}$):

$$M_2^{II} = \left(\frac{\mu_0}{4\pi}\right)\frac{3}{5}\gamma_I^4\hbar^2 I(I+1)\sum_k \frac{1}{r_{jk}^6} \tag{2.73}$$

For heteronuclear spins in a powder sample ($rad^2 s^{-2}$):

$$M_2^{IS} = \left(\frac{\mu_0}{4\pi}\right)\frac{4}{15}\gamma_I^2\gamma_S^2\hbar^2 S(S+1)\sum_k \frac{1}{r_{jk}^6} \tag{2.74}$$

M_2 is related to the linewidth (fwhm) by:

$$\Delta_0 = 2\sqrt{2\ln 2 M_2} \tag{2.75}$$

This formulation affords a useful tool for estimating the rigid lattice linewidth in the case where the dipolar coupling the dominant nuclear spin interaction.

The Voigt Profile

Since dipolar line broadening is typically Gaussian, the overall line shape for solids is a Voigt profile. This is a convolution of Gaussian and Lorentzian lines. The

full width half maximum (fwhm) of a Voigt profile V_{fwhm} has been found empirically[119]:

$$V_{fwhm} \approx 0.5346 G_{fwhm} \sqrt{0.2166 L_{fwhm}^2 + G_{fwhm}^2} \tag{2.76}$$

where G_{fwhm} and L_{fwhm} are the respective Gaussian and Lorentzian linewidths. Equation 2.76 estimates V_{fwhm} with 99.98% accuracy.

2.10.3 Ionic Diffusion in the Solid-State

Diffusion of ionic species (such as Li^+ in $LiBH_4$) in the solid-state occurs via crystal imperfections; the rate being dependent on the number of crystal imperfections and on temperature. The temperature dependence of the diffusion coefficient may take an Arrhenius form:

$$D = D_0 e^{\left(\frac{-E_a}{k_B T}\right)} \tag{2.77}$$

For a vacancy mediated diffusion mechanism, ions hop between empty sites with $\mathrm{E}_a = \Delta H_f + \Delta H_m$; here E_a is the sum of contributions from firstly defect-formation ΔH_f and then subsequent ion migration ΔH_m. For an interstitial mechanism, ions hop via sites between the rigid lattice ion positions and therefore defect-formation will not contribute to E_a. The Arrhenius prefactor D_0 is temperature independent and can be expressed in the following form[120]:

$$D_0 = \left(\frac{f_c a^2 \nu_0}{n}\right) e^{\left(\frac{\Delta S_f + \Delta S_m}{k_B}\right)} \tag{2.78}$$

where a is the jump distance, ΔS_f and ΔS_m are the entropy changes associated with vacancy formation and ion hopping. n is a dimensionality factor, which $= 2, 4, 6$ for 1D (linear), 2D (planar) and 3D (unrestricted) diffusion respectively.

f_c is a correlation factor accounting for subsequent jumps being dependent on former jumps, such as an ion returning to a vacancy it created by hopping. f_c is usually near to unity, and for uncorrelated motion equal to 1. f_c depends upon the crystal structure. ν_0 is the maximum vibrational frequency of an ion, with typical values of $10^{12} - 10^{13}$ Hz. From the above it can be seen that the hopping frequency has the same Arrhenius temperature dependence[121]:

$$\nu_c = \nu_0 e^{\left(\frac{-E_a}{k_B T}\right)} \tag{2.79}$$

The correlation time for a jump between two sites is the inverse of the hopping frequency, therefore direct comparison with equation 2.60 implies that the correlation time for diffusion τ_c is the same as that which characterises the auto-correlation function (equation 2.59).

2.10.4 Motional Narrowing caused by Diffusion

For nuclei with a large γ and small quadrupole coupling, such as ^7Li, section 2.10.2 shows how in the rigid lattice limit, the linewidth may be governed by strength of the dipolar interaction. When the hopping frequency ν_c is greater than the dipolar coupling, the dipolar coupling will begin to be motionally averaged, thus decreasing the linewidth. The central transition linewidth may progressively decrease with increasing temperature to the limiting value $\frac{1}{T_2^*}$, with an expected change in the line shape from Gaussian to Voigt[122]. BPP theory[94,123] gives the central transition linewidth under motional narrowing conditions Δ_{cent} to be:

$$\Delta_{cent}^2 = \Delta_0^2 \frac{2}{\pi} \tan^{-1} \Delta\pi\tau_c \tag{2.80}$$

where Δ_0 is the rigid lattice linewidth. This treatment assumes there is no long term change in the EFG at the site following the lithium jump[124].

2.10.5 Exchange Broadening of the Quadrupolar Satellites

^{7}Li spectra will typically display a set of quadrupolar satellites, as shown in figure 2.1. When Li^+ ions hop between chemically different sites, the spins experience the effect of different EFGs. In the slow exchange limit, $\frac{1}{\tau_c} \leq \Delta\nu_s$, where $\Delta\nu_s$ is the difference in the satellite frequency splittings. With increased temperature the rate of exchange will become comparable with $\Delta\nu_s$ (i.e. $\frac{1}{\tau_c} \sim \Delta\nu_s$). When this occurs, the probe spin will on average complete one full precession under the influence of EFGs from both sites. This causes broadening of both sets of satellites, until $\frac{1}{\tau_c} \sim 2\Delta\nu_s$ where coalescence occurs. The increase in the linewidth of the quadrupole satellites during exchange broadening is given by[124]:

$$\Delta_{sat} = \Delta'_{sat} + \frac{1}{\tau_c \pi} \tag{2.81}$$

where Δ'_{sat} is the motionally narrowed linewidth, before exchange broadening occurs.

2.10.6 Studying Dynamics on Different Time-Scales

Δ_0 is typically of the order of 10 - 20 KHz so line narrowing will be caused by a motional processes with a correlation time $\tau_c \approx 0.1$ ms. Spin-lattice relaxation may be caused by the same motion that causes line narrowing. However, as shown by equation 2.65, $\frac{1}{T_1}$ is smallest when the correlation time $\tau_c = \frac{1}{\omega_0}$. At the high magnetic field strengths used with modern spectrometers $\nu_0 \approx 10^8$ Hz, the correlation time for minimum T_1 is $\tau_c \approx 0.01$ μs. Measuring T_1 as a function of temperature therefore affords a method for studying the dynamics of the same process, but at higher temperatures where it is much more rapid.

2.11 Experimental Techniques

2.11.1 Sample Preparation and Handling

Metal hydrides are generally highly reactive with moisture and air. Most of the materials used in this thesis: lithium borohydride ($LiBH_4$), magnesium hydride (MgH_2) lithium nitride (Li_3N), lithium imide (Li_2NH) and lithium amide ($LiNH_2$) are all liable to degradation. The MOF studied here are porous and therefore hygroscopic, yielding a similar problem. Procedures were therefore implemented to circumvent sample degradation by oxygen and moisture during preparation and experiment. Diagnostic tests were also devised to confirm the quality of procedures and reveal when materials may have reacted.

For static NMR measurements, samples were loaded into 5 mm diameter glass tubes in an inert atmosphere provided by either a N_2 or Ar gas flow in a MBRAUN Unilab glovebox, with O_2 / H_2O <0.3 ppm. The NMR tubes were sealed off to a length < 20 mm encapsulating the sample in an inert gas.

For MAS measurements, samples were loaded into 4 mm diameter rotors again under inert atmosphere. When not in use, rotors containing samples were stored in a glovebox.

2.11.2 Overview of the NMR Experiment

Samples were placed within a coil of conducting wire, which in turn was inserted into a magnetic field. The majority of the measurements in this thesis were performed with a 7 T superconducting magnet; a 20 T superconducting magnet was used for high field work.

The coil is the inductor part of an LCR circuit which was tuned and matched to the Larmor frequency. An applied current through the coil generated an RF pulse

for spin excitation, which caused **M** to precess in the transverse plane. After the RF pulse, precession of **M** induced a weak current in the coil ($\sim \mu V$) which decays resulting in the FID.

The FID may be processed with various techniques; but the essence is a Fourier transformation to yield a spectrum of frequencies[125]. Apodization was used only when the line shape was unimportant in subsequent analysis, to optimize signal to noise and resolution. The main source of noise in the NMR experiment is due to thermal motion in the coil, since the signal is weak owing to the small difference in the populations of the Zeeman energy levels (section 2.4.1).

2.11.3 Temperature Control

At 7 T, temperatures above room temperature were achieved with an electrical heater stack inserted down the bore of the magnet to connect with the probe to immerse the sample in warm air. A home-built system with a heat exchanger and dry nitrogen as the coolant gas was used for measurements below room temperature. The complete temperature range available was 140 to 480 K, controlled by a temperature controller. 20 minutes equilibration time was given after changing the temperature, and a rapid air flow across the sample was ensured so that the sample temperature would converge with the temperature at the detector. An extra 10 minutes was allowed for temperature step sizes > 20 K and the maximum step size used was 40 K. The probe was re-tuned after equilibration. The probe tuning was monitored in very similar experiments in a previous PhD thesis by Powell[126] to verify that this approach was sufficient. The temperature of the $LiBH_4$ orthorhombic to hexagonal phase transition (section 4.2.4) occurred at the temperature expected, which provided further confidence.

2.11.4 Magic Angle Spinning (MAS)

The homonuclear and heteronuclear dipolar interactions (section 2.7), the CSA (section 2.8.1) and the first order quadrupole coupling (section 2.32) all share a frequency dependence on the geometrical factor $(3cos^2\theta - 1)$. θ is the angle between the principal z-axis of the interaction and $\mathbf{B_0}$, illustrated in figure 2.3. In a powder sample the random distribution of crystallite orientations means all values of θ are present. In particular, inhomogeneous line broadening occurs for interactions with spin operators for different spins which commute (CSA and the first order quadrupole coupling)[127]. During rotation, the average orientation dependence of a nuclear spin interaction is:

$$\left\langle 3cos^2\theta - 1 \right\rangle = \frac{1}{2}(cos^2\beta_{LR} - 1)(cos^2\beta_{CR} - 1) \tag{2.82}$$

where the angle β_{CR} is the angle between the principal z-axis of the interaction (z^{PAS}) and the spinning axis, and β_{LR} the angle between the spinning axis and $\mathbf{B_0}$; illustrated in figure 2.3.

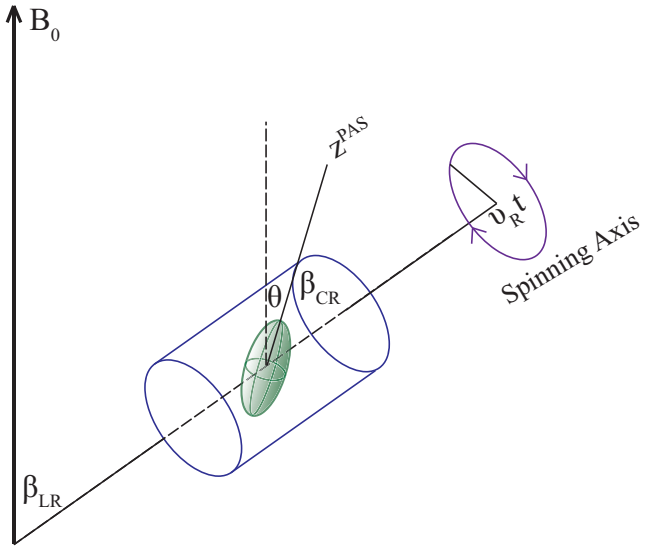


Figure 2.3: The axes of MAS. The green ellipsoid represents an interaction tensor. The z principal axis is z^{PAS}.

β_{LR} is under experimental control. When β_R=54.74^o (the magic angle), ($cos^2\beta_{LR}-1$) = 0, then $\langle 3cos^2\theta - 1\rangle = 0$ by mechanical rotation. This simulates molecular tumbling akin to that found in solution, averaging the inhomogeneous line broadening to 0. The result is improved resolution in solid-state NMR spectra, which are otherwise dominated by broad lines[128].

Upon averaging, only the isotropic resonance remains if ν_R is greater than the dephasing rate caused by the anisotropy (the line broadening), where ν_R is the rate of rotation. If ν_R is less, then oscillations of the anisotropic parts of the interactions listed above also occur at frequencies ν_R or $2\nu_R$. This results in spinning side bands (SSB) in the spectrum at frequencies $n\nu_R$ where n is an integer. The same effect is observed in the time domain signal as rotor echoes.

SSB can obscure isotropic resonances and render spectra hard to interpret. SSB may be removed by setting the MAS rate ν_R greater than the line broadening. However this is not always practically possible, so a simple alternative is to synchronize the spectral width to the rate of rotation, such that the dwell time between points in an FID is exactly 1 rotor period. This synchronises each point acquired to the top of each rotor echo, effectively removing rotor echos from an FID.

All MAS measurements in this thesis were performed with a 4 mm probe; MAS rates ranging between 8 and 14 KHz were routinely used. The MAS rate was generally chosen to place spinning sidebands to avoid obscuring isotropic resonances of different species.

MAS in Terms of Euler Angles and Reduced Wigner Rotation Matrix Elements

In general, two co-ordinate frames of reference may be related by Euler angles (α, β, γ). The orientation of the rotor with respect to the lab frame of reference

is given by ($\alpha_{LR} = \nu_R t$, $\beta_{LR} = 54.74^o$), and γ_{LR} is arbitrary since the rotor is symmetrical about the spinning axis. In this case (α_{LR},β_{LR}) are equivalent to the polar angles (ϕ, θ). The orientation of the crystallite (in the PAS) with respect to the rotor is given via another another set of Euler angles $(\alpha_{CR}, \beta_{CR}, \gamma_{CR})$.

To convert between the PAS and the rotor frame via $(\alpha_{CR}, \beta_{CR}, \gamma_{CR})$, Wigner rotation matrices $D^k_{mm'}$ are required, where k denotes the order of the matrix and m, m' the matrix elements. It is assumed ν_R is fast on the timescale of the interaction, such that SSB are eliminated. In this situation, only the D^k_{00} elements are required. The D^k_{00} are the reduced Wigner matrix elements d^k which depend only on β_{CR}[129].

$$\begin{aligned} D^0_{00}(\alpha_{CR}, \beta_{CR}, \gamma_{CR}) &= d^0 = 1 \\ D^2_{00}(\alpha_{CR}, \beta_{CR}, \gamma_{CR}) &= d^2 = \frac{1}{2}(3cos^2\beta_{CR} - 1) \\ D^4_{00}(\alpha_{CR}, \beta_{CR}, \gamma_{CR}) &= d^4 = \frac{1}{8}(35cos^4\beta_{CR} - 30cos^2\beta_{CR} + 3) \end{aligned} \tag{2.83}$$

Specifically, the equations 2.83 describe the orientation dependence of the inhomogeneous broadening due to the second order quadrupole coupling. It is easily seen that $d^2(\beta_{CR})$ is averaged completely to zero; however $d^4(\beta_{CR})$ is only partially averaged by MAS.

2.11.5 Continuous Wave Decoupling

The ability to perform an experiment in double resonance provides scope for a variety of techniques. Continuous wave (CW) decoupling is arguably the simplest of these[130].

At the time of writing, modern apparatus can achieve MAS rates $\approx$ 80 KHz, which provides sufficient improvement to resolution of most systems. However it is not always desirable to do MAS at $\approx$ 80 KHz. Here, it was necessary to selectively

remove heteronuclear dipolar coupling caused by $\hat{I}$ in the spectrum of $\hat{S}$. This was achieved with CW decoupling. This involved irradiating the sample with as high power pulse as possible at the resonance frequency ω_0^I of $\hat{I}$, during acquisition of a spectrum of $\hat{S}$. Application of ω_0^I will induce repeated transitions between energy levels of $\hat{I}$ at a rate dependent on the amplitude of the rf. This creates a time dependent oscillatory $\hat{I}$ magnetization. The heteronuclear dipolar Hamiltonian given by equation 2.39 contains the spin part $\hat{I}_z\hat{S}_z$, which in turn will oscillate. Average Hamiltonian theory can be used to show that $\hat{H}_{dd}$ averages to zero as long as transitions are rapid on the timescale of the coupling[131].

2.11.6 Spin Echoes

Immediately after an rf pulse, ringing in the coil occurs, usually lasting around 10-100 μs depending on the apparatus. If a single pulse experiment is considered, then there will be a dead time between the pulse and the acquisition, whilst ringing decays before the FID can be measured. For solids, loss of coherence is fast, often due to strong homonuclear dipolar or quadrupolar couplings. Therefore the loss of coherence during the dead time is significant. Significant line shape distortions occur and the signal to noise is reduced. The problem may be circumvented with an echo.

Two types of echo were used is this thesis:

Hahn-Echo: This was discovered by Hahn[132] to overcome the effect of B_0 inhomogeneity. The pulse sequence is simply $\frac{\pi}{2} - \tau_1 - \pi - \tau_2$, where τ_1 and τ_2 are time delays of around 20-100 μs. The $\frac{\pi}{2}$ pulse first creates transverse magnetization. The loss of coherence during τ_1 is refocused by a π pulse, bringing magnetization back into phase after a time τ_2, when a spectrum is recorded. Sufficient time is provided during the sequence for the dead time. It may be shown that the Hahn-

echo refocuses interactions which are linear in their spin operators (and depend upon the z-component of the spin); this includes the CSA and the heteronuclear dipolar coupling.

Solid-Echo: This was invented by Powles and Mansfield[133] and provides a more general approach. Similar to the spin echo, the sequence is: $(\frac{\pi}{2})_x - \tau_1 - (\frac{\pi}{2})_y - \tau_2$. Note the $\frac{\pi}{2}$ phase shift of the second pulse relative to the first. The dead time is avoided in the same manner. For I = 1 nuclei, the solid echo refocuses interactions which are bilinear or quadratic in the spin operators, such as the first order quadrupole coupling and the homonuclear dipolar coupling. An EXORCYCLED solid echo refocuses linear and bilinear inhomogeneous broadening simultaneously[134]. However, neither echo will refocus the broadening due to the second order quadrupole coupling.

2.11.7 Cross-Polarization

The objective of the first CP experiment[135] was to enhance the sensitivity of isotropically or chemically dilute nuclear spins. The absence of strong homonuclear dipolar couplings for dilute spins S usually results in very long spin-lattice relaxation times (often several minutes). The added benefit of CP is therefore increased repetition rate, since it is only necessary to wait for an abundant spins I to relax.

In the rotating frame of I a $\frac{\pi}{2}$ x-pulse on I generates magnetization along -y, which appears static. Application of a contact pulse with amplitude $\boldsymbol{B_1^I}$ on resonance with spins I along -y then generates quantization in the rotating frame. This *spin locks* the magnetization of I, M_I, so it will precess about -y. A simultaneous contact pulse on resonance with spins S quantities the energy levels of S. The amplitude $\boldsymbol{B_1^S}$ is chosen to fulfill the *Hartmann-Hahn* criterion[136]:

$$\gamma_I \boldsymbol{B_1^I} = \gamma_S \boldsymbol{B_1^S} \tag{2.84}$$

so that the energy level gaps of spins I and S are the same in the rotating frame. This causes the spin temperature of I to cool with a concomitant increase in temperature of S. This transfer of magnetization is mediated by the dipolar coupling, which contains the spin terms $\hat{I}_z.\hat{S}_z$. Energy conservation causes the redistribution between energy levels of I and S.

The efficiency of transfer is governed by the strength of the dipolar coupling. The cross relaxation time constant T_{IS} quantifies the rate of build up of S magnetization, although in competition with $T_{1\rho}$, the rotating frame relaxation time. The optimum contact time is where these competing factors result in a signal maximum.

Practically, this requires calibration of the amplitude of the contact rf pulses to achieve the correct B_1 fields. A ramped CP amplitude is normally used, improving the reliability of achieving the matching condition, particularly under MAS where the matching condition is split into sidebands with altered matching frequencies ($\pm\nu_r$ or $\pm 2\nu_r$)[137].

2.11.8 High Resolution of Quadrupolar Nuclei: The MQ-MAS Experiment

A consequence of a large C_Q is that the quadrupolar coupling ν_Q may be of the order 1-10 MHz; much larger than any other interactions in $\hat{H}_{int}$. $\hat{H}_Q^{(2)}$ causes rapid loss of coherence resulting in significant broadening to the central transition. It was shown is section 2.11.4 that MAS is only partially effective at removing inhomogeneous line broadening due to $\hat{H}_Q^{(2)}$. This often presents a problem for interpreting spectra with more than one nuclear environment.

Another consequence of large C_Q, is that the satellite transitions are usually too far off resonance to be excited. In practice, recording an NMR spectrum of a quadrupolar nucleus will therefore involve selection of the central transition. The frequency of the central transition can easily be derived from equation 2.35:

$$\nu_{\frac{1}{2},-\frac{1}{2}} = \left(\frac{C_Q}{4I(2I-1)}\right)^2 \frac{1}{\nu_0}[3-4I(I+1)] \times \left[\frac{1}{2}d^0A_{00} + 4d^2A_{02} + 9d^4A_{04}\right] \quad (2.85)$$

It is immediately seen from this that the d^0A_{00} term in equation 2.85 is isotropic and therefore gives rise to a quadrupolar induced shift in addition to the chemical shift, defined as:

$$\nu^{iso}_{\frac{1}{2},-\frac{1}{2}} = 3\left(\frac{P_Q}{4I(2I-1)}\right)^2 \frac{1}{10\nu_0}[3-4I(I+1)] \quad (2.86)$$

where the quadrupole product P_Q is:

$$P_Q = C_Q\sqrt{(1+\frac{\eta_Q^2}{3})} \quad (2.87)$$

There are three approaches towards removing the anisotropic broadening caused by d^4. The first is the double rotation (DOR) technique[138] which involves rotating the sample at either 30.6^o or 70.1^o and simultaneously at the magic angle to average d^4 to zero. The second is the dynamic angle spinning (DAS) method[139], which varies the spinning angle between specific pairs (e.g. 37.4^o 79.2^o) causing refocusing of the isotropic parts of the Hamiltonian, since $\nu_{\frac{1}{2},-\frac{1}{2}}$ depends on β_{RL}. A very similar approach is taken with the MQMAS technique[140,141], however refocusing is achieved by changing coherence order rather than β_{RL}, since $\nu^{(2)}_{Q(m_I,-m_I)}$, the frequency of a multiple quantum transition between energy levels $+m_I \rightarrow -m_I$, depends upon the coherence order m. MQMAS is much simpler to implement experimentally than DOR or DAS and therefore is generally the preferred method.

$\nu^{(2)}_{Q(m_I,-m_I)}$ may be easily shown from the formulation in section 2.6.2 to be:

$$\nu^{(2)}_{Q(m_I,-m_I)} = \left(\frac{C_Q}{4I(2I-1)}\right)^2 \frac{4m}{\nu_0} \times \left[C_0 d^0 A_{00} + C_2 d^2 A_{02} + C_4 d^4 A_{04}\right] \qquad (2.88)$$

RF pulses alone usually do not discriminate which coherences are excited. To achieve a multiple quantum transition experimentally, an appropriate phase cycle is used, which eliminates undesired coherences. For example, if $I = \frac{3}{2}$ then triple quantum coherence may be excited and allowed to evolve for a time period t_1, before a conversion pulse to single quantum coherence is applied and the system evolves for a second time period t_2 during which an FID is acquired. This is illustrated by the coherence transfer pathway in figure 2.4. During t_1 the system dephases according to $C_4(\Delta m_I = 3)$ and during t_2 rephasing is according to $C_4(\Delta m_I = 1)$, if the sample is spun at the magic angle. The value of m_I affects the rate of dephasing, so an isotropic echo is expected when:

$$t_1 C_4(\Delta m_I = 3) + t_2 C_4(\Delta m_I = 1) = 0 \qquad (2.89)$$

The echo forms during t_2 with a maximum after a time period kt_1. Equivalently an anti-echo may be reconstructed during t_1 at $-kt_1$ before the last pulse. Extraction of echoes and anti-echoes is practically achieved with a two dimensional dataset acquired using the states/hypercomplex method[142]. The value k for $I = \frac{3}{2}$ is:

$$k = \frac{C_4(\Delta m_I = 3)}{C_4(\Delta m_I = 1)} = -\frac{7}{9} \qquad (2.90)$$

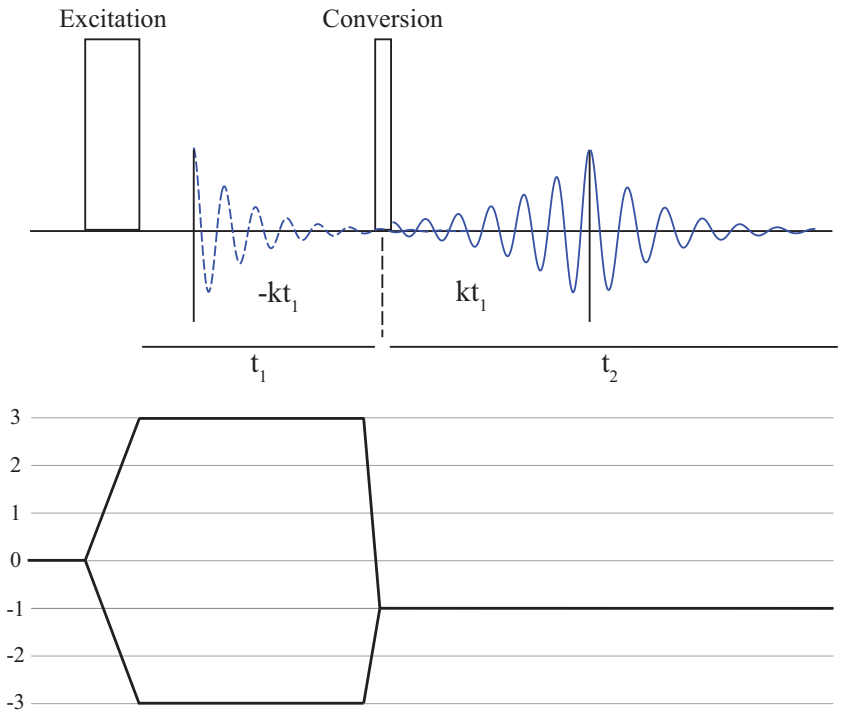


Figure 2.4: Pulse sequence and coherence transfer pathway for the two-pulse MQ-MAS experiment[143], which uses the triple quantum transition. The solid blue line represents the formation of the echo in the FID, and dashed blue line represents the reconstruction of the anti-echo.

MQMAS spectra in this thesis were processed using MATLAB software in conjunction with MatNMR[144], following the method laid out by Massiot *et al.*[143]; the details of the processing method used are given in *Appendix A*. After a shearing transformation is applied in the mixed frequency-time domain, the anisotropic part of the quadrupole interaction is removed from the ν_1 dimension, and a powder pattern with all the interactions is displayed in the ν_2 dimension. The resonances consist of a sum of the chemical shift (δ_{cs}^{iso}) and the quadrupolar induced shift ($\delta_{\frac{1}{2},-\frac{1}{2}}^{iso}$), so the position of the centre of gravity of a peak in the ν_2 dimension, in ppm, is simply:

$$\delta_{G2} = \delta_{cs}^{iso} + \delta_{\frac{1}{2},-\frac{1}{2}}^{iso} \tag{2.91}$$

The effect of a shearing transformation on the scale of the ν_1 dimension is to compress the spectral width by a factor of $(1+k)$. The evolution of δ_{cs}^{iso} under multiple quantum coherence is increased by a factor p, the coherence order. Also, the isotropic quadrupolar induced shift under multiple quantum coherence ($\delta_{\frac{p}{2},-\frac{p}{2}}^{iso}$) is scaled by a factor λ:

$$\delta_{\frac{p}{2},-\frac{p}{2}}^{iso} = \lambda\delta_{\frac{1}{2},-\frac{1}{2}}^{iso} \tag{2.92}$$

The position of the centre of gravity of a peak in the ν_1 dimension is therefore given by:

$$\delta_{G1} = \left(\frac{k-p}{1+k}\right)\delta_{cs}^{iso} + \left(\frac{k+\lambda}{1+k}\right)\delta_{\frac{1}{2},-\frac{1}{2}}^{iso} \tag{2.93}$$

For the evolution of triple quantum coherence of an $I = \frac{3}{2}$ nucleus, $p = -3$ and $\lambda = -3$. A complete set of MQMAS parameters (k, p and λ) is tabulated by Millot and Man[145]. It is important to note that under this representation of an MQMAS spectrum, the δ_{cs}^{iso} axis lies along the $\left(\frac{k-p}{1+k}\right)\nu_1$:$\nu_2$ line. δ_{cs}^{iso} of any resonance may therefore be calculated from the centre of gravity of the peak in ν_1 and ν_2 by:

$$\delta_{cs}^{iso} = \frac{10}{27}\delta_{G2} - \left(\frac{1+k}{p-\lambda}\right)\delta_{G1} \tag{2.94}$$

Likewise, $\delta_{\frac{1}{2},-\frac{1}{2}}^{iso}$ lies along the axis $\left(\frac{k+\lambda}{1+k}\right)\nu_1$:$\nu_2$. $\delta_{\frac{1}{2},-\frac{1}{2}}^{iso}$ may be calculated analogously by:

$$\delta_{\frac{1}{2},-\frac{1}{2}}^{iso} = \left(\frac{1+k}{p-\lambda}\right)\left[\delta_{G1} - \left(\frac{k-p}{1+k}\right)\delta_{G2}\right] \tag{2.95}$$

Example: MQMAS Spectra of HHTP + $NaBH_4$ / $B(OMe_3)$

The technique described above may be illustrated by the following study. 1D ^{11}B spectra of unknown compounds made from HHTP + $NaBH_4$ / $B(OMe_3)$ with a MeOH solvent are shown in figure 2.5 (HHTP = hexahydroxytriphenylene). In both cases, but particularly for HHTP + $NaBH_4$, it was not clear whether the two singularities were part of a highly anisotropic 2^{nd} order quadrupolar powder pattern line shape, or two chemically inequivalent sites. In the limit of a large EFG, the former is more likely, but in the case of a small EFG the latter is more likely. Therefore, the MQMAS technique was employed to improve the resolution by removing the anisotropic part of the second order quadrupolar interaction from the ν_1 dimension, so that only isotropic interactions remain in ν_1. ν_2 contains the equivalent of a 1D MAS spectrum.

The ^{11}B MQMAS spectra in figure 2.5 was recorded at 7 T, using a pulse sequence similar to that shown in figure 2.4. The excitation and conversion pulses were optimised on the samples to be 6 μs and 2 / 2.5 μs respectively. A 0.3 ms z-filter delay with 12 μs associated pulse was included after the conversion pulse prior to detection, to negate the need for large first order phase corrections. MAS rates were 12 KHz; the central transition was narrow enough to allow the spectral width to be synchronized with the rotor. A relaxation delay of 1.75 s was used, and 256 increments in the indirect dimension. Spectra were processed according to the method in *appendix A*.

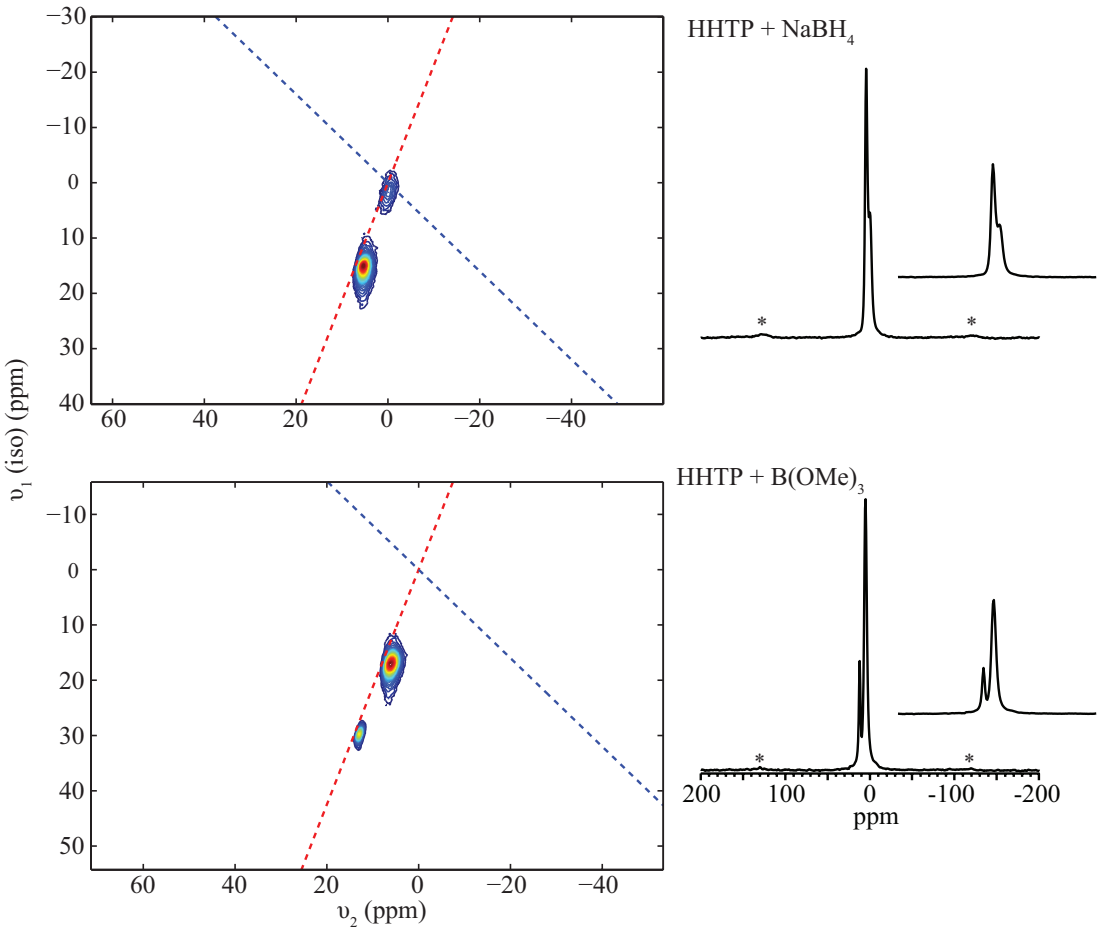


Figure 2.5: Left: 2D ^{11}B MQMAS spectra of unknown compounds formed from HHTP + $NaBH_4$ / $B(OMe_3)$ in solvent MeOH. The red line represents the δ_{cs}^{iso} axis, and blue line the direction of $\delta^{iso}_{\frac{1}{2},-\frac{1}{2}}$. Right: 1D ^{11}B spin-echo spectra of the same samples (expanded on the far right). $*$ denotes spinning sidebands.

Two separate resonances have been resolved for both samples. The resonance at 5 ppm appears to be the same, but different resonances occur at 1 and 15 ppm for HHTP + $NaBH_4$ / $B(OMe_3)$ respectively. The dispersion from the chemical shift axis (δ_{cs}^{iso}) in the direction of the quadrupolar induced shift ($\delta^{iso}_{\frac{1}{2},-\frac{1}{2}}$) is small (1 ppm) for the centre of gravity of all peaks, which implies a small EFG due to high symmetry at all chemical sites. Hence the 1D ^{11}B spectra show two inequivalent sites, but this is not known unequivocally without the aid of resolution in 2D. In this situation, the peaks are relatively narrow resulting in good resolution in the

1D, due to small CSA and dipolar couplings. MAS rates of 12 KHz have managed to partially average these interactions, resulting in spinning side bands with a low intensity (shown in the 1D spectra). Using the MQMAS, it is then a simple matter to estimate P_Q, and hence C_Q and η_Q using the measured $\delta^{iso}_{\frac{1}{2},-\frac{1}{2}}$ in conjunction with 2.86.

2.12 Experimental Strategy

In general, when choosing or designing an appropriate NMR experiment, it is necessary to consider firstly the nuclear properties of the available nuclei in a sample and secondly the type of molecular information desired. NMR experiments are useful for gaining insight into local molecular structure and dynamics, rather than bulk equivalents. As a consequence, NMR is particularly useful for the study of nano-crystalline materials which don't exhibit long range order. Many diffraction- and scattering-based techniques require a long range order in the crystal structure to yield tractable resolution. The following discussion will contrast the merits of each of the different nuclei available in materials used in this thesis, the types of experiments which were found most suitable for such nuclei and the specific molecular information that can be gained from these experiments.

^{11}B

Experiments with MAS are generally useful for understanding molecular structure, since MAS vastly reduces the broadening of the resonances caused by nuclear spin interactions by time averaging them. It has been shown (section 2.11.8) that for nuclei with a non-negligible second order quadrupole coupling (such as ^{11}B at 7 T), MAS may only partially average the effect of the second order quadrupole coupling. In such cases more sophisticated averaging methods such as the MQMAS technique appropriate for quadrupolar nuclei may be used for gaining resolution.

An important issue when using MAS on intermetallic or ionic metal hydrides (after desorption) is that the mechanical rotation of a metallic species in a magnetic field produces an opposing force to the rotation. This effect scales with magnetic field; lower field (7 T) was therefore found to be preferable over higher field (20 T) for study of the decomposed/desorbed metal hydrides in this thesis. Another issue

with metals is that they reflect RF radiation, which may show as spikes in the FID. Lower power pulses will reduce this effect.

^{6}Li and ^{7}Li

Whilst MAS may be very useful, measurement of nuclear spin properties in the absence of MAS may provide alternative molecular information. For example, where the C_Q is less than the spectral width (typically under the first order quadrupole coupling), the magnitude of the C_Q may be measured from the quadrupolar satellites, and used to identify or compare different species. In particular, for any given nucleus, a large C_Q suggests a less symmetric molecular environment about that nucleus. ^{7}Li has a quadrupole moment with a suitable magnitude to be effective with this type of treatment.

Static experiments (without MAS) also exist for gaining information about dynamics at the molecular level. NMR relaxometry may study motions on timescales ranging from 10^{-8} s for T_1 relaxation, to 10^{-5} s for $T_{1\rho}$ relaxation to 10^{-4} s for linewidth measurements. A common motional process which has correlation times in this range around ambient temperatures is solid-state ionic diffusion. This is useful for solid-state hydrogen storage systems where chemical decomposition is necessary for hydrogen release (such as complex metal hydrides), because mass transport will occur via solid-state diffusion.

NMR relaxometry measures the temperature dependence of T_1, $T_{1\rho}$ and the linewidths. Usually it was necessary to cool the sample to $\sim$ 150 K to obtain the rigid lattice linewidth, whereas it may be necessary to heat the sample to excess of 480 K to obtain a T_1 maximum. Such measurements may be limited by accessible temperatures of apparatus. $T_{1\rho}$ measurements may often be performed at more favourable temperatures, however effective spin-locking requires a $\mathbf{B_1}$ field that is larger than the width of the pattern; this is often not possible to achieve

in the solid phase.

In the systems studied in this thesis, the diffusing species was Li^+, hence ^{7}Li was chosen for relaxation measurements. ^{7}Li has both a larger gyromagnetic ratio and higher natural abundance, so is more tractable to work with than ^{6}Li. ^{7}Li has a strong homonuclear dipolar coupling which results in much shorter relaxation times compared with ^{6}Li. Therefore ^{7}Li is usually preferable over ^{6}Li for static measurements. However, the strong homonuclear dipolar coupling results in very broad ^{7}Li resonances; since the range of chemical shifts for lithium is small, MAS measurements on ^{7}Li are usually uninformative. In contract, ^{6}Li has a much smaller homonuclear dipolar coupling and is therefore often the preferable choice for species identification using MAS.

Less Tractable Nuclei: ^{14}N, ^{15}N and ^{25}Mg

The natural abundance, gyromagnetic ratio, quadrupole moment and value of I of NMR active nuclei govern how tractable they are to work with. For example, the Li-N-H system contains nitrogen, but both ^{14}N and ^{15}N are low γ nuclei and therefore not within the operable frequency range of some NMR probes. The abundance of ^{15}N is only 0.37 %, making very difficult to obtain signal. In contrast ^{14}N is 99.63 % abundant, but it has $I = 1$ and a large quadrupole moment, so experimental methods are still being developed for this nucleus in the solid-state[146]. However, the main reason nitrogen was not probed in this thesis was because both isotopes have a Larmor frequency below the range of the apparatus.

It is also worth noting the $LiBH_4$ / MgH_2 system contains magnesium. ^{25}Mg has $I = \frac{5}{2}$, a large quadrupole moment and a low γ; however it has a reasonable 10 % natural abundance. High field (20 T) may be used to make low γ nuclei more tractable, because the sensitivity to detection of a nucleus increases with magnetic field strength. Since the magnitude of the second order quadrupole coupling is

inversely proportional to field, high field is also advantageous for ^{25}Mg.

^{1}H

In principle, ^{1}H NMR would be a nucleus of choice, not only because of its 99 % abundance and high γ, but also since the interest here is on hydrogen storage. The large homonuclear dipolar coupling in ^{1}H makes it challenging to study in the solid-state, leading to decoupling methods such as DUMBO[147] and/or fast MAS[148] becoming routine on ^{1}H to gain optimum resolution. Even with the latest methods, resolving resonances at different shifts in ^{1}H spectra can be challenging for the same reason as for ^{7}Li; it yields broad lines and a narrow range of possible chemical shifts.

In this thesis, 1D and 2D ^{1}H experiments (section 4.2.10) with DUMBO decoupling did provide necessary resolution on the $LiBH_4$ / MgH_2 system. Unfortunately ^{1}H T_1 relaxation times in MgH_2 are found to be on the order of 900 s. Similarly long T_1 relaxation times have also been reported for LiH[149]. Therefore ^{1}H experiments on metal hydrides are not tractable. It is also worth mentioning that previous 1D ^{1}H MAS done by Powell[126] on the Li-N-H system did not resolve different species.

Static ^{1}H may also be informative on the diffusion of the H^+ ion in (complex) metal hydride systems; certainly diffusion was found to occur at higher temperatures > 350 ^{o}C for ^{1}H linewidth measurements on $LiBH_4$ in comparison to Li^+ diffusion[150,151]. Such experiments would require suitable apparatus.

Chapter 3

Metal Organic Frameworks: NOTT-MOF

3.1 Introduction: Progress on the Design of Metal Organic Frameworks for Hydrogen Storage

The crux of hydrogen storage in MOF is to achieve the high storage capacities found at high pressures and low temperatures (c.a. 70 - 100 bar and 77 K) at 298 K and under moderate pressure (1.5 - 30 bar). This may be achieved by increasing the H_2 binding energies in the framework. To realize the potential of MOF for on-board hydrogen storage, the isosteric heat of adsorption must be improved from around 4 - 5 kJmol^{-1} (NOTT-112) to ideally 15 - 25 kJmol^{-1} over the entire uptake range. The aim is that MOF will operate within the pressure range 1.5 - 30 bar at ambient temperatures[152]. Other strategies towards this goal include choice of ligand and metal centre, exposing metal cations, framework inter-weaving and doping with metal nano-particles[25].

Extensive research towards optimising the pore size by ligand choice for encapsulating hydrogen has been done[30,63]. The binding energies may be increased by decreasing pore width, but at the expense of storage capacity. As outlined in section 1.7, particular success has been found with carboxylate ligands[25].

Coordinative unsaturated metals provide stronger binding than organic linkers[153], owing to a stronger electrostatic field; this may be enhanced by appropriate ligand removal. Exposing metal sites is usually achieved by desolvating the frameworks; however this sometimes leads to framework collapse. The first successful example of this concept was demonstrated with $Mn_3[(Mn_4Cl)_3(BTT)_8]_2$ (BTT = 1,3,5-benzenetristetrazolate), which contains open Mn^{2+} coordination sites and exhibits isosteric heat of adsorption of 10.1 KJmol^{-1}. Most notably, the storage capacity at 90 bar and 298 K was 1.5$wt\%$ H_2 and 12 kg H_2 m^{-3}.[154]

Large pores centres experience no attractive forces from the walls, therefore are detrimental to the storage capacity. Framework inter-weaving may improve the

binding energies (e.g. $Cu_3(TATB)_2$, where TATB = 4,4',4"-s-triazine-2,4,6- triyl-tribenzoate)[155]). The effect is twofold: firstly it reduces pore sizes; secondly it also includes guest attractive species for H_2. Alternatively, the pores may be decorated with an adsorbent species such as carbon nanotubes to achieve the same effects[156].

Doping pores with Pt/C nano-particles allows the hydrogen spillover mechanism to occur where hydrogen molecules dissociate and spillover onto the surface of the MOF, increasing the overall binding energies. For example the gravimetric capacity of MIL-101 increased from 0.37 to 0.75 $wt\%$ H_2 with doping, at ambient temperature and 80 bar pressure[68,157].

An evolution of the above approaches is to dope pores with alternative metal centres. Recent computational and theoretical studies on the modelling of H_2 adsorbed into Li-MOF has suggested that a non-dissociative H_2-Li interaction may result, improving H_2 binding energies[158,159]. In particular, lithium is also a favourable choice due to its low atomic weight. Mulfort and Hupp[160] showed that frameworks doped by Li had the greatest improvement to both the isosteric heat of adsorption and H_2 capacity of all the alkali metals. However the primary reason for this was due to framework displacements rather than direct Li-H_2 contact[161]. Nouar *et al.*[162] reported similar improvements using Li-*rho*-ZMOF material. However, upon desolvation the Li^+ ions remained co-ordinated to 4 water molecules up to 300 ^oC prior to collapse of the framework, making the Li^+ centres inaccessible to H_2 whilst the framework remained assembled.

Yang *et al.*[163] have pursued an alternative approach to doping MOF by utilizing charged frameworks. They enable doping of the pores rather than the framework, which introduces a kinetic trapping mechanism for H_2. Subsequently the pore environments are determined not only by organic linkers and metal centres, but also by the cationic guest species. The counter cations are exchangeable, providing

a new degree of flexibility in MOF design. In the following, the work of Yang *et al.*[163] has been progressed and nuclear magnetic resonance is used to elucidate the nature of the Li^+ binding site[164]. In turn, it will be established how the inclusion of Li^+ into pores improves binding energies.

3.2 Synthesis and Characterisation: The structure of NOTT-MOF

Synthesis, XRD and IR characterisation were carried out by Yang *et al.*[164]. NOTT-206, NOTT-200 and NOTT-208 were constructed from the organic linkers[165] H_4L^1, H_4L^2 and H_4L^3 respectively co-ordinated with In^{3+} (figure 3.1). The combination of organic linkers with In^{3+} yielded negatively charged frameworks, stabilised by $Hdma^+$ for NOTT-206, and H_2ppz^{2+} for NOTT-200 and NOTT-208 (dma = dimethylamine, ppz = piperazine). Postsynthetic cation exchange of $Hdma^+$ or H_2ppz^{2+} for Li^+ produced NOTT-207, NOTT-201 and NOTT-209 respectively. Further detail on the synthesis are reported by Yang *et al.*[164].

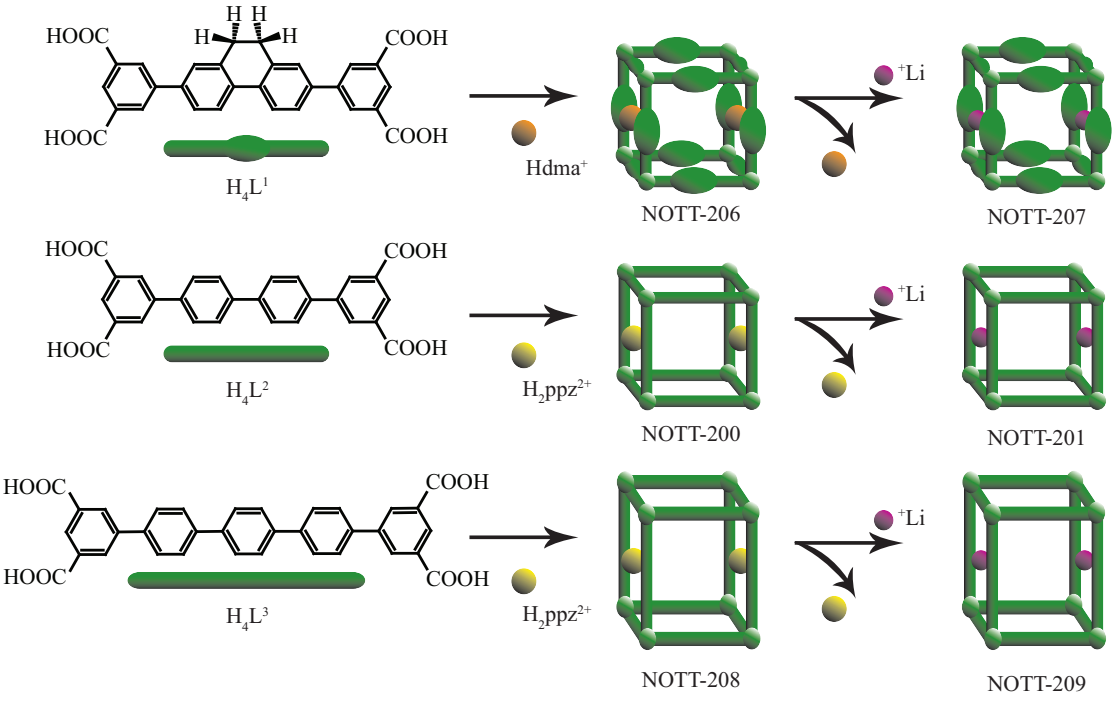


Figure 3.1: Schematic for the production of charged NOTT-MOF with different counter cations, followed by cation exchange processes. The doubly interpenetrating nets have been simplified to single cages for clarity. Reproduced from 164.

Single crystal X-ray structural analyses suggest three-dimensional frameworks with $[In(O_2CR)_4]$ nodes bridged by tetracarboxylate ligands. The structures of all 6 frameworks are illustrated in figure 3.2. Doubly interpenetrated frameworks allow the formation of three distinct channels A, B and C in NOTT-200 and NOTT-208. The structures are inherently similar, varying only by the increased length of the organic backbone for NOTT-208. This leads to the elongation of Channel A in NOTT-208. Channel A is occupied by free H_2O solvent molecules. Channel B contains ordered H_2ppz^{2+} molecules and channel C is empty, since it is too narrow to allow entrance. The In(III) centres possess a 7-fold co-ordinate geometry. Upon Li^+ exchange, equivalent single crystal transformations for both NOTT-208 to NOTT-209 and NOTT-200 to NOTT-201 are observed. Similarity

of the PXRD patterns before and after cation exchange imply retention of the framework structures. Release of the H_2ppz^{2+} ions unblocks channel B; and Li^+ then resides in channel C. In both NOTT-201 and NOTT-209, Li^+ is tetrahedrally bound by 4 oxygens, 2 from carboxylate groups and 2 from solvent water molecules.

Using $Hdma^+$ instead of H_2ppz^{2+} results in the biporous NOTT-206. Both channels A and B are blocked by $Hdma^+$. NOTT-206 crystallises in a more highly symmetric (tetragonal, $P4_I$) space group than NOTT-200/NOTT-208. Upon Li^+ exchange, a single crystal to single crystal transformation occurs to monoclinic. The two independent networks shift relative to each other leading to formation of a triporous network A,B,C. The In(III) centres change from 8-fold in NOTT-206 to 7-fold in NOTT-207, forming a structure more analogous to NOTT-201/NOTT-209. Similarly, channels A and B are unblocked and the Li^+ resides in channel C. However, oxygen atoms which occupied the In(III) co-ordination shell now protrude into channel C, resulting in Li^+ which is octahedrally co-ordinated by 6 oxygens from carboxylate groups and not solvent water molecules. Such an environment is rare in co-ordination polymers[166].

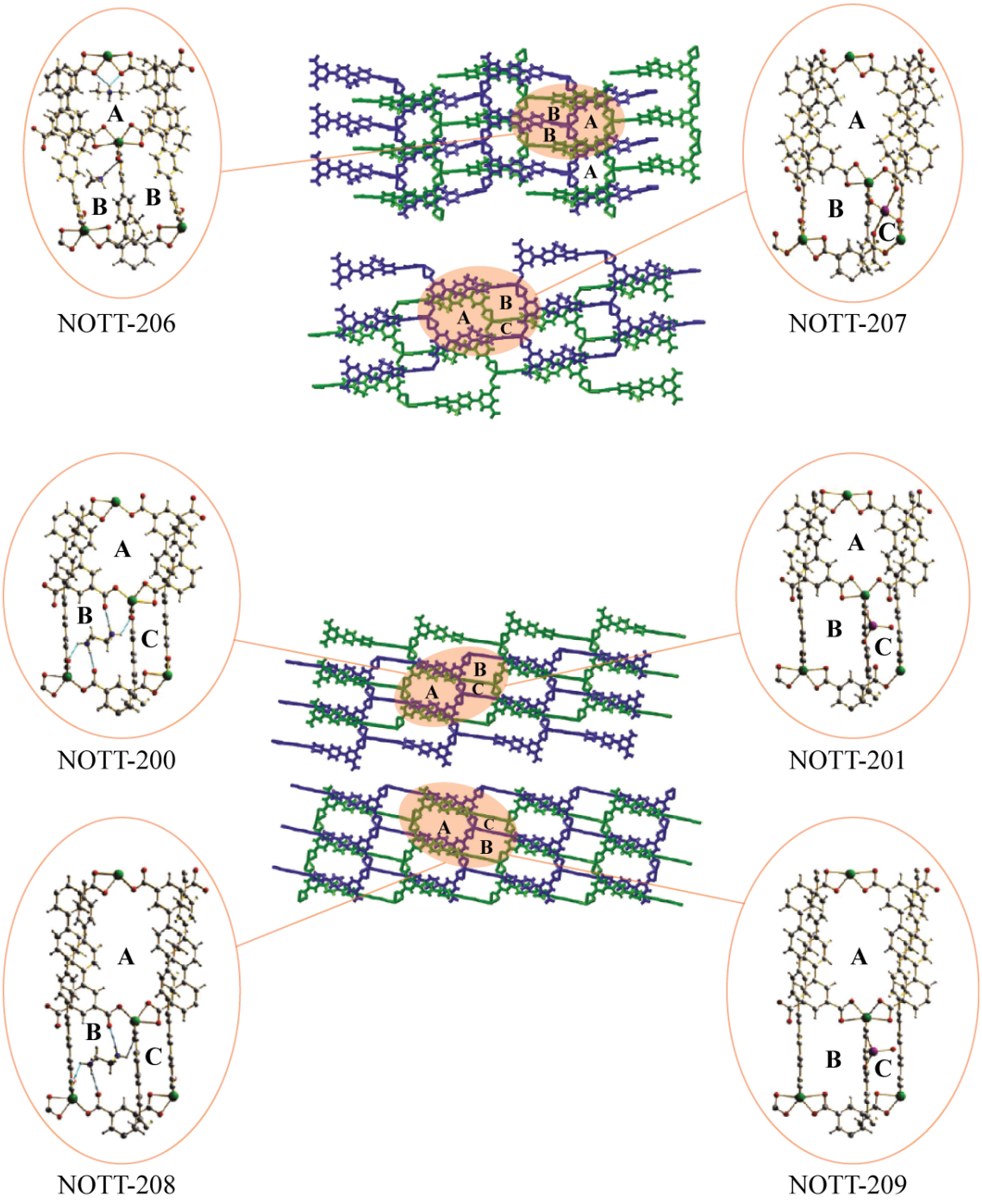


Figure 3.2: Single crystal X-ray structures of the doubly interpenetrated frameworks of charged NOTT-MOF. The inserts show a single unit. (Indium, green; oxygen, red; carbon, grey; hydrogen, white; nitrogen, blue; lithium, purple. The O...H-N hydrogen bonds are highlighted in cyan. Reproduced from 164.)

3.3 Lithium-7 Static NMR: Characterisation of Lithium Binding Sites

Wideline ^{7}Li NMR spectra were recorded at 7 T, using a solid echo pulse sequence with $\frac{\pi}{2}$ pulse lengths of 1.25 μs and an echo delay of 8.0 μs. The spectra presented in figure 3.3 were externally referenced to 1.0 M LiCl (aq).

The frequency separation of the intensity maxima of the quadrupolar satellites is directly proportional to C_Q. C_Q depends upon the product of the magnitude of the z-component of the electric field gradient (V_z) and the quadrupole moment (equations 2.31, 2.34). The magnitude of the electric field gradient about the ^{7}Li nucleus is entirely dependent upon the symmetry of the co-ordination environment. It may be seen from figure 3.3 that the spectrum of NOTT-207 has unresolved quadrupolar satellites. Therefore, a more symmetric environment about Li^+ exists than that of NOTT-201 or NOTT-209 where the satellites are resolved and the C_Q values are measured to be 50±2 and 47±2 kHz respectively. This is consistent with the XRD which found Li^+ in NOTT-207 to have a highly symmetrical octahedral co-ordination environment, but a less symmetrical tetrahedral co-ordination environment in NOTT-201 and NOTT-209.

Importantly for gas sorption, the pores must be dried of solvent molecules. The spectrum of the desolvated framework NOTT-207a shows no change to the C_Q values. This means the Li^+ site in NOTT-207a is unchanged. Since it comprises 6 oxygens from carboxylate groups and no water molecules, this is expected. However, an increase in C_Q to 145±2 kHz for NOTT-201a and 145±2 kHz for NOTT-209a suggests a significant decrease in symmetry about Li^+, confirming the loss of co-ordinated water molecules to leave an asymmetric open Li^+ centre.

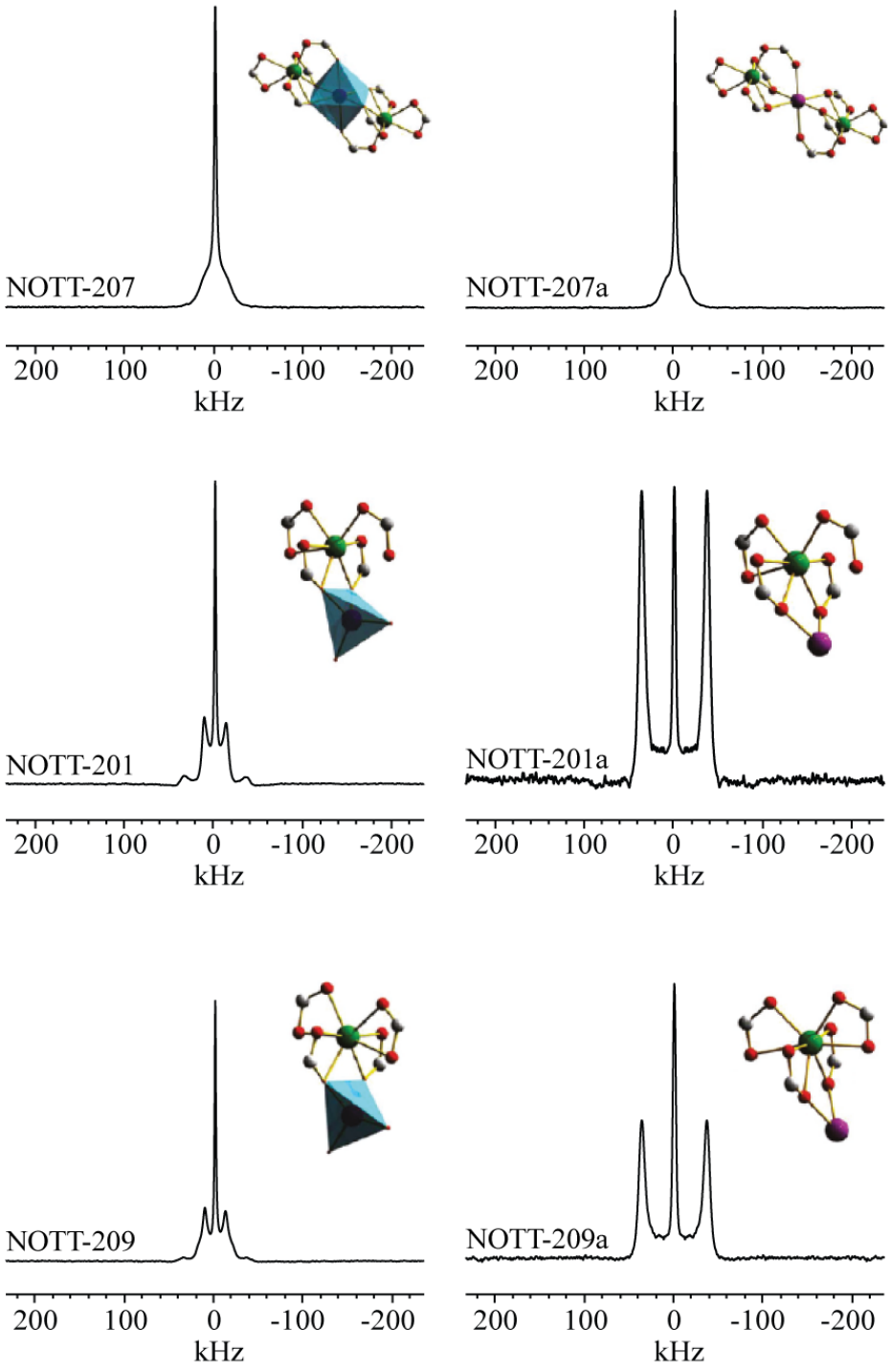


Figure 3.3: ^{7}Li NMR spectra and Li^{+} co-ordination environments in NOTT-MOF. Co-ordination environments at Li^{+} sites in NOTT-207, NOTT-201 and NOTT-209 shown as polyhedra. (Indium, green; oxygen, red; carbon, grey; hydrogen, white; nitrogen, blue; lithium, purple). The left panel are spectra for solvated frameworks and the right for desolvated. Reproduced from 164.

3.4 Discussion: H_2 Sorption Properties

H_2 Sorption Isotherms

H_2 gas sorption isotherms and enthalpies are given in figure 3.4 with associated parameters in table 3.1. Hysteretic sorption is observed for NOTT-206a and NOTT-200a but not for NOTT-207a and NOTT-201a. This implies that the reduced pore volume by larger $Hdma^+$ or H_2ppz^{2+} in contrast with Li^+ cations causes a strong kinetic trapping mechanism. The effect was larger for NOTT-206a, which retained 70 % of adsorbed H_2 down to 0.005 bar, due to the further contributing presence of the bulky 9-10-dihydrophenanthrene group with $Hdma^+$.

In contrast to NOTT-206a and NOTT-200a, the larger pore volumes of NOTT-208a due to the longer H_4L^3 organic linker results in reversible sorption isotherms without hysteresis. For the same reason, a larger storage capacity ($wt\%\ H_2$) is observed for NOTT-208a, with a 31 % (at 1 bar) increase upon Li^+ exchange to NOTT-209a. In contrast, the increase from NOTT-206a to NOTT-207a was 22 % and for NOTT-200a to NOTT-201a 6 %. N_2 isotherms (not included here) show much larger increases in gas uptake upon Li^+ exchange. This is attributed to the frameworks becoming comparatively more accessible to N_2 which has a larger kinetic diameter than H_2.

A trend has emerged that Li^+ exchange affords an increase in H_2 storage capacity. This may be partly due to the lower atomic weight of Li^+. The volume of H_2 absorbed (as a percentage of total pore volume) was shown to decrease from 81 % to 58 % (at 20 bar) between NOTT-206a and NOTT-207a confirming this. However the filled pore volume increased from 67 % to 76 % for NOTT-200a to NOTT-201a and 71 % to 74 % for NOTT-208a to NOTT-209a. This may be due to an increase in space after release of the bulky $Hdma^+$ or H_2ppz^{2+} cations in favour of Li^+; in particular the larger channels A and B are both unblocked with

Li^+ residing in the smaller channel C for all three: NOTT-207a, NOTT-201a and NOTT-209a.

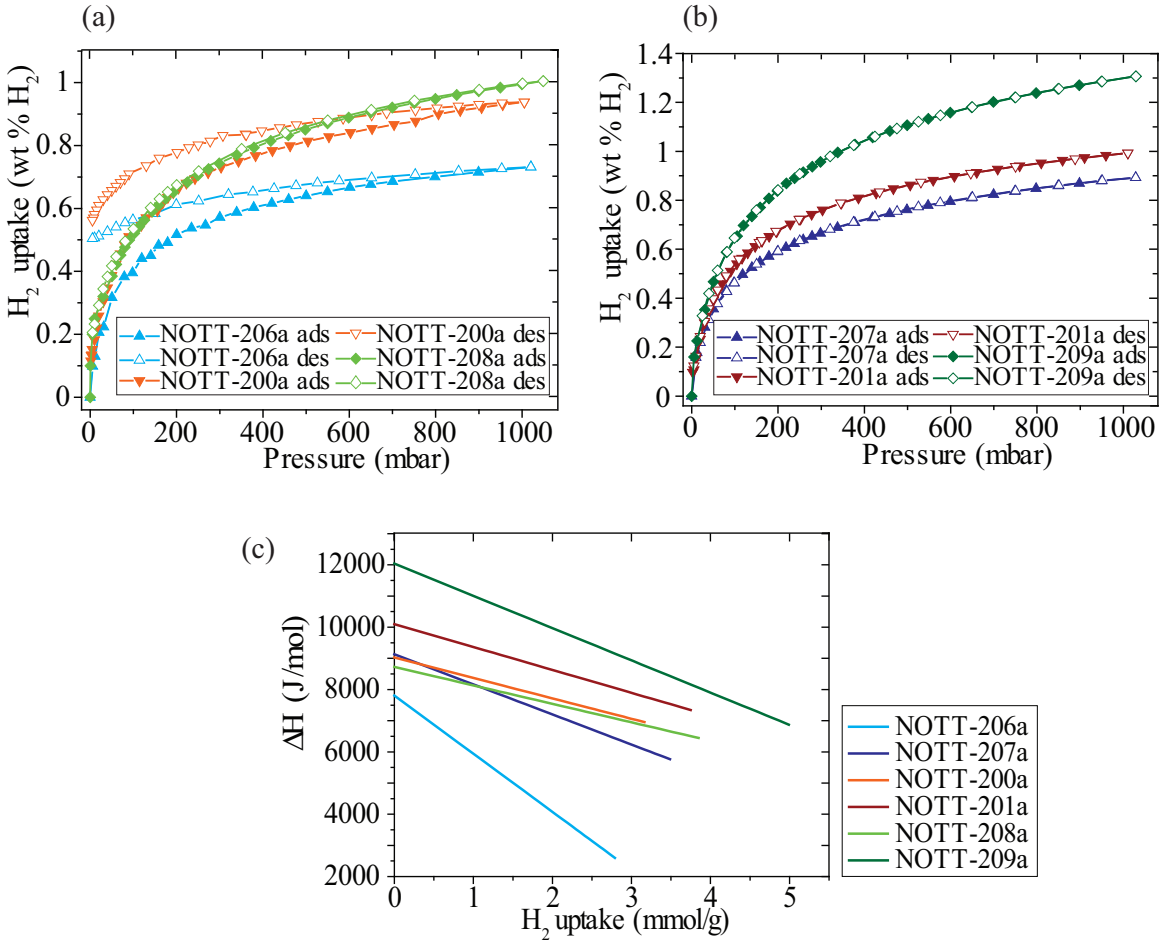


Figure 3.4: (a), (b): Gas sorption isotherms at 77 K; (c): isosteric heats of adsorption (ΔH) obtained from viral analysis of isothermal data, for H_2 in NOTT-MOF. No data points are shown for (c) due to the nature of analysis by interpolation. Reproduced from 164.

	NOTT-206a	NOTT-207a	NOTT-200a	NOTT-201a	NOTT-208a	NOTT-209a
Blocked Channel(s)	A, B	C	B	C	B	C
Pore Volume (cm^3/g)	0.191	0.322	0.289	0.360	0.351	0.410
H_2 filling ratio (1 / 20 bar) (%)	55 / 81	39/ 58	47 / 67	40 / 76	40 / 71	45 / 74
H_2 uptake (1 / 20 bar) ($wt\%$ H_2)	0.73 / 1.09	0.89 / 1.30	0.94 / 1.33	0.99 / 1.88	0.99 / 1.75	1.31 / 2.11
ΔH ($KJmol^{-1}$)	7.81	9.13	9.03	10.10	8.73	12.04

Table 3.1: Summary of physical parameters characterising NOTT-MOF. The H_2 filling ratio represents the volume of H_2 absorbed as a percentage of total pore volume, and ΔH is the value in the limit of zero surface coverage. Data taken from 164.

Isosteric Heats of H_2 Adsorption

Viral analysis of the isothermal data was performed by Yang *et al.*[163164] (see supporting information to these publications). Isothermal data was found to have strong linearity, with all regression coefficients larger than 0.99 when expressed in the form:

$$\ln\left(\frac{n}{p}\right) = A_0 + A_1 n + A_2 n^2 ... \tag{3.1}$$

where p is pressure, n amount absorbed and A_0, A_1 etc. are viral coefficients. In this form the data was interpolated using linear regression, and the isosteric heat of adsorption (ΔH) calculated as a function of H_2 uptake for two data-sets at 78 and 88 K, using the Clausius-Clapeyron equation:

$$\Delta H = R\frac{ln(p_2/p_1)}{1/T_1 - 1/T_2} \tag{3.2}$$

where R is the gas constant. The error in the enthalpies was estimated to be 0.1 $KJmol^{-1}$. No points are shown in figure 3.4 (c) because ΔH has been calculated using two data sets with points sampled at different intervals.

As expected, ΔH decreases with increasing gas adsorption (figure 3.4); the values at zero coverage are given in table 3.1. ΔH improves with use of Li^+ as the counterion for all of the three examples studied. A very recent study has used inelastic neutron scattering to show that H_2 predominantly interacts with carboxylate groups forming the backbone of the organic linkers in NOTT-209, rather than with Li^+[167]. It was suggested in this study that the presence of Li^+ changes the charge distribution within the organic linkers. In particular, the improvement in ΔH between NOTT-206a and NOTT-207a supports this, because no Li^+ is readily exposed to H_2 in NOTT-207a due to the closed octahedral co-ordination sphere. However to this end experimental evidence is not conclusive, since it is

also possible that change to the pore architecture/texture improves ΔH upon exchange of cations for Li^+.

The pore volumes increase with both the use of longer and less bulky organic linkers. Comparing data on NOTT-206a, NOTT-200a and NOTT-208a from table 3.1, no trend with ΔH is observed. However, pore volume is also noted to increase upon exchange of cations for Li^+; in every case ΔH increased with pore volume. This trend is surprising, since an inverse relationship between pore size and binding energy is normally expected[165]. The simultaneous increase in both these parameters has been reported for other Li^+ MOF[160].

3.5 Conclusion

In this chapter, static ^{7}Li NMR has been used to provide evidence for the change in co-ordination environment about lithium upon desolvation of NOTT-207, NOTT-201 and NOTT-209. Upon postsynthetic cation exchange of $Hdma^+$ or H_2ppz^{2+} for Li^+, increase in both the H_2 storage capacity and decrease in the isosteric heat of adsorption are observed. The biggest improvement in both these parameters was observed between NOTT-208 and NOTT-209. Simultaneous improvement to both parameters is challenging to achieve, since an increase in storage capacity normally requires an increase in pore volume. Therefore the above has provided a new strategy towards development of high capacity storage materials which may operate at more ambient temperatures. Postsynthetic cation exchange with Mg^{2+} ions has been suggested as a promising alternative to materials with Li^+ (≈ 22 $kJmol^{-1}$)[168]. ^{25}Mg has $I = \frac{5}{2}$ so offers the potential for a wide variety of NMR techniques suitable for quadrupolar nuclei for elucidating equivalent binding sites, such as MQMAS.

Chapter 4

The Lithium Borohydride / Magnesium Hydride System

4.1 Introduction: Hydrogen Storage using the Lithium Borohydride - Magnesium Hydride System

The lithium borohydride ($LiBH_4$) storage option has an impressive 13.6 $wt\%$ H_2 gravimetric capacity, with respect to decomposition to LiH. The decomposition is given by reaction 4.1, which is fully reversible. However, poor kinetics means high temperatures are required, to the extent that only half the available hydrogen is released even at temperatures as high as 600 ^oC[50,169]. Reaction 4.1 is strongly endothermic ($\Delta_r H$ 74 kJ mol^{-1} H_2). This means at T(1 bar) = 370 ^oC, temperatures and pressures outside the desired operable range of a fuel cell are required to cross the equilibrium pressure-temperature boundary in the direction of LiH formation.

$$LiBH_4 \leftrightarrow LiH + B + \frac{3}{2}H_2 \tag{4.1}$$

To make use of the high gravimetric capacity of $LiBH_4$, it is necessary to engineer the material towards faster decomposition at lower temperatures, which enhances the kinetics and thermodynamics. Various efforts include, nano-engineering by inclusion of $LiBH_4$ into carbon scaffolds[61], nano-confinement[170] or catalysis[171,172].

Alternatively $LiBH_4$ may be destabilised by reacting with a secondary compound in the form of a multi-component system, where the overall reaction has a lower enthalpy than that of decomposition of pure $LiBH_4$[58]. For this to occur, the materials must be intimately mixed; this may be achieved by mechanically milling. Destabilisation by a second hydride is preferable to minimize the gravimetric penalty[173], as illustrated by figure 4.1.

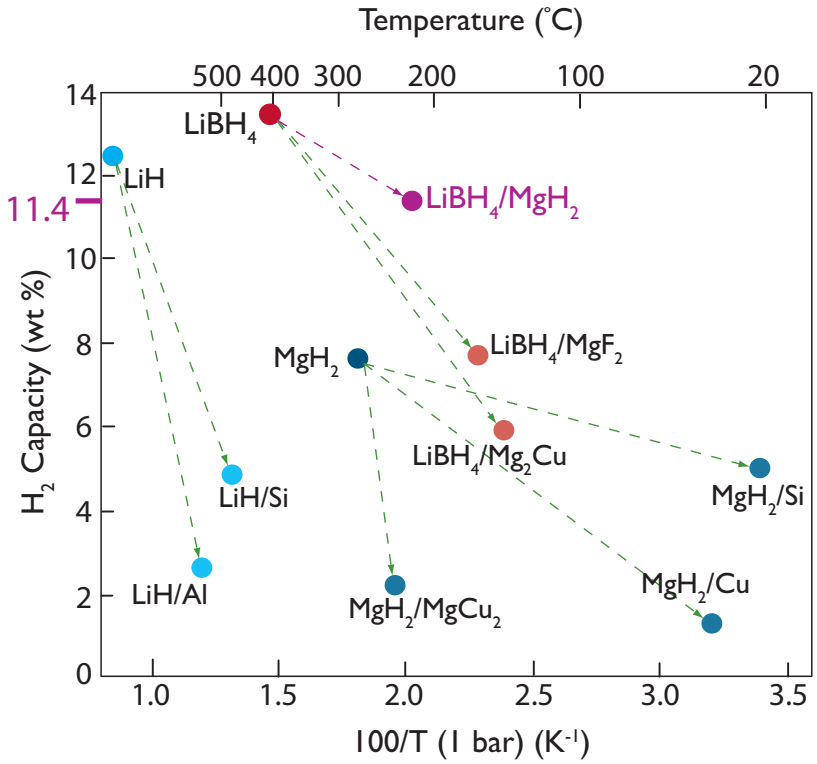


Figure 4.1: Reduction in gravimetric capacity and temperature upon destabilisation of $LiBH_4$ with MgH_2 (pink arrow). Destabilisation of other common light metal/chemical hydride systems with different additives are also presented for comparison[58].

Destabilisation of $LiBH_4$ by MgH_2 lowers the reaction enthalpy to 46 kJ mol^{-1} H_2, with a small reduction in gravimetric capacity to 11.4 $wt\%$ H_2. The dehydrogenation state is destabilised by the formation of MgB_2[174], shown by reaction 4.2.

$$2LiBH_4 + MgH_2 \leftrightarrow 2LiH + MgB_2 + 4H_2 \tag{4.2}$$

Notably, mechanical milling of mixtures of LiH with MgB_2 for ultra-long times (120 hrs) reduces the (de-)hydrogenation temperatures to below the melting temperature of $LiBH_4$ (270 ^oC[50]), allowing reversible hydrogen cycling within the solid phase[175]. It was shown in the same study that the rate of the solid-state reac-

tion is diffusion limited. An improvement in (de-)hydrogenation was also found, and attributed to smaller grain sizes produced by ball milling which creates a higher lattice strain. Considering the interaction between the two phases present, limitations to the rates are most likely due to inter-grain mass transport.

The destabilised reaction is also shown to be fully reversible, however the amorphous nature of the reaction intermediates[176] has made the mechanism of the reaction hard to elucidate and to this end a gap exists in the understanding of the $LiBH_4/MgH_2$ system. The first part of this chapter will use wideline NMR to study Li^+ diffusion in ball-milled $LiBH_4/MgH_2$. Then in the latter section of this chapter, a multi-nuclear NMR study is presented, which provides insight into the nature of the reaction intermediates.

4.2 Mechanically Milled Mixtures of Lithium Borohydride with Magnesium Hydride

4.2.1 Literature Review: Structure of and Dynamics in Lithium Borohydride

$LiBH_4$ undergoes a structural phase transition from orthorhombic[177] (LT phase) to hexagonal[178] (HT phase). The temperature at which this occurs ranges from between 381 and 384 K by neutron powder diffraction[178] to 390 K by ionic conductivity and NMR[179].

In the LT phase, the $[BH_4]^-$ units exhibit strong orientational disorder from temperatures above 50 K[180]. Early NMR relaxometry suggested that rapid reorientation of the $[BH_4]^-$ anions[181] drives the ^1H spin-lattice relaxation in the LT phase; exhibiting the shortest T_1 times around 160 K[182]. Later work confirmed this, and found that the static ^{11}B resonance was flanked by a pair of broadened quadrupolar satellites in the LT phase, which were removed upon the phase transition[183]. This was attributed to anisotropic reorientations of $[BH_4]^-$ group in the LT phase; indeed 2 types of rotation of the $[BH_4]^-$ tetrahedron were inferred from spin-lattice relaxation measurements, and recent PND measurements showed substantial orientational disorder of $[BH_4]^-$ tetrahedra, even down to 50 K[180]. The 2 types of rotation were later characterised as rotations about C_2 and C_3 axes[184,185]; where the motion around C_3 is energetically favourable in the LT phase. In the HT phase, both types of rotation become almost equally favourable, allowing deviations from ideal C_3 geometry, and causing the overall rotation to become more isotropic. This was accompanied by an increase in the mean square atomic displacement parameters[178].

Tarasov *et al.*[186] found that a pake pattern in the ^7Li spectrum appeared at ~ 333

K owing to the first order quadrupole coupling, with C_Q = 36.8±0.4 kHz. This was assigned to the rearrangement of the lithium sub-lattice, rather than the motional averaging of dipole-dipole couplings by Li^+ diffusion. In contrast, Matsuo *et al.*[179] observed a broad resonance line up to 385 K, and then a Pake pattern with the same C_Q at higher temperatures. Li^+ ion conductivity measurements on $LiBH_4$ found an order of magnitude increase in the ionic conductivity upon the phase transition[179]. This was used to explain the sudden narrowing of the ^{7}Li NMR resonance. The temperature variation of the ^{7}Li spin-lattice relaxation times in $LiBH_4$ showed a minimum around 493 K. Agreement between the activation energy (0.53 eV) measured by ionic conductivity and NMR confirmed that the motional process driving ^{7}Li spin-lattice relaxation was Li^+ hopping. Molecular dynamics simulations showed that the Li^+ ion diffusion pathway in HT phase of $LiBH_4$ originates from a splitting of the atom location into adjacent sites with equal probability of occupancy, in the crystallographic *c*-direction. Metastable interstitial sites exist in the *a*-*b*-plane, allowing Frenkel defects to form[187]. Recently, Epp and Wilkening[105] observed ^{6}Li and ^{7}Li spin-lattice relaxation as a function of Larmor frequency and showed that this results from two-dimensional Li^+ hopping in the hexagonal phase. This is consistent with observations by Callear *et al.*[180] that upon the phase transition, realignment of BH_4^- tetrahedra create facile channels, which Li^+ ions subsequently hop along with restricted dimensionality to 2D.

Soloninin *et al.*[151] showed that superionic Li^+ diffusion is also the cause of ^{1}H and ^{11}B spin-lattice relaxation behavior in the HT phase. At temperatures above 440 K, line narrowing observed in both ^{1}H and ^{11}B spectra coincides with the onset of the slower diffusion of a B- and H-containing species. It was previously confirmed using ^{1}H T_{1D} measurements[150] and CPMG measurements[188], that diffusion of the $[BH_4]^-$ anion occurred rather than direct mobility of H. However these measurements did not distinguish whether H transport occurs via migration of $[BH_4]^-$

or the BH_3 vacancies[189]. In fact, it was suggested with DFT calculations that for the decomposition of pure $LiBH_4$ migration of $[BH_4]^-$ and BH_3 vacancies, H^- and Li^+ ions via interstitial sites would all occur. This contrasted with previous reports that suggested that the mobility of hydrogen occurs via neutral H_2 interstitials[190,191]; it was pointed out that diffusion of charged species through the bulk is necessary for LiH formation.

4.2.2 Literature Review: Correlated Ion Hopping Studied by Spin-Lattice Relaxation

If hopping events are non-random, then the motion is said to be correlated. In such situations, the loss of correlation is non-exponential. Hence $G(\tau)$ may be modelled empirically by a stretched exponential, introduced in section 2.9.5. This describes a system with a favourable pathway of lower activation energy E_a^* for the elementary jump, which has a higher probability of being followed. E_a^* may be related to the overall activation energy expected after many ion hops E_a:

$$E_a^* = \alpha E_a \tag{4.3}$$

where α is the stretching parameter in equation 2.63, taking the range of values $0 < \alpha < 1$. E_a is related to the gradient of the high temperature (HT) flank of a spin-lattice relaxation time (T_1) curve, and E_a^* to the low temperature (LT) flank[97]. A T_1 minimum occurs when $\omega_0 = \frac{1}{\tau_c}$, where $\frac{1}{\tau_c}$ may be considered as the ion jump rate. On the LT side of the minimum, $\omega_0 >> \frac{1}{\tau_c}$, which means a nuclear spin completes many precessions before an ion has had time to jump. Therefore only the elementary jump will be sampled on the spin-lattice relaxation timescale; hence E_a^* is expected.

Conversely, in the T_1 region $\omega_0 << \frac{1}{\tau_c}$ (HT flank), many jumps occur during one

complete precession of the probe spin. Therefore the spin-lattice relaxation time is sensitive to long range diffusion in this regime. Long range diffusion implies an increased probability that higher energy barriers are also surmounted[192,193], hence E_a is expected.

The above effect often occurs in disordered solids, and thus α may be considered as a measure of the degree of disorder. When $\alpha = 1$, all pathways have equal probability, hopping is random and $G^{\alpha}(\tau)$ is exponential. However when $\alpha < 1$, hopping events sampled on a short time scale ($\omega_0 >> \frac{1}{\tau_c}$) are not entirely random, so the gradient of the LT flank of $J^{(q)}(\omega)$ (equation 2.64) is E_a^*.

4.2.3 Synthesis and Characterisation: Ball Milling Lithium Borohydride with Magnesium Hydride

Ball (mechanical) milling was carried out by Price[194]. $LiBH_4$ was ball-milled with MgH_2 for 1 hour using a Fritsch Rotary P5 planetary ball mill, at a speed of 300 rpm. Samples were maintained in an inert argon atmosphere both during transfer and milling. Steel ball bearings (10 mm diameter) were used, with a 20:1 ball to powder ratio. Samples were milled for 10 minute periods, followed by 10 minute rests, to prevent temperature build-up within the milling pots.

As-purchased $LiBH_4$ (Acros Organics 95%) and MgH_2 (Alfar Aesar 98 %) occur as large crystallites. For the hand-milled samples, materials were ground to a fine powder by hand using a pestle and mortar for about 1 minute, inside a glove box.

Six samples listed in table 4.1 are studied in the following work with static ^{7}Li NMR.

Sample label	Sample description
1	As-purchased $LiBH_4$
2	Hand ground $LiBH_4$
3	Hand ground 2:1 $LiBH_4/MgH_2$
4	Mechanically milled $LiBH_4$
5	Mechanically milled 2:1 $LiBH_4/MgH_2$
6	Mechanically milled 0.3:1 $LiBH_4/MgH_2$

Table 4.1: List of prepared samples for static ^{7}Li measurements.

Sample 1 comprised a few hundred large crystals of $LiBH_4$, so is considered to have very high degree of crystallinity. Grinding the sample is expected to reduce the crystal size, in proportion with the amount of effort put into grinding. High energy ball-milled samples (4, 5 and 6) are expected to have the smallest crystallites, and hand ground samples (2 and 3) to have larger crystals, but smaller than those for an unground sample (1)[192,195].

4.2.4 Lithium-7 Static NMR: General Line Shape Analysis

Wideline ^{7}Li NMR spectra were recorded at 7 T as a function of temperature for samples 2, 4 and 5, using a solid echo pulse sequence with $\frac{\pi}{2}$ pulse lengths of 1.2 μs and an echo delay of 60.0 μs. Where necessary, time domain signals were left shifted to the echo maximum. The spectra presented in figure 4.2 were externally referenced to 1.0 M LiCl (aq). Samples 1 and 2 exhibited identical line shape behavior, as did samples 3 and 4. Sample 6 was very different, and will be discussed later. Hence for brevity, figure 4.2 contains spectra of just samples 2, 4 and 5.

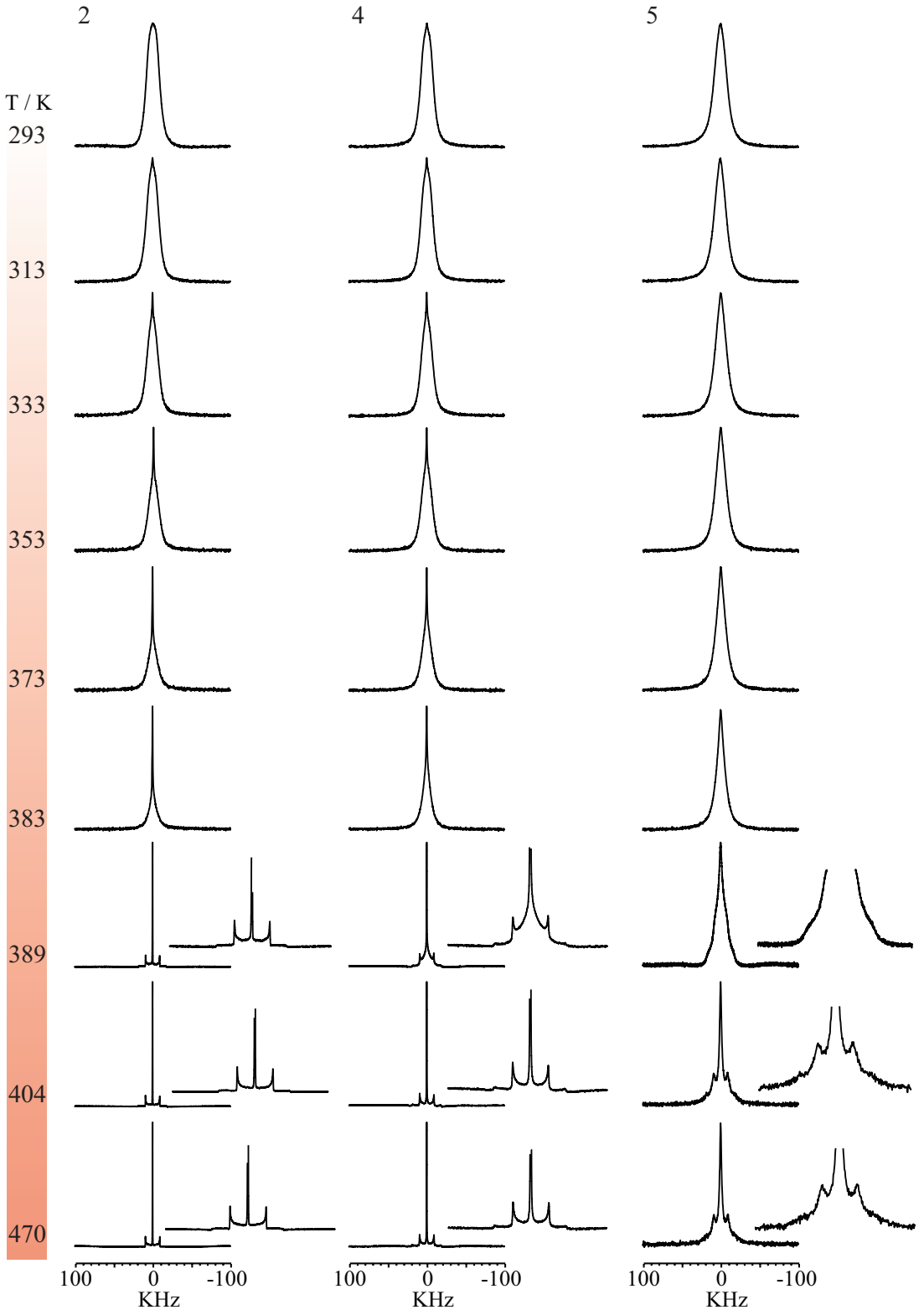


Figure 4.2: Variable temperature wideline ^{7}Li spectra of samples 2, 4 and 5. Spectra at the highest temperatures have been expanded to show the Pake pattern fine structure.

The stark change in the line shape between 383 and 389 K (all samples) indicates the phase transition occurs in this temperature region, in agreement with all previous studies, except Tarasov *et al.*[186]. The change in line shape in this temperature region is a signature of $LiBH_4$. This was used as a comparator to assess samples which were stored in sealed glass NMR tubes at later dates, for evidence of oxidation.

The linewidth of the ^{7}Li spectrum of sample 1 (unground $LiBH_4$) with and without high power CW ^{1}H decoupling is compared in table 4.2 for the LT phase.

Experiment	With CW decoupling	Without CW decoupling
Linewidth(183 K) (kHz)	16.8	16.3
Linewidth(293 K) (kHz)	11.8	11.5

Table 4.2: ^{7}Li linewidths recorded at 183 and 293 K for sample 1 with and without CW decoupling for the LT phase.

The similarity between the linewidths with and without ^{1}H decoupling suggests that the Li - H dipolar coupling does not contribute to the $LiBH_4$ linewidth, in agreement with previous observations made by Tarasov *et al.*[186]. This is expected, since the $[BH_4]^-$ ion rotates rapidly even at 160 K.

Upon increasing temperature from 293 to 383 K, it can be seen from the spectra for all samples shown in figure 4.2 that the line shape changes, and narrows substantially with increasing temperature. Between 333 and 383 K, the line shape could no longer be described by a single Gaussian, Lorentzian or Voigt component. The line shapes were investigated using a SIMPSON simulated I = $\frac{3}{2}$ spectrum which contained a central transition flanked by a pair of quadrupolar satellites. It was not possible to accurately reproduce the line shape with the simulated spectrum, since to achieve broad enough satellites by line broadening the simulated FID led to an over-broadened central transition. This suggests a distribution of

EFGs must exist, resulting in additional broadening to the quadrupolar satellites. Indeed, such an interpretation is consistent with the notion of orientationally disordered $[BH_4]^-$ tetrahedra reported by Callear *et al.*[180], which would be expected to lead to a distribution of EFGs. To support this interpretation, the line shape was fitted to two components. Voigt profiles yielded the best fit; a Voigt line shape is not surprising, since the line shape will change from pure Gaussian to pure Lorentzian with the onset of motion. Since the crystallographic data shows that only one lithium site exists in the LT phase, two components could be considered to be a mixture of orthorhombic and hexagonal phases in the sample upon crossing the phase transition. However, considering the likely temperature gradient present across the sample due to the nature of the experimental setup, this behavior is only expected within c.a. 10 K of the phase transition. In particular, comparison of spectra at 389 K with those at 383 K show no evidence for a residual orthorhombic component. Instead, two components may be considered contributions to the spectrum from central and satellite transitions. However the intensity ratios were estimated from the integral of the components, and did not match up to the expected 2:3 for central : satellite transitions[196]. Two phase line shapes have been found in a similar study, where each phase was assigned to either the amorphous inter-grain regions generated by ball milling or the bulk[197]. This is another possible interpretation, but can only be made conclusively in the context of supporting data from other types of experiments which give further insight into the structural changes upon hand and ball milling. Necessary experiments are discussed in section 4.2.9.

4.2.5 Lithium-7 Static NMR: Comparison of Samples 1 to 6

The sudden line narrowing associated with the phase transition (figure 4.2) was complete by 389 K, and no further significant changes occurred in the spectra in the subsequent temperature range. Figure 4.3 shows spectra of samples 2 to 6 recorded at 460 K in the HT phase. As expected, the spectrum shows a narrow central line flanked by two powder-broadened satellite transitions. The sudden line narrowing results from an increase in the Li^+ diffusion coefficient[150].

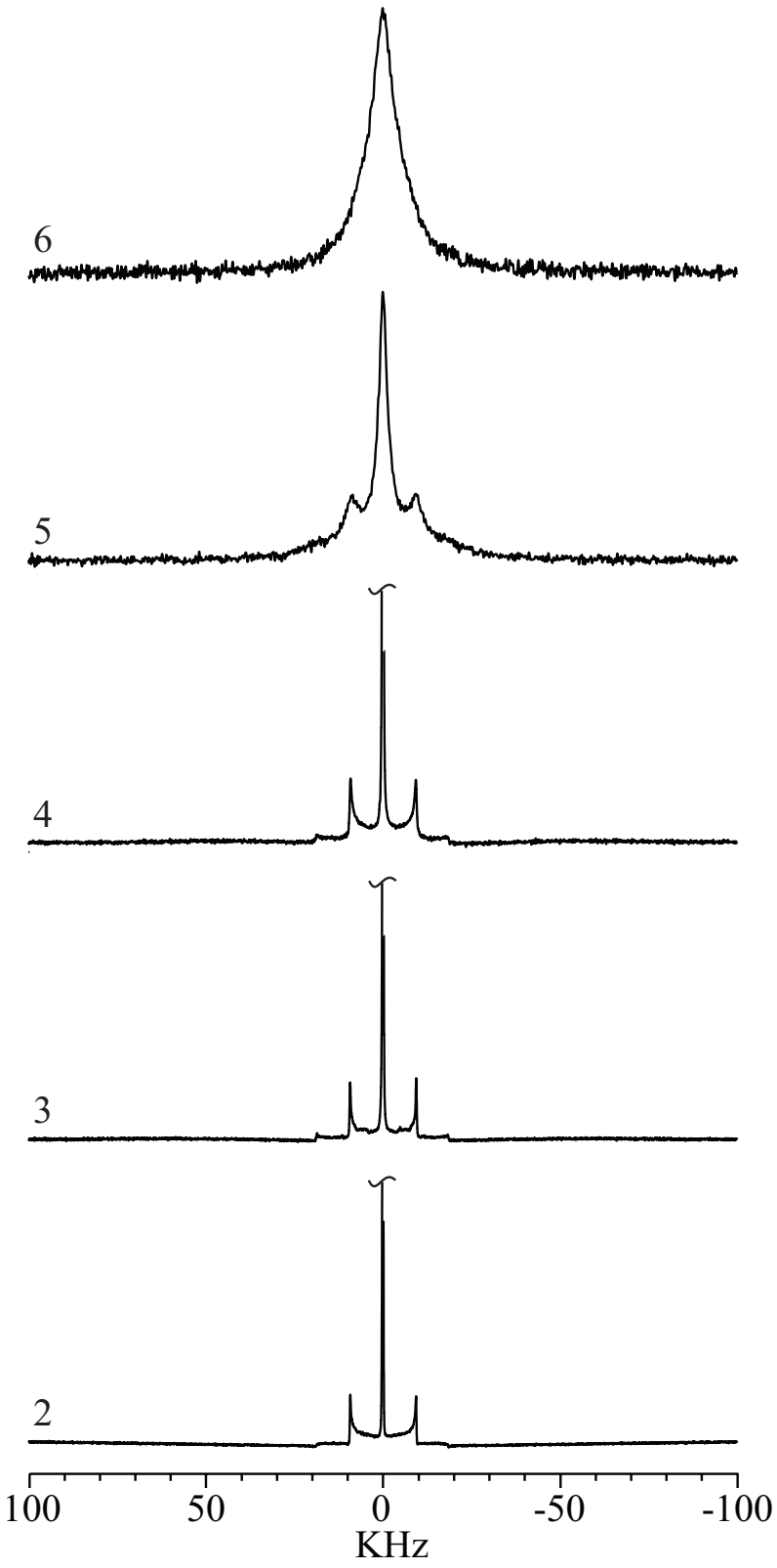


Figure 4.3: Wideline ^{7}Li spectra at 460 K of samples 2 - 6.

The linewidth of the central and satellite transitions (CT / ST), and the C_Q values from the spectra in figure 4.3 are given in table 4.3. The C_Q values are in good agreement with that previously reported for $LiBH_4$ of 37.0 kHz[198]. The satellite transition linewidths were measured by optimising the line broadening of a SIMPSON simulated spectrum to fit the satellites for samples 2 to 5. The spectrum of sample 6 was too broad to show the satellite fine structure.

Sample	CT Linewidth (Hz)	ST Linewidth (Hz)	C_Q (kHz)
2	150	127	37.0(5)
3	150	136	37.2(5)
4	300	295	36.9(5)
5	2050	2064	36.6(5)
6	14300	-	-

Table 4.3: ^{7}Li linewidths and C_Q values from spectra recorded at 460 K.

Examining the HT spectra in figure 4.3 further, the appearance of a single, well resolved Pake pattern, with sharp quadrupolar satellites for samples 2 and 3 suggests that Li^+ ions hop between sites of the same EFG. The central and satellite transition linewidths are both very similar for all samples, suggesting that the origin of the broadening in 4 and 5 affects the whole spectrum and not just the satellites. This suggests that all lithium sites have the same EFGs for samples 1 - 5; therefore are equivalent. Similarity of C_Q values between samples 1 - 5 suggests that neither hand grinding, ball milling nor addition of MgH_2 up to a 2:1 ratio significantly changes the nature of the single lithium site. It is noted that the homonuclear dipolar broadening was motionally averaged at lower temperatures (shown in figure 4.2). The origin of the broadening between samples shown in figure 4.3 is therefore due to an increase in the range of chemical shifts, rather than a distribution of EFGs, which would only broaden the satellite transitions.

The similarity between the linewidths of samples 2 and 3 show that grinding $LiBH_4$

by hand with or without the addition of MgH_2 makes no difference to the NMR spectrum. This means grinding $LiBH_4$ by hand with or without MgH_2 makes no difference on the molecular length scale. In contrast, the spectrum of ball-milled $LiBH_4$ (sample 4) is broader than that of hand ground $LiBH_4$ (sample 2). Ball milling therefore results in an increase in the distribution of chemical shifts; implying changes to the structure on a shorter length scale than possible with hand grinding, by substantial break down of crystallites. A significant increase in the linewidth is observed for sample 5, upon addition of MgH_2 in a 2:1 $LiBH_4$:MgH_2 ratio, and even more so for sample 6 with a 0.3:1 ratio. It is possible that the inclusion of MgH_2 grains results in lower crystallinity of the ball-milled samples, but the possibility of a dipolar interaction with ^{25}Mg in either metallic Mg (from broken Mg - H bonds by ball milling) or MgH_2 cannot be ruled out either.

The vast amount of line broadening observed for sample 6 suggests much more significant structural changes, such as a further reduction in grain size resulting in a more amorphous sample. Alternatively it suggests significant changes in the nature of the dynamics resulting in the change or removal of the phase transition. Since crystal structure and ion dynamics are inextricably linked, a combination of both is likely.

4.2.6 Discussion: Lithium-7 Line Shape Analysis in both Low and High Temperature Phases

The line shape changes between 293 and 383 K shown in figure 4.2 indicate motional narrowing is occurring in the orthorhombic phase. Proton decoupling measurements indicate the rotation of the $[BH_4]^-$ anion is already rapid in comparison to the linewidth, but translational motion of hydrogen or $[BH_4]^-$ is not expected until 440 K[150,151,188]. Therefore the line shape changes are attributed to the onset of Li^+ diffusion. This is in contrast to Epp and Wilkening[105] who observed no

change below 380 K, concluding that τ_c is of the order of 10^{-3} s in this temperature range. In fact, Matsuo *et al.*[179] found τ_c to decrease up to 10^{-5} s in the LT phase using conductivity measurements. This is of the same order of magnitude the NMR linewidth so motional narrowing will be expected just prior to the phase transition. Indeed the formation of facile ion channels in the LT phase would create a favourable pathway for Li^+ ion diffusion.

Hand grinding made little difference to the ^{7}Li spectra, but ball milling resulted in spectral broadening, and the addition of MgH_2 increased this effect. These effects may be seen in spectra from the LT phase (figure 4.2) and from the HT phase (figure 4.3). Similar spectral features have been observed by Winter and Heitjans[199] for micro- and nano-crystalline Li_xTiS_2. Here, it is shown from the similarity of the central and satellite transition linewidths in the HT phase (figure 4.3), that ball milling does not create a distribution of EFGs. Therefore only a single lithium site exists in the HT phase. No change to the EFGs upon ball milling implies that the bulk crystal structure is unchanged. Therefore whilst ball milling for 1 hour may reduce grain sizes, it does not affect the samples to the extent observed in other studies which used longer ball milling times[175,200]. Furthermore, the phase transition remains at exactly the same temperature after ball milling, suggesting the inherent crystal structure of the materials is retained, within the grains.

4.2.7 Lithium-7 Static NMR: Spin-Lattice Relaxation Measurements

^{7}Li spin-lattice relaxation times (T_1) were measured as a function of temperature, on samples 1 - 5 (figure 4.4) with the saturation recovery method. Saturation was achieved with a train of 100 $\frac{\pi}{2}$ pulses of duration 1.2 μs, spaced by 10 μs. The FID was collected with a solid-echo. The resulting recovery of magnetization

could be described by a single exponential, and a fit yielded T_1. The accessible temperature range was between the phase transition at 390 K and the instrument maximum of 470 K. The maximum spin lattice relaxation rate was just attained for most samples.

The motional process driving spin-lattice relaxation is Li^+ diffusion, which is assumed to obey a simple Arrhenius law. Various different assumptions about the mechanism of relaxation have been made. Matsuo *et al.*[179] have assumed T_1 relaxation is due to homonuclear dipolar couplings (equation 2.68). In contrast, Soloninin *et al.*[151] assume the contribution from heteronuclear spins ^1H and ^{11}B also make a significant contribution to T_1 in addition to ^7Li homonuclear dipolar couplings (equations 2.67). Since Li^+ ions jump between equivalent sites with the same EFG, it was assumed that quadrupolar relaxation would be negligible. Epp and Wilkening[105] showed that the HT flank for ^6Li ($\omega_0\tau_c < 1$) had a logarithmic field dependence, which was a result of diffusion being confined to 2-dimensions in the high-temperature phase.

In light of the disparity between different models, which albeit yielded very similar Arrhenius parameters, relaxation was assumed to be driven by a randomly fluctuating field, with no specific assumptions about the relaxation mechanism. Initially, Li^+ hopping was assumed to be entirely random and therefore loss of correlation exponential. Since it was only possible to acquire the LT flank, a 2-dimensional correlation function is not expected to make a difference. The data given in figure 4.4 was therefore fitted to a single Lorentzian (equation 2.65). Good agreement was found for the activation energy $E_a = 0.52$ eV, and the correlation time $\tau_0 = 4 \times 10^{-15}$ s, between sample 1 (unground $LiBH_4$) and previously reported values[105,151,179]. A progressive lowering of E_a with concomitant increase in τ_0 was observed between samples 1 to 5. However, τ_0 increased by 2 orders of magnitude, to values around 10^{-13} s for samples 4 and 5 which had been mechanically milled. Given that $\frac{1}{\tau_0}$ may be interpreted as the maximum vibrational frequency of an

ion, then τ_0 should be of the order 10^{-14} s. This suggested that this model was not sufficient for mechanically milled samples.

Mechanical milling generates diffusion pathways with lower activation energy by providing more cracks, dislocations and interfaces for ions to travel along[195]. Since the data in figure 4.4 is in the region $\omega_0 > \frac{1}{\tau_c}$, it is reasonable to expect the spin-lattice relaxation times to be affected by correlated ionic hopping, owing to hand grinding and mechanical milling. The spin-lattice relaxation data in figure 4.4 was therefore fitted in terms of a stretched exponential. α, τ_0 and C (the pre-factor which is related to the strength of the interaction) were varied in the fit, but E_a was fixed to 0.52 eV; the expected value for unground $LiBH_4$. The optimised fit parameters are given in table 4.4. It can be seen that using a stretched exponential generates a set of τ_0 and C values for all samples which are close, considering the size of the error from least squares fitting. Whilst τ_0 is an order of magnitude higher than the attempt frequency expected for an ion, it is consistent with previously reported values[151,179]. Samples 2 and 3 show that hand grinding causes a decrease in α from 0.99 to 0.8, and samples 4 and 5 show a further decrease to 0.63 or 0.56 with mechanical milling. The large error associated with the α and E_a parameters for sample 1 originates from a poorer quality fit to the acquired data; smaller errors for the other samples suggest better quality data.

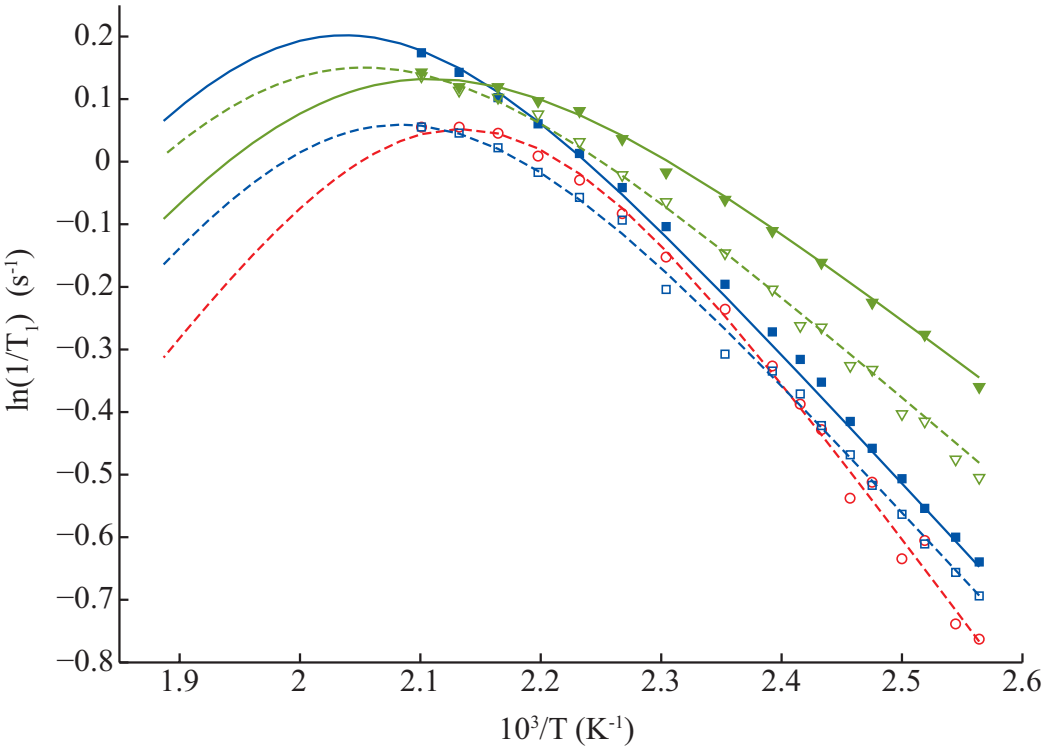


Figure 4.4: Temperature variation of the spin-lattice relaxation rate for samples: 1, red open circles; 2, blue open squares; 3, blue filled squares; 4, green open triangles; 5, green filled triangles. The lines are fits to a stretched exponential function.

Sample	α	τ_0 (10^{-15}s)	C (10^8s^{-2})	E_a^* (eV)
1	1 ± 0.4	3.6	8.3	0.52 ± 0.2
2	0.8 ± 0.2	5.4	8.4	0.4 ± 0.1
3	0.80 ± 0.07	7.15	11.6	0.42 ± 0.05
4	0.63 ± 0.09	7.60	10.1	0.33 ± 0.06
5	0.56 ± 0.05	5.94	9.6	0.29 ± 0.04

Table 4.4: Parameters from fitting data in figure 4.4 to a stretched exponential. E_a was fixed to 0.52 eV for all fits. E_a^* was obtained using the relation $E_a^* = E_a\alpha$.

4.2.8 Discussion: The Effects of Ball Milling on Lithium Ion Diffusion. Lithium-7 Spin-Lattice Relaxation Measurements.

The α parameter for sample 1 was 1, which suggested the motion in unground $LiBH_4$ can be regarded as random, following the BPP assumption of an exponential loss of correlation. Therefore the microscopic diffusion pathway within the grains has a barrier height (E_a^*), equal to that of the long-range pathway of $E_a = 0.52$ eV. The sizes of the errors for sample 1 are large; this has been ascribed to poorer quality data. Assuming the error size for sample 1 could be reduced to similar values to those of the other samples, it is reasonable to suggest the value of α is lower for all the other samples. For samples 2 and 3, a small change in α occurs to 0.8 for both samples. Since α can be interpreted as the degree of disorder, this suggests a small increase in disorder with hand grinding. However for samples 4 and 5, a larger change in α has occurred, suggesting ball milling has substantially increased disorder in samples 4 and 5, and introduced diffusion pathways with lower activation energies (E_a^*). These pathways are interpreted as microscopic jumps along grain surfaces, since similarity in the C_Q values and phase transition temperature between samples 1 - 5 (given in section 4.2.5) suggest equivalent Li^+ sites across the bulk of the material. Ball milling would be expected to break down the particle sizes, and hence fits with the notion of an increased surface area required for diffusion with lower E_a^*.

Turning attention to a subtle point, the α value for sample 5 is lower than that for sample 4, even though within the associated error. This suggests when $LiBH_4$ is ball-milled with MgH_2, the MgH_2 grains contribute to the creation of lower energy diffusion pathways. The aggressive nature of high-energy ball milling has compounded $LiBH_4$ particles with MgH_2 particles, mixing the different phases much more intimately than for hand grinding. This would lead to inter-facial

regions being created between the different phases, resulting in a lattice strain mismatch which can provide a more favourable diffusion pathway. However noting the sizes of the errors associated with α for samples 5 and 4, this idea can only be tenuous here.

It is important to note that the comparable values of α for samples 2 and 3 are distinctly different from those of 4 and 5 taking into account the sizes of the errors, confirming the importance of high energy ball milling for an effect on the diffusion pathway. It is noted that similar trends have been observed in other micro- and nano-crystalline cationic conductors; including $LiNbO_3$ [192,193] and Li_xTiS_2 [199].

4.2.9 Other Useful Experiments: Methods of Quantifying Grain Sizes

Transmission electron microscopy (TEM) may be used to show that ball milling breaks up crystallites into smaller grains. Infra-Red (IR) spectra of such materials show peak shifts and broadening[197]. This suggests the materials comprise two regions: one being inside the grains where crystallinity is preserved, the other being inter-grain regions which are amorphous.

The overarching idea to this study is that the grain size and hence the number of surface regions depends upon the preparation method (hand milling or ball milling). Certainly T_1 measurements have supported this notion, however this could be substantiated with other analytical methods. In particular, grain size and orientation can be found from direct measurement on a transmission electron micrograph[201]. The point of shearing or slippage during ball milling depends upon where weaknesses are in the lattice, giving rise to a distribution of grain sizes. Small grains (> 50 nm) may easily be overlooked owing to contrast limits and particles within agglomerates can be difficult to detect yielding inaccuracy in

this method[202].

X-ray diffraction (XRD) is an alternative method often used to provide contrasting grain size information; several approaches exist. It is usually necessary to deconvolute contributions to the line broadening from instrumental imperfections, arising from slit widths, imperfect focusing and penetration depths[203]. After this, the simplest method uses the Scherrer equation[204,205] which estimates the average grain size from the line broadening; this method assumes cubic crystals, with no crystal imperfections (strains, stacking faults, etc.). Alternatively, microstrain analysis (Stokes-Wilson method) does include an additional component to the line broadening arising from crystallographic imperfections[202,203]. In addition, the Warren-Averbach method models a Bragg peak as a Fourier series, thus allowing separation of the size from the strain contributions to the Fourier coefficients. For nano-crystalline materials, a log-normal grain size distribution is often assumed; and thus may be evaluated[206,207]. It has been shown that XRD can determine grain sizes accurately on the 10 nm scale, however for larger grain sizes ($\sim$2 μm) this method breaks down[208].

An alternative method is to measure the BET surface area from a gas sorption isotherm (usually nitrogen), and estimate the grain size from this. BET is particularly sensitive to small particles (larger surface area to volume ratio), which yields contrasting information to TEM and complementary to XRD, however it will give inaccurate answers for a skewed distribution of particle sizes. Furthermore, it won't detect the individual particles comprising agglomerates[205]. Also it is worth bearing in mind that non-spherical molecules (such as N_2) may be polarisable on charged surfaces, and the uptake-pressure can vary according to whether horizontal or vertical stacking is favoured[202].

4.2.10 Other Useful Experiments: Spin Diffusion Measurements to Determine the Average Grain Size

An attempt was made in this thesis to quantify the average grain size of as-milled 2:1 $LiBH_4/MgH_2$ (sample 5) using NMR. A two dimensional ^1H - ^1H spin diffusion experiment was performed at 7 T, with $\frac{\pi}{2}$ pulse length of 2.5 μs at an MAS rate of 12 kHz, recorded with 512 t_1 (indirect dimension) increments. A mixing time for spin diffusion to occur was allowed prior to t_1. DUMBO decoupling was applied to both dimensions, scaling the spectral width by the factor 0.63 to 152 and 179 ppm in t_2 and t_1 respectively. Further experimental details can be found in Lee[209]. Put briefly, spin diffusion may be understood as the propagation of magnetization via the flip-flop terms (mixing the Zeeman states) in the homonuclear dipolar Hamiltonian (equation 2.38). Thus the rate of spin diffusion depends upon the inter-nuclear distance.

1D saturation recovery measurements with DUMBO found the ^1H T_1 value for MgH_2 to be in the order of 900 s. The increment with a 5000 s recovery delay for sample 5 (at ambient temperature) is presented in figure 4.5. The T_1 value of LiH is also noted to be exceptionally long[149]; long T_1 values are common for metal hydrides. For samples with such long T_1 times the following method is certainly not tractable, and this limited the amount of data which could be collected in this study.

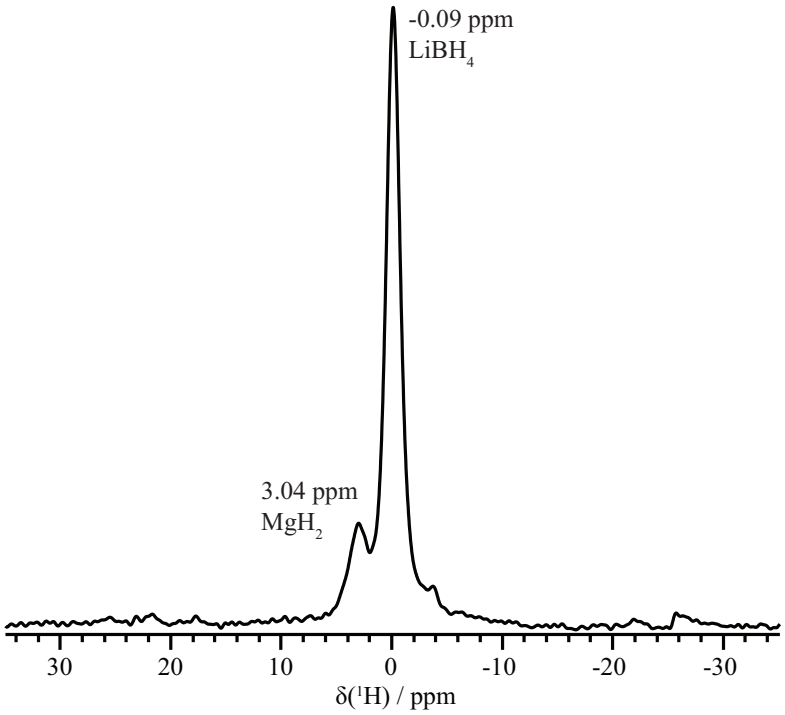


Figure 4.5: ^{1}H saturation recovery spectrum of sample 5 acquired with DUMBO decoupling. The relaxation delay for this spectrum was 5000 s. The ppm scale referenced to TMS.

Figure 4.6 presents two sets of spectra; (a) for alanine and (b) for sample 5. The purpose of including spectra of alanine is to show the experiment used works effectively on a well-understood model system. It can be seen that for alanine, there are no cross peaks at 0 ms mixing time, but with 1 ms mixing time substantial cross peak intensity correlates all three carbons C_α, C_β and C_γ.

The build up of cross peak intensity increases with mixing time, and decreases with inter-nuclear distance. Since ball-milled samples comprise discrete grains of crystalline material, the inter-nuclear distance is considered equivalent to distance between $LiBH_4$ grains and MgH_2 grains in this experiment. The spectrum of sample 5 shows little or no cross-peaks up to 10 ms mixing time. Clearly the resolution and sensitivity of the experiment were sufficient, as a separate MgH_2 resonance is visible from $LiBH_4$. Sufficient resolution was also found in the 1D

(figure 4.5). Spin diffusion experiments are able to probe length scales around 1 nm to 500 nm, where the spin diffusion time is limited by T_1 relaxation[210]. The absence of cross peaks therefore gives an indication of the order of magnitude of the grain size in sample 5. It is noted that the milling parameters used for sample preparation in this study correspond to a relatively short milling time at low energy, in comparison with other studies on ball milling[175,211]. With milling times < 1 hr, grain sizes on the order ~ 100 nm have been observed in similar Li^+ ionic conductors/complex metal hydrides[204,212,213]. Grain sizes ~ 100 nm would give at best ~ 10 % build up with ~ 10 ms mixing times, hence the absence of cross peaks.

The spin-diffusion method has the advantage over TEM, that in principle it should detect the smallest grains easily, however as found here, spin relaxation is likely to occur before transfer across larger grains. This therefore provides complementary information to TEM, and a contrasting information to XRD, which is sensitive to similar grain sizes but with limited accuracy. A model for calculating domain sizes has been derived by Schmidt-Rohr and Spiess[210], which assumes a distribution of domain sizes. However this model assumes that the interfaces between domains are sharp; it has been found in some cases of ball milling that the interfaces contain amorphous regions[197,204]. Also, it is worth noting that particle agglomeration would not be detected unless it were between the different phases.

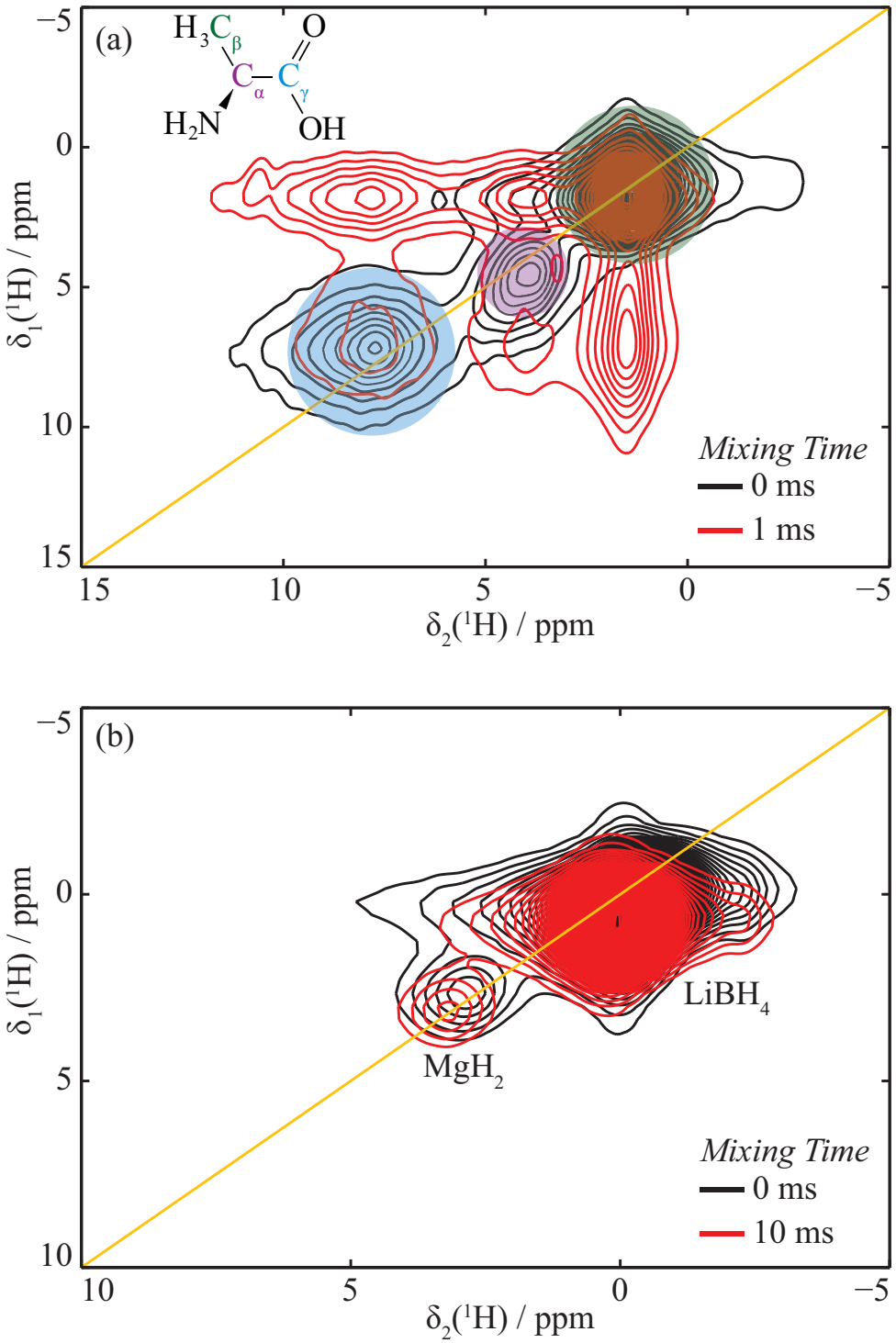


Figure 4.6: ^{1}H - ^{1}H correlation spectra of (a) alanine with 0 and 1 ms; (b) sample 5 with 0 and 10 ms, mixing times for black and red respectively. The yellow line is the diagonal. Spectra were acquired with DUMBO decoupling in both dimensions. The assignment of the alanine spectrum is denoted by the colours: green, purple and blue for C_α, C_β and C_γ respectively.

4.2.11 Other Useful Experiments: $T_{1\rho}$ Relaxation Measurements

The rotating frame relaxation time, $T_{1\rho}$, will be sensitive to motions which are on the timescale of the RF irradiation frequency. High power RF irradiation is of the order 100 KHz, which is about 3 orders of magnitude less than ω_0. Therefore a $T_{1\rho}$ minimum will occur at lower temperatures than a T_1 minimum. Calculations suggest that the $T_{1\rho}$ minimum would coincide with the accessible temperature range between the phase transition 390 K, and the maximum temperature of the probe, 470 K. Measurement of $T_{1\rho}$ in this regime will therefore afford a method of acquiring a HT flank, which will yield the same value of the activation energy for long-range Li^+ diffusion, E_a, in analogy to that of the HT flank of a T_1 curve.

It is noted that in the presence of paramagnetic impurities, the $T_{1\rho}$ is a factor of 4 larger than T_1 [104]. Measurements of $T_{1\rho}$ would therefore also confirm whether Mg metal was coupled to lithium, and affecting the relaxation rate.

4.3 *Ex situ* NMR Study on the Decomposition of the Lithium Borohydride/Magnesium Hydride System

4.3.1 Literature Review: Decomposition of the Lithium Borohydride/Magnesium Hydride System

Reaction Pathway and Product Formation Dependence on Temperature, Pressure and Stoichiometry

The decomposition pathway of $LiBH_4/MgH_2$ (reaction 4.2) is dependent on pressure and temperature. Figure 4.7 has reproduced the Van't Hoff plot[214] originally constructed from experimental data acquired by Mauron *et al.*[169] and Vajo *et al.*[174], showing the location of the equilibrium pressure boundaries for the decompositions of $LiBH_4$ and $LiBH_4/MgH_2$. It may be seen that T(1 bar) = 459 ^oC for direct decomposition of $LiBH_4$ (reaction 4.1); whereas T(1 bar) = 164 ^oC for decomposition of thermodynamically destabilised $LiBH_4$ by MgH_2. Therefore the direct decomposition to elemental boron may be suppressed with lower temperatures and higher H_2 gas partial pressures, chosen to keep the reaction in the temperature - pressure region above the equilibrium pressure boundary where just formation of MgB_2 would occur[215]. It may also be seen that the equilibrium pressure of MgH_2 is higher than that of $LiBH_4$. Therefore, lower temperatures and higher pressures favour the decomposition of the MgH_2 component independently of $LiBH_4$[194,216].

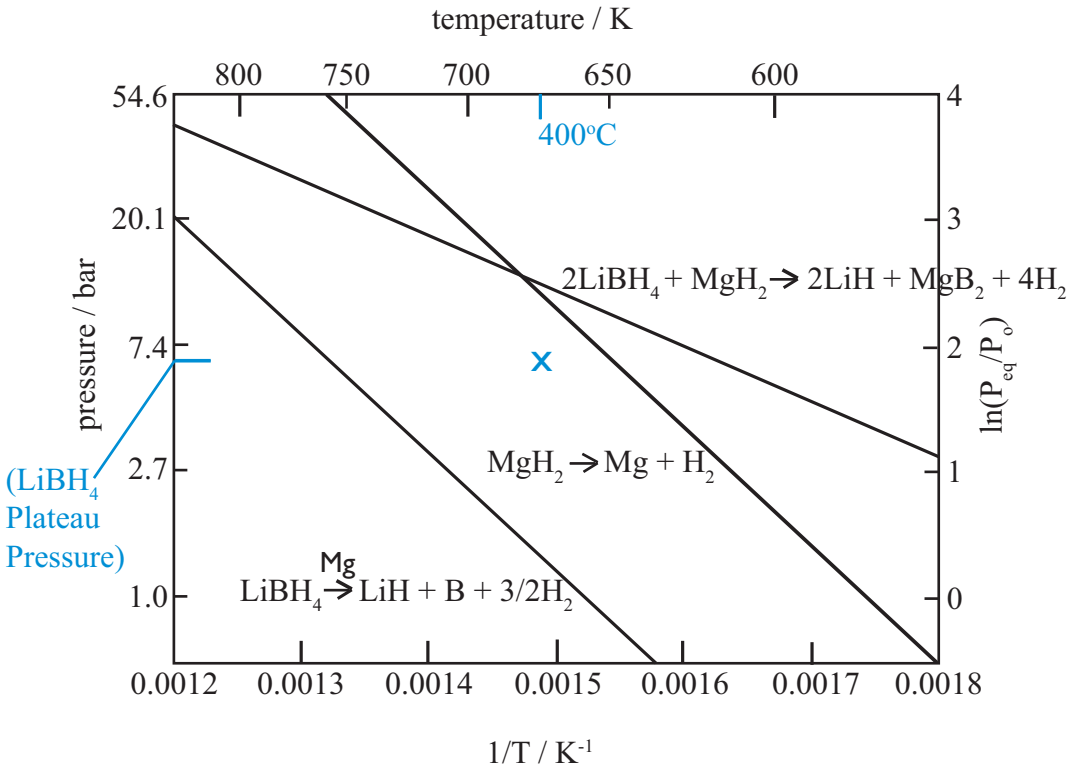


Figure 4.7: Van't Hoff plot showing the equilibrium pressure boundaries for the decomposition of MgH_2, $LiBH_4$ and $LiBH_4/MgH_2$. The blue cross marks the starting point of isothermal decomposition at 400 °C. Reproduced from reference [214].

MgB_2 forms via nucleation growth[217], where an elevated temperature may be used to compensate for the reduction in kinetics owing to elevated pressure required to suppress direct decomposition of $LiBH_4$. Formation of MgB_2 is under kinetic control, probably limited by Mg mass transport; the reaction progresses more rapidly when Mg is also in the molten state. On the other hand, direct decomposition of destabilised molten $LiBH_4$ is catalysed by solid Mg metal[216,218]. Thus direct decomposition of $LiBH_4$ is kinetically favoured when thermodynamically allowed[219]. The choice of reaction conditions is therefore critical to the success of the operation of the $LiBH_4/MgH_2$ system.

Yu *et al.*[220] observed a shift in the XRD *d*-spacings near the final stages of the Mg

- catalysed direct decomposition of $LiBH_4$ at temperatures $> 420\ ^oC$. This indicated that Mg metal also destabilised LiH, resulting in the formation of Mg_xLi_{1-x} alloys (x < 1) towards the end of the reaction. Under such conditions, Mg-rich systems (0.3:1 stoichiometry) exhibited vastly improved hydriding rates over 2:1 stoichiometric systems. Mg_xLi_{1-x} alloys may form in both stoichiometric and Mg rich systems, where formation is entirely dependent on the partial pressure of the system[221]. However Mg-rich systems showed the presence of both the hexagonal-close-packed α-alloy (x > 0.816) and body-centred-cubic (x > 0.7) β-alloy; but systems which contain a stoichiometric imbalance towards excess lithium convert entirely to the β-alloy[222]. Debate over the formation of Mg_xLi_{1-x} arose in the literature; Price *et al.*[223] demonstrated that a low base partial pressure ($< 6 \times 10^{-2}$ mbar H_2) must be maintained upon cooling to prevent re-hydrogenation of Mg_xLi_{1-x} to LiH and Mg, due to phase instability. Alloy formation was also favoured under dynamic vacuum, as opposed to H_2 partial pressure. In many studies, conditions did not favour alloy formation.

Intermediate Phases Formed During Decomposition

An *in situ* neutron diffraction experiment on a stoichiometric 2:1 system under both finite H_2 partial pressure and dynamic vacuum showed the loss of the $LiBH_4$ phase before the formation of LiH. However for 0.3:1 samples the loss of $LiBH_4$ was concomitant with the formation of LiH. It was therefore suggested than an amorphous intermediate formed in the 2:1 system but not the 0.3:1, undetected by PND.

Proposed reaction intermediates include $LiBH_2$ or LiB_3H_8[50,169]; in principle any $[B_mH_n]^{q-}$ species could occur. An *in situ* synchrotron PXRD study revealed the formation of new crystallographic phases during the decomposition of pure $LiBH_4$[224]. A recent NMR study used ^{11}B MAS and CPMAS NMR found the in-

termediate species formed for decomposition of pure $LiBH_4$ was the hydrolytically stable *closo*-$[B_{12}H_{12}]^{2-}$ [225,226]. Further confirmation has come from subsequent *ab initio* studies which found a lower enthalpy of formation [227,228] compared to other boranes. Since $[B_{12}H_{12}]^{2-}$ is very thermodynamically stable, this species is likely to block the reaction pathway, causing the overall high enthalpy of decomposition of $LiBH_4$.

NMR studies on ball-milled mixtures of LiH and MgB_2 at 21.1 T show the formation of a ternary $(Mg_{1-x}Li_{2x})B_2$ type species ($x < 1$) at very long milling times (c.a. 120 hours) [149,200,229]. The intermediate is thought to form via Li^+/Mg^{2+} ion exchange. This species was deduced from the presence of spinning bands (SSB) in the ^{6}Li spectrum, whilst the ^{11}B spectrum remained unchanged implying hexagonal boron layers were not affected by the ion exchange mechanism. Substantial broadening in the ^{25}Mg spectrum implied the presence of an amorphous intermediate. Hydrogenation of such milled mixtures to form $LiBH_4/MgH_2$ is very rapid; this was attributed to the presence of the $(Mg_{1-x}Li_{2x})B_2$ intermediate. However, it is noted that no reversibility of this system was shown, and it was therefore not clarified whether this species would reform upon cycling, or decomposition of a milled mixture of $LiBH_4/MgH_2$. In contrast to Hwang *et al.* [225], no evidence for a $[B_{12}H_{12}]^{2-}$ was seem.

Herein, MAS NMR will be used to investigate the reaction intermediates and products throughout the decomposition of as-milled samples of $LiBH_4/MgH_2$ at different temperatures and stoichiometries.

4.3.2 Synthesis and Characterisation: Decomposition of Lithium Borohydride/Magnesium Hydride under Different Conditions

Two sets of samples were synthesised by Meggouh [230] and Price [194]. The first was produced with isothermal decomposition of ball-milled mixtures of $LiBH_4$ with MgH_2, using a Sieverts type apparatus. Samples were first heated to a fixed temperature in a pre-pressurised vessel with H_2 gas ($\sim$ 40 bar). Upon lowering the pressure, the equilibrium may adjust according to the Le Chatelier principle; in this case lowering the pressure favoured product formation. The pressure-composition isotherms (PCI) shown in figure 4.8(A), were all recorded at 400 ^{o}C. During isothermal decomposition, two plateaux may be observed, depending on the rate at which the vessel is evacuated. The first at $\sim$ 20 - 25 bar corresponds to the evolution of H_2 gas from the decomposition of MgH_2, which is less thermodynamically stable than $LiBH_4$ under these conditions due to its higher equilibrium pressure. The second at $\sim$ 7 bar is the decomposition of $LiBH_4$ in the catalytic/destabilising presence of magnesium metal. The decomposition of a stoichiometric (2:1) mixture was quenched by rapid cooling at specific points along the isotherm (marked on the PCI plots in figure 4.8), leading to a set of 4 samples S0, S1(b), S1(c) and S1(d). A lithium rich (2:0.9) mixture was prepared by the same method; in this thesis just the fully decomposed sample (S3) is studied.

The second set of samples were decomposed under a temperature heating ramp to an end point of 500 ^{o}C, inside a sealed unit. During decomposition, the H_2 partial pressure rose to in excess of 30 bar. In the initial stages, reaction conditions are below the equilibrium pressure boundary for both Mg-catalysed direct decomposition of $LiBH_4$ and destabilised decomposition, however as the H_2 partial pressure rose above the equilibrium pressure boundary the direct decomposition became thermodynamically forbidden. Stoichiometric (2:1) and magnesium rich

(0.3:1) samples fully decomposed in this manner are studied (S2 and S4 respectively). Thermogravimetric analysis (TGA) measurements on S2 and S4 are shown in figure 4.8(B).

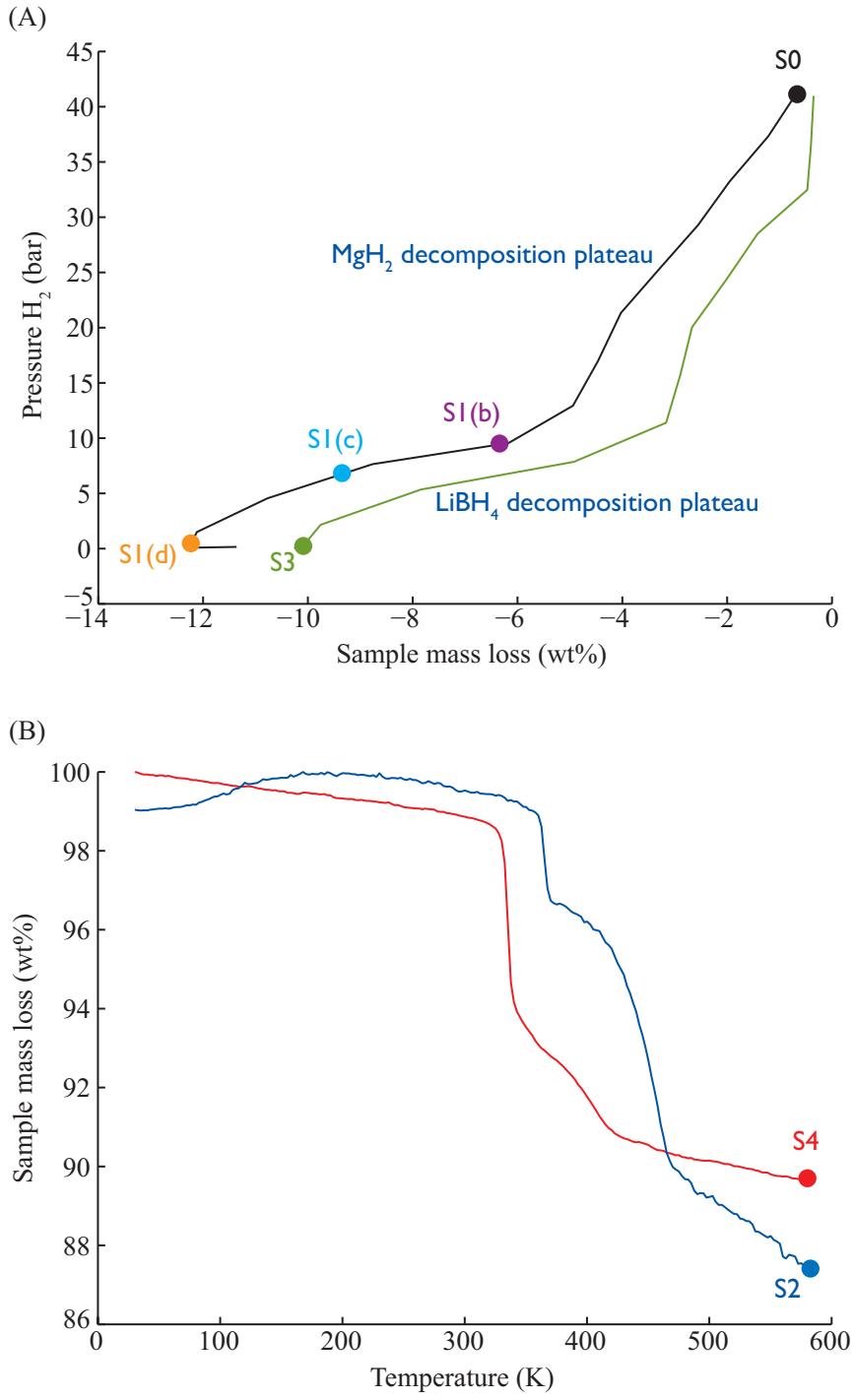


Figure 4.8: (A) PCI plots (from the Sieverts method) show decomposition under isothermal conditions at 400 ^{o}C: black, 2:1 stoichiometry; green, 2:0.9. (B) TGA plots for the decomposition under a temperature ramp to 500 ^{o}C: blue, 2:1; red, 0.3:1. The points S0, S1(b), S1(c), S1(d), S2, S3 and S4 denote points where samples were extract/quenched for *ex situ* NMR.

The sample labeling system is set out in table 4.5. For convenience, a new system is introduced here, but note that the 2:1 and 0.3:1 ball-milled mixtures are the same samples as used above (in section 4.2).

sample label	Stoichiometry	Decomposition temperature	Description
S0	2:1	Isothermally at 400^oC	As-milled $LiBH_4/MgH_2$
S1(b)	2:1	Isothermally at 400^oC	S0 quenched at the start of $LiBH_4$ decomposition
S1(c)	2:1	Isothermally at 400^oC	S0 quenched near the middle of $LiBH_4$ decomposition
S1(d)	2:1	Isothermally at 400^oC	S0 quenched at the end of $LiBH_4$ decomposition
S2	2:1	Heating ramp to 500^oC	Quenched at the end of $LiBH_4$ decomposition
S3	2:0.9	Isothermally at 400^oC	Quenched at the end of $LiBH_4$ decomposition
S4	0.3:1	Heating ramp to 500^oC	Quenched at the end of $LiBH_4$ decomposition

Table 4.5: List of prepared samples.

Routine differential scanning calorimetry (DSC), XRD and in some cases PND detected the crystalline reactants ($LiBH_4$ and MgH_2) and products (Mg, MgB_2, LiH and Mg_xLi_{1-x} where conditions allowed)[216,221]. However *in situ* PND showed that during decomposition the mixture became amorphous, and it was not possible to identify the amorphous intermediates with either XRD or PND[176]. Neutron scattering (inelastic and dynamic) experiments (both *in situ* and *ex situ*) were employed in an attempt to probe the composition during the amorphous interme-

diate stages. Unfortunately the signals were very weak, and it was not possible to distinguish the amorphous phase within suitable error[194,230].

4.3.3 Sample Handling and Testing for MAS Studies

Sample handling, rotor packing and storage when not in use was done in a glove box.

A test was performed to examine the extent of oxidation of $LiBH_4$ during experiments. A sample of $LiBH_4/MgH_2$ was exposed to the atmosphere in a controlled environment to allow the natural degradation product(s) to form. $LiB(OH)_4$ is known to form from $LiBH_4/MgH_2$ upon exposure to oxygen[231]. The ^{11}B MAS spectrum of the oxidation products was recorded and is compared to that of $LiBH_4$ in figure 4.9. A change in shift is observed from -41 ppm for $LiBH_4$ to 1 ppm, which is assigned to $LiB(OH)_4$ and in good agreement with the literature value[232]. Different spinning side band patterns for the different species may also be seen from the spectra in figure 4.9.

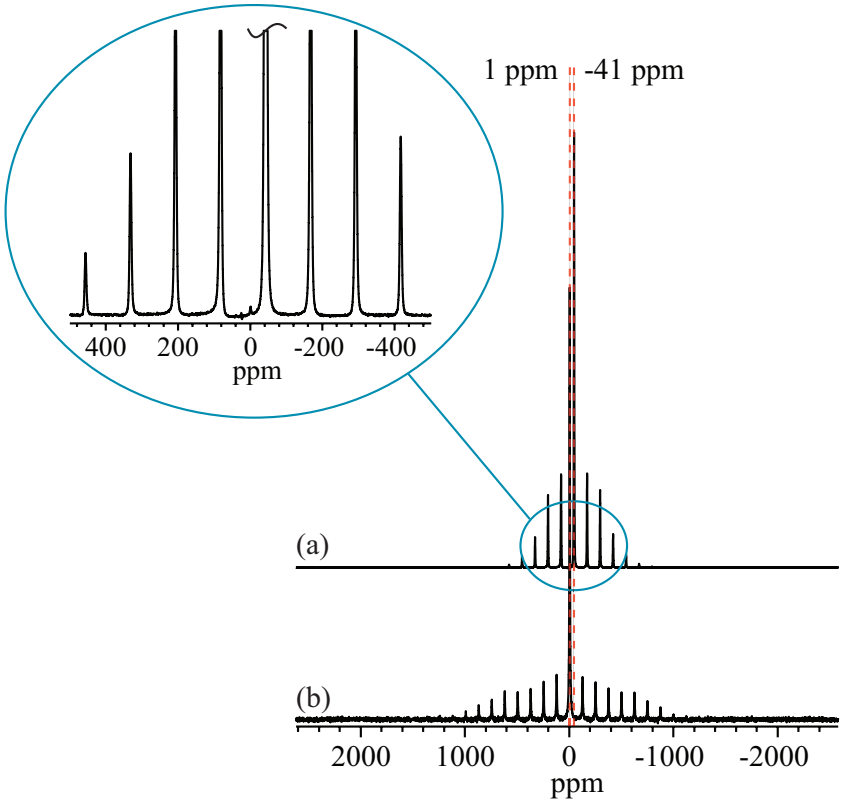


Figure 4.9: ^{11}B MAS spectra of: (a) $LiBH_4$ after 100 hours storage in a rotor under atmospheric conditions; (b) $LiB(OH)_4$. The expansion of (a) shows a small peak at 1 ppm due to $LiB(OH)_4$ impurity in stock material.

A tiny peak in the $LiBH_4$ spectrum at 1 ppm is identified as a small amount of $LiB(OH)_4$ impurity from stock material. No growth of this peak was observed throughout all experiments performed on $LiBH_4$, suggesting no oxidation during experiments. Thus it was deemed unnecessary to take further precautions, such as using dry nitrogen to perform MAS.

4.3.4 ^{11}B, ^{6}Li and ^{25}Mg MAS NMR Spectroscopy: Decomposition at 400^{o}C

^{6}Li and ^{25}Mg MAS spectra were recorded at 20 T, using a single pulse - acquire method, with relaxation delays of 60 and 1 s and $\frac{\pi}{2}$ pulse lengths of 5 and 9.5 μs respectively. MAS rates between 8 - 12 kHz were used, limited by opposing magnetic forces induced by mechanical rotation of metallic species present in the samples. The highest attainable MAS rate for a particular sample was generally used. All ^{6}Li and ^{25}Mg spectra were referenced to 1 M LiCl(aq) and $MgCl_2$(aq) respectively, which also served as suitable $\frac{\pi}{2}$ pulse length calibration compounds.

All ^{11}B MAS spectra were recorded at 7.1 T, with relaxation delay of 2 s sufficient for all samples and $\frac{\pi}{2}$ pulse length of 3 μs. MAS rates used were limited 9 - 13 kHz for the same reasons as above. Spectra were referenced to $BF_3.OEt_2$, also used for calibration of $\frac{\pi}{2}$ and π pulse lengths. A rotor synchronized spin - echo was used in order to excite and refocus only the central transition of ^{11}B (I = $\frac{3}{2}$), to negate the need for a large 1^{st} order phase correction.

^{11}B, ^{6}Li and ^{25}Mg MAS spectra of samples S0, S1(b), S1(c) and S1(d) quenched at the points marked on the isotherm in figure 4.8(A), are presented in figure 4.10.

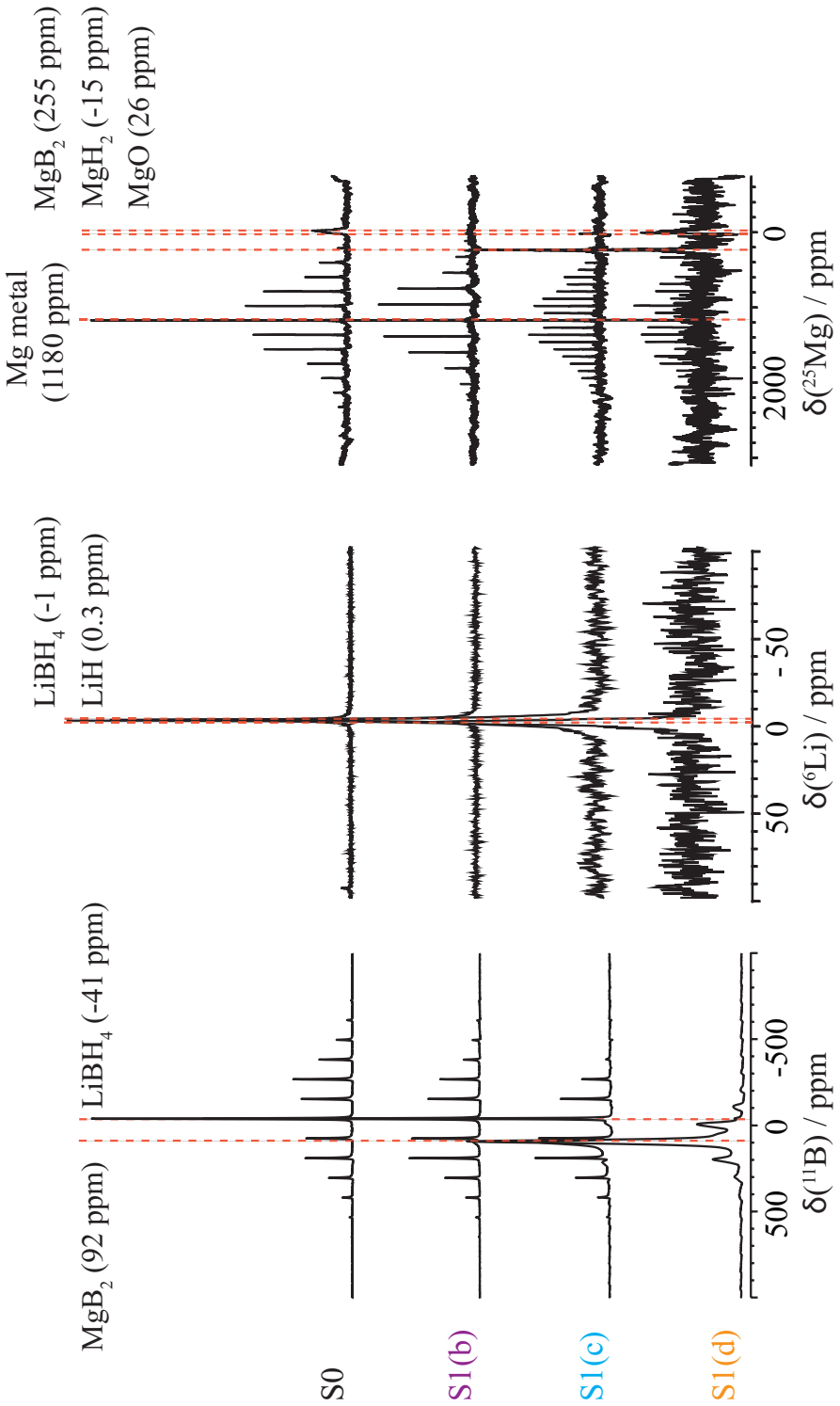


Figure 4.10: ^{11}B, ^{6}Li and ^{25}Mg MAS spectra of stoichiometric samples quenched during isothermal decomposition at 400^{o}C. ^{6}Li and ^{25}Mg were recorded at 20 T, and ^{11}B at 7.1 T. The resonance offset for ^{25}Mg was set to centre the spectral width at 1180 ppm; whereas ^{11}B and ^{6}Li are centred at ω_0.

^{25}Mg Spectra

Resonances observed at -15, 26 and 255 ppm could be assigned to MgH_2, MgO and MgB_2 based upon their chemical shift (CS) values[229]. The resonance at 1180 ppm is the Knight shifted Mg metal resonance[233]. As expected, MgH_2 present in S0 (as-milled) has completely decomposed by the start of the $LiBH_4$ plateau, as it is not present in S1(b). Growth of the MgB_2 peak is not observed until S1(d), at the end of the decomposition. A resonance due to Mg metal is observed in all spectra, but its intensity decreases as the decomposition progresses, due to Mg reacting with $LiBH_4$ to form MgB_2. The presence of Mg metal in S0 suggests that mechanical milling itself breaks Mg - H chemical bonds, most likely caused by the heat generated by the milling process. Such mechanical activation caused by ball milling $LiBH_4/MgH_2$ has been previously observed Wan *et al.*[175]. The intensity of the resonance assigned to MgO does not change during the NMR experiment, implying MgO was formed during decomposition, and confirming that the NMR rotors provide a sufficiently airtight environment for sample preservation.

^{6}Li Spectra

High field (20 T) was used for ^{6}Li to increase the frequency range of chemical shifts (according to equation 2.43), hence improving resolution. Samples S0, S1(b) and S1(c) all have a resonance at -1 ppm, which is assigned to $LiBH_4$ based upon its chemical shift. In sample S1(d), an upfield resonance at 0.3 ppm can be assigned to LiH, which forms late in the decomposition. Note the good agreement with literature values of -1.3 and 0.3 ppm for $LiBH_4$ and LiH respectively[200,229].

The ^{6}Li shifts of LiOH and LiO_2 are known to be 1.3 and 2.7 ppm respectively[149]; no evidence is found for the presence of LiOH or LiO_2.

^{11}B Spectra

The resonances at -41 and 92 ppm are assigned to $LiBH_4$ and MgB_2 respectively[200]. The difference between the MgB_2 chemical shift from the reported value of 102 ppm (143 ppm if $LiBH_4$ is used as the reference instead of $BF_3.OEt_2$) is attributed to the dependence of the quadrupolar induced shift (QIS) on $\boldsymbol{B_0}$, which has opposite sign to the chemical shift, since reported values were recorded at a much larger field, 21.4 T. Evidence in the next section will substantiate this.

4.3.5 ^{11}B MAS NMR Spectroscopy: Varying Temperature and Stoichiometry

The properties of the ^{11}B nucleus result in high sensitivity, a resolvable dispersion of chemical shifts and a manageable second order quadrupole coupling at 7 T. ^{11}B is therefore an excellent choice for probing the amorphous products/intermediates.

Figure 4.11 presents 1D ^{11}B spectra of fully decomposed samples. Resonances are observed at 92, -41 and one at either -4, -2 or -9 ppm for S2, S3 and S4 respectively. The resonances at -41 and 92 ppm again are assigned to $LiBH_4$ and MgB_2 respectively. It is noted that a more substantial amount of $LiBH_4$ remains in the spectrum of S2 and S4, in comparison to the spectra of S1(d) (figure 4.10) and S3.

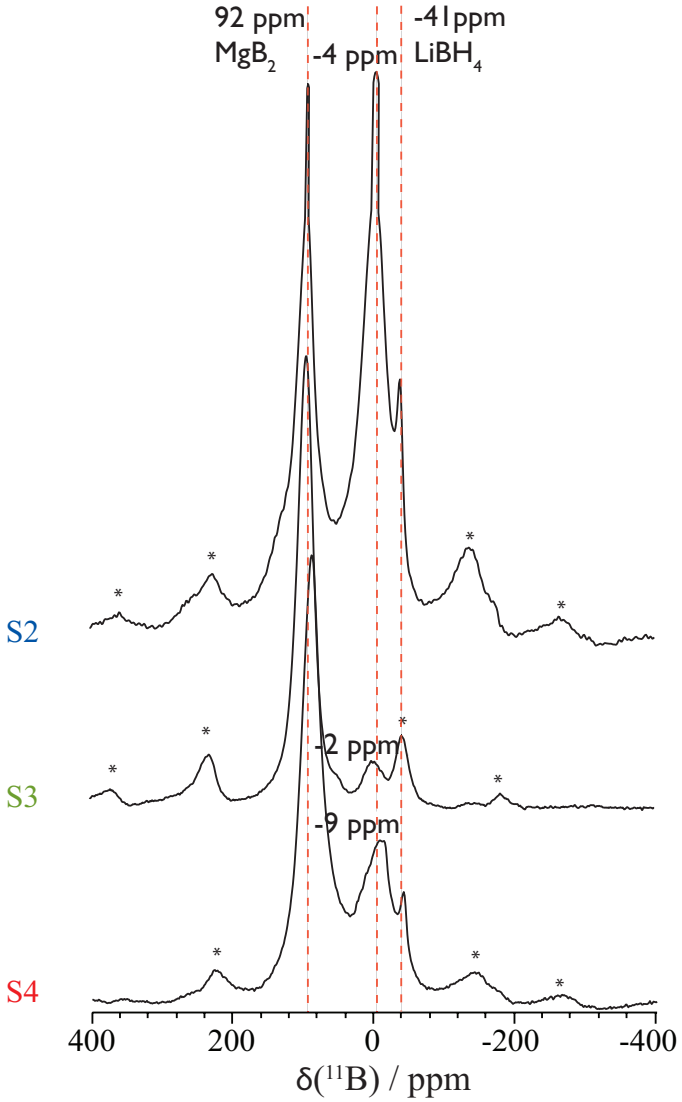


Figure 4.11: ^{11}B direct excitation MAS spectra of fully decomposed samples S2, S3 and S4.

The resonances of the intermediates/products are broad in comparison to the narrow resonance of $LiBH_4$ implying amorphous products formed during decomposition. The MQMAS technique was therefore employed in an identical fashion to that in 2.11.8, aiming to improve resolution by separating the resonances in two dimensions by removing the broadening due to the second order quadrupole coupling from the indirect dimension. In particular, the aim was to search for other boron based intermediate species than those identified in the 1D spectra.

MQMAS spectra shown in figure 4.12 were recorded with the two-pulse experiment with excitation and conversion pulses calibrated on the sample to be 7 or 8 and 2.5 μs respectively. When a z-filter was used, the delay time and pulse length were 0.3 ms and 12 μs respectively. A large range of chemical shifts meant it was not possible to synchronize the rotor with the spectral width in this set of experiments, since the maximum achievable MAS rates were too low.

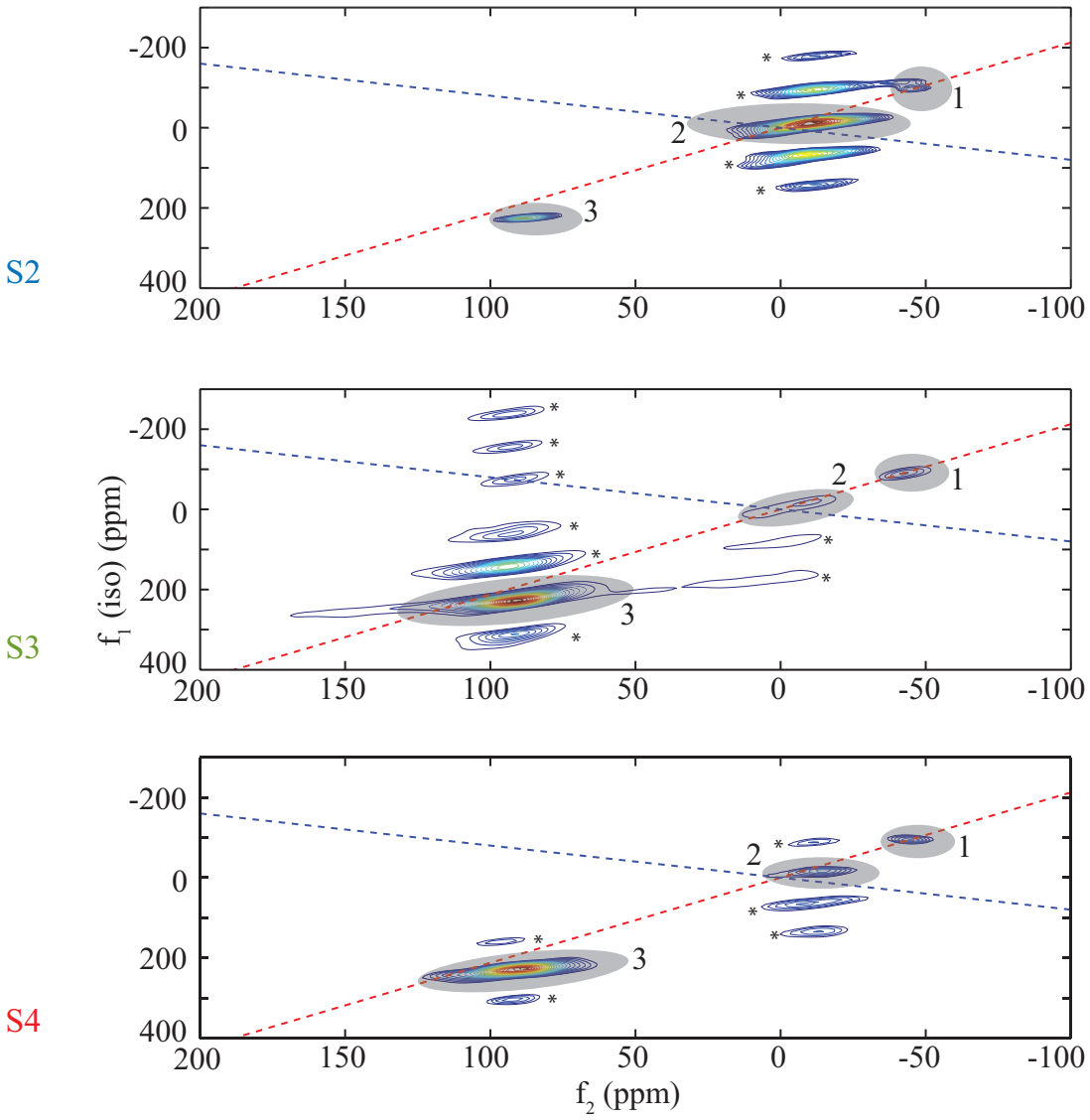


Figure 4.12: ^{11}B MQMAS Spectra of fully decomposed samples. The red line represents the CS axis, and blue line the direction of the QIS. $*$ denote spinning side bands. The spectrum of S3 was recorded with a z-filter.

The centre of gravity of peaks 1 and 2 lies along the CS axis but peak 3 is off axis. The dispersion from the CS axis is due to the QIS. From this the magnitude of the QIS for peak 3 (assigned to MgB_2) was estimated to be -11 ppm, using equation 2.95. The ^{11}B C_Q for MgB_2 was then estimated with equations 2.86 and 2.87 to lie in the range 1.75 to 2.02 MHz for $\eta = 1$ to 0 respectively, which is similar to the reported values of $C_Q \sim 1.66$ MHz and $\eta = 0$ for crystalline MgB_2[234]. Unfortunately additional amorphous broadening of the resonances meant that a second order quadrupolar line shape could not be resolved, so it was not possible to estimate C_Q and η more precisely by fitting to simulated line shapes. Using these parameters, SIMPSON simulations at 7 and 21 T were used to confirm that a QIS of $\sim$ -11 ppm is expected at 7 T, in comparison to $\sim$ -1.2 ppm expected at 21 T, accounting for the difference in the shifts at these two different fields[200].

Peak 1 is assigned to $LiBH_4$ on the basis of its chemical shift. In a similar fashion to above, a negligible QIS for $LiBH_4$ was predicted. The ^{11}B C_Q for $LiBH_4$ was estimated to be of the order 10 - 100 kHz from the width of the sideband patterns in the 1D ^{11}B spectra. It is reasonable to expect a very low C_Q value since $[BH_4]^-$ tetrahedra are highly symmetric.

The shifts of the species at site 2 are -4, -2 and -9 ppm for S2, S3 and S4 respectively. $[B_{12}H_{12}]^{2-}$ has a chemical shift of -12 ppm and amorphous boron a shift of 2 ppm[225]. Given the above, it is impossible to assign site 2 unequivocally at this point.

The QIS for $[B_{12}H_{12}]^{2-}$ was also estimated to be -1.5 ppm at 7.0 T, using $C_Q \sim$ 750 MHz and $\eta = 0$[235]. Since the α-rhombohedral allotrope of elemental boron has identical icosahedral cage structure to that of $[B_{12}H_{12}]^{2-}$[236], the QIS was assumed to be roughly the same. Therefore it is likely that the resonances overlap, and cannot be separated by MQMAS due to a similar dispersion along the QIS direction.

To facilitate the assignment of peak 2, ^{1}H - ^{11}B cross - polarisation (CP) was employed to distinguish the proton content of this species. CP spectra of samples S2, S3 and S4 presented in figure 4.13 were recorded at 7 T, with a ^{1}H $\frac{\pi}{2}$ excitation pulse length of 2.5 μs and relaxation delay of 2 s. The Hartman-Hahn match was calibrated to maximise magnetization transfer, using high power $\mathbf{B_1}$ fields of 100 and 71 KHz on ^{1}H and ^{11}B respectively. With a ^{11}B carrier frequency of 96.3 MHz, this field is large enough to excite the entire range of ^{11}B resonances in the direct excitation spectra shown in figure 4.11, thus making the CP used here non-selective towards any particular species.

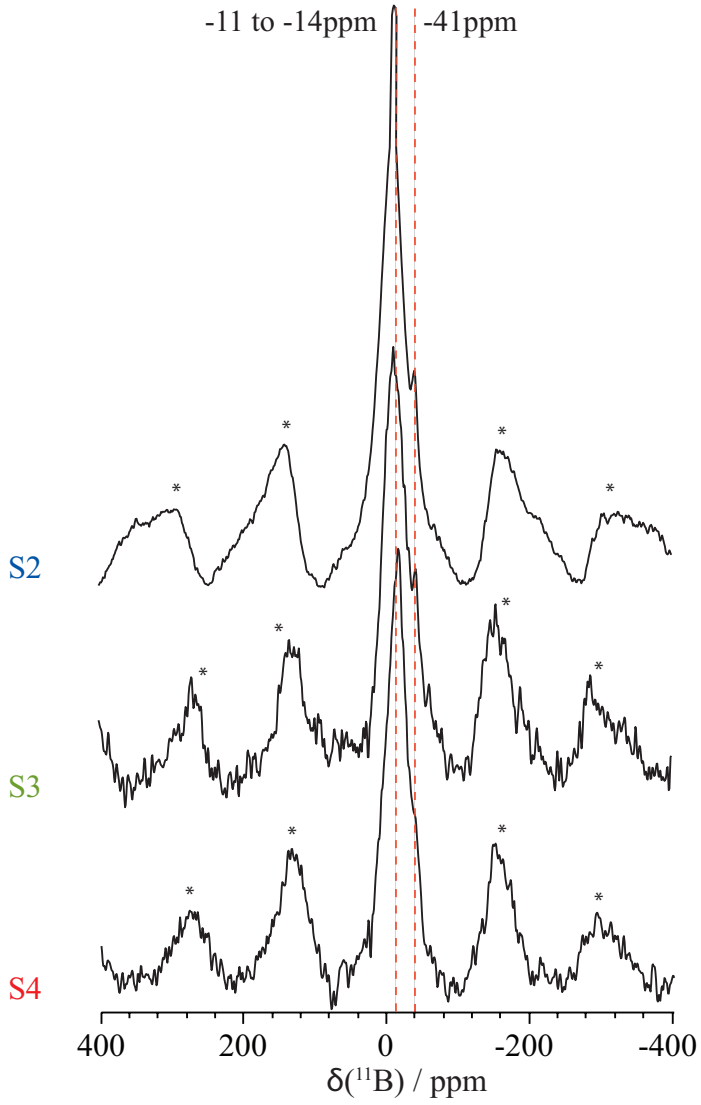


Figure 4.13: ^{1}H - ^{11}B CP spectra of fully decomposed samples.

The optimal contact time was taken as the point of maximum magnetization transfer on a build up curve; ranging between 0.075 and 0.2 ms, in good agreement with 0.05 ms previously reported for $[B_{12}H_{12}]^{2-}$, confirming magnetization transfer over the bond length range[225]. No resonance at 92 ppm was observed in CP spectra, implying that MgB_2 was not cross-polarised. Since the MgB_2 phase grows via nucleation, where the discrete domains of MgB_2 contain no protons[217], contact between MgB_2 and protons is not expected.

The dominant resonance in the CP spectra (figure 4.13) was observed at -11, -12 and -14 ppm for S2, S3 and S4 respectively. On this basis, it can be concluded that all samples contain $[B_{12}H_{12}]^{2-}$. A resonance at -41 ppm is also observed in CP spectra, assigned to CP within the $[BH_4]^-$ anion; this resonance does not change position at all, implying the field had not drifted between direct excitation and CP experiments. Therefore the difference between the shifts in the CP spectra (figure 4.13) and direct excitation spectra (figure 4.11) suggests the presence of elemental boron as well as $[B_{12}H_{12}]^{2-}$. The elemental boron phase contains no protons and can not therefore be cross polarised. The range of chemical shifts for the intermediate peak in ^{11}B direct excitation spectra (-4, -2 and -9 ppm for S2, S3 and S4 respectively) therefore must originate from the overlap of elemental boron and $[B_{12}H_{12}]^{2-}$ resonances, skewing to an average chemical shift depending on the proportion of each phase present in each sample.

4.3.6 Discussion: Effects of Temperature and Pressure on Intermediate Formation

Samples S1(d) and S2 both have 2:1 stoichiometry, but S1(d) was decomposed isothermally at 400 ^oC and S2 was decomposed under a temperature ramp to 500 ^oC. S1(d) contains little if any $[B_{12}H_{12}]^{2-}$ and elemental boron, whereas S2 contains a significant amount of both. The appearance of $[B_{12}H_{12}]^{2-}$ and elemental

boron appear to be coupled, suggesting that elemental boron results from full dehydrogenation of $[B_{12}H_{12}]^{2-}$. Along the pathway which leads to $[B_{12}H_{12}]^{2-}$ formation, no reaction with Mg metal occurs, since $[B_{12}H_{12}]^{2-}$ or its subsequent decomposition to elemental boron and H_2 gas do not contain Mg. This pathway then essentially corresponds to the direct decomposition of $LiBH_4$, and the role of Mg metal is to act as a catalyst. A substantial amount of $[B_{12}H_{12}]^{2-}$ remains in S2 and S4 compared with MgB_2, which is not surprising given that $[B_{12}H_{12}]^{2-}$ is very thermodynamically stable.

The difference in S1(d) and S2 is attributed to different reaction conditions. The blue cross on the van't Hoff plot in figure 4.7 shows the point that S1(b) to S1(d) were held at 400 ^oC during isothermal decomposition, where the chamber was evacuated to maintain a roughly constant $LiBH_4$ plateau pressure. This point is below the equilibrium pressure boundary for a destabilised $LiBH_4/MgH_2$ reaction but above the boundary for the Mg-catalysed direct decomposition of $LiBH_4$; thus the latter was thermodynamically forbidden under these conditions. Conversely, sample S2 was heated to a higher end temperature under lower initial pressures; in the early stages of the $LiBH_4$ decomposition the conditions held the system at a point below the $LiBH_4$ equilibrium pressure boundary, where the direct decomposition of $LiBH_4$ was the kinetically favourable reaction. The evolution of H_2 gas as $LiBH_4$ decomposed raised the pressure of the system to above the $LiBH_4$ equilibrium pressure boundary resulting in the halting of the decomposition of $LiBH_4$ via $[B_{12}H_{12}]^{2-}$, causing a large proportion of $[B_{12}H_{12}]^{2-}$ to remain in the mixture at the end. Then the reaction progressed via the destabilised $LiBH_4/MgH_2$ route to its endpoint.

It had been previously speculated that $[B_{12}H_{12}]^{2-}$ may be an intermediate to decomposition of the destabilised $LiBH_4/MgH_2$ as well as direct decomposition of $LiBH_4$[176]. However no evidence for $[B_{12}H_{12}]^{2-}$, or any other intermediate is seen in S1(b), S1(c) or S1(d) quenched along the isothermal route. This suggests

that no such intermediate is formed, or at least within the limits of detection with *ex situ* NMR. Formation and subsequent loss of any intermediate during the quenching process is very unlikely, since the quenching/rapid cooling process would discourage further decomposition or reformation which would remove such intermediate.

4.3.7 Discussion: Effects of Stoichiometry on Intermediate Formation

Both direct excitation and CP spectra show evidence for the formation of a small amount of $[B_{12}H_{12}]^{2-}$ in S3; the lithium-rich sample decomposed isothermally at 400 ^{o}C. This is surprising, since the direct decomposition of $LiBH_4$ was also thermodynamically forbidden in S3. To encourage the sample to decompose fully, the reaction chamber was evacuated to $< 6 \times 10^{-2}$ mbar H_2 at the end of the destabilised $LiBH_4$ decomposition plateau. At this point the maximum amount of MgB_2 possible was formed. Upon evacuation beyond this point, the reaction conditions fell below the equilibrium pressure for direct decomposition of $LiBH_4$. Since a residual amount of $LiBH_4$ remained at this point due to a lithium-rich stoichiometry, it was possible at this point for $[B_{12}H_{12}]^{2-}$ and elemental boron to form. Certainly one would expect a magnesium-deficient (lithium-rich) sample to yield excess boron containing species upon complete decomposition, in comparison to S1(d) which had no $[B_{12}H_{12}]^{2-}$ and/or elemental boron.

The magnesium-rich sample decomposed under a heating ramp to 500 ^{o}C (S4) showed formation of $[B_{12}H_{12}]^{2-}$. The thermodynamic situation is identical to that of S2, so this is expected. However the intermediate peak at -9 ppm for S4 in figure 4.11 was much lower in intensity than that at -4 ppm for S2 relative to MgB_2, implying a smaller proportion of boron containing species in S4. This is not surprising, since S4 is magnesium rich (boron deficient).

It was speculated by Price *et al.*[176] from *in situ* PND measurements that 2:1 samples would form an amorphous $[B_mH_n]^{q-}$ type species, but 0.3:1 samples would not, during the destabilised decomposition. S2 and S4 were decomposed in the same manner (under a temperature ramp) as that performed by Price *et al.*[176]. The formation of $[B_{12}H_{12}]^{2-}$ in both S2 and S4 suggests stoichiometry has no effect on whether an amorphous intermediate will form or not, rather it is formed from the direct decomposition when reaction conditions move the system into this regime.

4.3.8 Discussion: Evidence for $Mg_{1-x}Li_{2x}B_2$ Formation

No spinning side bands (SSB) were observed in the ^{6}Li spectra for samples S1(b), S1(c) and S1(d) in figure 4.10. SSB were associated by Hu *et al.*[229] with the amorphous $Mg_{1-x}Li_{2x}B_2$ intermediate formed by ion exchange during long-time ball milling of LiH/MgB_2 mixtures. This intermediate had the same ^{6}Li chemical shift as LiH, 0 ppm. ^{25}Mg spectra recorded here are not substantially broadened, which was another characteristic of this intermediate. Thus there is no evidence for the formation of the $Mg_{1-x}Li_{2x}B_2$ intermediate from the decomposition of $LiBH_4/MgH_2$. The broadening of the ^{6}Li and ^{25}Mg spectra observed by Hu *et al.*[229] is equally likely to originate from the formation of amorphous LiH/MgB_2 phases, caused by the long milling times used in those studies.

4.3.9 ^7Li NMR Spectroscopy: Detection of Alloys Under Varying Temperature and Stoichiometry

^{7}Li characteristically exhibits strong homonuclear dipolar couplings owing both to its high natural abundance and large gyromagnetic ratio. Typically this is the dominant contribution to the broad spectral lines observed in the rigid lattice limit

(linewidths ∼20 - 30 kHz). The diamagnetic chemical shift range is typically very small (± 10 ppm), since lithium has a low atomic number. This often renders the diamagnetic shifts uninformative at 7 T. Figure 4.14 shows that a small, but distinct and reproducible resonance at 134 ppm (0.013 % of ω_0 for ^{7}Li) occurs for sample S1(d) at reasonable intensity, but at a very low intensity for S2 and S4. Such a large shift observed in a ^{7}Li spectrum is invariably indicative of a Knight shift. In similar materials, Mg_xLi_{1-x} alloys have been reported to occur under conditions where the partial pressure $p(H_2) < 1$ bar, generated by dynamic vacuum[220,223]. Such metallic phases would result in a Knight shift.

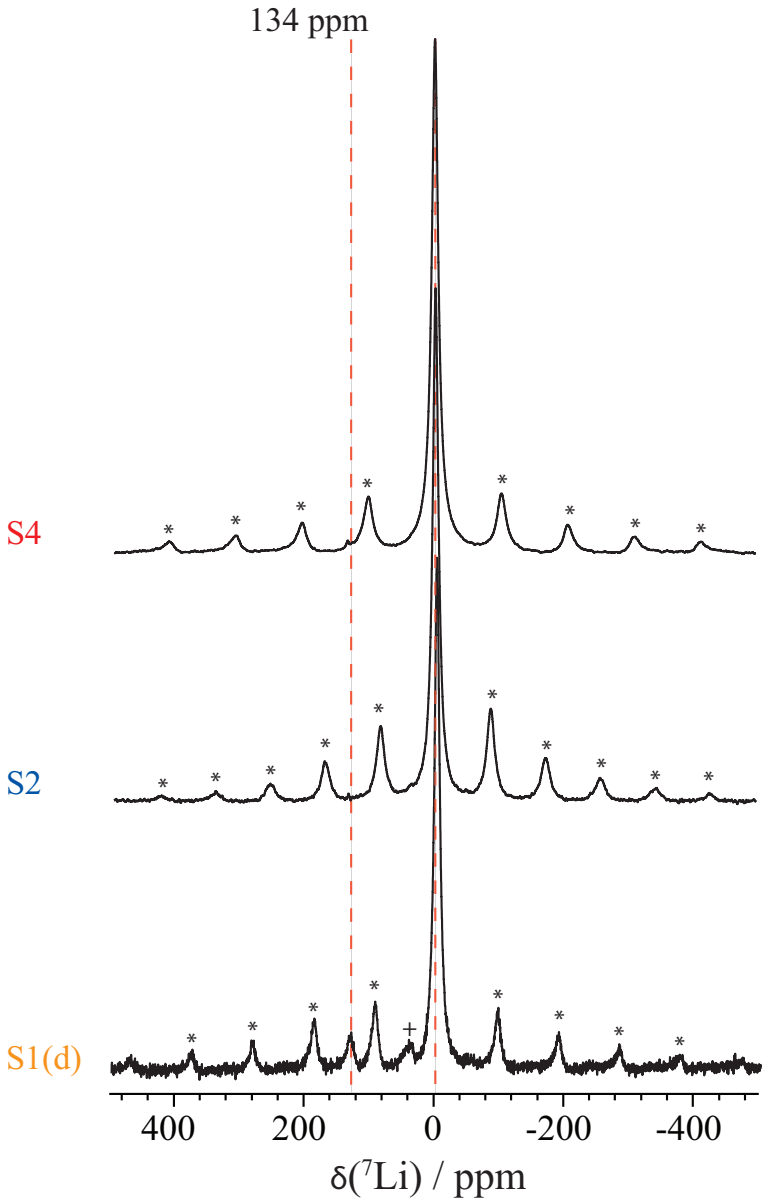


Figure 4.14: ^{7}Li MAS spectra of Fully Decomposed Samples.

The Knight shift of lithium metal is well known to be 256 ppm. Lynch *et al.*[237] also measured the Knight shift of Mg_xLi_{1-x} alloys over the full stoichiometric range of x = 0 to 1. The lithium Knight shift was found to move downfield towards a frequency minimum at x = 0.5. 134 ppm is in good agreement with the expected Knight shifts for the α - alloy (x > 0.816).

An associated decrease in the Knight shift of magnesium metal from 1180 ppm

might also be expected in the spectrum of the fully decomposed sample S1(d) (figure 4.10); this is not observed. Lynch *et al.*[237] have shown that the Knight shift in the ^{25}Mg spectrum for low concentration alloys (< 5 % Li) is within 0.005 % of the Knight shift of pure magnesium metal. It is reasonable to expect the Knight shift of the deficient species (lithium) to be much more sensitive to alloying, since the Fermi levels of lithium will be more heavily perturbed by the presence of the dominant magnesium conduction band, than vice versa. Furthermore, it is noted that another study has documented the Knight shift of pure magnesium metal as 1150 ppm[84], in good agreement with 1180 ppm found here. Therefore mild alloying produces no change to the ^{25}Mg Knight shift within experimental error.

^{7}Li spectra of samples S0, S1(b), S1(c) and S1(d) in figure 4.15 show the appearance of Mg_xLi_{1-x} over the entire range for isothermal decomposition at 400 ^{o}C. Integration of the intensity of the alloy resonance shows slight growth between S1(b) and S1(c), but more significant growth for S1(d), which suggests a significant amount of the alloy is formed at the end of the decomposition.

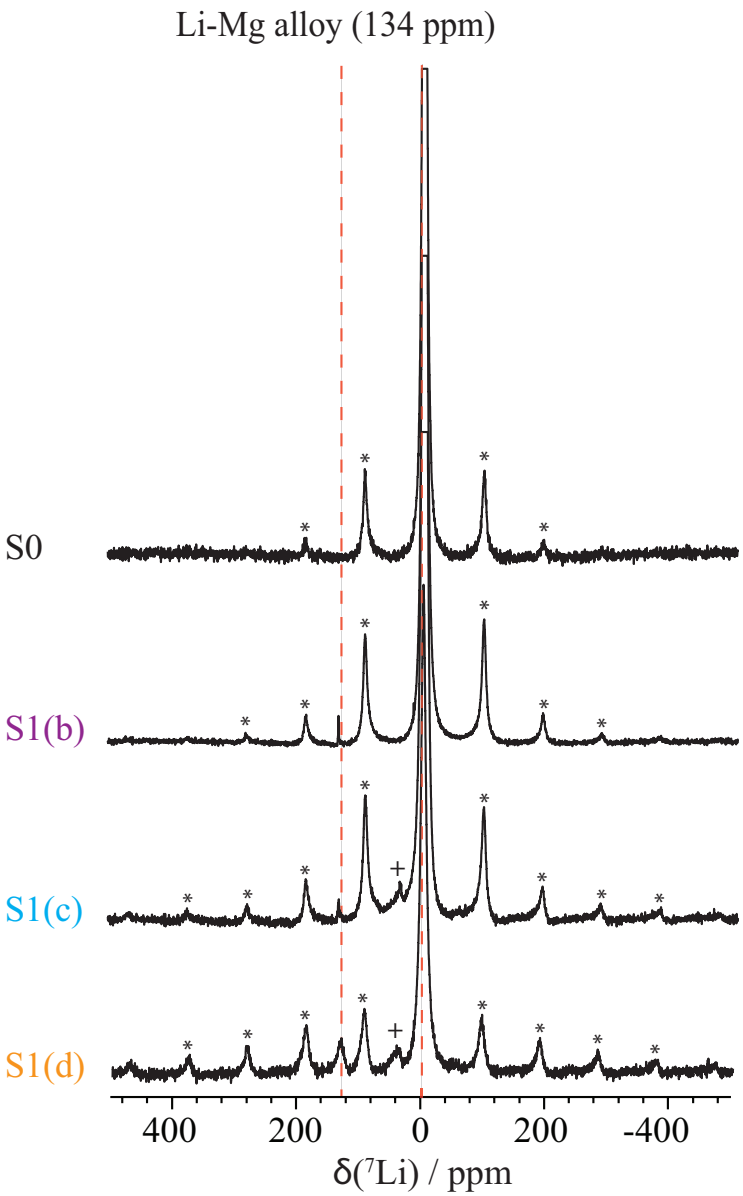


Figure 4.15: ^{7}Li MAS spectra of samples quenched during the decomposition at 400^{o}C.

4.3.10 Discussion: Formation of Lithium-Magnesium Alloys

By examining the spectra in figure 4.14, it can be seen that S1(d) contains significantly more alloy than S2 or S4. S4 is magnesium rich, so might be expected to produce more alloy, but actually it produces less than S1(d) and a similar amount

to S2. Thus the formation of the alloy was promoted by isothermal decomposition, compared to decomposition under a temperature ramp. This is because the alloy was formed in the final stage of isothermal decomposition where the pressure in the reaction vessel was reduced to very low pressure. This situation matched the conditions generated by dynamic vacuum where formation of alloys have been previously reported[223]. Magnesium rich stoichiometry may only promote the formation of the alloy when it is thermodynamically allowed. The origin of the small amount of alloy in S2, S4, S1(b) and S1(c) is probably formed during sample quenching, where rapid cooling prevented further evolution of H_2 resulting in a pressure drop during the quenching period, since switching off the vacuum pump is not likely to coincide exactly with cooling.

The detection of vast amounts of LiH from the ^{6}Li spectra and Mg metal from the ^{25}Mg spectra in figure 4.10 for sample S1(d), suggests that the amount of alloy formation is small even at the end of the isothermal decomposition. Alloy formation in S1(d) is therefore likely to have also been terminated by quenching.

No alloy was detected in lithium-rich (magnesium-deficient) S3 even though is was formed from isothermal decomposition, hence the spectrum is not shown here. Clearly at the final point of the decomposition of S3, all the magnesium metal had been used to form MgB_2, and no residual metal was available to form the alloy at the end of the reaction.

4.4 Conclusion

Static ^{7}Li NMR spectra of $LiBH_4$ which has been ground by hand and mechanically, with and without the addition of MgH_2 provide evidence for the diffusion of the Li^+ ion in the orthorhombic phase, prior to the phase transition. Ball milling may break down the sample into smaller grains, however it does not change the structure on a molecular level. The inherent crystal structure is therefore pre-

served within the bulk of the grains, as evidenced by no change in or addition of extra EFGs, and also no change in the temperature of the phase transition.

High energy ball milling increases the surface area of the material, which provides pathways of lower activation energy for Li^+ diffusion. The low temperature flank of the ^7Li spin-lattice relaxation curve in the hexagonal phase is sensitive to motion along lower activation energy pathways. Subsequent analysis therefore assumed non-random Li^+ hopping, where the surface diffusion pathways are preferred for elementary jumps. Ball milling MgH_2 with $LiBH_4$ in a stoichiometric (2:1) ratio made the surface area of $LiBH_4$ grains an even more favourable pathway.

Ex situ NMR has been employed to study the decomposition of the $LiBH_4/MgH_2$ system. Stoichiometry has been shown not to affect the formation of $[B_{12}H_{12}]^{2-}$, rather its formation is a thermodynamic consequence, occurring only when $LiBH_4$ decomposes directly. The destabilised $LiBH_4/MgH_2$ decomposition progresses straight to amorphous MgB_2 and no evidence of an intermediate has been observed here. Since $[B_{12}H_{12}]^{2-}$ is very thermodynamically stable, it can act to hinder the decomposition and thus lower the performance of the system in terms of hydrogen storage.

No evidence for the formation of the $Mg_{1-x}Li_{2x}B_2$ intermediate is found upon dehydrogenation of the $LiBH_4/MgH_2$ system. The formation of Mg_xLi_{1-x} alloys has been confirmed; their formation is very sensitive to the H_2 partial pressure. It is confirmed that no substantial oxidation occurred in the experimental methods used.

Chapter 5

The Lithium Nitride - Imide - Amide System

5.1 Introduction: Progress on the design of the Li-N-H Storage System

Quite remarkably, lithium nitride (Li_3N) boasts potential as both an electrode material and as a hydrogen storage material. Potential as a battery anode arises from its high energy to weight ratio owing to low equivalent weight, however a low decomposition potential renders it ultimately ineffective[238,239]. Potential as a hydrogen storage material was demonstrated first by Chen *et al.*[240], who reported inter-conversion between Li_3N and Li_2NH (imide) and subsequent conversion of Li_2NH to $LiNH_2$ (amide) allowed the overall cycling of 9.3 wt% H_2, measured in desorption (figure 5.1).

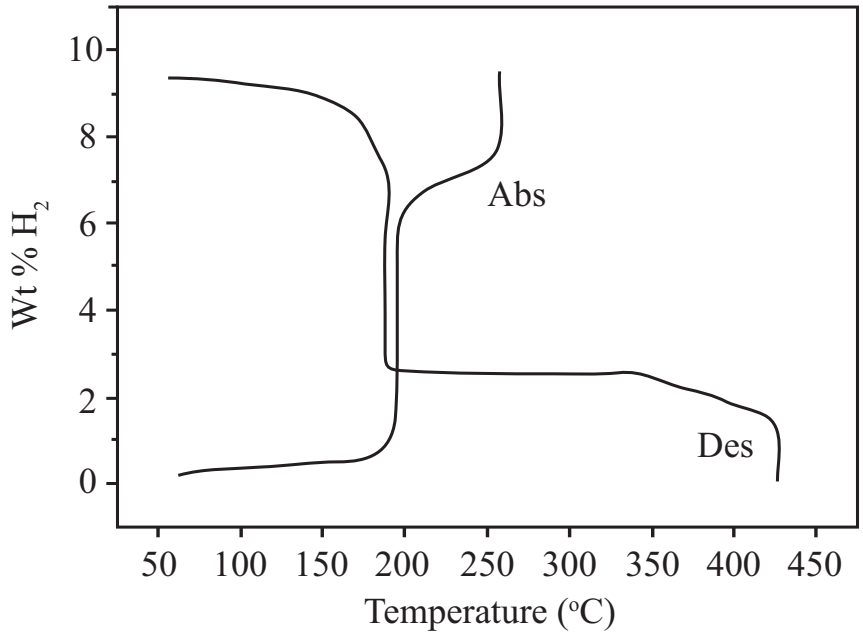


Figure 5.1: Weight change during the first hydrogenating cycle of the Li-N-H system, (reproduced here from 240).

Inter-conversion may be expressed chemically as[241]:

$$Li_3N + 2H_2 \rightarrow Li_2NH + LiH + H_2 \leftrightarrow LiNH_2 + 2LiH \tag{5.1}$$

Upon dehydrogenation, the solid-state conversion from the amide to the imide proceeds via first decomposition of $LiNH_2$ into Li_2NH and gaseous NH_3. Subsequent combination of NH_3 with LiH follows, causing successive rapid reformation of $LiNH_2$, releasing H_2 until $LiNH_2$ is depleted[242–244]. The overall conversion from $LiNH_2$ to Li_2NH may be expressed by a succinct chemical equation[245]:

$$LiH + LiNH_2 \rightarrow \frac{1}{2^n} LiH + \frac{1}{2^n} LiNH_2 + \sum_{k=1}^{n} \frac{1}{2^k} Li_2NH + \sum_{k=1}^{n} \frac{1}{2^k} H_2 \rightarrow Li_2NH + H_2 \tag{5.2}$$

Complete desorption of hydrogen from the amide to the nitride via chemical decomposition is strongly endothermic (161 $kJmol^{-1}$) requiring temperatures in excess of 420 ^oC, however partial desorption from amide to imide is much more thermodynamically favorable (45 $kJmol^{-1}$), releasing 6.3 wt% H_2 at temperatures below 200 ^oC under dynamic vacuum. However, terminating the process at this point is detrimental to the storage capacity. Furthermore, hydrogenating kinetics are sluggish to the extent that just 4.5 wt% H_2 is absorbed in 1000 minutes at 175 ^oC. Under similar conditions it was shown that dehydrogenation could only progress as far as the imide[246].

Developments towards improving hydrogenating kinetics and thermodynamics include altering the material composition to the formation of quaternary hydrides such as $Li_3(BH_4)(NH_2)_2$[247,248], by use of multinary systems such as the Li - Mg - N - H system[249] or by addition of catalysts such as $TiCl_3$[63,250].

The common method of high energy ball milling has been applied to grind mixtures of $LiNH_2$ and LiH together, and these mixtures demonstrate improved hydrogenating kinetics[251]. SEM images showed an increase in the distribution of grain sizes, with reductions from > 100 nm to ≈ 10 nm after 100 hours ball milling[212]. Particle agglomeration caused the maximal surface area to occur at 25 hrs of milling. Decreased particle size results in more intimate mixing of reactant materials and

decreased diffusion distances, and increased surface area improves material contact. This results in improved kinetics, a 40 % decrease in activation energy for dehydrogenation after 24 hours of milling, and the subsequent benefit that loss of NH_3 was suppressed[213]. Loss of NH_3 has been linked with reduction in system capacity and degradation over multiple cycles[246,251]. However, increased levels of hydrolysis to LiOH have been associated with increased milling times owing to increased specific surface area; 5 hours milling saw a 2 wt% reduction to the gravimetric capacity. Notably, NMR spectroscopy showed that milling produced a chemically new lithium site attributed to the inter facial defect region between $LiNH_2$ and LiH grains[252].

Alternative approaches towards harnessing the advantages of nano-structured materials take a more refined chemical assembly approach. Such emerging technologies include encapsulation of materials in mesoporous scaffolds[253], thin films[254] and spherical nano-particles[255]. Spherical Li_2NH nano-particles synthesised via a plasma metal reaction based upon the Kirkendall effect[256] exhibited a specific surface area greater than that achieved by milling and retained a higher gravimetric capacity. Rapid absorption of 6 wt% occurred in $\approx$ 1 minute at 200 ^oC and 35 bar H_2, and the nano-sphere structure was retained after cycling.

Herein, Li_3N with novel nanowire morphology is studied by NMR, which has been made with a new rapid plasma metal method. In the latter part of this chapter bulk Li_2NH, $LiNH_2$ and mixed phase material alternatives which cycle ammonia in place of hydrogen are also examined with NMR.

5.2 Lithium Nitride Nanowires

5.2.1 Literature Review: Studies on Lithium Nitride

The structure of bulk α-Li_3N consists of graphite-like $[Li_2N]^-$ hexagonal structured planes, separated by Li^+ ions[257,258]. The planes are perpendicular to the crystallographic c-axis (figure 5.2). Li_3N belongs to the *P6/mmm* space group. Herein, inter-planar Li^+ and intra-planar Li^+ ions will be denoted Li(1) and Li(2) respectively. The inter-atomic distances of Li(2) - N and Li(1) - N are 2.107 $\AA$ and 1.940 $\AA$ respectively. Li_3N is strongly ionic with essentially N^{3-} co-ordinated by six $Li^+(2)$ and two $Li^+(1)$ above and below the plane[259,260]. The β-Li_3N polymorph is formed at pressures > 0.5 GPa and remains stable at ambient conditions[261–263]. The synthesis of pure phase α-Li_3N is reported[264], and herein the crystal structure of Li_3N is shown to be the α-polymorph.

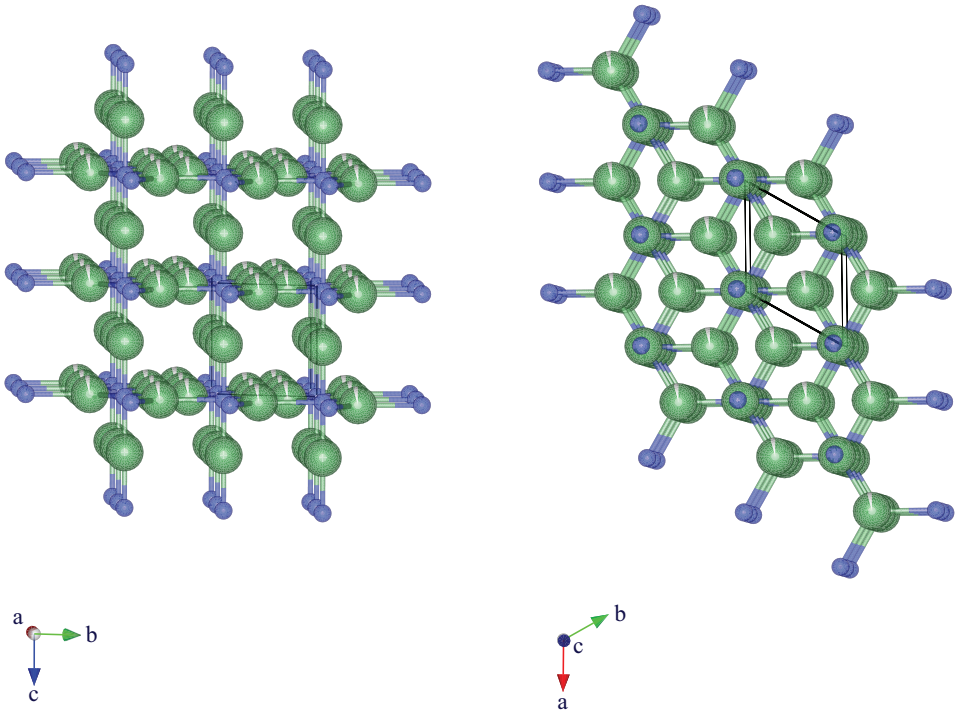


Figure 5.2: Crystal structure of α-Li_3N viewed along the *a* and *c*-axis. (Nitrogen, blue; lithium, green.)

Li^+ ion conductivity was found to be strongly anisotropic at ambient temperatures[265]. It comprises two components; the intra-layer component which involves ionic diffusion within the $[Li_2N]^-$ plane between Li(2) sites, and the inter-layer component which involves exchange between Li(1) and Li(2) sites[266]. Recent conductivity measurements in the range 300 - 385 K showed an overall E_a = 0.42 eV.

The inter-layer process was found to have ionic conductivity 10^{-1} $\Omega^{-1}cm^{-1}$ at 300 K for a Czochralski-grown single crystal[267]. Temperature dependent NMR second order quadrupole shifts, linewidths and spin-lattice relaxation times confirmed this process had an E_a^{inter} = 0.6 eV[113,124].

The intra-layer process was found to be slower at 300 K, with ionic conductivity 10^{-3} $\Omega^{-1}cm^{-1}$ and $E_a^{intra} = 0.27$ eV for a Czochralski-grown single crystal[267]. However at lower temperatures, it is the dominant process. X-ray diffraction studies found a 1 - 2 % largely temperature-independent lithium vacancy concentration within the $[Li_2N]^-$ layers created by thermal vibrations[268,269]. Hydrogen-doped single crystals showed E_a as low as 0.2 eV for intra-layer diffusion resulting in enhanced ionic conductivity by a factor of about 10, but depending on the extent of doping[269,270]. The ionic conductivity for intra-layer diffusion was found to depend upon the concentration of $[NH]^{2-}$ and $[NH]^-$ complexes. It was therefore proposed that the presence of H^+ ions allows $[NH]^{2-}$ groups to form leading to the weakening of Li - N bonds, thereby facilitating the creation of Li^+ Frenkel defects[271]. This could lead to a vacancy-mediated diffusion process[272], where the presence of H^+ ions effectively contributed to charge balancing of Li^+ vacancies.

Calculations of Li^+ trajectories performed at 300 and 400 K with molecular dynamics (MD) were able to reproduce the macroscopic self-diffusion properties[273]. However the microscopic diffusion properties were predicted to be far more complex than a simple vacancy-mediated mechanism[274]. In addition to the diffusion

of point defects, ion hops within the $[Li_2N]^-$ layers were found to be strongly correlated with previous ion jumping events, leading to solitary-wave character. Above 400 K, strongly correlated ion hops leads to slippage of the entire Li^+ sublattice, caused by simultaneous ion hops of several neighboring ions. Subsequently, adjacent regions may also undergo slippage, leading to an overall caterpillar-like motion. A concomitant process was also found, where interstitial ions diffuse preferentially in corridors above and below the $[Li_2N]^-$ planes. Inter-layer diffusion occurs via the same interstitial sites between the $[Li_2N]^-$ and Li^+ layers.

5.2.2 Synthesis and Characterisation: Lithium Nitride Nanowires

Novel low-dimensional Li_3N nano-structures were synthesised by Gregory and Gordon[275] and Gordon *et al.*[276], using the vapour-liquid-solid (VLS) mechanism[277]. Firstly, thermal heating caused the decomposition of Li_3N, forming Li-metal droplets which acted as nucleation sites, thereby self-catalysing growth. The morphology varies with synthetic conditions; in this study, temperatures ranged between 700 to 800 ^oC and pressures 70 - 850 kPa, with growth times between 1 to 14 days. As illustrated by SEM images (figure 5.3), lower temperatures and pressures yielded wire-like structures, whereas high temperatures and low pressures yielded ribbon-like structures. Formation of ribbon-like structures was attributed to melting of Li_3N, which enhanced the decomposition rate leading to an increased number of nucleation sites, which allowed an increased deposition rate of N_2 onto Li seeds. Alternating the temperature gradient led to a combination of straight and zigzag nanowires, owing to switching growth direction caused by extreme temperature changes.

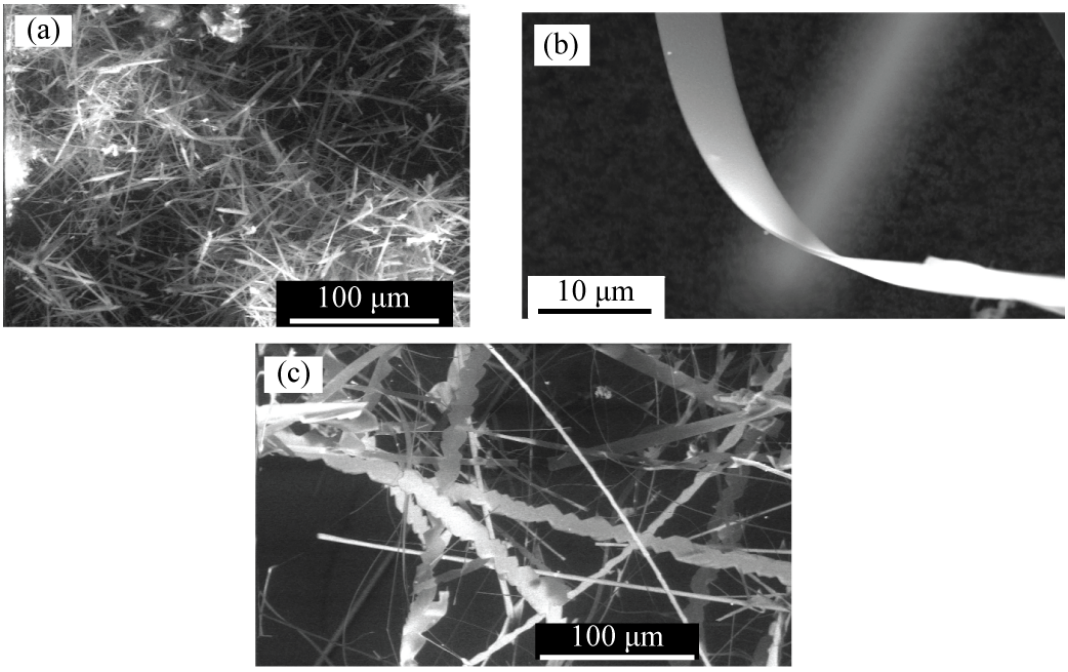


Figure 5.3: SEM images of Li_3N low-dimensional nano-structures synthesised under (a) relatively low temperature and pressure (c.a. 700 ^{o}C and 70 - 350 KPa, (b) similar low pressures and higher temperature (c.a. 800 ^{o}C), (c) higher pressures (c.a 850 KPa) and under an alternating temperature gradient (centred at c.a. 750 ^{o}C). Figure reproduced from 276.

Energy-dispersive X-ray spectroscopy revealed an absence of metal impurities in as-prepared Li_3N nano-structures thus confirming the self-assisted VLS growth mechanism. PXRD measurements revealed that the refined unit cell parameters of the nano-structures were in close agreement to the bulk material. Transmission electron microscopy (TEM) and selected area electron diffraction (SAED) experiments identified the formation of two types of nanowires with different growth orientations. Type A nanowires have a growth plane of $\{1\bar{2}10\}$ and growth direction of $<10\bar{1}0>$, where as type B nanowires have a growth direction of [0001]. This leads to the following structural model. Type A nanowires are organised with the crystallographic c-axis perpendicular to direction of growth, with $[Li_2N]^-$ layers running along the fibre (figure 5.4). Type A nanowires originated from lower pres-

sures and temperatures, shown in the SEM image (a) of figure 5.3. Alternatively, Type B nanowires are organised with the c-axis parallel to the direction of growth. Type B were made under high pressure and an alternating temperature gradient (figure 5.3(c)). The structure of Li_3N nanowires is in direct analogy with previously reported boron nitrate 'nanotubes', which form via stacking of hexagonal layers in the overall wire morphology[278]. Further details may be found in Gordon *et al.*[276]; this reference has been included in *Appendix B* of this thesis.

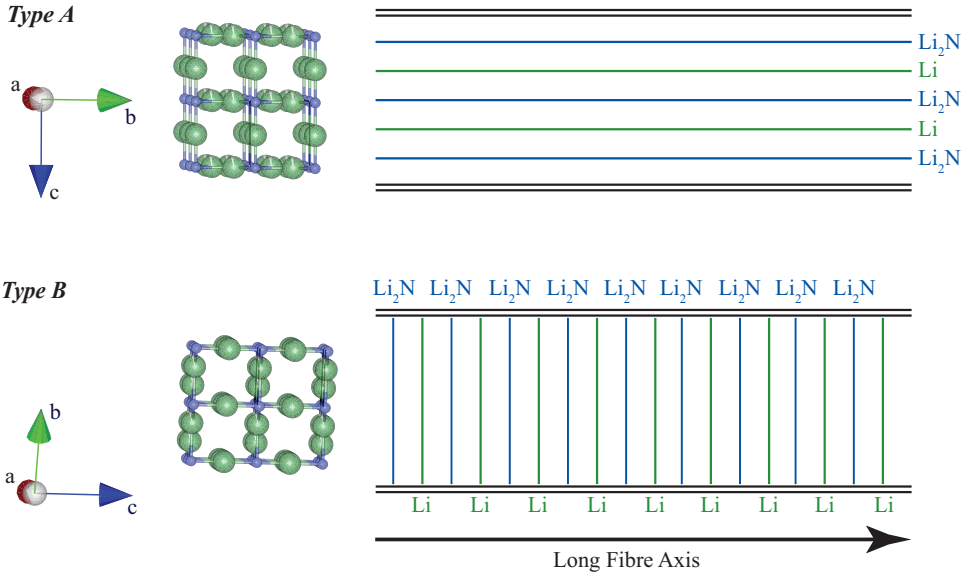


Figure 5.4: Schematic illustration of the growth direction of: type A nanowires perpendicular to the crystallographic c-axis; type B parallel to the c-axis. Figure reproduced from 276.

Solid-state microwave (MW) synthesis[279] provides selective rapid heating, ultra fast cooling and is more energy efficient than thermal heating. However temperature control may be difficult with this method. To improve the production rates of Li_3N nanowires the MW synthesis method was employed by Tapia-Ruiz *et al.*[280] and Tapia-Ruiz[281] with catalytic silver, gold and palladium additives. SEM images of these nano-structures are given in figure 5.5. Li_3N is an excellent MW susceptor, owing to the presence of mobile ions in the material[282]. MW heating creates a Li-metal plasma mixed with Li + N vapour. Subsequent condensation

of Li-metal alloy droplets on bulk Li_3N then provides an equivalent nucleation site for nanowire growth. TEM showed that the nanowires had dimensions of 100-800 nm diameter and 20-50 μm in length. A LiOH layer is thought to have formed around the nanowires during TEM measurements.

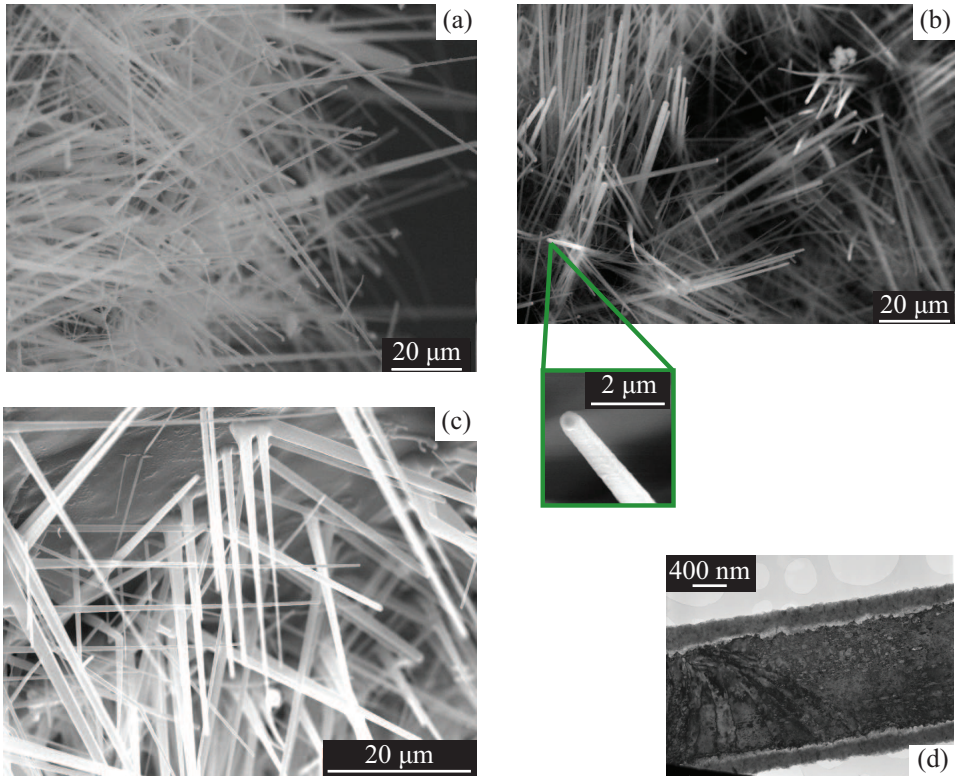


Figure 5.5: SEM images of Li_3N nanowires made by microwave synthesis with catalytic substrates: (a) gold, (b) silver, (c) palladium; (d) bright field TEM image showing the likely LiOH outer layer from the Li_3N core. The SEM image insert of (b) is enlarged to show the Li-Ag alloy substrate. Figure reproduced from 276.

5.2.3 Lithium-7 Static NMR: Characterisation of the Nanowires

Wideline ^{7}Li NMR spectra were recorded at 7 T using a solid echo pulse sequence with $\frac{\pi}{2}$ pulse lengths of 1.2 to 1.8 μs and echo delays of 10 to 15 μs, optimised to produce in-phase spectra. All spectra in this section were referenced to 1.0 M

LiCl(aq).

Nanowires Synthesised by Conventional Heating

Variable temperature ^{7}Li static NMR spectra recorded previously (figure 5.6) of type A nanowires were almost identical to that expected for α-polymorph of bulk Li_3N. The spectra contained a central transition flanked by two sets of Pake pattern quadrupolar satellites with C_Q values within reasonable error of those for Li_3N; 286 and 580 kHz for Li(1) and Li(2) respectively[124,283]. This confirms the presence of continuous layers within the nanowires, in agreement with nanowire diameters of 100-800 nm, since C_Q values are unperturbed. The quadrupolar interaction is not expected to be sensitive to this range. Good resolution of the satellites without additional broadening confirms that vacancy levels are similar to those observed in the bulk material. The temperature variation was also found to be akin to that seen for bulk Li_3N; the spectra underwent motional narrowing up to $\sim$ 300 K, then at higher temperatures the quadrupolar satellites broadened out of the spectrum due to exchange of Li^+ ions between Li(1) and Li(2) sites.

^{7}Li static NMR spectral analysis of type B nanowires revealed the presence of a third set of satellites with C_Q = 424 kHz, best seen at temperatures between 240 to 300 K where the linewidths had been motionally narrowed but exchange broadening had not yet occurred (figure 5.6). The experimental ratios of these sites were Li(2):Li(1):Li(3) = 9.3:4.9:1, in contrast to Li(2):Li(1) = 2:1 for either bulk or type A Li_3N. Since type B nanowires have substantially more layer-edge sites than type A according to the model in figure 5.4, the Li(3) site is assigned to layer-edge lithium. Layer-edge sites may differ due to non-uniform nanowire growth at the edge, or simply because Li_3N structure comprises two different alternate $[Li_2N]^-$ and Li^+ layers. This would suggest several inequivalent Li sites. Here, only one of these layer-edge sites is observed.

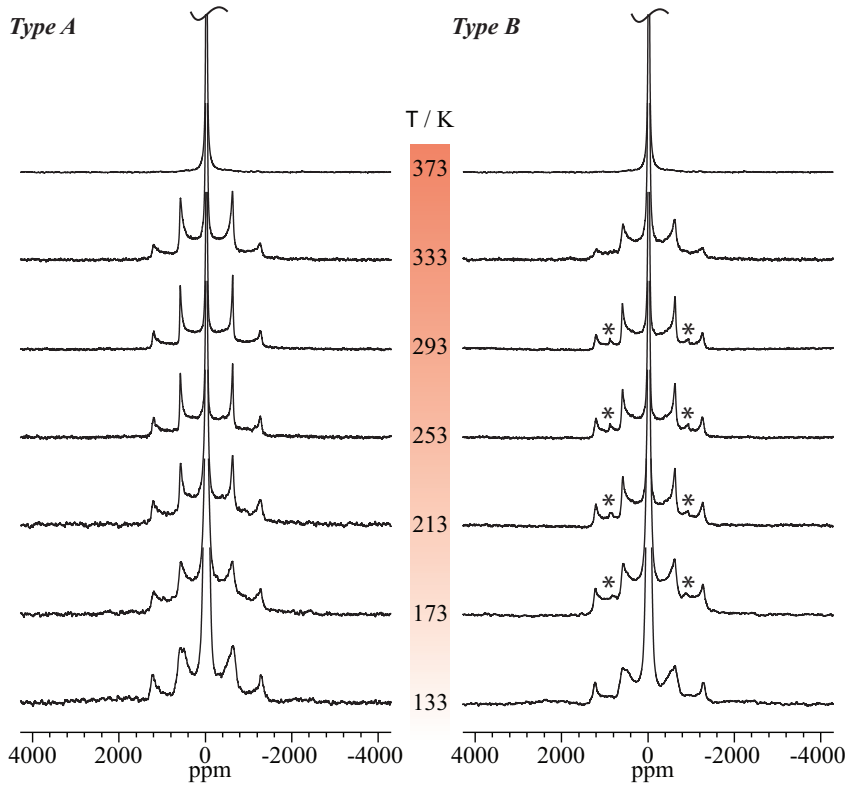


Figure 5.6: Variable temperature ^{7}Li NMR static spectra of type A and B nanowires. * denotes the Li(3) satellites visible at intermediate temperatures. By coincidence, the Li(2) satellites have double the C_Q of the Li(1) satellites, within error.

Nanowires Synthesised by MW Heating

^{7}Li static NMR spectra of nanowires grown with catalytic gold, silver and palladium substrates, herein denoted as Li - Au, Li - Ag and Li - Pd respectively, are shown in figure 5.7. Two sets of Pake pattern quadrupolar satellites are observed with C_Q values the same as bulk Li_3N, and no satellites corresponding to Li(3) are observed throughout the entire temperature range. This suggests that MW synthesis favours the formation of type A nanowires. Since temperature control under MW synthesis is hard to achieve, it is likely that it was not possible to achieve the precise alternating temperature gradient conditions required for type B nanowire formation.

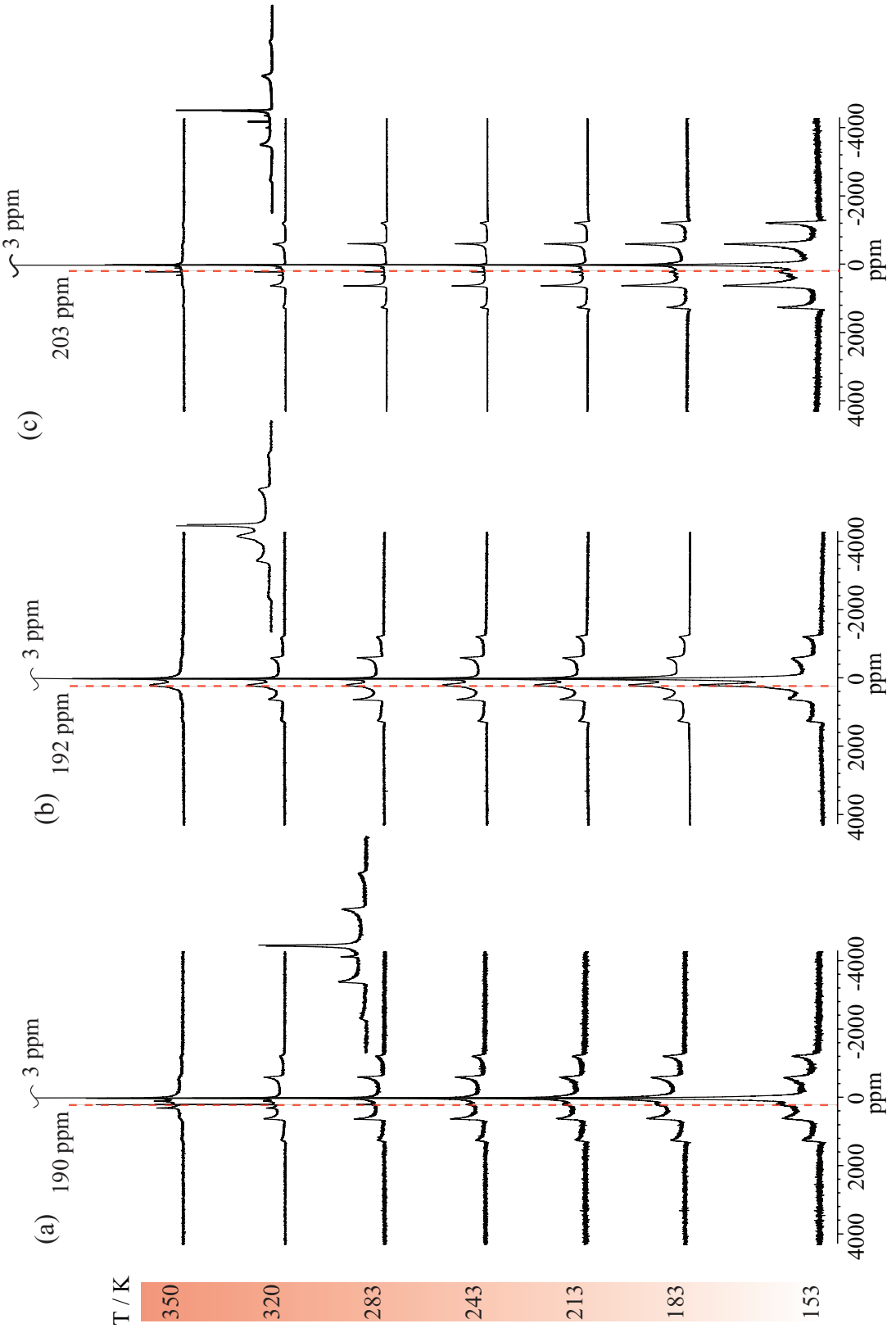


Figure 5.7: Variable temperature ^{7}Li NMR static spectra of type A Li_3N nanowires grown with catalytic substrates: (a) Li - Au, (b) Li - Ag, (c) Li - Pd.

As mentioned in previous chapters, the dipolar linewidth is relatively large and diamagnetic chemical shift range is small by comparison in ^{7}Li spectra. Different chemical sites are therefore seldom resolved in static ^{7}Li measurements, particularly at relatively low field strength (c.a 7 T). Unsurprisingly, the Li(1) and Li(2) sites in Li_3N are not resolved here, and attempts to resolve them in previous work using high resolution MAS and CW decoupling of protons of both ^{6}Li and ^{7}Li were not successful. SQUID magnetic susceptibility measurements showed Li_3N to be diamagnetic, hence only the diamagnetic shift would be expected[284]. The resonances observed at 190, 192 and 203 ppm for nanowires grown with Li - Au, Li - Ag and Li - Pd substrates respectively are therefore indicative of a second paramagnetic species (figure 5.7). Taking the method of synthesis and nanowire growth into consideration, this is likely to be a Knight shift caused by the presence of metallic species. The chemical shift of lithium metal is 256 ppm[237], so the Knight shifts observed in the spectra in figure 5.7 are assigned to Li - metal alloys. To the best of our knowledge, values for the Knight shift of the above alloys have not been previously reported.

It is noted that the resonances for the Li - Au and Li - Pd alloys narrow with temperature, however the Li - Ag resonance doesn't. The low intensities of these peaks made studying this further not tractable, however it is speculated that the origin of this additional line broadening may be either due to greater disorder in the Li - Ag alloy, a mixture of alloy multiple phases, or a combination of the two.

5.2.4 Lithium-7 Static NMR: Line Shape Analysis

Line narrowing of the central transition

Narrowing of the ^{7}Li linewidth with increasing temperature may be seen from the spectra in figure 5.7. The central transition was deconvoluted with a single Gaussian function to obtain the overall width. It is noted that this serves as a sufficient approximation where the dominant contribution to the line width is homonuclear dipolar broadening and also where the individual Li(1) and Li(2) chemical sites cannot be resolved. Line narrowing as a function of temperature has been plotted in figure 5.8 (A).

By calculating the correlation time with the standard BPP equation (2.80), an Arrhenius plot could be constructed. By fitting a linear regression line to the portion undergoing motional narrowing, it was possible to obtain the activation energy E_a and the correlation time at ambient temperature τ_c for the associated motional process in Li - Ag, Li - Au and Li - Pd nanowires. These values are compared with those for bulk Li_3N in table 5.1.

Sample	Li - Ag	Li - Au
E_a (eV)	0.081 ± 0.004	0.083 ± 0.003
τ_c(298K) ($\times 10^{-7}$ s)	12.1 ± 0.6	9.7 ± 0.4
Sample	Li - Pd	Bulk Li_3N
E_a (eV)	0.090 ± 0.004	0.114 ± 0.007
τ_c(298K) ($\times 10^{-7}$ s)	4.5 ± 0.2	4.8 ± 0.3

Table 5.1: Arrhenius parameters obtained from motional narrowing of the central transition in the ^{7}Li spectrum.

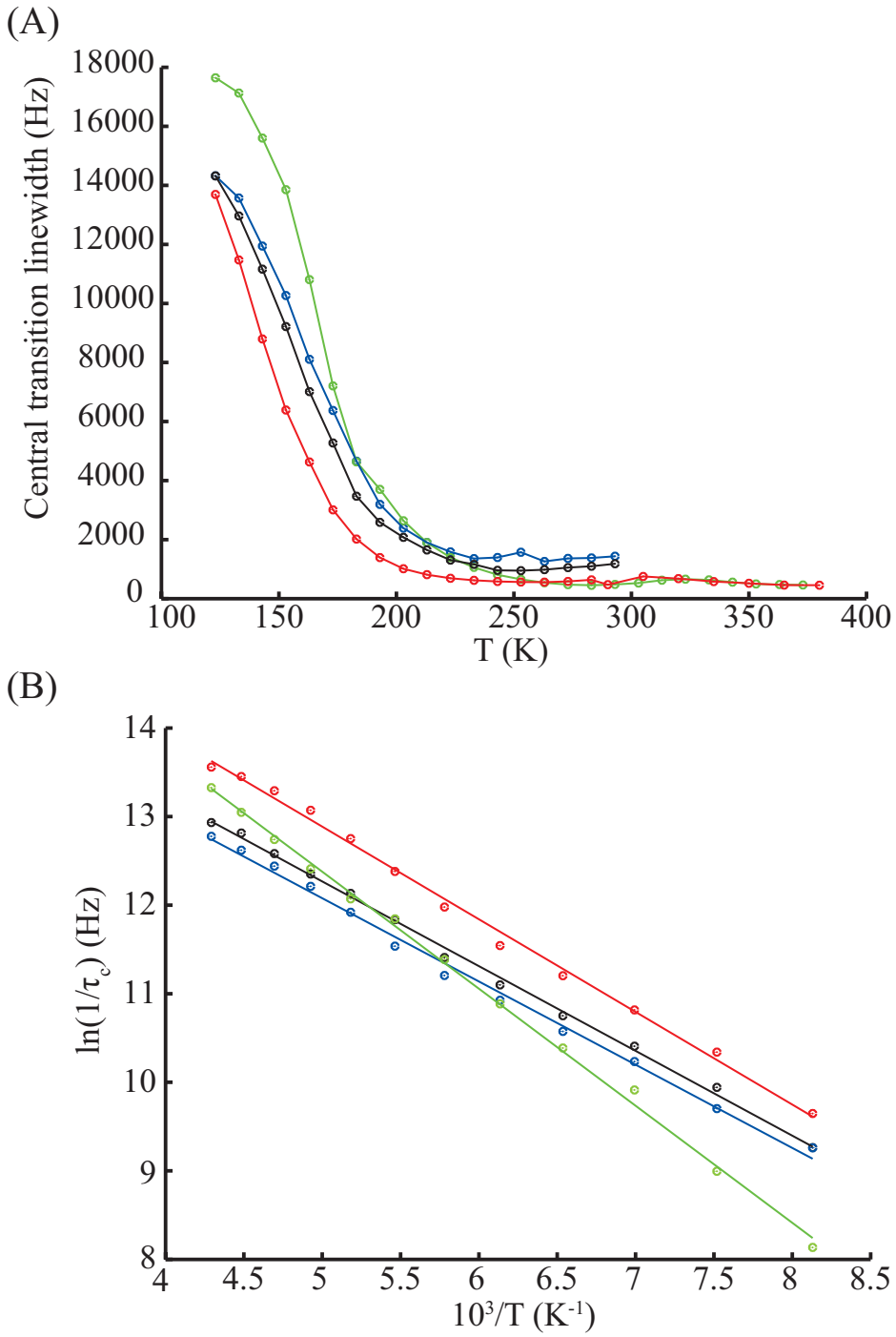


Figure 5.8: (A) ^{7}Li central transition linewidth narrowing with temperature, (B) Arrhenius plot of the temperature dependence of the correlation time. Green, pure Li_3N; blue, Li_3N nanowires grown with Li - Ag substrate; black, with Li - Au; red, with Li - Pd. Note the line in (A) is just to guide the eye, whereas in (B) it is the linear regression line.

The E_a for bulk Li_3N found here is 0.11 eV, in contrast to 0.2 eV reported by Messer *et al.*[124]. Gomez[284] attributed this difference to a higher concentration of H^+ doping ions in this sample compared to that studied by Messer *et al.*[124]. Indeed a higher vacancy concentration was also determined by neutron diffraction for the same bulk Li_3N by Gregory *et al.*[264]. The cause of the line narrowing in all the nanowires is therefore intra-layer diffusion of lithium ions, between equivalent sites.

The activation energies and room temperature correlation times for type A and B nanowires synthesised via the thermal heating method are 0.075 and 0.035 eV, and 9.58×10^{-7} and 2.33×10^{-6} s respectively. There is close agreement in the activation energies between type A nanowires synthesised via thermal heating and the set synthesised via the MW method, confirming the identity of the latter as type A.

The TEM image in figure 5.5 suggested that the alloys were coated with a LiOH wall. The set of samples used for NMR measurements were separate from those used for SEM and TEM images, and the sample handling techniques for NMR measurements ensured no exposure to air. Note that ^{7}Li NMR linewidths measured by Follstaedt and Biefeld[285] for LiOH show onset of motional narrowing around 320 ^{o}C, 200 ^{o}C higher than that of intra-layer diffusion, accompanied by a much higher $E_a = 1.3$ eV. Motional narrowing plotted in figure 5.8 can therefore be assigned to intra-layer diffusion in Li_3N, and not the LiOH wall. If any LiOH exists in samples used in NMR, it is clearly below detection levels.

Line narrowing of the Li(2) satellites

Since the central transition in the Li_3N spectra of figure 5.5 has a contribution from both Li(1) and Li(2) sites, the line narrowing of the Li(2) satellites was studied to confirm the above observations. Li(2) satellites were fitted by hand with the aid

of a simple MATLAB GUI to a Pake pattern generated using SIMPSON. Variable parameters in the fitting included the amplitude of the pattern, exponential line broadening, zeroth and first order phasing and the spectral frequency position. With this tool, it was possible to make a good approximation to the Li(2) satellite line narrowing (figure 5.9).

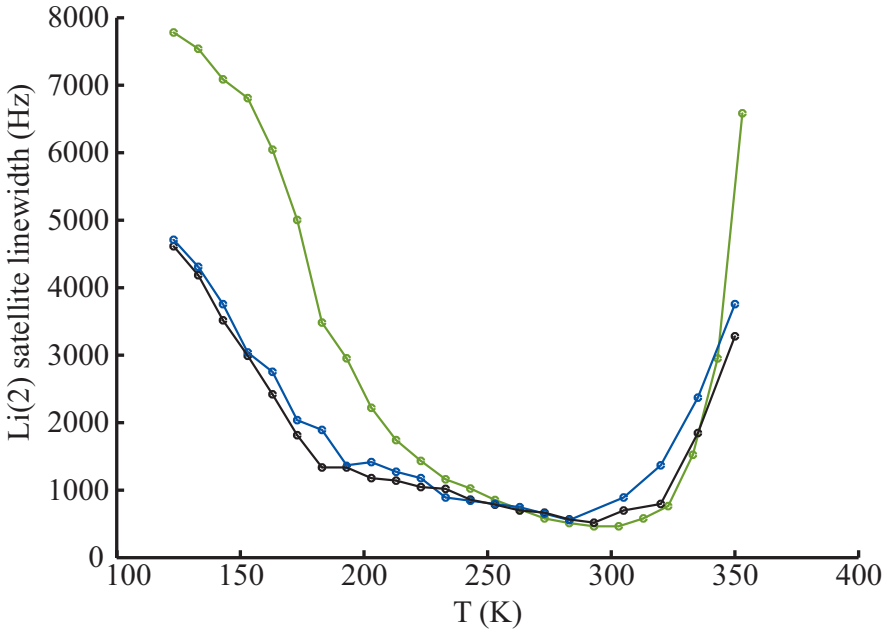


Figure 5.9: Temperature dependence of the ^{7}Li Li(2) satellite transition linewidth. Green, pure Li_3N; blue, Li_3N nanowires grown with Li - Ag substrate; black, with Li - Au. Note the line here is just to guide the eye.

The broadening of the Li(2) satellite linewidths occurring at temperatures > 300 K is a consequence of ion exchange between Li(2) and Li(1) sites due to inter-layer diffusion. It was therefore possible to split this data set into two portions. The lower temperature portion which contains motional narrowing may be analysed in terms of intra-layer diffusion with correlation time τ_c^{intra}, and the higher temperature portion which contains exchange broadening due to inter-layer diffusion with correlation time τ_c^{inter}. Arrhenius analysis for both regions are presented in figure 5.10, and the extracted E_a and τ_c(298K) in table 5.2 for both data portions.

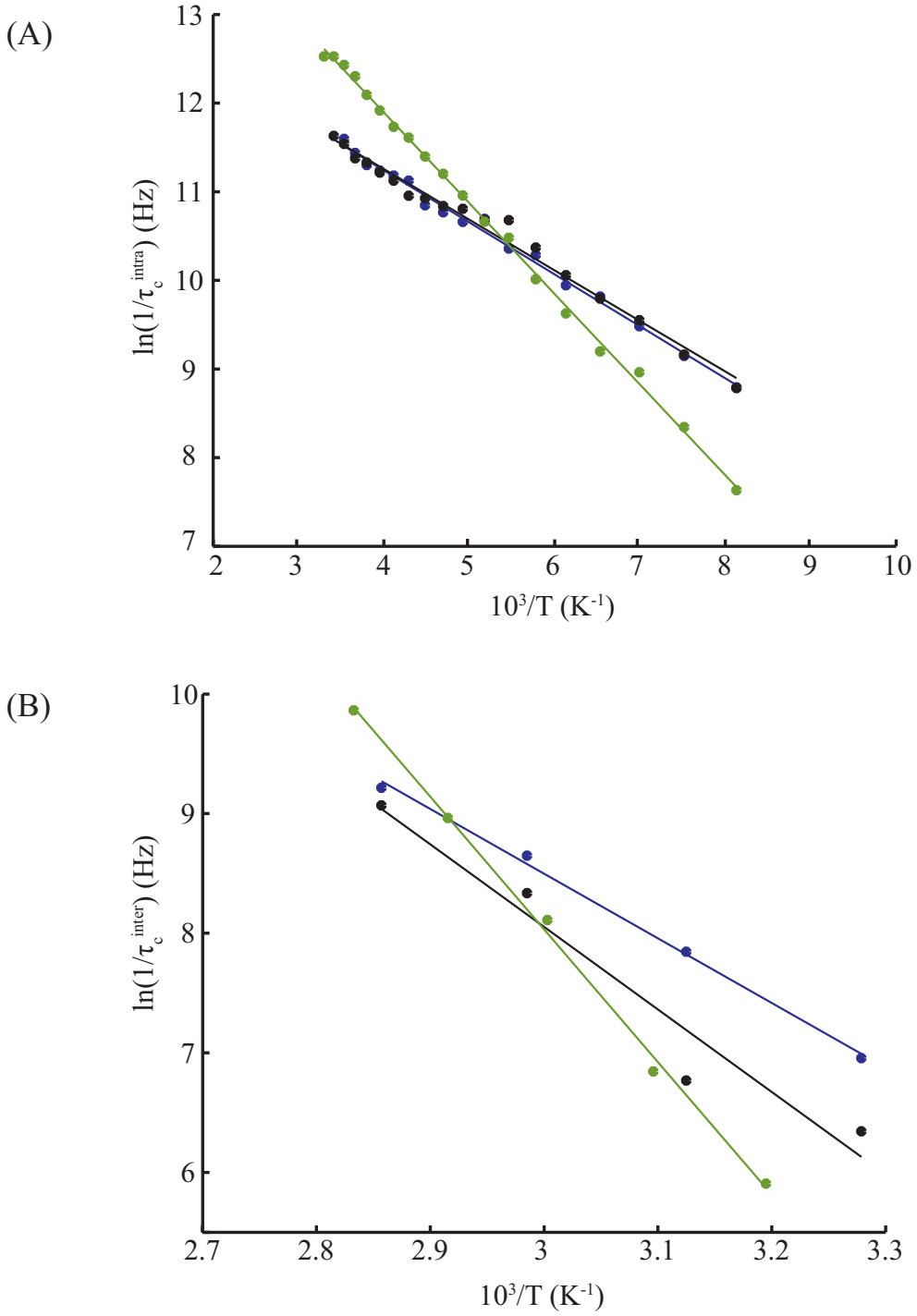


Figure 5.10: Arrhenius plots associated with the temperature dependence of the ^{7}Li Li(2) satellite transition linewidths: (A) for line narrowing associated with intra-layer diffusion; (B) for exchange broadening associated with inter-layer diffusion. Green, pure Li_3N; blue, Li_3N nanowires grown with Li - Ag substrate; black, with Li - Au. The straight lines are linear regression lines.

Sample	Li - Ag	Li - Au	Bulk Li_3N
Intra-layer diffusion			
E_a^{intra} (eV)	0.051 ± 0.002	0.049 ± 0.003	0.088 ± 0.002
τ_c^{intra}(298K) ($\times 10^{-6}$ s)	9.0 ± 0.4	9.0 ± 0.6	3.53 ± 0.08
Inter-layer diffusion			
E_a^{inter} (eV)	0.47 ± 0.07	0.6 ± 0.4	0.957 ± 0.002
τ_c^{inter}(298K) ($\times 10^{-3}$ s)	1.4 ± 0.2	3.7 ± 0.3	16.80 ± 0.04

Table 5.2: Arrhenius parameters obtained from motional narrowing and exchange broadening of the Li(2) satellite transitions in ^{7}Li spectra.

The shape of the satellites in the spectrum of the Li - Pd sample (figure 5.7) did not fit well to a simulated Pake pattern and hence were omitted from this analysis. For intra-layer diffusion, the same trend of a lowered E_a^{intra} and increased τ_c^{intra} upon nano-structuring is observed. However, a consistent discrepancy (underestimation of E_a^{intra} and a linked overestimation of τ_c^{intra}) is found via this method; these numbers should only be considered as supporting the above trend rather than precise values.

For inter-layer diffusion, the value of E_a^{inter} for bulk Li_3N is larger than expected, but E_a^{inter} for Li - Ag and Li - Au are close to the literature value for bulk Li_3N, considering impurity levels are higher in these samples. Again, a lowered E_a^{inter} occurs upon nanostructuring, however τ_0^{inter} is also lowered upon nano-structuring.

It can also be seen that $\tau_c^{inter}(298K) < \tau_c^{intra}(298K)$. Inter-layer diffusion is a more energetic process compared to intra-layer diffusion; inter-layer diffusion becomes a faster process at temperatures greater than $\sim$ 410 K, as expected[273].

5.2.5 Discussion: Lithium Ion Diffusion and Hydrogenating Rates in Lithium Nitride Nanowires

Changes to Li^+ diffusion in Nano-structured Li_3N

For intra-layer diffusion, the E_a^{intra} decreases and τ_c^{intra} increases or remains the same upon nano-structuring of Li_3N, compared with the bulk values. If this were due to an increase in the number of point charged defects (H^+ doping ions) introduced by the nanowire growth via the VLS mechanism, then a decrease in the τ_c^{intra} by a factor of 10 would also be expected[124], for increase in the H^+ defect concentration from $\sim 10^{19}$ to 10^{21} per cm^3. Increase in τ_c^{intra} therefore suggests that the reduction in E_a^{intra} is not due to an increase in the number of point charged defects.

As discussed in chapter 4, grain surfaces are known to provide favourable pathways for self-diffusion, usually reflected by a lowered E_a obtained from NMR[193,197,199]. Such regions were previously generated by ball milling, which generates a distribution of grain sizes. This led to a distribution of lithium sites, which caused a distribution of lithium chemical shifts. The ^7Li line shapes in the spectra of the Li - Pd nanowires (figure 5.7) narrow to a similar width as bulk Li_3N, but the Li - Au and Li - Ag central transitions are broader in the motionally narrowed limit. This is attributed to the increase in surface regions, created by nanowire morphology. This in turn causes the decrease in activation energy for intra-layer and inter-layer diffusion in nano-structured Li_3N.

For inter-layer diffusion, the E_a^{inter} and τ_c^{inter} both decrease upon nano-structuring. Wolf and Catlow[274] showed that inter-layer diffusion occurred via hopping between interstitial sites, which is akin to the more naive vacancy-mediated model. In this model, it is reasonable to observe simultaneous decrease in both E_a^{inter} and τ_c^{inter}, since a lower barrier height allows less time to be taken per jump (or alternatively

larger number of hopping attempts).

Wolf and Catlow[274] showed for intra-layer diffusion that in addition to random diffusion of point defects, both correlated ion hopping occurred and favourable corridor pathways existed above and below the $[Li_2N]^-$ planes at 300 K. Nano-confinement of a Li_3N lattice will inhibit slippage effects of the $[Li_2N]^-$ layers. This would lead to an increase in τ_c^{intra} depending on the extent of nano-confinement. This effect therefore outweighs the decrease in τ_c^{intra}, expected from a simple vacancy-mediated model, which describes the point defect diffusion component of intra-layer diffusion. It is noted that τ_c^{intra} increases even more for type B nanowires, where the geometry of type B nanowires causes the $[Li_2N]^-$ layers to be confined in both a and b directions.

Improved Hydrogenation Rates in Nano-structured Li_3N

Li^+ ion diffusion is intrinsically linked to solid-state hydrogenating of the Li-N-H system[286]. As part of the overall study of low-dimensional nano-structured Li_3N, the H_2 sorption properties were investigated in comparison to bulk Li_3N using differential pressure analysis. The results are presented in figure 6 of *Appendix B*. A three-fold improvement in the hydrogen uptake time was observed coupled with better retention of overall capacity upon multiple cycles, probably due to the decrease in ammonia loss. Raman spectroscopy evidenced the formation of the hydrogenated compounds Li_2NH and $LiNH_2$, and SEM images evidenced the preserved morphology upon hydrogenating. Nano-structuring with nano-porous scaffolds has been noted previously for preventing problems with particle annealing over multiple cycles, often encountered with materials prepared by ball milling[41,62,287].

Lowering of solid-state hydrogenating rates can be linked to changes in the kinetics of Li^+ ion diffusion (E_a and τ_c). However nanowire type structures also

provide a large increase in reaction surface area, which may also contribute to the improvement in H_2 sorption kinetics.

5.3 Bulk Lithium Imide - Amide Non-Stoichiometric Mixed Phase Materials

5.3.1 Literature Review: Crystal Structures and Dynamics in Lithium Amide and Lithium Imide

Crystal Structure of Lithium Amide

$LiNH_2$ crystallizes in the tetragonal space group $I4^-$ with nitrogen in a close-packed fluorite-like cubic arrangement[288,289]. Subsequent studies have merely made adjustments to the covalent N - H bond length (to 0.97 and 0.98 $\AA$)[290] and the H - N - H bond angle (to 104.0^o)[291]. In all studies, large displacement parameters were found for lithium and hydrogen positions, indicative of ionic mobility.

Crystal Structure of Lithium Imide

The structure of Li_2NH was shown to be face-centered-cubic (fcc) with respect to NH^{2-} anions, crystallizing with the anti-fluorite arrangement topographically equivalent to LiO_2, with Li^+ filling the tetrahedral positions[292]. The absence of quadrupolar satellites in NMR spectra recorded by Haigh *et al.*[283] confirmed that lithium was situated in sites of cubic symmetry, in comparison to the amide which showed a small C_Q = 119 kHz. Subsequent PND[293] and synchrotron XRD[294] studies attempted to determine the position of the hydrogen atoms. Both confirmed the fcc NH^{2-} sub-lattice, with random occupancy of hydrogen in either one of four 16e sites, or one of twelve 48h sites about the nitrogen atom, respectively. Further work suggested that the low temperature (LT) structure (below the order-disorder transition) could be equally well assigned to either a disordered

cubic superstructure with twice the lattice constant previously reported with Li^+ partially occupying the $32e$ octahedral sites within the NH^{2-} sub-lattice, or fully occupied orthorhombic structure[295].

Several DFT studies attempted to determine the orientation of the N - H bond[295–298]. These studies assumed a fully-occupied orthorhombic structure because this was more tractable than a supercell which would account for partial Li^+ occupancy. Some disagreement between these studies and experimental diffraction patterns prevailed. Therefore, it was suggested that metastable states could exist. Alternatively, quantum delocalisation of hydrogen via a tunneling mechanism may account for the random distribution of hydrogen atoms[299]. Luduena *et al.*[300] examined this possibility with a combination of path integral molecular dynamics and ^1H solid-state NMR, using cubic crystal structures as a start point instead. The orientation of the N - H bond was determined to have an average angle of 30^o to the c-lattice vector at 300 K and quantum delocalisation effects were shown to be negligible. Agreement between measured and predicted chemical shifts also suggested a mobile Li^+ sub-lattice.

Ab initio calculations of the lowest energy structure by different groups[301,302] have converged on very similar structural models in agreement with experimental structures proposed by Balogh *et al.*[295]. Li_2NH is unusual because it has more cations (H^+ and Li^+) than tetrahedral sites. For antifluorite structures, it is expected that cations will be associated with tetrahedral sites. On this basis Mueller and Ceder[301] proposed a structure where 1 in 6 tetrahedral sites are shared by 4 cations in tetrahedral arrangement, either H^+ in $8b$ sites or Li^+ in $8a$ sites. Thus the N - H bonds point towards some of the $48f$ tetrahedral sites, leaving the remainder for Li^+. The remaining Li^+ occupies $\frac{1}{3}$ of $32e$ octahedral sites as found experimentally. At low temperatures, the most favourable arrangement of the above is where an occupied $32e$ site is adjacent to an $8a$ vacancy. Monte Carlo simulations showed a tendency for octahedral Li^+ ions to collapse into $8a$ vacancies due to

the instability of incomplete Li^+ tetrahedra, with increasing temperature. Indeed it is proposed that Li_2NH may be kinetically trapped at lower temperatures in a metastable structure, depending on preparation temperature and method[303]. Miceli *et al.*[302] derived a very similar structural model, but place a larger emphasis on the importance of motion invoking the use of $16c$ interstitial sites prior to formation of $8a$ tetrahedra. This provides correlation between the occupancy of the $8a$ and $32e$ sites by lithium jumps via $16c$ sites. The time-averaged structure has $Fd\bar{3}m$ symmetry.

The Order-Disorder Transition in Lithium Imide

Differential thermal analysis revealed an order-disorder transition associated with reorientation of NH^{2-} ions[304]. *Ab initio* molecular dynamics simulations[305] showed that at around 385 K ($2.6 \times 10^{-3} K^{-1}$), the lithium sub-lattice rearranges, allowing ion mobility along NH^{2-} channels to increase. This is accompanied by a simultaneous rearrangement of the N - H bonds, leading to a more isotropic charge distribution about NH^{2-}, such that the distorted NH^{2-} sub-lattice becomes almost perfect fcc. The high temperature phase was determined by neutron diffraction[295] to be disordered cubic with hydrogen atoms randomly located on $192l$ sites. Simulations suggest this is a time-averaged structure, where Li^+ oscillates about fcc lattice sites before having enough energy to diffuse.

Inherent structural disorder means a method such as NMR, which is sensitive to local environments, is an effective tool for examining the structure transformation[306]. Comparison between computed and experimentally recorded ^{6}Li and ^{1}H chemical shifts at different temperatures distinguished the existence of partially occupied, interstitial, chemically inequivalent Li^+ sites. The orientation of the N - H bond was confirmed, pointing towards anti-fluorite tetrahedral sites. Upon approach to 300 K, the ^{6}Li spectrum smoothed into a single resonance with an

average chemical shift, where Li^+ experiences all possible environments on the time scale of the experiment. This provides evidence for rapid lithium diffusion in the HT (high temperature) structure, thus leading to the order-disorder transition.

Li^+ dynamics in Lithium Imide

Clearly, a complete description of the structure of Li_2NH includes ion dynamics. Blomqvist *et al.*[307] compared dynamics in Li_2NH with $LiNH_2$. Ion trajectory maps showed that upon the order-disorder transition complete isotropic rotation of the N - H bond in Li_2NH occurs, whereas only $[NH_2]^-$ 180^o re-orientations take place in $LiNH_2$ even up to 700 K. Momentum transfer from rapid N - H rotations is linked to the onset of superionicity in the imide, but in the amide static $[NH_2]^-$ groups cause a blockage to Li^+ diffusion. Mean square displacement parameters suggest that the inclusion of vacancies in Li_2NH had a negligible effect, in contrast to both Li_3N and $LiNH_2$. By analogy with Li_3N (section 5.2.1), the presence of Li - H bonds creates the covalent character of Li_2NH, essentially weakening Li - N bonds enough to allow Frenkel defect formation and hence diffusion[269,272].

Materials of fluorite (such as CaF_2[271]) and anti-fluorite structure (such as Li_2O[308,309]) are well known to have high conductivities due to their channel-like structure. David *et al.*[286] suggested that diffusion in Li_2NH might be equivalent to that observed in LiO_2 via correlated hopping between tetrahedral sites at lower temperatures, and between tetrahedral and octahedral sites at higher temperatures.

Li *et al.*[310] measured the ionic conductivity in Li_2NH to be 10^{-4} $\Omega^{-1}cm^{-1}$ at ambient temperatures, but rising to 10^{-3} $\Omega^{-1}cm^{-1}$ at 400 K (above the order - disorder transition). The measurements reported occurred at temperatures > 310 K, showing a continuous increase in the conductivity, and no discontinuity at the order - disorder transition temperature. The activation energy of Li^+ hopping

was measured to be 0.63 eV, in agreement with 0.58 eV previously reported[311]. Simulations suggested that the Li^+ hopping process was most likely to be jumps between tetrahedral - octahedral sites along the [001] direction. However, calculations were unable to distinguish whether either a Frenkel defect pair or charge lithium vacancy mechanism was most likely. Li *et al.*[310] attributed lower mobility Li^+ in $LiNH_2$ to the tetragonal crystal structure, which is too energetically stable to allow the formation of Frenkel defect pairs.

Intermediate Lithium Imide - Amide Phases

In situ neutron diffraction studies evidence the formation of intermediate imide-like phases during interconversion between Li_3N, Li_2NH and $LiNH_2$, with a concentration-dependent lattice parameter exhibiting overall cubic structure[286,312–315]. Lithium rich $Li_{2+y}NH$ phases were observed between Li_3N and Li_2NH, possessing very similar lattice parameters to Li_2NH[313]. $Li_{2+y}NH$ was suppressed at low pressures; instead, the formation of Li_4NH occurred, followed by non-stoichiometric $Li_{4-2x}NH$ mediating conversion between Li_4NH and Li_2NH via a solid-state reaction[315,316]. Structural similarity between Li_4NH and Li_2NH would allow interfaces with minimal strain, and ordering of the anionic lattice would allow inter-growth. At pressures greater than 5 bar, non-stoichiometric phases were prohibited completely because the chemical potential of gaseous H_2 was sufficient to drive Li_3N to $LiNH_2$[314].

Inter-conversion between Li_2NH and $LiNH_2$ was also accompanied by a change in the lattice unit cell volume[312]. A lithium-deficient phase of the form $Li_{2-y}NH_{1+y}$ was proposed, where such intermediate non-stoichiometric phases are suggested to form via short-lived Frenkel defects involving diffusion of Li^+ and H^+[286]. The mechanism for inter-conversion proposed is given in reaction 5.3 where $\square$ denotes a vacancy. After defect formation, Li^+ may be expelled for conversion of Li_2NH

to $LiNH_2$, or H^+ expelled for the reverse.

$$\begin{aligned} 2LiNH_2 &\leftrightarrow [LiLiNH_2]^+ + [\square NH_2]^- \\ Li_2NH &\leftrightarrow [\square LiNH]^- + Li^+ \end{aligned} \tag{5.3}$$

Subsequent creation of micro-structural defects causes change in the local structure to tetragonal while the long-range cubic structure is retained on average.

Reaction kinetics for the $LiNH_2$ to Li_2NH conversion were shown by *ab initio* methods to improve with increased LiH surface area[317], achieved via ball milling[213]. This is because NH_3 formation is more favourable at the LiH surface than in the bulk. NH_3 is formed by combination of $[\square\ NH_2]^-$ with H^+. The latter must diffuse through the bulk, which is rate limiting.

Likewise, the reverse (hydrogenation of Li_2NH) is also energetically favourable at the Li_2NH surface[318]. Formation of LiH is rate limiting in this case owing to diffusion of H^- through the bulk, preceded by Frenkel defect pair formation. Formation of the H^+ site interstitial is essential for N - H bond formation. Since the Li^+ interstitial is more energetically favourable, this acts as an accompanying defect for H - related defects, so is the prime species involved in mass transport[319].

In summary, there has been extensive debate over the precise structure of Li_2NH, in particular over Li^+ occupancy and N - H bond orientation. The shortcomings of XRD and PND are that these methods sample time-averaged LT structures, where Li^+ is mobile on a faster time scale than the experiment[301,302]. The power of an experimental method such as NMR which samples the local environment has already been acknowledged as being crucial in such an instance[300,306]. Therefore, in the rest of this chapter, knowledge of Li^+ conductivity[310] will be substantiated by static ^{7}Li NMR line shape analysis and T_1 relaxation measurements, on Li_2NH and $LiNH_2$.

5.3.2 Synthesis and Characterisation: Ammonia Storage in the Lithium Imide - Amide System

An alternative reaction pathway for the Li-N-H system to that given by equations 5.1 and 5.2 has been pioneered by Tapia-Ruiz *et al.*[320] and Tapia-Ruiz[281]. In contrast to the above, the system absorbs and releases ammonia in place of hydrogen, by the following reaction:

$$\begin{aligned} 2Li_3N + NH_3 &\leftrightarrow 3Li_2NH \\ 3Li_2NH + 3NH_3 &\leftrightarrow 6LiNH_2 \end{aligned} \tag{5.4}$$

Ammonia combustion may be conducted in an environmentally benign way, used directly with a SO fuel cell, or decomposed into H_2 and N_2 gas for use with a PEM fuel cell, releasing H_2O[321]. With a moderate vapour pressure (8 bar at room temperature), compressed storage of ammonia is vastly more efficient than that of hydrogen, however toxicity and flammability concerns make it more desirable to store chemically. Reaction 5.4 presents a single-phase ammonia storage system which avoids the formation of LiH; thus with anticipated increased homogeneity and lifetime.

MW synthesis generates high temperatures rapidly, so it is especially useful for optimising kinetics of slow reactions such as sorption in metal hydrides. The MW synthesis[279] method was used to synthesize Li_2NH in 40 minutes (sample (a)), and subsequently samples (b) and (c) after 55 and 60 minutes. Reflections due to tetragonal $LiNH_2$ were just discernible in PXRD spectra of (b) and (c), but the main phase observed was cubic Li_2NH. Raman spectra of (a), (b) and (c) recorded by Tapia-Ruiz[281] are shown in figure 5.11. Peaks at c.a. 3175 (ν_{sym}) and 3236 cm^{-1} (ν_{asym}) in sample (a) are due to N - H stretches of Li_2NH; broadening of these peaks suggested defects within the Li-N-H crystal. Peaks at c.a. 3260 cm^{-1}

(ν_{sym}) and 3310 - 3320 cm^{-1} (ν_{asym}) indicate N - H vibrations of $LiNH_2$ in (b) and (c), in addition to the broad peak at c.a. 3180 cm^{-1}, overall implying presence of a non-stoichiometric, $Li_{1+x}NH_{2-x}$ intermediate, iso-structural with Li_2NH. Herein samples (b) and (c) will be called Li_2NH-like samples. Also, small changes to the cubic lattice parameter were found from PXRD making it possible to infer that $Li_{1+x}NH_{2-x}$ samples (b) and (c), have x = 0.29 and 0.23 respectively.

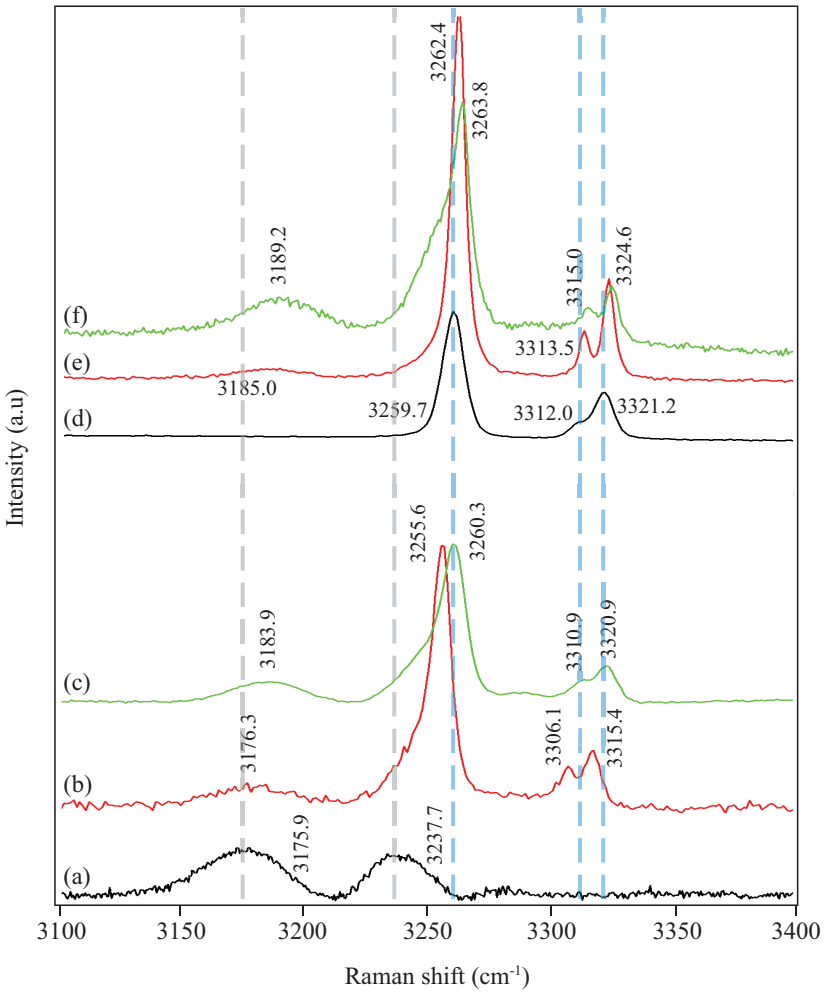


Figure 5.11: Raman spectra of samples (a) Li_2NH; (b), (c) Li_2NH - like; (d) $LiNH_2$; (e), (f) $LiNH_2$ - like. Sharp peaks at c.a. 3260 cm^{-1} (ν_{sym}) and 3306 - 3324 cm^{-1} (ν_{asym}) are assigned to N - H vibrations of $LiNH_2$, and broad peaks at c.a. 3175 (ν_{sym}) and 3236 cm^{-1} (ν_{asym}) to N - H stretches of Li_2NH. Blue and grey dashed lines are along $LiNH_2$ and Li_2NH Raman shifts respectively. Figure reproduced from 320.

Full conversion to $LiNH_2$ was not achieved by MW synthesis. It is postulated that an ammonia rich environment led to ultra-fast conversion from Li_3N to $LiNH_2$, then high temperatures achieved in MW synthesis caused decomposition to Li_2NH and NH_3.

$LiNH_2$ was synthesised with conventional heating (not MW) under a constant ammonia flow (sample (d)). By limiting the amount of ammonia in the reaction vessel it was possible to synthesize $LiNH_2$ - like samples, (e) and (f). Raman spectra of (d), (e) and (f) are given in figure 5.11. Peaks at c.a. 3259 (ν_{sym}) and 3312 - 3321 cm^{-1} (ν_{asym}) were assigned to vibrational modes in $LiNH_2$ in sample (d). The broad humps at c.a. 3175 cm^{-1} corresponding to ν_{sym} in Li_2NH were weakly observed for samples (e) and (f) in addition to those corresponding to $LiNH_2$. Small differences in the Raman shift between samples implied differences in the local structure, suggesting a non-stoichiometric $Li_{1+x}NH_{2-x}$ intermediate. Both samples (e) and (f) displayed PXRD patterns similar to $LiNH_2$, but broadening of the 51^o 2θ peak suggested that a component of the cubic anti-fluorite phase was present. It was possible to determine x = 0.67 and 0.64 from the lattice parameter. Herein samples (e) and (f) will be called $LiNH_2$-like samples. All the samples used for NMR in the following are summarised in table 5.3.

Label	Sample	x	preparation
(a)	Imide: Li_2NH	1	Li_3N and NH_3 via MW heating
(b)	Imide-like: $Li_{1+x}NH_{2-x}$	0.29	Li_3N and NH_3 via MW heating
(c)	Imide-like: $Li_{1+x}NH_{2-x}$	0.23	Li_3N and NH_3 via MW heating
(d)	Amide: $LiNH_2$	0	Li_3N and NH_3 via conventional heating
(e)	Amide-like $Li_{1+x}NH_{2-x}$	0.67	Li_3N and NH_3 via conventional heating
(f)	Amide-like $Li_{1+x}NH_{2-x}$	0.64	Li_3N and NH_3 via conventional heating
(i)	Imide: Li_2NH	1	Li and NH_3 via conventional heating
(ii)	Amide: $LiNH_2$	0	Li and NH_3 via conventional heating

Table 5.3: Summary of Li_2NH and $LiNH_2$ type samples. (i) and (ii) will be introduced in the following section.

5.3.3 Lithium-7 Static NMR: Variable Temperature Line Shapes of Lithium Amide and Lithium Imide

All spectra and measurements in the following section were aquired at 7 T, using a solid echo with $\frac{\pi}{2}$ pulse lengths between 1.2 and 1.8 μs and echo delays between 8 and 20 μs.

Preliminary wideline ^{7}Li NMR experiments on $LiNH_2$ and Li_2NH have been performed by Powell[126]. In that set of samples, $LiNH_2$ was synthesised by reacting NH_3 with Li metal using thermal heating (sample (i)). A subsequent drop in the pressure of NH_3 ($<$ 1 mbar) yielded Li_2NH (Sample (ii)). Solid-echo spectra in figure 5.12 of these samples reveal a dipolar broadened central transition, and the spectra of Li_2NH also display a set of broadened quadrupolar satellites, which fitted well to Gaussian lines. With increasing temperature a small amount of line narrowing allowed a set of quadrupolar satellites in the spectrum of $LiNH_2$ to become visible, with C_Q = 120 kHz, in good agreement with that previously

reported[283]. In the spectra of Li_2NH, substantial line narrowing of the central transition occurred.

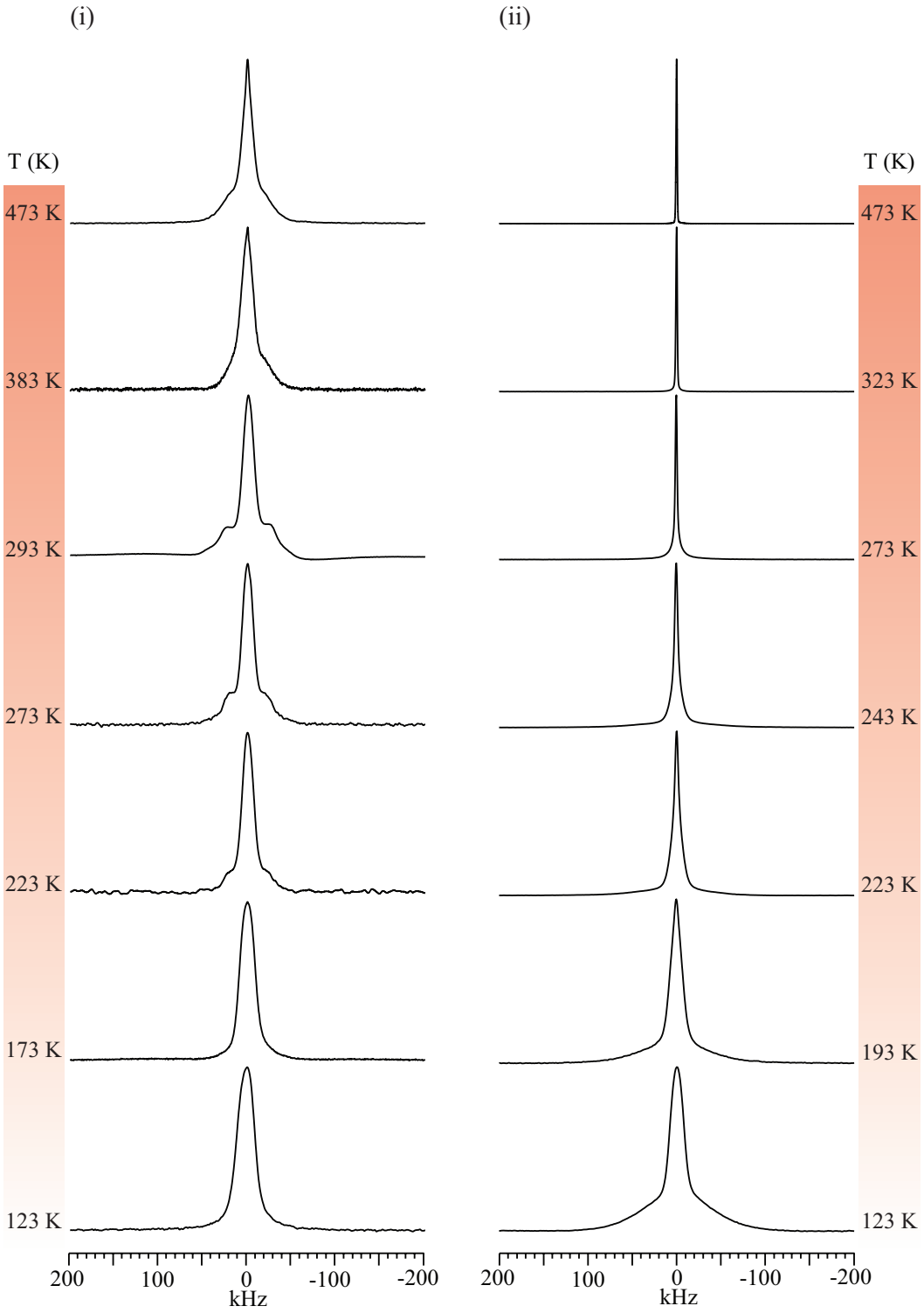


Figure 5.12: Variable temperature wideline ^{7}Li spectra of samples (i) and (ii) recorded by Powell[126].

5.3.4 Lithium-7 Static NMR: ^{1}H Decoupling Measurements

It was suggested by Powell[126] that since the EFG does not appear to change in sample (ii), the Li^+ hopping process below $\sim 2.7 \times 10^{-3}$ K^{-1} (the order-disorder transition) would be hopping between tetrahedral sites along the [100] direction. Then, by analogy with lithium oxide[308,309], the process above $\sim 2.7 \times 10^{-3}$ K^{-1} was assigned to an additional conduction pathway between tetrahedral and vacant octahedral sites. Such behaviour is typical of anti-fluorite type structures.

To confirm in the first instance whether line narrowing in (ii) was caused by Li^+ ion diffusion, spectra recorded at 183 K with and without high power CW ^{1}H decoupling ($\sim$ 75 kHz) were compared. Linewidths given in table 5.4 show that within measurement error, ^{1}H decoupling makes not difference to the linewidth.

Experiment	With CW decoupling	Without CW decoupling
Linewidth (Hz)	16576	15448

Table 5.4: ^{7}Li linewidths recorded at 183 K for sample (ii) with and without CW decoupling.

Since CW decoupling does not change the linewidth, this implies no contribution from ^{1}H - ^{7}Li dipolar couplings exists in the broad spectra at the low end of the temperature range in figure 5.12. Isotropic rotation of the N - H bond has been associated with the order-disorder transition[307], but clearly hydrogen is sufficiently mobile to be self-decoupled from lithium at low temperatures as well. Quantum delocalisation of hydrogen is a possible mechanism causing this[299], since an estimate of the correlation time $\tau_c(300K) = 10^{-12}$ s and activation energy $E_a = 260$ meV suggest rapid ^{1}H motion by a quantum tunneling mechanism even at 183 K.

Thus the linewidth may only comprise contributions from heteronuclear ^{14}N and

homonuclear ^{7}Li dipolar couplings. It is noted that whilst ^{14}N has 99 % natural abundance, its low gyromagnetic ratio (-2.71 $\times 10^{7}$ rad s^{-1} T^{-1}) means it will have a negligible contribution to the linewidth in comparison with ^{7}Li. Line narrowing in sample (ii) shown by the spectra in figure 5.12 is therefore due to removal of ^{7}Li homonuclear dipolar couplings, caused by Li^{+} hopping.

5.3.5 Lithium-7 Static NMR: Line Shape Analysis on Samples (a), (b) and (c)

Solid-echo ^{7}Li spectra of samples (a), (b) and (c) are presented in figure 5.13. In all three samples, a broad feature near the base line indicates a set of broadened quadrupolar satellites, with C_Q similar to that of $LiNH_2$. The exact C_Q has not been estimated here, since it is impossible to locate the satellite maxima. PXRD confirmed that (a), (b) and (c) all possess the cubic anti-fluorite structure; thus a vanishing C_Q would have been expected. However it has become apparent from the structural debate that partial occupancy of lithium sites exists, creating static disorder of the lithium sub-lattice in the rigid lattice limit. This would be expected to give rise to a finite C_Q (also observed for sample (ii)) at low temperatures.

Increased temperature reveals motional narrowing of the ^{7}Li resonance for samples (a), (b) and (c), akin to that of sample (ii). This was accompanied by complete removal of quadrupolar satellites by $\sim$ 300 K. Static disorder will give rise to a range of Li^{+} sites in Li_2NH, hence a distribution of C_Q values are expected. Removal of the quadrupolar satellites is therefore attributed to exchange broadening of Li^{+} ions between sites of different C_Q, in direct analogy with that observed in Li_3N.

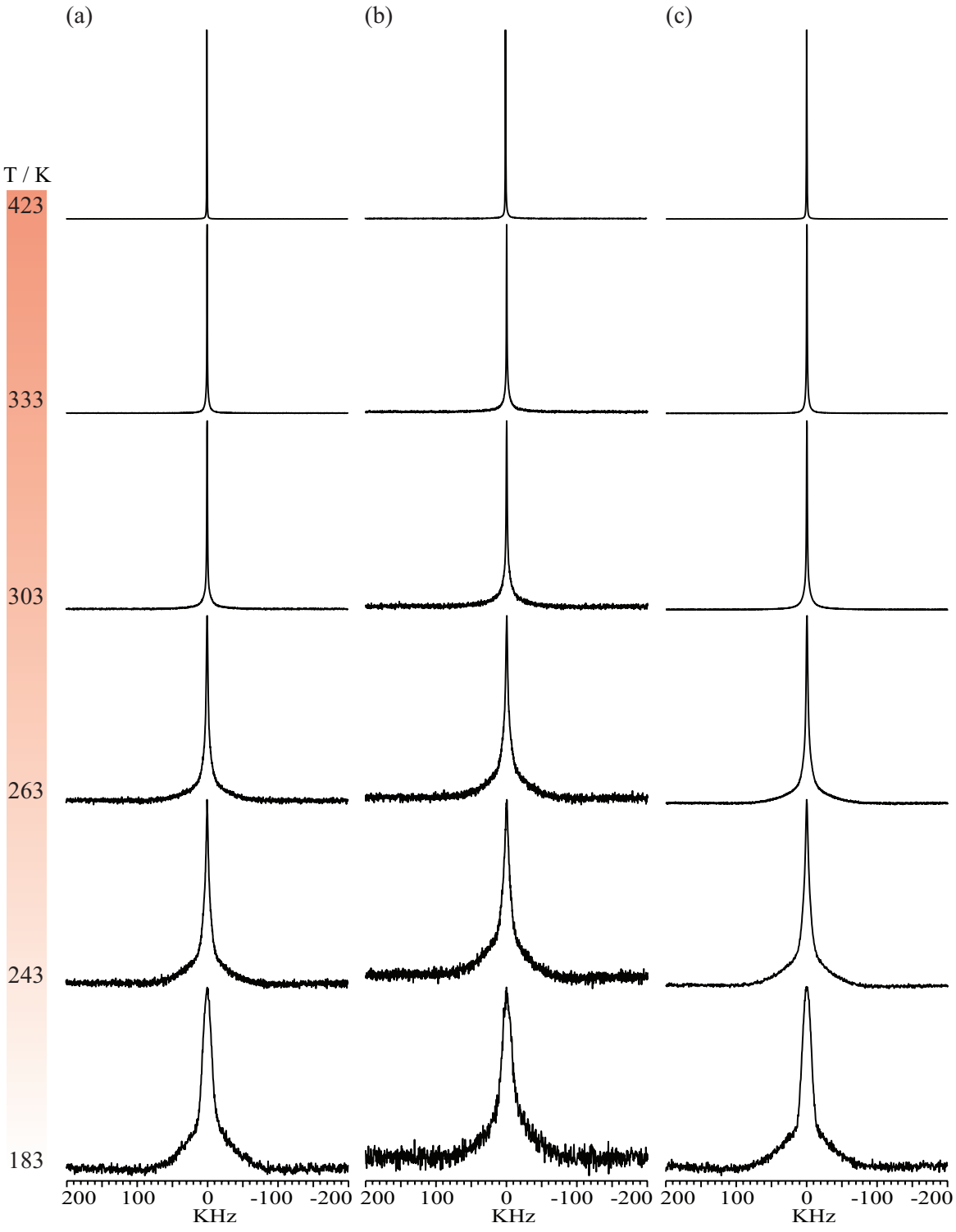


Figure 5.13: Variable temperature wideline ^{7}Li spectra of samples (a), (b) and (c).

^{7}Li linewidths are plotted as a function of temperature in figure 5.14 (A). Samples (a), (b) and (c) all display similar motional narrowing behaviour, caused by Li^+ ion dynamics. The onset of motional narrowing in (b) and (c) appears to be ~ 20 K higher in temperature than in (ii) and (a). A large enough change in the lattice constant associated with non-stoichiometry could change the Li^+ jump distances, and hence the correlation times. However, the lattice constant of sample (b) is less than that of (a), but for (c) is is larger than that for (a). Since no trend emerges here, the changes in the lattice constant are insignificant with respect to Li^+ dynamics. Instead this difference is thought to originate from the resonances of (b) and (c) comprising a combination of both a small amount of a broader component of lithium in the $LiNH_2$ tetragonal $I4^-$ structure, and a larger dominant component in the Li_2NH fcc cubic crystal structure. As the dominant component of Li_2NH narrows, the height of the resonance increases relative to the width, to maintain the same intensity. Thus the small contribution from the broader $LiNH_2$ is effectively broadened away into the baseline of the spectrum. At intermediate temperatures whilst the motional narrowing process is occurring, the broad component therefore contributes to the FWHM, but becomes negligible as the linewidths of (b) and (c) converge on the same value as that for (ii) and (a), in the narrowed limit.

The correlation times were calculated with equation 2.80 and are plotted as a function of temperature in figure 5.14 (B). An Arrhenius analysis yielded the parameters in table 5.5. Visual inspection of figure 5.14 (A) suggests (a) is different from (b) and (c), however the very good agreement between E_a and τ_c confirms the same Li^+ ion dynamics exists in all three samples. E_a for sample (ii) is also in very good agreement. The small discrepancy in τ_c probably originates from the small increase in linewidth of (a), (b) and (c) compared with (ii) during motional narrowing, owing to the presence of $LiNH_2$ in these samples.

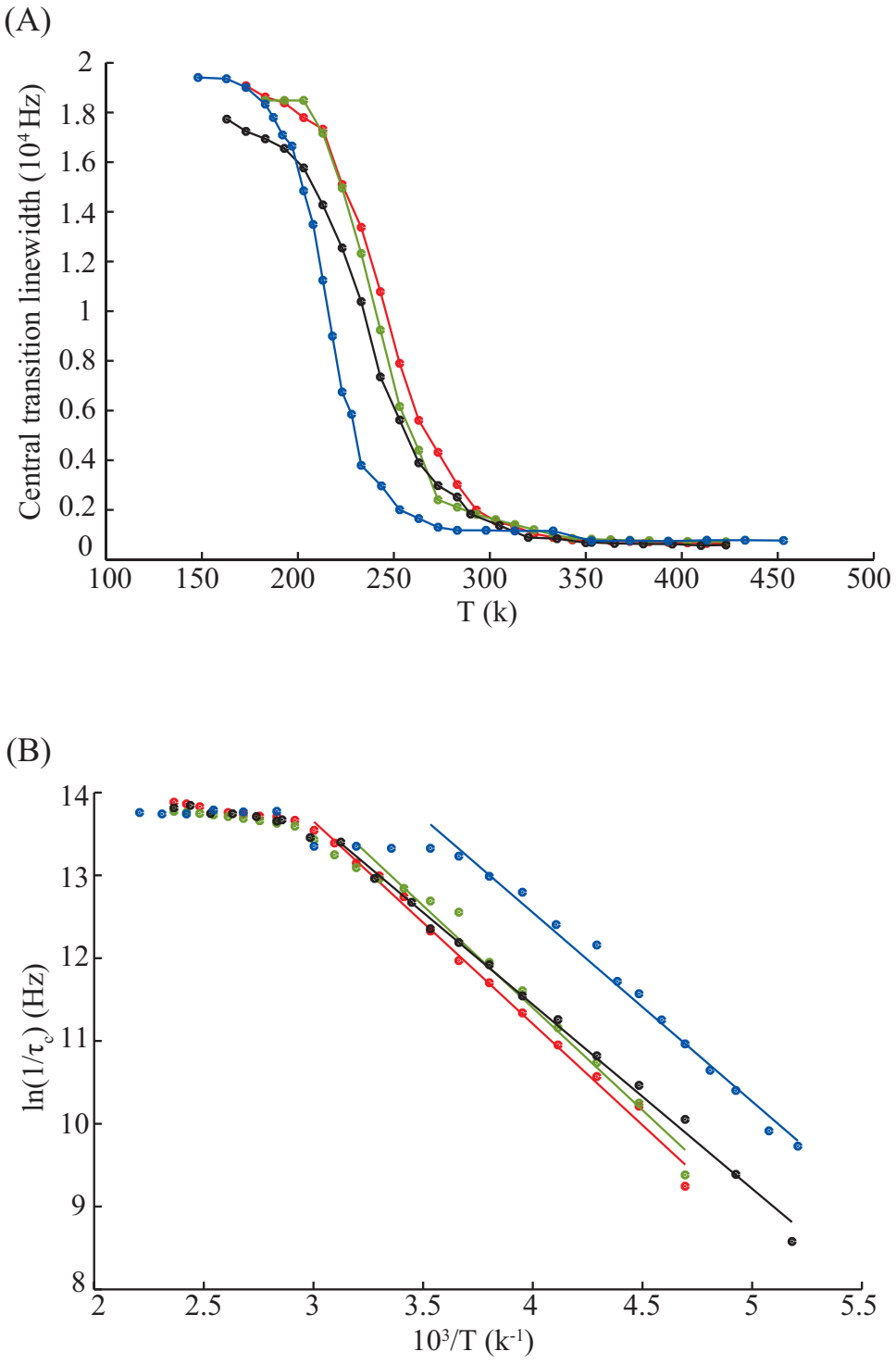


Figure 5.14: (A) ^{7}Li linewidth variation with temperature; (B) Arrhenius plot of the temperature dependence of the correlation time. Black is sample (a); red (b); green (c); blue (ii). Note the line in (A) is just to guide the eye, whereas in (B) the linear regression line is used to calculate the activation energy.

Sample	(ii)	(a)	(b)	(c)
E_a (eV)	0.18 ± 0.01	0.171 ± 0.008	0.19 ± 0.01	0.19 ± 0.02
τ_c(298K) ($\times 10^{-6}$ s)	0.82 ± 0.05	2.6 ± 0.1	2.8 ± 0.2	2.3 ± 0.2

Table 5.5: Arrhenius parameters for Li^+ hopping obtained from motional narrowing of the central transition in the ^{7}Li spectrum.

5.3.6 Lithium-7 Static NMR: Spin-Lattice Relaxation Measurements on Samples (a), (b) and (c)

^{7}Li spin-lattice relaxation times (T_1) were measured as a function of temperature on samples (a), (b) and (c) (figure 5.15) with the saturation recovery method. Saturation was achieved with a train of 100 $\frac{\pi}{2}$ pulses spaced by 100 μs. The FID was collected with a solid-echo. A single exponential was sufficient to describe the recovery of magnetization, and a fit yielded T_1.

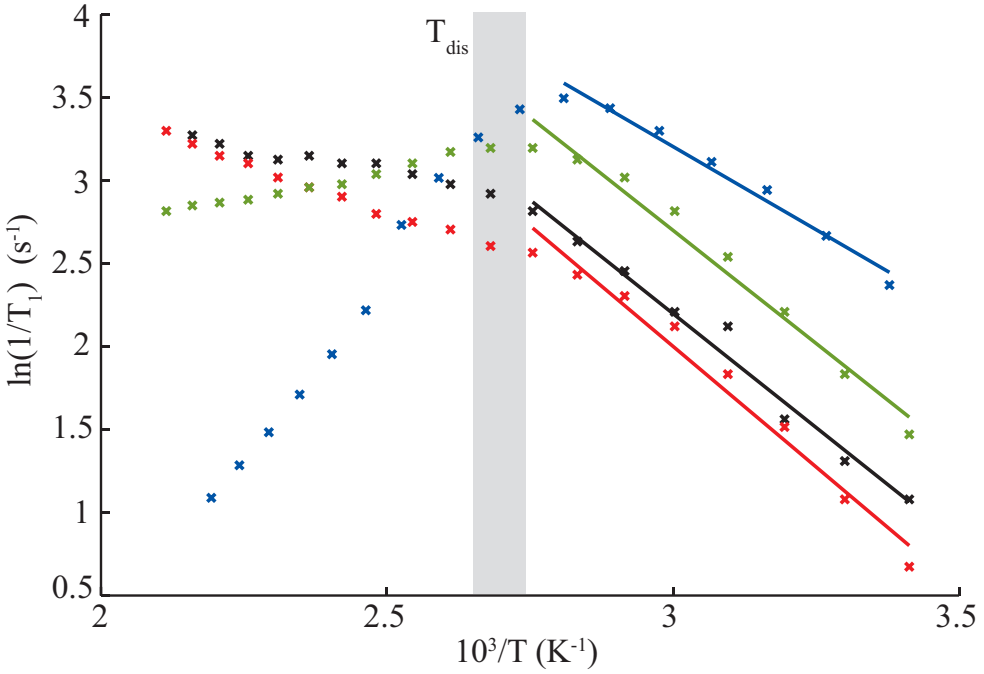


Figure 5.15: Temperature dependence of ^{7}Li T_1 relaxation times for samples: black (a); red (b); green (c); blue (ii). The order-disorder transition temperature (T_{dis}) is marked by the shaded region. At temperatures below the order-disorder transition a linear regression line has been used to estimate the activation energy.

At first glance, it appears that the order-disorder transition occurs at $10^3/T_{dis} \sim 2.5$ K^{-1} for sample (ii). In contrast samples (a), (b) and (c) all show $10^3/T_{dis} \sim 2.7$ K^{-1}, which is close to the expected temperature for this to occur. For (ii), first glance shows a minimum occurs at this temperature. Closer examination showed that this peak to be quite asymmetric. This may be indicative of non-exponential correlation, but given that this occurs at the expected temperature of the order-disorder transition, this is most likely to be a discontinuity owing to the phase transition. Zero-field muon spin resonance (μSR) studies by Powell[126] also showed very clearly a discontinuity in the muon depolarization rate at $10^3/T \sim 2.7$ K^{-1} in sample (ii).

The shape of the data where $10^3/T > 2.7$ K^{-1} is linear, so it is assumed this is in the low temperature limit $\omega_0\tau_c >> 1$. A simple mono-exponential correlation

function was chosen, free from assumption about the relaxation mechanism. When $\omega_0\tau_c >> 1$, the simplification is valid:

$$\ln \frac{1}{T_1} \approx \frac{C}{\omega_0^2 \tau_0} - \frac{E_a}{k_B T} \tag{5.5}$$

where C is an amplitude/strength factor. Hence E_a is estimated from linear regression of $\ln \frac{1}{T_1}$ against $\frac{1}{T}$ as shown in figure 5.15 and given in table 5.6:

Sample	(ii)	(a)	(b)	(c)
E_a (eV)	0.17 ± 0.03	0.24 ± 0.03	0.25 ± 0.04	0.23 ± 0.04

Table 5.6: Activation energies obtained from Arrhenius analysis of ^{7}Li T_1 relaxation times in the limit $\omega_0\tau_c >> 1$ from linear regression.

Fitting T_1 data in figure 5.15 to a Lorentzian spectral density function tended to over-predict the activation energies c.a. 0.25 eV for Li_2NH and 0.31 eV for samples (a) - (c); it is noted this was accompanied by reasonable estimate around 10^{-13} - 10^{-14} s for τ_0. The difference in the predicted parameters from the different models used here is ascribed to the fact that the region examined ($\omega_0\tau_c >> 1$ - the LT phase) is far from the $\frac{1}{T_1}$ maximum, due to the order-disorder transition occurring at ~ 2.7 K^{-1}. A linear regression line is only an approximation, and a Lorentzian spectral density function would be more accurate, however usually a $\frac{1}{T_1}$ maximum is required to give a reliable fit to a Lorentzian spectral density function.

5.3.7 Lithium-7 Static NMR: Line Shape Analysis on Samples (d), (e) and (f)

Solid-echo ^7Li spectra of samples (d), (e) and (f) are presented in figure 5.16. In the temperature range 153 - 313 K, the line shape resembled a single Gaussian

broadened central transition, flanked by a set of Gaussian broadened quadrupolar satellites. Above $\sim$ 313 K, all three samples (d), (e) and (f) underwent a significant change in the line shape whereby the top of the resonance narrowed but the bottom remained comparatively broad. This change progressed to the point where the narrow component became much more apparent in the spectrum over the residue broad component. The linewidths at the highest temperatures of the broad and narrow components were $\sim$ 12 kHz and $\sim$ 1 kHz respectively.

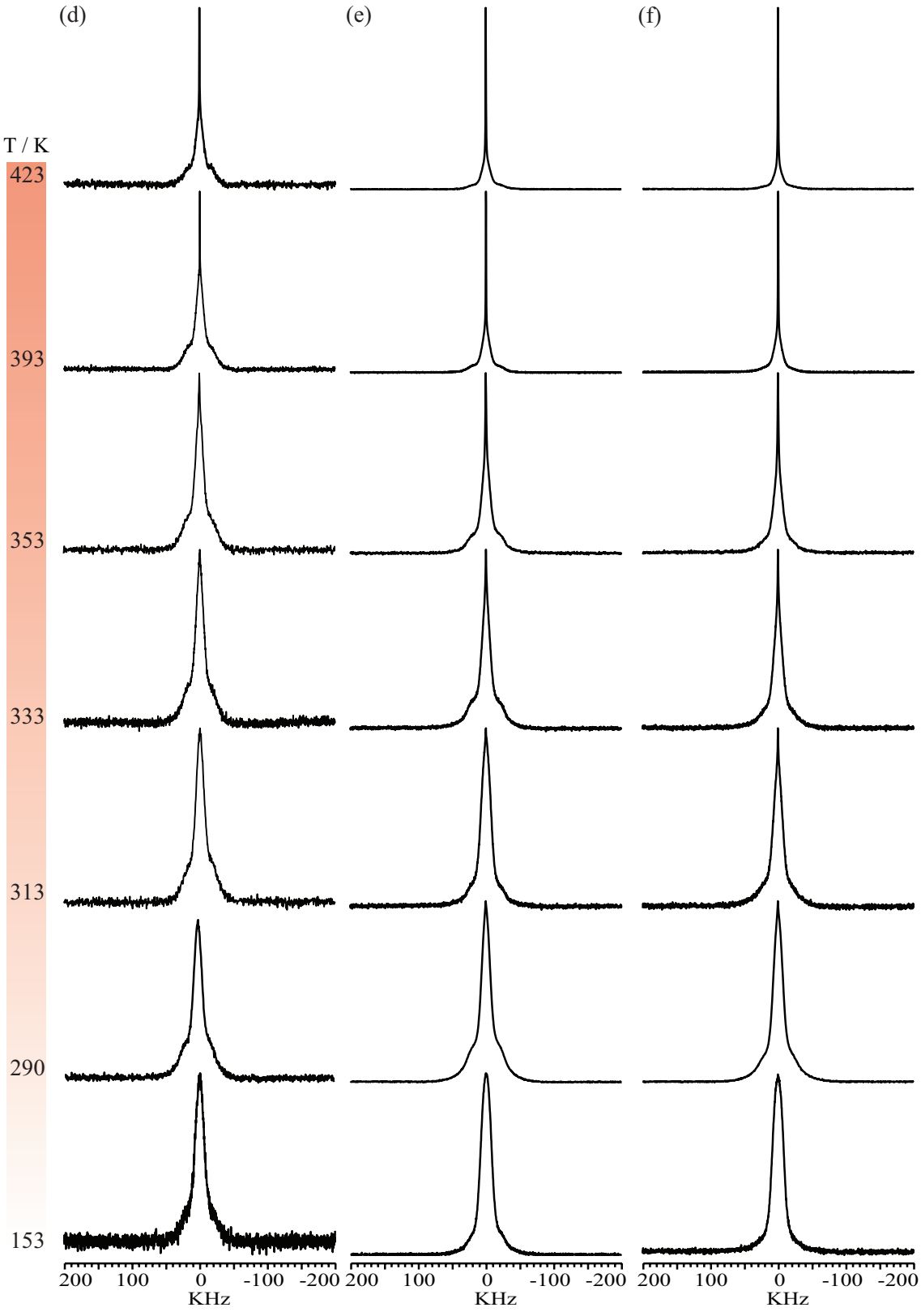


Figure 5.16: Variable temperature wideline ^{7}Li spectra of samples (d), (e) and (f).

Above $\sim$ 313 K, the line shape could be deconvoluted into 3 Gaussian components, as shown in figure 5.17. The red peak was placed to fit the quadrupolar satellites, so that the blue and green peaks would converge on the broad and narrow central transition components respectively. The narrow component showed a similar linewidth to that expected for Li_2NH (sample (ii)), which enters the motionally narrowed region at $\sim$ 313 K, whereas the broad component had a similar linewidth to $LiNH_2$ (sample (i)) which does not narrow significantly from its rigid lattice linewidth.

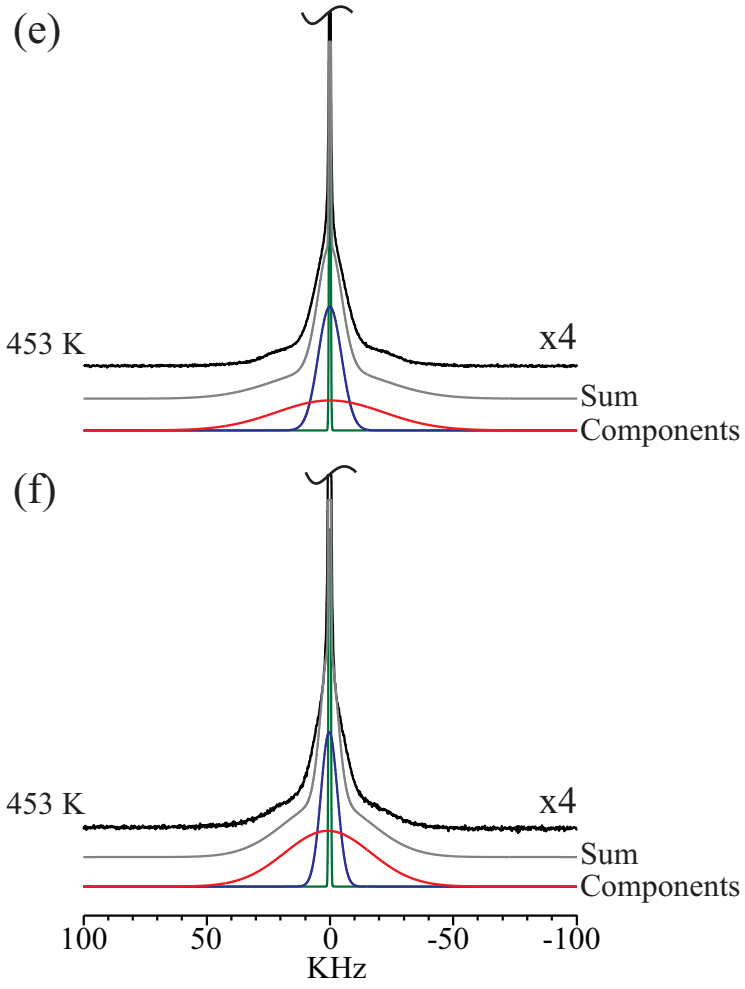


Figure 5.17: Wideline ^{7}Li spectra of samples (d) and (e) at 453 K. The grey profile is the sum of deconvolution peaks: green, imide; blue, amide; red, satellite component.

Samples (e) and (f) are known from PXRD, IR and Raman spectroscopy to contain a minor component of Li_2NH, but the majority is $LiNH_2$, so a mixed phase line shape as described is quite reasonable. However sample (d) was not expected to exhibit any evidence of a mixed phase, however the line shape change is far more substantial than that of sample (ii). The concentration of a cubic Li_2NH-like phase in (d) may have been below the detection limit of other spectroscopies; since sample (d), whilst maintaining tetragonal $I4^-$ $LiNH_2$ structure, is less-stoichiometric than (i), leading to defects.

The C_Q values for samples (d), (e) and (f) were estimated to be around 105 $\pm$10 kHz, in contrast to 120 kHz for (i). Resolution of the satellites is poor due to substantial broadening, giving rise to large error ($\pm$10 kHz). In this case there is a small discrepancy between samples. In order to investigate this, CASTEP calculations[322] were performed to estimate the C_Q in $LiNH_2$ from crystallographic data given by David *et al.*[286] and Yang *et al.*[290]. Whilst the published crystal structures differ in terms of the proton co-ordinates, all predict Li^+ ions occupy 2a, 2c and 4f Wyckoff sites. Simulations of the ^{7}Li wideline spectrum with these parameters (given in table 5.7) show reasonable agreement with that obtained from (d), (e) and (f), at least within the error of the calculation.

Structure	Site	C_Q/kHz	η
David *et al.*[286]	2a	-45.0	0.00
	2c	+331	0.00
	4f	-198	0.27
Yang *et al.*[290]	2a	-64.0	0.00
	2c	+235	0.00
	4f	-158	0.25

Table 5.7: CASTEP calculations of the quadrupolar coupling constant C_Q and asymmetry parameter η in $LiNH_2$.

Resolution of the satellites for sample (i) shown in figure 5.12 around 293 K is better than for samples (d), (e) and (f) (figure 5.16). This implies additional broadening in (d), (e) and (f), which indicates structural heterogeneity in these samples, which may be in the form of either mixed phases or additional sample defects resulting from non-stoichiometry. Both effects also lead to a distribution of C_Q values, which may not necessarily be centred on the same value, as it would depend on the probability of certain defects occurring. It may be seen from figure 5.17, that the quadrupolar satellites are still present at the highest temperatures (453 K). Since (d), (e) and (f) comprise mostly $LiNH_2$, no exchange broadening would have been expected since Li^+ dynamics are negligible in these samples. However, at low temperatures the satellites have an additional contribution from Li_2NH, which exchange broadens away with increased temperature, leaving just the $LiNH_2$ satellites.

5.3.8 Discussion: Structure and Dynamics in Lithium Imide

By analogy with Li_2O, David *et al.*[286] suggested that a tetrahedral to tetrahedral hopping process may be expected at lower temperatures, and the onset of a tetrahedral to octahedral at higher temperatures. μSR studies certainly suggested that the tetrahedral - tetrahedral hopping might occur below the order - disorder transition (370 K), and tetrahedral - octahedral hopping may occur above[126]. However computational studies have suggested that both processes are important for Li^+ diffusion[302] below the order - disorder transition. This is also confirmed by conductivity measurements in the temperature range $\sim$ 310 - 420 K spanning below and above the transition, assigned to tetrahedral - octahedral hopping with an activation energy of 0.63 eV[310]. Using this data, a prediction of the temperature required to narrow the ^{7}Li resonance with tetrahedral - octahedral hopping suggested this would not occur until $\sim$ 310 K. At this temperature, the ^{7}Li has narrowed (onset was at around 160 K), confirming the motional nar-

rowing process is tetrahedral - tetrahedral hopping. Likewise, it is estimated that the spin lattice relaxation time would not be sensitive to tetrahedral - octahedral hopping until $\sim$ 500 K, and the zero field μSR depolarization rate (equivalent to an NMR linewidth) would not narrow until $\sim$ 350 K. It is therefore a coincidence that tetrahedral - octahedral hopping is detected at a close temperature to the order- disorder transition with μSR. The activation energies obtained for the Li^+ hopping from line narrowing and spin-lattice relaxation also suggest that tetrahedral - tetrahedral hopping has been observed here, since they are all in the range 0.17 - 0.25 eV, which is much lower than the activation energy for tetrahedral - octahedral hopping (0.63 eV). The activation energy for tetrahedral - tetrahedral hopping of 0.076 eV predicted by μSR was suggested to be an underestimation by Powell[126], by comparison with similar work on lithium nitrido-metallates.

The quadrupolar satellites for (a), (b) and (c) are shown in figure 5.13 to have broadened by 300 K (3.3 $\times 10^{-3}$ K^{-1}), suggesting there is an exchange process which occurs in the LT phase of Li_2NH. Exchange could be either between tetrahedral and octahedral sites, or between inequivalent tetrahedral sites originating from static disorder. The temperature range of exchange broadening coincides with the motional narrowing associated with hopping between inequivalent tetrahedral sites, and tetrahedral - octahedral hopping is not expected until temperatures $>$ 310 K, suggesting exchange is between inequivalent tetrahedral sites. It is also noted that exchange between chemically inequivalent sites in the very similar Li_3N (exchange broadening of the Li(2) satellites) does not onset until around $\sim$ 300 K also.

5.4 Conclusion

Here it is shown that Li_3N nanowires may be characterised in terms their Li^+ dynamics. It was found that MW synthesis forms type A nanowires exclusively; which is likely since the precise temperature control required for type B could not be achieved by MW synthesis. Lithium - alloy substrates were detected by their Knight shifts, confirming that the growth method was a VLS mechanism. Similarity in the C_Q values agree with the proposed structural model illustrated by figure 5.4, where the hexagonal layered structure is retained in wire formation. The wires form on large length scale (100 - 800 nm diameter) to incorporate this. Decrease in E_a^{intra} and increase in τ_0^{intra} were found from both line narrowing of the central transition and the Li(2) satellite transitions for Li - Ag and Li - Au, in comparison to bulk Li_3N. For Li - Pd, this was observed just from line narrowing of the central transition; narrowing of Li(2) satellite transitions could not be measured. Simultaneous decrease in E_a^{inter} and τ_0^{inter} were found from exchange broadening of the Li - Ag and Li - Au satellites. The reason for the universal decrease in both E_a^{intra} and E_a^{inter} is attributed to the increase in surface regions, which provide pathways with lower energy barriers than that of the bulk. Concomitant decrease in E_a^{inter} with decrease in τ_0^{inter} upon nano-structuring confirms the inter-layer diffusion mechanism is akin to a single vacancy-mediated process, at least within the temperature range studied here. However, increase in τ_0^{intra} with a concomitant decrease in E_a^{intra} is attributed to the more complex micro-dynamics associated with intra-layer diffusion. Improvements to solid-state hydriding rates may be linked to lowering E_a upon nano-structuring, but is equally likely to be caused by increase in reaction surface area.

A full description of the structure of Li_2NH will require details of Li^+ mobility to be included. Therefore non-stoichiometric Li_2NH and $LiNH_2$ intermediates were synthesised using ammonia in place of hydrogen. The ^7Li static NMR line shape

changes occurring with temperature suggest the existence of dual phases; comprising a component of Li_2NH which narrows by 300 K due to Li^+ hopping, and a component of $LiNH_2$ which remains broad up to 460 K. NMR line narrowing and spin-lattice relaxation measurements occur in temperature regimes where the Li^+ ion hopping process is between equivalent tetrahedral sites; to the best of our knowledge this is the first experimental evidence for this process. The temperature range of measurements in this study was too low to detect the tetrahedral - octahedral process. The low temperature line shapes of Li_2NH are indicative of lithium static disorder, which becomes dynamic in the same temperature range as the onset of the tetrahedral - tetrahedral ion hopping process.

Chapter 6

Final Summary and Concluding Remarks

Final Summary and Concluding Remarks

In this thesis, solid-state NMR has been used to contribute to the knowledge of three different hydrogen storage systems. By way of a summary, the technological significance of the results from this thesis will be discussed.

In chapter 3, the NOTT-MOF: NOTT-207, NOTT-201 and NOTT-209 were studied. In particular, the change in co-ordination environment was elucidated with the aid of static ^{7}Li spectra, upon desolvation. Desolvation is essential for use of MOF for hydrogen storage because it unblocks the pores, allowing gas sorption. The contribution of NMR in this situation was to obtain uncluttered spectra by focusing on just a single nucleus, which could not be done using XRD. Covalent-organic frameworks (COF) are a promising alternative to MOF, however in general COF are insoluble and exhibit long range disorder making them challenging to characterise. COF systems are similar to the HHTP + $NaBH_4$ / $B(OMe_3)$ systems presented in section 2.11.8, where boron-containing compounds occur between organic linkers. ^{11}B MQMAS was demonstrated to be an effective way of resolving different sites in these systems.

In chapter 4, the $LiBH_4/MgH_2$ system was studied. The first part of this study concentrated on the effect of $LiBH_4$ particle size reduction, with and without the inclusion of an MgH_2 phase, on Li^+ diffusion, by ball milling. Mass transport between phases is considered to be the rate limiting part of solid-state hydrogenation cycling[175]. Ball milling is an effective strategy for improving the cycling kinetics of (complex) metal hydrides; this study demonstrates this in terms of Li^+ diffusion. Here, NMR was able to probe diffusion at the molecular level, which complements bulk ionic conductivity methods.

The second part of chapter 4 used a multi-nuclear *ex situ* NMR study to elucidate the necessary thermodynamic conditions required for $[B_{12}H_{12}]^{2-}$ formation.

$[B_{12}H_{12}]^{2-}$ formation is undesirable, because it is very thermodynamically stable and therefore blocks the dehydrogenation pathway, resulting in a lower system capacity. Also, further evidence for the formation of Mg_xLi_{1-x} alloys has been provided. Mg_xLi_{1-x} has proved difficult to detect because its formation is very sensitive to H_2 partial pressure. This is significant, because it affords a method for complete dehydrogenation of the $LiBH_4/MgH_2$ system, effectively increasing the system capacity. If an *in situ* NMR study were possible, this might be able to probe the possible presence of any intermediates which were either highly transient, or else lost by the quenching process. In particular, isothermal decomposition could hold the equilibrium at a specific point, to allow time for an NMR experiment.

Finally, in chapter 5 the Li-N-H system was studied. In the first part, MW synthesis was demonstrated as an effective method of growing Li_3N in a novel nanowire morphology, on lithium - alloy substrates. In contrast to ball milling, the formation of nano-materials via a chemical growth method may also increase the material surface area, resulting in similar improvements to hydrogenating kinetics and thermodynamics. Evidence of improved Li^+ diffusion is found from a lowered activation energy, resulting from the increased surface area of nanowire morphology. In this case, a three-fold improvement in hydrogenating rates was also observed which may be linked to either or both the improved Li^+ diffusion and increased reaction surface area for H_2. In this situation, NMR has afforded no structural data, however it has provided a unique perspective on the dynamics of these systems, allowing characterisation in terms of the dynamics.

In the second part of chapter 5, mixed $LiNH_2$ and Li_2NH phase materials were synthesised with ammonia uptake in place of hydrogen. Ammonia affords an effective alternative to hydrogen for use in a PEM fuel cell. Here, NMR has been able to detect the presence of both phases isotypic of either $LiNH_2$ or Li_2NH in terms of Li^+ dynamics. In particular, NMR line narrowing evidences a tetrahedral

- tetrahedral hopping process, which onsets at much lower temperatures than possible for the tetrahedral - octahedral process. To the best of our knowledge, this is the first experimental evidence for this process.

In conclusion, the power of NMR has been demonstrated not only as a method which may confirm the results of other analytical techniques, but as a method which probes materials at the molecular level, providing a unique and fundamental understanding of their operation.

References

[1] T. E. Drennen and J. E. Rosthal, *Pathways to a Hydrogen Future*, Elsevier, 1st edn., 2007.

[2] C. E. Thomas, *International Journal of Hydrogen Energy*, 2009, **34**, 6005–6020.

[3] C. J. Winter, *International Journal of Hydrogen Energy*, 2009, **34**, S1–S52.

[4] D. A. J. Rand and R. M. Dell, *Hydrogen Energy*, The Royal Society of Chemistry, 1st edn., 2008.

[5] M. Conte, P. Prosini and S. Passerini, *Materials Science and Engineering B-Solid State Materials for Advanced Technology*, 2004, **108**, 2–8.

[6] S. Satyapal, J. Petrovic, C. Read, G. Thomas and G. Ordaz, *Catalysis Today*, 2007, **120**, 246–256.

[7] K. Morrow, D. Karner and J. Francfort, *Plug-in Hybrid Electric Vehicle Charging Infrastructure Review*, November 2008.

[8] *Postnote: Prospects for a Hydrogen Economy*, 2002.

[9] D. Das and T. N. Veziroglu, *International Journal of Hydrogen Energy*, 2001, **26**, 13–28.

[10] J. E. Funk, *International Journal of Hydrogen Energy*, 2001, **26**, 185–190.

[11] R. B. Gupta, in *Hydrogen Fuel*, Taylor & Francis Group, LLC, 1st edn., 2009.

[12] J. A. Turner, *Science*, 1999, **285**, 687–689.

[13] A. Zuttel, *Naturwissenschaften*, 2004, **91**, 157–172.

[14] *US DOE Hydrogen Storage: Technical Plan, Interim Update.*, 2012, `http://www1.eere.energy.gov/hydrogenandfuelcells/mypp/pdfs/storage.pdf`.

[15] C. Weidenthaler and M. Felderhoff, *Energy & Environmental Science*, 2011, **4**, 2495–2502.

[16] A. Bain and W. D. Van Vorst, *International Journal of Hydrogen Energy*, 1999, **24**, 399–403.

[17] D. B. Rapp and J. E. Shelby, *Journal of Non-Crystalline Solids*, 2004, **349**, 254–259.

[18] W. L. Mao and H. K. Mao, *Proceedings of the National Academy of Sciences of the United States of America*, 2004, **101**, 708–710.

[19] G. C. Welch, R. R. S. Juan, J. D. Masuda and D. W. Stephan, *Science*, 2006, **314**, 1124–1126.

[20] D. Teichmann, W. Arlt, P. Wasserscheid and R. Freymann, *Energy & Environmental Science*, 2011, **4**, 2767–2773.

[21] M. P. Stracke, G. Ebeling, R. Cataluna and J. Dupont, *Energy & Fuels*, 2007, **21**, 1695–1698.

[22] A. Klerke, C. H. Christensen, J. K. Norskov and T. Vegge, *Journal of Materials Chemistry*, 2008, **18**, 2304–2310.

[23] U. Eberle, M. Felderhoff and F. Schueth, *Angewandte Chemie-International Edition*, 2009, **48**, 6608–6630.

[24] C. Fellay, P. J. Dyson and G. Laurenczy, *Angewandte Chemie-International Edition*, 2008, **47**, 3966–3968.

[25] L. J. Murray, M. Dinca and J. R. Long, *Chemical Society Reviews*, 2009, **38**, 1294–1314.

[26] A. C. Dillon and M. J. Heben, *Applied Physics A-Materials Science & Processing*, 2001, **72**, 133–142.

[27] J. Dong, X. Wang, H. Xu, Q. Zhao and J. Li, *International Journal of Hydrogen Energy*, 2007, **32**, 4998–5004.

[28] H. W. Langmi, A. Walton, M. M. Al-Mamouri, S. R. Johnson, D. Book, J. D. Speight, P. P. Edwards, I. Gameson, P. A. Anderson and I. R. Harris, *Journal of Alloys and Compounds*, 2003, **356**, 710–715.

[29] H. W. Langmi, D. Book, A. Walton, S. R. Johnson, M. M. Al-Mamouri, J. D. Speight, P. P. Edwards, I. R. Harris and P. A. Anderson, *Journal of Alloys and Compounds*, 2005, **404**, 637–642.

[30] K. L. Lim, H. Kazemian, Z. Yaakob and W. R. W. Daud, *Chemical Engineering & Technology*, 2010, **33**, 213–226.

[31] W. Grochala and P. P. Edwards, *Chemical Reviews*, 2004, **104**, 1283–1315.

[32] U. Eberle, G. Arnold and R. von Helmolt, *Journal of Power Sources*, 2006, **154**, 456–460.

[33] S. Orimo, Y. Nakamori, J. R. Eliseo, A. Zuettel and C. M. Jensen, *Chemical Reviews*, 2007, **107**, 4111–4132.

[34] A. Zuettel, A. Borgschulte and S. Orimo, *Scripta Materialia*, 2007, **56**, 823–828.

[35] P. P. Edwards, V. L. Kuznetsov and W. I. F. David, *Philosophical Transactions of the Royal Society A-Mathematical Physical and Engineering Sciences*, 2007, **365**, 1043–1056.

[36] C. Dresbach, A. Krombbolz, M. Ebert and J. Bagdahn, *Microsystem Technologies-Micro-and Nanosystems-Information Storage and Processing Systems*, 2006, **12**, 473–480.

[37] A. L. Kenward and W. E. Piers, *Angewandte Chemie-International Edition*, 2008, **47**, 38–41.

[38] R. H. Crabtree, *Energy & Environmental Science*, 2008, **1**, 134–138.

[39] C. H. Christensen, R. Z. Sorensen, T. Johannessen, U. J. Quaade, K. Honkala, T. D. Elmoe, R. Kohler and J. K. Norskov, *Journal of Materials Chemistry*, 2005, **15**, 4106–4108.

[40] L. Schlapbach and A. Zuttel, *Nature*, 2001, **414**, 353–358.

[41] B. Sakintuna, F. Lamari-Darkrim and M. Hirscher, *International Journal of Hydrogen Energy*, 2007, **32**, 1121–1140.

[42] T. B. Marder, *Angewandte Chemie-International Edition*, 2007, **46**, 8116–8118.

[43] F. H. Stephens, V. Pons and R. T. Baker, *Dalton Transactions*, 2007, 2613–2626.

[44] M. Latroche, *Journal of Physics and Chemistry of Solids*, 2004, **65**, 517–522.

[45] J. Graetz, *Chemical Society Reviews*, 2009, **38**, 73–82.

[46] S. R. Johnson, P. A. Anderson, P. P. Edwards, I. Gameson, J. W. Prendergast, M. Al-Mamouri, D. Book, I. R. Harris, J. D. Speight and A. Walton, *Chemical Communications*, 2005, 2823–2825.

[47] A. Zaluska, L. Zaluski and J. O. Strom-Olsen, *Journal of Alloys and Compounds*, 1999, **288**, 217–225.

[48] O. Friedrichs, F. Aguey-Zinsou, J. R. A. Fernandez, J. C. Sanchez-Lopez, A. Justo, T. Klassen, R. Bormann and A. Fernandez, *Acta Materialia*, 2006, **54**, 105–110.

[49] B. Bogdanovic and M. Schwickardi, *Journal of Alloys and Compounds*, 1997, **253**, 1–9.

[50] A. Zuttel, S. Rentsch, P. Fischer, P. Wenger, P. Sudan, P. Mauron and C. Emmenegger, *Journal of Alloys and Compounds*, 2003, **356**, 515–520.

[51] H. Q. Kou, X. Z. Xiao, J. X. Li, S. Q. Li, H. W. Ge, Q. D. Wang and L. X. Chen, *International Journal of Hydrogen Energy*, 2012, **37**, 1021–1026.

[52] T. Durojaiye, A. Ibikunle and A. J. Goudy, *International Journal of Hydrogen Energy*, 2010, **35**, 10329–10333.

[53] Z. T. Xiong, J. J. Hu, G. T. Wu and P. Chen, *Journal of Alloys and Compounds*, 2005, **395**, 209–212.

[54] Y. Liu, Z. Xiong, J. Hu, G. Wu, P. Chen, K. Murata and K. Sakata, *Journal of Power Sources*, 2006, **159**, 135–138.

[55] G. P. Meisner, M. L. Scullin, M. P. Balogh, F. E. Pinkerton and M. S. Meyer, *Journal of Physical Chemistry B*, 2006, **110**, 4186–4192.

[56] S. S. Srinivasan, M. U. Niemann, J. R. Hattrick-Simpers, K. McGrath, P. C. Sharma, D. Y. Goswami and E. K. Stefanakos, *International Journal of Hydrogen Energy*, 2010, **35**, 9646–9652.

[57] J. Yang, A. Sudik, D. J. Siegel, D. Halliday, A. Drews, R. O. Carter, C. Wolverton, G. J. Lewis, J. W. A. Sachtler, J. J. Low, S. A. Faheem, D. A. Lesch and V. Ozolins, *Angewandte Chemie-International Edition*, 2008, **47**, 882–887.

[58] J. J. Vajo and G. L. Olson, *Scripta Materialia*, 2007, **56**, 829–834.

[59] D. J. Siegel, C. Wolverton and V. Ozolins, *Physical Review B*, 2007, **76**, 134102: 1–6.

[60] Z. Z. Fang, X. D. Kang, P. Wang, H. W. Li and S. I. Orimo, *Journal of Alloys and Compounds*, 2010, **491**, L1–L4.

[61] A. F. Gross, J. J. Vajo, S. L. Van Atta and G. L. Olson, *Journal of Physical Chemistry C*, 2008, **112**, 5651–5657.

[62] D. T. Shane, R. L. Corey, C. McIntosh, L. H. Rayhel, R. C. Bowman, J. J. Vajo, A. F. Gross and M. S. Conradi, *Journal of Physical Chemistry C*, 2010, **114**, 4008–4014.

[63] H. Reardon, J. M. Hanlon, R. W. Hughes, A. Godula-Jopek, T. K. Mandal and D. H. Gregory, *Energy & Environmental Science*, 2012, **5**, 5951–5979.

[64] F. Y. Cheng, Z. L. Tao, J. Liang and J. Chen, *Chemical Communications*, 2012, **48**, 7334–7343.

[65] K. J. Fijakowski and W. Grochala, *Journal of Materials Chemistry*, 2009, **19**, 2043–2050.

[66] M. E. Bluhm, M. G. Bradley, R. Butterick, U. Kusari and L. G. Sneddon, *Journal of the American Chemical Society*, 2006, **128**, 7748–7749.

[67] A. Zecchina, S. Bordiga, J. G. Vitillo, G. Ricchiardi, C. Lamberti, G. Spoto, M. Bjorgen and K. P. Lillerud, *Journal of the American Chemical Society*, 2005, **127**, 6361–6366.

[68] Y. Liu, J. Zeng, J. Zhang, F. Xu and L. Sun, *International Journal of Hydrogen Energy*, 2007, **32**, 4005–4010.

[69] Y. Yan, X. Lin, S. Yang, A. J. Blake, A. Dailly, N. R. Champness, P. Hubberstey and M. Schröder, *Chemical Communications*, 2009, 1025–1027.

[70] A. G. Wong-Foy, A. J. Matzger and O. M. Yaghi, *Journal of the American Chemical Society*, 2006, **128**, 3494–3495.

[71] P. Benard and R. Chahine, *Langmuir*, 2001, **17**, 1950–1955.

[72] F. L. Darkrim, P. Malbrunot and G. P. Tartaglia, *International Journal of Hydrogen Energy*, 2002, **27**, 193–202.

[73] R. Stroebel, J. Garche, P. T. Moseley, L. Joerissen and G. Wolf, *Journal of Power Sources*, 2006, **159**, 781–801.

[74] E. Masika and R. Mokaya, *Journal of Physical Chemistry C*, 2012, **116**, 25734–25740.

[75] L. Regli, A. Zecchina, J. G. Vitillo, D. Cocina, G. Spoto, C. Lamberti, K. P. Lillerud, U. Olsbye and S. Bordiga, *Physical Chemistry Chemical Physics*, 2005, **7**, 3197–3203.

[76] N. P. Stadie, J. J. Vajo, R. W. Cumberland, A. A. Wilson, C. C. Ahn and B. Fultz, *Langmuir*, 2012, **28**, 10057–10063.

[77] E. Masika, R. A. Bourne, T. W. Chamberlain and R. Mokaya, *Acs Applied Materials & Interfaces*, 2013, **5**, 5639–5647.

[78] H. Li, M. Eddaoudi, M. O'Keeffe and O. M. Yaghi, *Nature*, 1999, **402**, 276–279.

[79] S. Cheng, S. Liu, Q. Zhao and J. Li, *Energy Conversion and Management*, 2009, **50**, 1314–1317.

[80] S. S. Han, H. Furukawa, O. M. Yaghi and W. A. Goddard, *Journal of the American Chemical Society*, 2008, **130**, 11580–11581.

[81] M. Duer, *Solid-State NMR Spectroscopy*, Blackwell Publishing, 2004, pp. 2–34.

[82] C. Slichter, *Principles of Magnetic Resonance*, 3rd edn., 1989, pp. 157–165.

[83] S. Brown, *MPAGS Postgraduate NMR Course: Density Operator Theory*, 2010.

[84] M. Bak, J. T. Rasmussen and N. C. Nielsen, *Journal of Magnetic Resonance*, 2000, **147**, 296–330.

[85] R. V. Pound, *Physical Review*, 1950, **79**, 685–702.

[86] M. Duer, *Introduction to Solid-State NMR Spectroscopy*, Blackwell Publishing, 1st edn., 2004, pp. 237–248.

[87] A. Abragam, *The Principles of Nuclear Magnetic Resonance*, Oxford University Press, 1st edn., 1961, pp. 232–246.

[88] G. E. Pake, *Journal of Chemical Physics*, 1948, **16**, 327–336.

[89] C. Slichter, *Principles of Magnetic Resonance*, 3rd edn., 1989, pp. 65–80.

[90] W. D. Knight, *Physical Review*, 1949, **76**, 1259–1260.

[91] C. Kittel, *Introduction to Solid State Physics*, J. Whiley & Sons, 8th edn., 2005, pp. 373–378.

[92] A. Abragam, *The Principles of Nuclear Magnetic Resonance*, Oxford University Press, 1st edn., 1961, pp. 199–206.

[93] F. Rushworth, *Nuclear Magnetic Resonance*, Gordon and Breach, 1st edn., 1973, pp. 145–150.

[94] N. Bloembergen, E. M. Purcell and R. V. Pound, *Physical Review*, 1948, **73**, 679–712.

[95] A. Horsewill, *MPAGS Postgraduate NMR Course: Nuclear Spin Relaxation*, 2010.

[96] C. Slichter, *Principles of Magnetic Resonance*, 3rd edn., 1989, pp. 190–198.

[97] P. Heitjans, A. Schirmer and S. Indris, in *Diffusion in Condensed Matter: Methods, Materials, Models*, ed. P. Heitjans and J. Karger, Berlin, 2005, book section 9, p. 367.

[98] G. Williams and D. C. Watts, *Transactions of the Faraday Society*, 1970, **66**, 80–85.

[99] D. L. Sidebottom, P. F. Green and R. K. Brow, *Journal of Non-Crystalline Solids*, 1995, **183**, 151–160.

[100] F. Alvarez, A. Alegria and J. Colmenero, *Physical Review B*, 1991, **44**, 7306–7312.

[101] J. Colmenero, A. Alegria, J. M. Alberdi, F. Alvarez and B. Frick, *Physical Review B*, 1991, **44**, 7321–7329.

[102] J. Bjorkstam and M. Villa, *Magnetic Resonance Review*, 1980, **6**, 1–57.

[103] M. Meyer, P. Maass and A. Bunde, *Physical Review Letters*, 1993, **71**, 573–576.

[104] A. Kuhn, M. Kunze, P. Sreeraj, H. D. Wiemhoefer, V. Thangadurai, M. Wilkening and P. Heitjans, *Solid State Nuclear Magnetic Resonance*, 2012, **42**, 2–8.

[105] V. Epp and M. Wilkening, *Physical Review B*, 2010, **82**, 020301: 1–4.

[106] A. Avogadro and M. Villa, *Journal of Chemical Physics*, 1977, **66**, 2359–2367.

[107] R. K. Wangsness and F. Bloch, *Physical Review*, 1953, **89**, 728–739.

[108] R. Kubo and K. Tomita, *Journal of the Physical Society of Japan*, 1954, **9**, 888–919.

[109] A. G. Redfield, *Ibm Journal of Research and Development*, 1957, **1**, 19–31.

[110] C. Slichter, *Principles of Magnetic Resonance*, 3rd edn., 1989, pp. 206–215.

[111] A. Abragam, *The Principles of Nuclear Magnetic Resonance*, Oxford University Press, 1st edn., 1961, pp. 289–298.

[112] E. R. Andrew and D. P. Tunstall, *Proceedings of the Physical Society of London*, 1961, **78**, 1–11.

[113] D. Brinkmann, M. Mali, J. Roos, R. Messer and H. Birli, *Physical Review B*, 1982, **26**, 4810–4825.

[114] C. P. Poole and H. A. Farach, *Relaxation in Magnetic Resonance*, Academic Press, 1st edn., 1971, pp. 44–53.

[115] C. Poole and H. Farach, *The Theory of Magnetic Resonance*, John Wiley & Sons, 1st edn., 1972, pp. 377 – 384.

[116] J. H. Vanvleck, *Physical Review*, 1948, **74**, 1168–1183.

[117] A. Abragam, *The Principles of Nuclear Magnetic Resonance*, Oxford University Press, 1st edn., 1961, pp. 97–113.

[118] R. Goc, *Solid State Nuclear Magnetic Resonance*, 1998, **13**, 55–61.

[119] J. J. Olivero and R. L. Longbothum, *Journal of Quantitative Spectroscopy & Radiative Transfer*, 1977, **17**, 233–236.

[120] S. R. Elliott, *The Physics And Chemistry Of Solids*, John Wiley & Sons, 1st edn., 1998, pp. 172–184.

[121] J. S. Blakemore, *Solid State Physics*, Cambridge University Press, 2nd edn., 1985, pp. 479–480.

[122] C. P. Poole and H. A. Farach, *Relaxation in Magnetic Resonance*, Academic Press, 1st edn., 1971, pp. 98–102.

[123] A. Abragam, *The Principles of Nuclear Magnetic Resonance*, Oxford University Press, 1st edn., 1961, pp. 424–467.

[124] R. Messer, H. Birli and K. Differt, *Journal of Physics C-Solid State Physics*, 1981, **14**, 2731–2746.

[125] R. R. Ernst and W. A. Anderson, *Review of Scientific Instruments*, 1966, **37**, 93–102.

[126] A. Powell, *Ph.D. thesis*, University of Nottingham, 2009.

[127] M. M. Maricq and J. S. Waugh, *Journal of Chemical Physics*, 1979, **70**, 3300–3316.

[128] E. R. Andrew, A. Bradbury and R. G. Eades, *Nature*, 1958, **182**, 1659.

[129] D. M. Brink and G. R. Satchler, *Angular Momentum*, Oxford Science, 3rd edn., 1993.

[130] A. L. Bloom and J. N. Shoolery, *Physical Review*, 1955, **97**, 1261–1265.

[131] C. Slichter, in *Principles of Magnetic Resonance*, Springer-Verlag, 3rd edn., 1989, ch. 8, pp. 409–416.

[132] E. L. Hahn, *Physical Review*, 1950, **80**, 580–601.

[133] J. G. Powles and P. Mansfield, *Physics Letters*, 1962, **2**, A961–A974.

[134] S. Antonijevic and S. Wimperis, *Journal of Magnetic Resonance*, 2003, **164**, 343–350.

[135] A. Pines, M. G. Gibby and J. S. Waugh, *Journal of Chemical Physics*, 1973, **59**, 569–995.

[136] S. R. Hartmann and E. L. Hahn, *Physical Review*, 1962, **128**, 2042–2053.

[137] G. Metz, X. L. Wu and S. O. Smith, *Journal of Magnetic Resonance Series A*, 1994, **110**, 219–227.

[138] A. Samoson, E. Lippmaa and A. Pines, *Molecular Physics*, 1988, **65**, 1013–1018.

[139] K. T. Mueller, B. Q. Sun, G. C. Chingas, J. W. Zwanziger, T. Terao and A. Pines, *Journal of Magnetic Resonance*, 1990, **86**, 470–487.

[140] A. Medek, J. S. Harwood and L. Frydman, *Journal of the American Chemical Society*, 1995, **117**, 12779–12787.

[141] J. P. Amoureux and M. Pruski, in *Encyclopedia of Nuclear Magnetic Resonance*, ed. D. M. Grant and R. K. Harris, Wiley, 2002, vol. 9, ch. Advances in MQMAS NMR, pp. 226 – 251.

[142] R. E. Ernst, G. Bodenhausen and A. Wokaun, in *Principles of Nuclear Magnetic Resonance in One and Two Dimensions*, Oxford Science, 1st edn., 1987, ch. 6.5.3, pp. 323–325.

[143] D. Massiot, B. Touzo, D. Trumeau, J. P. Coutures, J. Virlet, P. Florian and P. J. Grandinetti, *Solid State Nuclear Magnetic Resonance*, 1996, **6**, 73–83.

[144] J. D. van Beek, *Journal of Magnetic Resonance*, 2007, **187**, 19–26.

[145] Y. Millot and P. P. Man, *Solid State Nuclear Magnetic Resonance*, 2002, **21**, 21–43.

[146] L. A. O'Dell, *Progress in Nuclear Magnetic Resonance Spectroscopy*, 2011, **59**, 295–318.

[147] A. Lesage, D. Sakellariou, S. Hediger, B. Elena, P. Charmont, S. Steuernagel and L. Emsley, *Journal of Magnetic Resonance*, 2003, **163**, 105–113.

[148] E. Salager, R. S. Stein, S. Steuernagel, A. Lesage, B. Elena and L. Emsley, *Chemical Physics Letters*, 2009, **469**, 336–341.

[149] J. Z. Hu, J. H. Kwak, Z. G. Yang, X. F. Wan and L. L. Shaw, *Journal of Power Sources*, 2010, **195**, 3645–3648.

[150] R. L. Corey, D. T. Shane, R. C. Bowman and M. S. Conradi, *Journal of Physical Chemistry C*, 2008, **112**, 18706–18710.

[151] A. V. Soloninin, A. V. Skripov, A. L. Buzlukov and A. P. Stepanov, *Journal of Solid State Chemistry*, 2009, **182**, 2357–2361.

[152] S. K. Bhatia and A. L. Myers, *Langmuir*, 2006, **22**, 1688–1700.

[153] Y. Yan, I. Telepeni, S. Yang, X. Lin, W. Kockelmann, A. Dailly, A. J. Blake, W. Lewis, G. S. Walker, D. R. Allan, S. A. Barnett, N. R. Champness and M. Schröder, *Journal of the American Chemical Society*, 2010, **132**, 4092–4094.

[154] M. Dinca, A. Dailly, Y. Liu, C. M. Brown, D. A. Neumann and J. R. Long, *Journal of the American Chemical Society*, 2006, **128**, 16876–16883.

[155] D. F. Sun, S. Q. Ma, Y. X. Ke, D. J. Collins and H. C. Zhou, *Journal of the American Chemical Society*, 2006, **128**, 3896–3897.

[156] K. P. Prasanth, P. Rallapalli, M. C. Raj, H. C. Bajaj and R. V. Jasra, *International Journal of Hydrogen Energy*, 2011, **36**, 7594–7601.

[157] Y. W. Li and R. T. Yang, *Journal of the American Chemical Society*, 2006, **128**, 726–727.

[158] S. S. Han and I. Goddard, William A., *Journal of Physical Chemistry C*, 2008, **112**, 13431–13436.

[159] A. Mavrandonakis, E. Tylianakis, A. K. Stubos and G. E. Froudakis, *Journal of Physical Chemistry C*, 2008, **112**, 7290–7294.

[160] K. L. Mulfort and J. T. Hupp, *Inorganic Chemistry*, 2008, **47**, 7936–7938.

[161] K. L. Mulfort, T. M. Wilson, M. R. Wasielewski and J. T. Hupp, *Langmuir*, 2009, **25**, 503–508.

[162] F. Nouar, J. Eckert, J. F. Eubank, P. Forster and M. Eddaoudi, *Journal of the American Chemical Society*, 2009, **131**, 2864–2870.

[163] S. Yang, X. Lin, A. J. Blake, G. S. Walker, P. Hubberstey, N. R. Champness and M. Schröder, *Nature Chemistry*, 2009, **1**, 487–493.

[164] S. Yang, G. S. B. Martin, J. J. Titman, A. J. Blake, D. R. Allan, N. R. Champness and M. Schröder, *Inorganic Chemistry*, 2011, **50**, 9374–9384.

[165] X. Lin, I. Telepeni, A. J. Blake, A. Dailly, C. M. Brown, J. M. Simmons, M. Zoppi, G. S. Walker, K. M. Thomas, T. J. Mays, P. Hubberstey, N. R. Champness and M. Schröder, *Journal of the American Chemical Society*, 2009, **131**, 2159–2171.

[166] U. Olsher, R. M. Izatt, J. S. Bradshaw and N. K. Dalley, *Chemical Reviews*, 1991, **91**, 137–164.

[167] S. Yang, S. K. Callear, A. J. Ramirez-Cuesta, W. I. F. David, J. Sun, A. J. Blake, N. R. Champness and M. Schröder, *Faraday Discussions*, 2011, **151**, 19–36.

[168] R. B. Getman, J. H. Miller, K. Wang and R. Q. Snurr, *Journal of Physical Chemistry C*, 2011, **115**, 2066–2075.

[169] P. Mauron, F. Buchter, O. Friedrichs, A. Remhof, M. Bielmann, C. N. Zwicky and A. Zuettel, *Journal of Physical Chemistry B*, 2008, **112**, 906–910.

[170] T. Sun, J. Liu, Y. Jia, H. Wang, D. Sun, M. Zhu and X. Yao, *International Journal of Hydrogen Energy*, 2012, **37**, 18920–18926.

[171] M. Au, A. R. Jurgensen, W. A. Spencer, D. L. Anton, F. E. Pinkerton, S. J. Hwang, C. Kim and R. C. Bowman, *Journal of Physical Chemistry C*, 2008, **112**, 18661–18671.

[172] U. Bosenberg, J. W. Kim, D. Gosslar, N. Eigen, T. R. Jensen, J. M. B. von Colbe, Y. Zhou, M. Dahms, D. H. Kim, R. Gunther, Y. W. Cho, K. H. Oh, T. Klassen, R. Bormann and M. Dornheim, *Acta Materialia*, 2010, **58**, 3381–3389.

[173] J. Yang, A. Sudik and C. Wolverton, *Journal of Physical Chemistry C*, 2007, **111**, 19134–19140.

[174] J. J. Vajo, S. L. Skeith and F. Mertens, *Journal of Physical Chemistry B*, 2005, **109**, 3719–3722.

[175] X. F. Wan, T. Markmaitree, W. Osborn and L. L. Shaw, *Journal of Physical Chemistry C*, 2008, **112**, 18232–18243.

[176] T. E. C. Price, D. M. Grant, V. Legrand and G. S. Walker, *International Journal of Hydrogen Energy*, 2010, **35**, 4154–4161.

[177] J. P. Soulie, G. Renaudin, R. Cerny and K. Yvon, *Journal of Alloys and Compounds*, 2002, **346**, 200–205.

[178] M. R. Hartman, J. J. Rush, T. J. Udovic, R. C. Bowman and S. J. Hwang, *Journal of Solid State Chemistry*, 2007, **180**, 1298–1305.

[179] M. Matsuo, Y. Nakamori, S. Orimo, H. Maekawa and H. Takamura, *Applied Physics Letters*, 2007, **91**, 224103: 1–3.

[180] S. K. Callear, E. A. Nickels, M. O. Jones, M. Matsuo, S. I. Orimo, P. P. Edwards and W. I. F. David, *Journal of Materials Science*, 2011, **46**, 566–569.

[181] G. W. Ossman and J. W. McGrath, *Journal of Chemical Physics*, 1967, **47**, 5452–5453.

[182] T. Tsang and T. C. Farrar, *Journal of Chemical Physics*, 1969, **50**, 3498–3502.

[183] A. V. Skripov, A. V. Soloninin, Y. Filinchuk and D. Chernyshov, *Journal of Physical Chemistry C*, 2008, **112**, 18701–18705.

[184] A. Remhof, Z. Lodziana, P. Martelli, O. Friedrichs, A. Zuettel, A. V. Skripov, J. P. Embs and T. Straessle, *Physical Review B*, 2010, **81**, 214304: 1 – 9.

[185] F. Buchter, Z. Lodziana, P. Mauron, A. Remhof, O. Friedrichs, A. Borgschulte, A. Zuettel, D. Sheptyakov, T. Straessle and A. J. Ramirez-Cuesta, *Physical Review B*, 2008, **78**, 094302: 1–9.

[186] V. P. Tarasov, S. I. Bakum, V. I. Privalov and A. A. Shamov, *Zhurnal Neorganicheskoi Khimii*, 1990, **35**, 1815–1819.

[187] T. Ikeshoji, E. Tsuchida, T. Morishita, K. Ikeda, M. Matsuo, Y. Kawazoe and S. Orimo, *Physical Review B*, 2011, **83**, 144301: 1–5.

[188] D. T. Shane, R. C. Bowman and M. S. Conradi, *Journal of Physical Chemistry C*, 2009, **113**, 5039–5042.

[189] K. Hoang and C. G. Van de Walle, *International Journal of Hydrogen Energy*, 2012, **37**, 5825–5832.

[190] S. Hao and D. S. Sholl, *Physical Chemistry Chemical Physics*, 2009, **11**, 11106–11109.

[191] A. Borgschulte, A. Zuttel, P. Hug, A. M. Racu and J. Schoenes, *Journal of Physical Chemistry A*, 2008, **112**, 4749–4753.

[192] D. Bork and P. Heitjans, *Journal of Physical Chemistry B*, 2001, **105**, 9162–9170.

[193] M. Wilkening, D. Bork, S. Indris and P. Heitjans, *Physical Chemistry Chemical Physics*, 2002, **4**, 3246–3251.

[194] T. E. C. Price, *Ph.D. thesis*, University of Nottingham, 2010.

[195] V. Berube, G. Radtke, M. Dresselhaus and G. Chen, *International Journal of Energy Research*, 2007, **31**, 637–663.

[196] M. Witschas and H. Eckert, *Journal of Physical Chemistry A*, 1999, **103**, 10764–10775.

[197] P. Heitjans and S. Indris, *Journal of Physics-Condensed Matter*, 2003, **15**, R1257–R1289.

[198] J. E. Espidel, R. K. Harris and K. Wade, *Magnetic Resonance in Chemistry*, 1994, **32**, 166–172.

[199] R. Winter and P. Heitjans, *Journal of Physical Chemistry B*, 2001, **105**, 6108–6115.

[200] L. L. Shaw, X. F. Wan, J. Z. Hu, J. H. Kwak and Z. G. Yang, *Journal of Physical Chemistry C*, 2010, **114**, 8089–8098.

[201] J. Guerrero-Paz and D. Jaramillo-Vigueras, *Nanostructured Materials*, 1999, **11**, 1123–1132.

[202] A. Weibel, R. Bouchet, F. Boulc'h and P. Knauth, *Chemistry of Materials*, 2005, **17**, 2378–2385.

[203] B. E. Warren, *X-Ray Diffraction*, Dover Publications, 2nd edn., 1990, pp. 251–275.

[204] P. Heitjans and S. Indris, *Journal of Materials Science*, 2004, **39**, 5091–5096.

[205] S. Indris, R. Amade, P. Heitjans, M. Finger, A. Haeger, D. Hesse, W. Grunert, A. Borger and K. D. Becker, *Journal of Physical Chemistry B*, 2005, **109**, 23274–23278.

[206] C. E. Krill and R. Birringer, *Philosophical Magazine A-Physics of Condensed Matter Structure Defects and Mechanical Properties*, 1998, **77**, 621–640.

[207] H. P. Klug and L. E. Alexander, *X-Ray Diffraction Procedures*, John Wiley & Sons, 2nd edn., 1974, pp. 642–708.

[208] Y. Zhong, D. Ping, X. Song and F. Yin, *Journal of Alloys and Compounds*, 2009, **476**, 113–117.

[209] D. F. Lee, *Ph.D. thesis*, Chapt 2, University of Nottingham, 2010.

[210] K. Schmidt-Rohr and H. W. Spiess, *Multidimensional Solid-State NMR and Polymers*, Academic Press, 2nd edn., 1994, pp. 411–423.

[211] J. Guerrero-Paz and D. Jaramillo-Vigueras, *Nanostructured Materials*, 1998, **10**, 1209–1222.

[212] R. A. Varin, M. Jang and M. Polanski, *Journal of Alloys and Compounds*, 2010, **491**, 658–667.

[213] L. L. Shaw, R. Ren, T. Markmaitree and W. Osborn, *Journal of Alloys and Compounds*, 2008, **448**, 263–271.

[214] U. Bosenberg, D. B. Ravnsbaek, H. Hagemann, V. D'Anna, C. B. Minella, C. Pistidda, W. van Beek, T. R. Jensen, R. Bormann and M. Dornheim, *Journal of Physical Chemistry C*, 2010, **114**, 15212–15217.

[215] F. E. Piinkerton, M. S. Meyer, G. P. Meisner, M. P. Balogh and J. J. Vajo, *Journal of Physical Chemistry C*, 2007, **111**, 12881–12885.

[216] T. E. C. Price, D. M. Grant, I. Telepeni, X. B. Yu and G. S. Walker, *Journal of Alloys and Compounds*, 2009, **472**, 559–564.

[217] H. Kou, X. Xiao, L. Chen, S. Li and Q. Wang, *Transactions of Nonferrous Metals Society of China*, 2011, **21**, 1040–1046.

[218] J. F. Mao, Z. Wu, T. J. Chen, B. C. Weng, N. X. Xu, T. S. Huang, Z. P. Guo, H. K. Liu, D. M. Grant, G. S. Walker and X. B. Yu, *Journal of Physical Chemistry C*, 2007, **111**, 12495–12498.

[219] U. Boesenberg, S. Doppiu, L. Mosegaard, G. Barkhordarian, N. Eigen, A. Borgschulte, T. R. Jensen, Y. Cerenius, O. Gutfleisch, T. Klassen, M. Dornheim and R. Bormann, *Acta Materialia*, 2007, **55**, 3951–3958.

[220] X. B. Yu, D. M. Grant and G. S. Walker, *Chemical Communications*, 2006, 3906–3908.

[221] G. S. Walker, D. M. Grant, T. C. Price, X. B. Yu and V. Legrand, *Journal of Power Sources*, 2009, **194**, 1128–1134.

[222] L. A. Zeng, H. Miyaoka, T. Ichikawa and Y. Kojima, *Journal of Physical Chemistry C*, 2010, **114**, 13132–13135.

[223] T. E. C. Price, D. M. Grant, D. Weston, T. Hansen, L. M. Arnbjerg, D. B. Ravnsbak, T. R. Jensen and G. S. Walker, *Journal of the American Chemical Society*, 2011, **133**, 13534–13538.

[224] L. Mosegaard, B. Moller, J. E. Jorgensen, U. Bosenberg, M. Dornheim, J. C. Hanson, Y. Cerenius, G. Walker, H. J. Jakobsen, F. Besenbacher and T. R. Jensen, *Journal of Alloys and Compounds*, 2007, **446**, 301–305.

[225] S. J. Hwang, R. C. Bowman, J. W. Reiter, J. Rijssenbeek, G. L. Soloveichik, J. C. Zhao, H. Kabbour and C. C. Ahn, *Journal of Physical Chemistry C*, 2008, **112**, 3164–3169.

[226] S. Orimo, Y. Nakamori, N. Ohba, K. Miwa, M. Aoki, S. Towata and A. Zuttel, *Applied Physics Letters*, 2006, **89**, 021920: 1–3.

[227] N. Ohba, K. Miwa, M. Aoki, T. Noritake, S. Towata, Y. Nakamori, S. Orimo and A. Zuettel, *Physical Review B*, 2006, **74**, 075110: 1–7.

[228] V. Ozolins, E. H. Majzoub and C. Wolverton, *Journal of the American Chemical Society*, 2009, **131**, 230–237.

[229] J. Z. Hu, J. H. Kwak, Z. G. Yang, X. F. Wan and L. L. Shaw, *Applied Physics Letters*, 2009, **94**, 141905: 1–3.

[230] M. Meggouh, *Ph.D. thesis*, University of Nottingham, 2013.

[231] K. Brinkman, J. Gray, B. Hardy and D. Anton, *The Hydrolysis and Oxidation Behavior of Lithium Borohydride and Magnesium Hydride Determined by Calorimetry*, 2011, `http://sti.srs.gov/fulltext/WSRC-STI-2008-00155.pdf`.

[232] H. Noth and B. Wrackmeyer, *Nuclear Magnetic Resonance Spectroscopy of Boron Compounds*, Springer-Verlag, 1978, vol. 14.

[233] T. J. Bastow and S. Celotto, *Solid State Nuclear Magnetic Resonance*, 2009, **35**, 217–222.

[234] A. P. Gerashenko, K. N. Mikhalev, S. V. Verkhovskii, A. E. Karkin and B. N. Goshchitskii, *Physical Review B*, 2002, **65**, 132506: 1–4.

[235] Y. L. Pascal and O. Convert, *Magnetic Resonance in Chemistry*, 1991, **29**, 308–315.

[236] N. Greenwood and A. Earnshaw, *Chemistry of the Elements*, Butterworth - Heinemann, 2nd edn., 1997.

[237] G. F. Lynch, M. J. Stott and A. R. Williams, *Solid State Communications*, 1973, **13**, 1675–1679.

[238] D. H. Gregory, *Chemical Record*, 2008, **8**, 229–239.

[239] D. H. Gregory, *Journal of Materials Chemistry*, 2008, **18**, 2321–2330.

[240] P. Chen, Z. T. Xiong, J. Z. Luo, J. Y. Lin and K. L. Tan, *Nature*, 2002, **420**, 302–304.

[241] F. W. Dafert and R. Miklauz, *Monatshefte für Chemie und verwandte Teile anderer Wissenschaften*, 1910, **31**, 981–996.

[242] P. Chen, Z. T. Xiong, J. Z. Luo, J. Y. Lin and K. L. Tan, *Journal of Physical Chemistry B*, 2003, **107**, 10967–10970.

[243] Y. H. Hu and E. Ruckenstein, *Journal of Physical Chemistry A*, 2003, **107**, 9737–9739.

[244] S. Isobe, T. Ichikawa, S. Hino and H. Fujii, *Journal of Physical Chemistry B*, 2005, **109**, 14855–14858.

[245] T. Ichikawa, N. Hanada, S. Isobe, H. Y. Leng and H. Fujii, *Journal of Physical Chemistry B*, 2004, **108**, 7887–7892.

[246] G. P. Meisner, F. E. Pinkerton, M. S. Meyer, M. P. Balogh and M. D. Kundrat, *Journal of Alloys and Compounds*, 2005, **404**, 24–26.

[247] F. E. Pinkerton, G. P. Meisner, M. S. Meyer, M. P. Balogh and M. D. Kundrat, *Journal of Physical Chemistry B*, 2005, **109**, 6–8.

[248] A. Borgschulte, M. O. Jones, E. Callini, B. Probst, S. Kato, A. Zuttel, W. I. F. David and S. Orimo, *Energy & Environmental Science*, 2012, **5**, 6823–6832.

[249] S. Orimo, Y. Nakamori, G. Kitahara, K. Miwa, N. Ohba, T. Noritake and S. Towata, *Applied Physics A-Materials Science & Processing*, 2004, **79**, 1765–1767.

[250] T. Ichikawa, S. Isobe, N. Hanada and H. Fujii, *Journal of Alloys and Compounds*, 2004, **365**, 271–276.

[251] F. E. Pinkerton, *Journal of Alloys and Compounds*, 2005, **400**, 76–82.

[252] J. Z. Hu, J. H. Kwak, Z. Yang, W. Osborn, T. Markmaitree and L. L. Shaw, *Journal of Power Sources*, 2008, **181**, 116–119.

[253] H. Wu, W. Zhou, K. Wang, T. J. Udovic, J. J. Rush, T. Yildirim, L. A. Bendersky, A. F. Gross, S. L. Van Atta, J. J. Vajo, F. E. Pinkerton and M. S. Meyer, *Nanotechnology*, 2009, **20**, 204002: 1–7.

[254] Y. Nakamori, T. Yamagishi, M. Yokoyama and S. Orimo, *Journal of Alloys and Compounds*, 2004, **377**, L1–L3.

[255] L. Xie, J. Zheng, Y. Liu, Y. Li and X. Li, *Chemistry of Materials*, 2008, **20**, 282–286.

[256] A. D. Smigelskas and E. O. Kirkendall, *Transactions of the American Institute of Mining and Metallurgical Engineers*, 1947, **171**, 130–142.

[257] E. Zintl and G. Brauer, *Zeitschrift Für Elektrochemie Und Angewandte Physikalische Chemie*, 1935, **41**, 102–107.

[258] A. Rabenau and H. Schulz, *Journal of the Less-Common Metals*, 1976, **50**, 155–159.

[259] H. Schulz and K. Schwarz, *Acta Crystallographica Section A*, 1978, **34**, 999–1005.

[260] K. Differt and R. Messer, *Journal of Physics C-Solid State Physics*, 1980, **13**, 717–724.

[261] M. Mali, J. Roos and D. Brinkmann, *Physical Review B*, 1987, **36**, 3888–3890.

[262] H. J. Beister, S. Haag, R. Kniep, K. Strossner and K. Syassen, *Angewandte Chemie-International Edition in English*, 1988, **27**, 1101–1103.

[263] A. Huq, J. W. Richardson, E. R. Maxey, D. Chandra and W. Chien, *Journal of Alloys and Compounds*, 2007, **436**, 256–260.

[264] D. H. Gregory, P. M. O'Meara, A. G. Gordon, J. P. Hodges, S. Short and J. D. Jorgensen, *Chemistry of Materials*, 2002, **14**, 2063–2070.

[265] B. A. Boukamp and R. A. Huggins, *Physics Letters A*, 1976, **58**, 231–233.

[266] D. Brinkmann, W. Freudenreich and J. Roos, *Solid State Communications*, 1978, **28**, 233–237.

[267] U. V. Alpen, A. Rabenau and G. H. Talat, *Applied Physics Letters*, 1977, **30**, 621–623.

[268] H. Schulz and K. H. Thiemann, *Acta Crystallographica Section A*, 1979, **35**, 309–314.

[269] J. Wahl, *Solid State Communications*, 1979, **29**, 485–490.

[270] M. F. Bell, A. Breitschwerdt and U. Vonalpen, *Materials Research Bulletin*, 1981, **16**, 267–272.

[271] M. Dixon and M. J. Gillan, *Journal of Physics C-Solid State Physics*, 1978, **11**, L165–L169.

[272] T. Lapp, S. Skaarup and A. Hooper, *Solid State Ionics*, 1983, **11**, 97–103.

[273] M. L. Wolf, J. R. Walker and C. R. A. Catlow, *Journal of Physics C-Solid State Physics*, 1984, **17**, 6623–6634.

[274] M. L. Wolf and C. R. A. Catlow, *Journal of Physics C-Solid State Physics*, 1984, **17**, 6635–6648.

[275] D. H. Gregory and A. G. Gordon, *International patent*, 2004.

[276] A. G. Gordon, N. Tapia-Ruiz, C. M. Jewell, H. K. Edwards, C. W. Dunnill, J. M. Blackman, C. P. Snape, P. D. Brown, I. McLaren, E. Bichoutskaia, J. J. Titman and D. H. Gregory, *In preparation*.

[277] R. S. Wagner and W. C. Ellis, *Applied Physics Letters*, 1964, **4**, 89–90.

[278] L. Guo and R. N. Singh, *Nanotechnology*, 2008, **19**, 065601: 1–6.

[279] R. Gedye, F. Smith, K. Westaway, H. Ali, L. Baldisera, L. Laberge and J. Rousell, *Tetrahedron Letters*, 1986, **27**, 279–282.

[280] N. Tapia-Ruiz, G. S. B. Martin, I. McLaren, J. J. Titman and D. H. Gregory, *In preparation*.

[281] N. Tapia-Ruiz, *Ph.D. thesis*, University of Glasgow, 2013.

[282] C. O. Kappe, *Angewandte Chemie-International Edition*, 2004, **43**, 6250–6284.

[283] P. J. Haigh, R. A. Forman and R. C. Frisch, *Journal of Chemical Physics*, 1966, **45**, 812–816.

[284] R. Gomez, *Ph.D. thesis*, University of Nottingham, 2005.

[285] D. M. Follstaedt and R. M. Biefeld, *Physical Review B*, 1978, **18**, 5928–5937.

[286] W. I. F. David, M. O. Jones, D. H. Gregory, C. M. Jewell, S. R. Johnson, A. Walton and P. P. Edwards, *Journal of the American Chemical Society*, 2007, **129**, 1594–1601.

[287] P. A. Huhn, M. Dornheim, T. Klassen and R. Bormann, *Journal of Alloys and Compounds*, 2005, **404**, 499–502.

[288] H. Jacobs and R. Juza, *Zeitschrift Für Anorganische Und Allgemeine Chemie*, 1972, **391**, 271.

[289] M. Nagib and H. Jacobs, *Atomkernenergie*, 1973, **21**, 275–278.

[290] J. B. Yang, X. D. Zhou, Q. Cai, W. J. James and W. B. Yelon, *Applied Physics Letters*, 2006, **88**, 041914: 1–3.

[291] M. H. Sorby, Y. Nakamura, H. W. Brinks, T. Ichikawa, S. Hino, H. Fujii and B. C. Hauback, *Journal of Alloys and Compounds*, 2007, **428**, 297–301.

[292] R. Juza and K. Opp, *Zeitschrift Für Anorganische Und Allgemeine Chemie*, 1951, **266**, 325–330.

[293] K. Ohoyama, Y. Nakamori, S. Orimo and K. Yamada, *Journal of the Physical Society of Japan*, 2005, **74**, 483–487.

[294] T. Noritake, H. Nozaki, M. Aoki, S. Towata, G. Kitahara, Y. Nakamori and S. Orimo, *Journal of Alloys and Compounds*, 2005, **393**, 264–268.

[295] M. P. Balogh, C. Y. Jones, J. F. Herbst, L. G. Hector and M. Kundrat, *Journal of Alloys and Compounds*, 2006, **420**, 326–336.

[296] J. F. Herbst and L. G. Hector, *Physical Review B*, 2005, **72**, 125120: 1–8.

[297] T. Mueller and G. Ceder, *Physical Review B*, 2006, **74**, 134104: 1–7.

[298] B. Magyari-Kope, V. Ozolins and C. Wolverton, *Physical Review B*, 2006, **73**, 220101: 1–4.

[299] C. J. Zhang, M. Dyer and A. Alavi, *Journal of Physical Chemistry B*, 2005, **109**, 22089–22091.

[300] G. A. Luduena, M. Wegner, L. Bjalie and D. Sebastiani, *Chemphyschem*, 2010, **11**, 2353–2360.

[301] T. Mueller and G. Ceder, *Physical Review B*, 2010, **82**, 174307: 1–7.

[302] G. Miceli, M. Ceriotti, M. Bernasconi and M. Parrinello, *Physical Review B*, 2011, **83**, 054119: 1–5.

[303] J. Yang, J. Lamsal, Q. Cai, W. B. Yelon and W. J. James, *MRS Proceedings*, 2008, **1098**, 041914: 1–3.

[304] R. A. Forman, *Journal of Chemical Physics*, 1971, **55**, 1987–1988.

[305] C. M. Araujo, A. Blomqvist, R. H. Scheicher, P. Chen and R. Ahuja, *Physical Review B*, 2009, **79**, 4.

[306] M. Bonnet, M. Iannuzzi, D. Sebastiani and J. Hutter, *Journal of Physical Chemistry C*, 2012, **116**, 18577–18583.

[307] A. Blomqvist, C. M. Araujo, R. H. Scheicher, P. Srepusharawoot, W. Li, P. Chen and R. Ahuja, *Physical Review B*, 2010, **82**, 024304: 1–5.

[308] T. W. D. Farley, W. Hayes, S. Hull, M. T. Hutchings and M. Vrtis, *Journal of Physics-Condensed Matter*, 1991, **3**, 4761–4781.

[309] M. Hayoun, M. Meyer and A. Denieport, *Acta Materialia*, 2005, **53**, 2867–2874.

[310] W. Li, G. T. Wu, Z. T. Xiong, Y. P. Feng and P. Chen, *Physical Chemistry Chemical Physics*, 2012, **14**, 1596–1606.

[311] B. A. Boukamp and R. A. Huggins, *Physics Letters A*, 1979, **72**, 464–466.

[312] A. Huq, J. W. Richardson, E. R. Maxey, D. Chandra and W. Chien, *Journal of Physical Chemistry C*, 2007, **111**, 10712–10717.

[313] E. Weidner, D. J. Bull, I. L. Shabalin, S. G. Keens, M. T. F. Telling and D. K. Ross, *Chemical Physics Letters*, 2007, **444**, 76–79.

[314] D. J. Bull, E. Weidner, I. L. Shabalin, M. T. F. Telling, C. M. Jewell, D. H. Gregory and D. K. Ross, *Physical Chemistry Chemical Physics*, 2010, **12**, 2089–2097.

[315] D. J. Bull, N. Sorbie, G. Baldissin, D. Moser, M. T. F. Telling, R. I. Smith, D. H. Gregory and D. K. Ross, *Faraday Discussions*, 2011, **151**, 263–270.

[316] R. Marx, *Zeitschrift Für Anorganische Und Allgemeine Chemie*, 1997, **623**, 1912–1916.

[317] G. Miceli, C. S. Cucinotta, M. Bernasconi and M. Parrinello, *Journal of Physical Chemistry C*, 2010, **114**, 15174–15183.

[318] G. Miceli and M. Bernasconi, *Journal of Physical Chemistry C*, 2011, **115**, 13496–13501.

[319] K. Hoang, A. Janotti and C. G. van de Walle, *Physical Review B*, 2012, **85**, 064115: 1–12.

[320] N. Tapia-Ruiz, G. S. B. Martin, J. J. Titman and D. H. Gregory, *In preparation*.

[321] C. Zamfirescu and I. Dincer, *Journal of Power Sources*, 2008, **185**, 459–465.

[322] S. J. Clark, M. D. Segall, C. J. Pickard, P. J. Hasnip, M. J. Probert, K. Refson and M. C. Payne, *Zeitschrift Für Kristallographie*, 2005, **220**, 567–570.

Appendix A: Processing MQMAS Data

MQMAS data was acquired and processed according to the scheme laid out by Massiot *et al.*[143]. The steps in the processing are as follows:

- The 2D dataset was split up into echo (S_E) and anti-echo (S_A) parts according to:

$$\begin{aligned} S_E(t_1,t_2) &= S_x(t_1,t_2) - iS_y(t_1,t_2) \\ S_A(t_1,t_2) &= S_x(t_1,t_2) + iS_y(t_1,t_2) \end{aligned} \tag{1}$$

  where S_y was phase shifted by $90^o/|p|$ relative to S_x with $|p| = 3$ for triple quantum excitation by phase cycling the excitation pulse during the experiment.

- S_E and S_A are then separately processed according to the following:
  - In the direct dimension:
    - The data was DC offset corrected, apodized and zerofilled before complex FT. 0^{th} order phasing was applied and 1st order also if necessary (phasing should always produce 'in phase', not 'anti-phase' spectra).
    - The data was sheared by the factor k = +0.7778 for the S_E and -0.7778 for S_A. (Note that for triple quantum excitation for $I = \frac{3}{2}$, $m = 3$ and $k = 7/9 = 0.7777...$ where k is often also called the MQMAS gradient.)
  - In the indirect dimension:
    - DC offset corrected, apodized and zerofilled before complex FT.
    - No phasing or shearing occurs in the indirect dimension.

– After processing S_A, this data set should be reversed in ω_1 (the indirect dimension after shearing) to $-\omega_1$.

– The separately processed data sets are then added:

$$S(\omega_1, \omega_2) = S_E(\omega_1, \omega_2) + S_A(-\omega_1, \omega_2) \tag{2}$$

Appendix B: Low-Dimensional Nanostructures of Lithium Nitride (*In preparation*)

Science AAAS

Submitted Manuscript: Confidential 27 December 2011

Low-dimensional nanostructures of lithium nitride

Alexandra G. Gordon[1], Nuria Tapia-Ruiz[2], Catherine M. Jewell[2], Hannah K. Edwards[1,3], Charles W. Dunnill[2], James M. Blackman[4], Colin P. Snape[4], Paul D. Brown[3], Ian McLaren[5], Elena Bichoutskaia[1], Jeremy J. Titman[1] and Duncan H. Gregory[2*].

[1] School of Chemistry, University of Nottingham, University Park, Nottingham NG7 2RD, UK

[2] WestCHEM, School of Chemistry, University of Glasgow, Glasgow G12 8QQ, UK.

[3] Department of Mechanical, Materials and Manufacturing Engineering, University of Nottingham, University Park, Nottingham NG7 2RD, UK.

[4] Department of Chemical and Environmental Engineering, University of Nottingham, University Park, Nottingham NG7 2RD, UK.

[5] School of Physics and Astronomy, University of Glasgow, Glasgow G12 8QQ, UK.

*Correspondence to: duncan.gregory@glasgow.ac.uk.

†Additional author notes should be indicated with symbol (for example, for current addresses).

One Sentence Summary:

Li_3N nanostructures demonstrating outstanding H_2 sorption and Li^+ ion transport assemble by analogy to those constructed from graphene or BN layers.

Abstract:

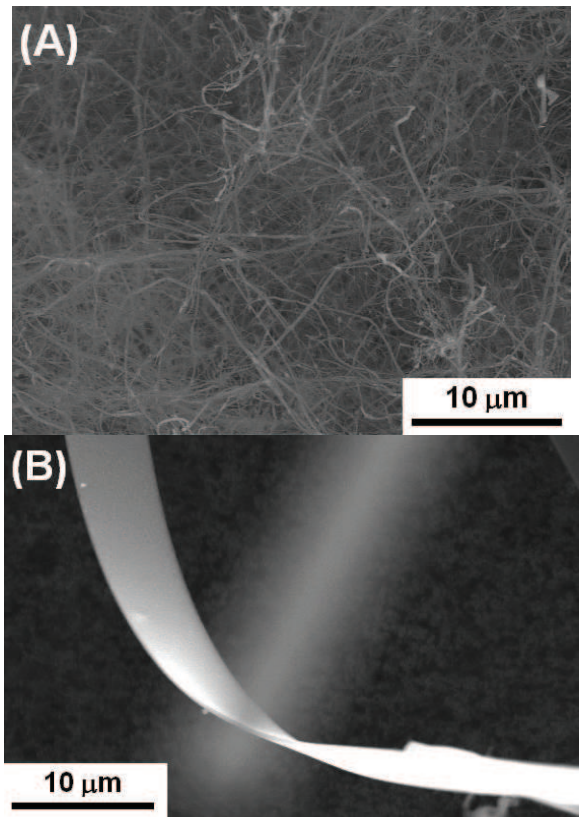
Given the similarities in symmetry and dimensionality in the structures of graphite, boron nitride and lithium nitride (Li_3N), we postulated that equivalent 1D (wire/fibre) and 2D (sheet/ribbon) nanostructures might be accessible for the latter compound. Given also certain similarities between the physical properties of the elemental components of lithium nitride and gallium nitride, we also postulated that low dimensional nanostructures might be grown by comparable methods and mechanisms. We demonstrate here that 1D and 2D Li_3N nanostructures can be grown at high temperature and reduced pressure. The structures are composed of assemblies of "sp^2-like" Li -N layers resembling those in C and BN. Experimental and computational data suggest that the electronic and optical properties can be tuned as a function of the nanostructure dimensions. Further Li^+ (and by inference H^+) diffusion is enhanced in these nanomaterials, yielding materials with high Li^+ ion mobility and outstanding hydrogen sorption kinetics.

Main text:

As the only stable binary compound formed between an alkali metal and nitrogen, lithium nitride (Li_3N) is not only unique but also a material with remarkable properties and a basis for energy applications involving the storage of lithium and hydrogen. It has also been proposed as a means of converting CO_2 into useful products (*1*), as the electron injection layer (EIL) in organic light emitting diodes (OLEDs) (*2*) and as an unusual reducing agent in preparative organic and organometallic chemistry (*3*). As a hydrogen store, Li_3N can accommodate up to 10.4 wt% H_2 reversibly (*4*). In the solid state, hydrogen uptake and release kinetics are mediated by the H^+ and Li^+ transport properties and Li_3N was originally proposed for use as an electrolyte in all-solid-state Li^+ ion batteries given its exceptional ionic conductivity at room temperature (*ca.* 10^{-4} *S* cm^{-1}) (*5*,*6*). This value exceeds that found in other potential solid electrolytes such as oxides $La_{0.5}Li_{0.5}TiO_3$ (2 x 10^{-5} S cm^{-1}) (*7*) and $Li_{3.5}V_{0.5}Ge_{0.5}O_4$ (10^{-5} S cm^{-1}) (*8*) or glass ceramics *e.g.* $Li_7P_3S_{11}$ (3.2 x 10^{-3} S cm^{-1}) (*9*). Moreover, when doped with transition metals (*e.g.* Mn, Fe, Co, Ni, Cu) (*10,11,12*,*13*,*14*), Li_3N can be employed as an anode in secondary batteries with 2-3 times the theoretical capacity of lithiated graphite, C_6Li (372 mA h g^{-1}) (*15*). For hydrogen storage applications, slow kinetics for H_2 sorption and high (de)hydrogenation temperatures are the primary hurdles to overcome before the Li-N-H system can be exploited commercially. Following a materials design principle drawn from analogies to graphite and boron nitride, here we present the synthesis of low dimensional (1D and 2D) Li_3N nanostructures and their subsequent characterization. From a combination of experiments and calculations, we demonstrate how modifications to electronic structure, enhancement of surface area and reduction of diffusion lengths lead to dramatic changes in hydrogen sorption, ionic and electronic transport behaviour. To our knowledge, these are the first examples of anisotropic nanomaterials formed from an s-block element and nitrogen.

Nanostructures of Li_3N can be grown following the heating and cooling of the bulk nitride powder under a reduced pressure of nitrogen (Supplementary Materials; Materials and Methods). Powder X-ray diffraction (PXD) data for the fine powder product matches to hexagonal α-Li_3N (*P*6/*mmm*; *a* = 3.656(2) Å; *c* = 3.868(4) Å) (Supplementary Materials; Fig. S1), with refined cell parameters in close agreement to the bulk material (*16*). The morphology of the nanostructured material can be tailored by controlling the preparative conditions, *e.g.* mass of the starting material, temperature and temperature gradient. At 700 °C, long nanofibers with diameters

ranging from 200 nm to 2 μm and lengths in excess of 10 μm were produced (Fig. 1A). At 800 ºC, however, the process yielded long, flat ribbons with lengths in excess of 100 μm, widths of 2 μm or more and thicknesses of the order of 10 - 100 nm (Fig. 1B). Altering the temperature gradient combined with employing a higher reaction temperature (750 °C; supplementary information) had a dramatic effect on the morphology of the products, leading to a mixture of straight and zig-zag structures (Fig. 1C).



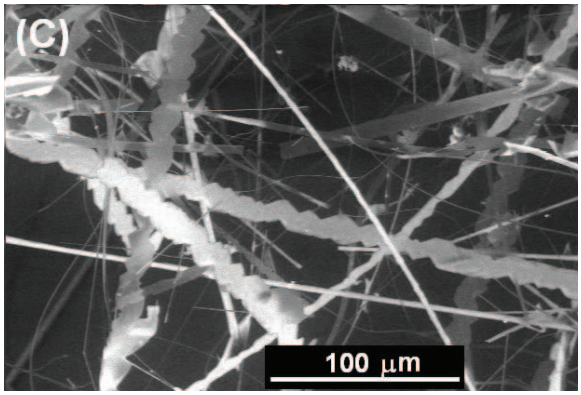


Fig. 1. SEM images illustrating the effect of the synthetic conditions on product morphology to yield: (a) Li_3N nanofibers at low temperature (700 °C) and pressure; (b) High magnification image of Li_3N nanoribbons at higher temperature (800 °C) and low pressure; (c) Li_3N nanofibers and zig-zag ribbons produced at an intermediate temperature (750 °C), with a variable temperature gradient across the volume of the reaction vessel and at low pressure.

One might rationalise the growth of the 1D nanostructures in terms of a likely self-assisted vapour-liquid-solid (VLS) mechanism. Under vacuum Li_3N will decompose at a temperature below the ambient pressure decomposition temperature (815 °C; $\Delta H_{(298K)}$= -171.3 +/- 7.7 kJ mol^{-1}) (17, 18) (equation 1), forming Li droplets. These Li seeds would act as nucleation sites for the $N_{2(g)}$ species, which supersaturate the Li droplets and eventually lead to anisotropic growth and Li_3N fiber formation.

$$2\ Li_3N_{(s)} \rightarrow 6\ Li_{(l)} + N_{2(g)} \qquad (1)$$

EDS spectra reveal peaks only from nitrogen (and oxygen from brief air exposure) consistent with single phase Li_3N (Supplementary Materials; Fig. S2). The absence of metal impurity peaks corroborates a self-assisted growth mechanism. Stach *et al.* previously demonstrated "self-catalytic" growth of GaN nanowires when heating a GaN thin-film under a vacuum of 10^{-7} torr. Ga droplets and gallium/nitrogen vapour species combine for subsequent GaN nanowire nucleation and growth producing the pure semiconducting product (*19*). The comparison to GaN is apposite in that both binary nitrides are formed from low melting point metals. We attribute

the zig-zag morphology obtained in higher temperature syntheses to a repetitive switch of the growth direction in the wire due to the extreme temperature differences within the vessel, inducing faults alternating along the *a*- and *c*-axes of the Li_3N layered structure.

Nanoribbon growth is often associated with a vapour-solid (*VS*) mechanism (*20*,*21*) and the formation of this Li_3N morphology (Fig. 1B) can be rationalised by the coexistence (competition) of a *VS* mechanism with a *VLS* mechanism at high temperature as has been observed for GaN and Ga_2O_3 (*22*). Congruent sublimation of GaN has been proposed from experiment as an alternative to decomposition to $Ga_{(l)}$ and $N_{2(g)}$ (*23*, *24*). A *VS* mechanism for lithium nitride nanoribbon formation would similarly appear to invoke direct deposition from $Li_3N_{(g)}$. Just as observed for $CdS_{(g, s)}$ in the original *VS* whisker growth experiments performed by Sears (*21*), we observe nucleation and growth at the cooler section of the reaction vessel. Li *et al.* also noticed different morphologies in GaN as a function of reaction temperature (*25*). For example, they obtained GaN nanoribbons when using temperatures of 950-960 °C and GaN nanowires when these temperatures were reduced to 870-890 °C.

The layered structure of Li_3N (hexagonal *P*6/*mmm*) shares salient features with those of graphite and BN. [Li_2N] layers (which alternate with layers of Li(1) atoms stacked perpendicular to the *c*-axis) contain Li atoms in a trigonal planar coordination to N (*16*) by analogy to sp^2 hybridised carbon in the graphene layers of graphite or to boron and nitrogen in BN. Like layered chalcogenides, MQ_2 (*M* = early transition metal; *Q* = S, Se) therefore, it is tempting to classify Li_3N as an inorganic fullerene-like (IF) material (*26*,*27*). The formation of anisotropic fibers, in fact, is an indicator of the close structural relation not only between Li_3N, graphite and BN but also between Li_3N and other IF materials. The extraordinary ability to adopt different low dimensional morphologies can lead to shape-tuneable properties as already seen in the few examples of other nanostructured semiconducting nitrides. For example, GaN nanorings and nanowires exhibit differences in the phonon intensities in Raman spectra that are expected to be manifested in unexpected optical properties (*25*).

Transmission electron microscopy (TEM) and selected area electron diffraction (SAED) experiments were performed to identify the growth processes in the nanostructures and test the structural analogies between Li_3N, graphite and BN (and to some extent other IFs). Two types of single crystalline, straight fibers with different growth orientations (***A*** and ***B***) were identified. A *type **A*** nanofiber is shown in Fig. 2, with a growth plane of $\{1\bar{2}10\}$ and a growth direction of

$<10\bar{1}0>$. Secondly, *type* ***B*** nanofibers were also observed and conversely have a growth direction of [0001], as shown in Fig. 3. Thus Li_3N nanofibres exist in which the hexagonal $[Li_2N]$ layers are stacked either parallel or perpendicular to the principal fiber axis. Both these nanofibers exhibited layers of polycrystalline material at the surface (typically 10-50 nm thick) which were identified by SAED as LiOH from hydrolysis during the brief transfer to the microscope. Prolonged air-exposure resulted in the complete pseudomorphic transformation of the Li_3N structures to crystalline nanofibers of LiOH. The ***A*** and ***B*** type nanofibers (shown schematically in Supplementary Materials; Fig. S3) correspond to materials obtained at lower reaction temperature (Fig. 1A) and when altering the temperature gradient (Fig. 1C), respectively. Carbon nanofibres can assemble in an analogous fashion; graphene layers can be oriented either perpendicular or parallel to the principal fiber axis (*28-29*). BN fibers display structures in which hexagonal BN layers are similarly arranged. For example, those synthesised *via* the high temperature reaction of BN, B_2O_3 and B under nitrogen align with the (002) basal planes perpendicular to the fiber axis (*30*) whereas the converse is seen in BN nanofibers produced *via* nitridation of electrospun fibres of B_2O_3 and polyvinylbutryal (PVB) in ethanol (*31*).

Similarly, SAED confirmed that the ribbon-like nanostructures (Fig. 1B) were single crystalline sheets of Li_3N. These ribbons presented two different orientations with either a $(1\bar{2}10)$ habit plane or a (0001) habit plane as indicated in (Fig. 4). SAED showed satellites attributable to LiOH, as observed in the fibers. The former habit plane resembles that found in type ***A*** and ***B*** nanofibers, whereas the latter is completely different from either.

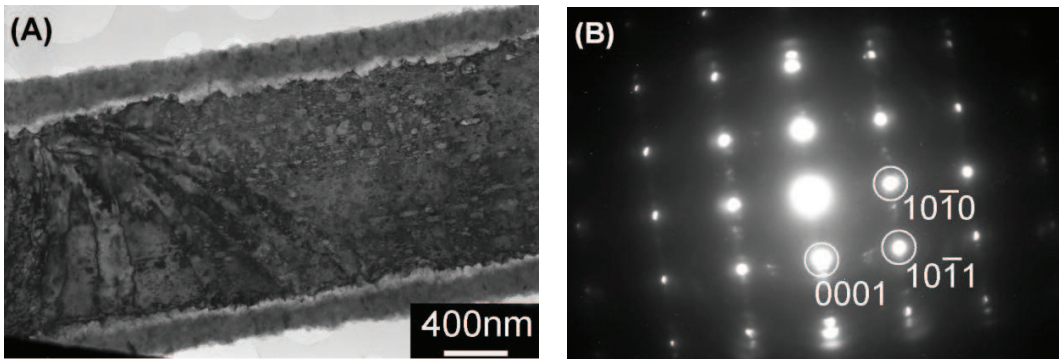


Fig. 2. TEM images and SAED pattern of a type ***A*** Li_3N nanofiber with a LiOH surface layer. (a) high magnification bright field image which delineates the Li_3N core from the LiOH outer layer; (b) associated SAED pattern showing the <**1**2**1**0> projection of Li_3N taken from the centre of the fiber demonstrating the <10**1**0> direction to be consistent with the nanofiber growth direction.

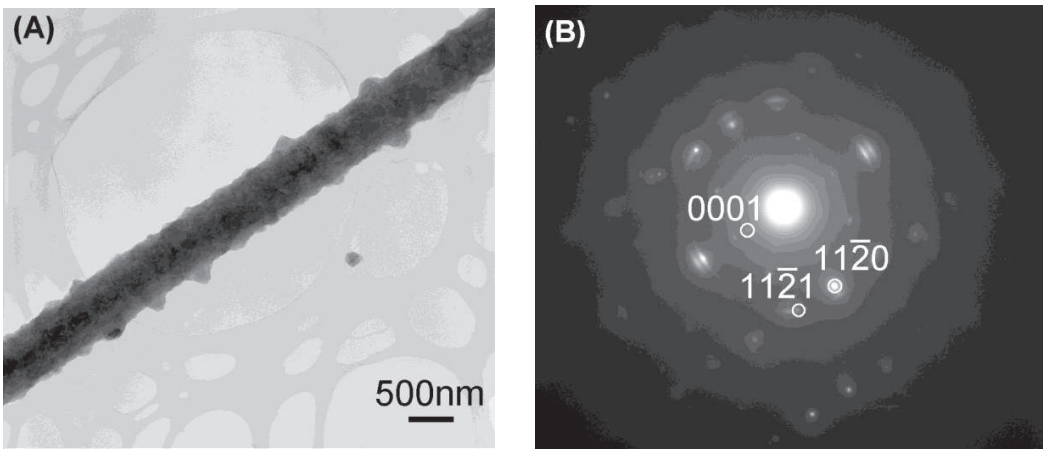


Fig. 3. (a) bright field TEM image of a Li_3N nanofiber of type ***B*** with a rough surface due to the formation of LiOH; (b) SAED pattern in the Li_3N <01**1**0> projection, with arcs due to LiOH, showing the <0001> direction to be consistent with the nanofiber growth direction.

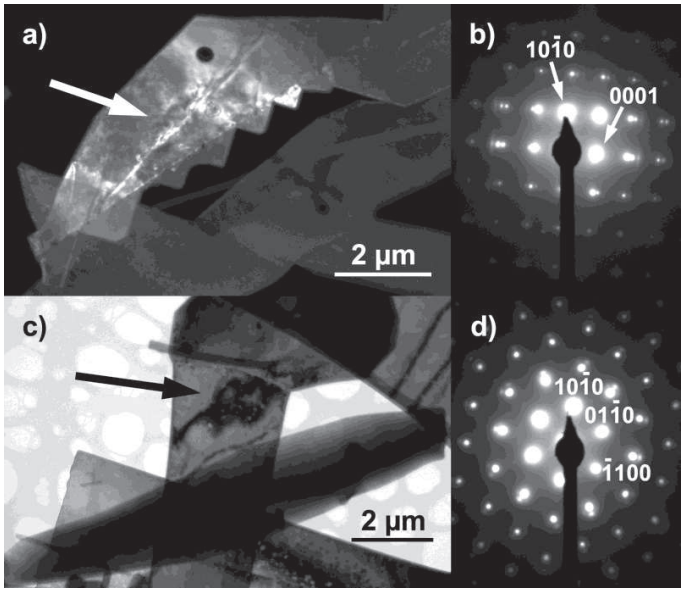


Fig. 4. TEM images and diffraction patterns from Li_3N 2D nanosheets; (A) dark field image of a sheet with a saw-tooth edge; (B) selected area electron diffraction (SAED) pattern of this sheet demonstrating a $(1\bar{2}10)$ habit plane for the sheet, with sawtooth edges perpendicular to $[10\bar{1}0]$ and [0001] directions; (C) bright field image of a straight-edged sheet with (D) an SAED pattern for this sheet, demonstrating a (0001) habit plane.

Wideline ^{7}Li (I=3/2) solid-state NMR spectra at 298 K for ***A*** (Fig. 5A) show two sets of powder-broadened satellites with quadrupolar couplings (C_q) of 580 and 284 kHz. These can be assigned to the Li(1) (inter-layer) and Li(2) (intra-layer) sites in the crystal structure of the Li_3N fiber by direct comparison with the bulk material, for which the C_q values are essentially identical (*32*). In contrast, for ***B*** (Fig. 5B) an additional satellite with C_q = 424 kHz (labelled with asterisks) is observed. We have assigned this satellite to a new lithium environment and one interpretation could be that this exists at the edge of the $[Li_2N]$ layers and is coordinatively unsaturated (coordination number "3-δ") at the surface of the fiber. Note that for ***B***, Li(1) C_q = 572 kHz and Li(2) C_q = 284 kHz, meaning that there is a slight decrease in the quadrupolar coupling for Li(1) in addition to the appearance of the new site. This decrease is not significant enough to suggest a substantial structural change, however. Variable-temperature (VT) wideline ^{7}Li solid-state NMR measurements between 133 and 373 K enabled the Li^+ ion transport properties of *type **A*** and ***B*** Li_3N nanofibers to be determined (Supplementary Materials; S4). The

line narrowing observed particularly for the Li(2) satellite lines between 133 K and 293 K can be interpreted in terms of *intra*-layer Li^+ diffusion, by analogy with the corresponding behaviour for bulk Li_3N (*33*). Similarly, the broadening that occurs above 293 K and eventually causes both sets of satellites to disappear into the baseline results from *inter*-layer diffusion *via* exchange of Li^+ between the Li(1) and Li(2) sites. Assuming simple Arrhenius behavior, the activation energy for the former intra-layer process can be measured from the temperature variation of the linewidth (Supplementary Materials) and was found to be 0.075 and 0.053 eV for *type **A*** and ***B*** Li_3N nanofibers respectively, which should be compared with the value of 0.121 eV, previously obtained for bulk Li_3N (*34*) (Supplementary Materials; Table S1).

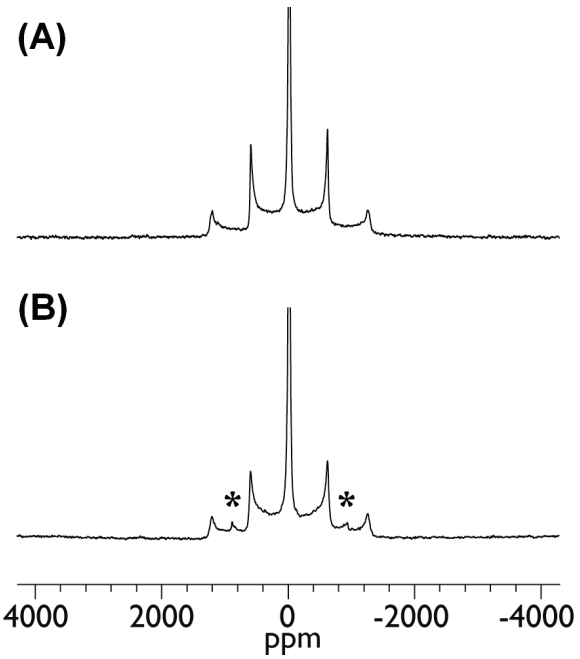


Fig. 5. Wideline ^7Li NMR spectra at 298 K for (a) type ***A*** and (b) type ***B*** nanofibers. An additional pair of satellites is observed for the type ***B*** nanofibers and is indicated by asterisks.

Electronic and optical properties of bulk and single layers of Li_3N were computed using the GGA/PBE+D level of density functional theory (DFT) as implemented in CASTEP code (*35*) (more details can be found in Supplementary Materials). Our calculations confirm that bulk Li_3N is a semiconductor with an indirect band gap of about 1.3 eV, where the valence band is mainly

derived from nitrogen 2s and 2p states and the conduction band mainly originates from lithium 2s states. Huo *et al.* recently obtained a wider band gap (1.8 eV) from TDOS and PDOS calculations with a conduction band consisting of both N 2p and Li 2s states (*36*).Calculations predict that a single crystal surface of Li_3N is metallic, indicating that bulk Li_3N might have a metallic surface and that nano-sheets or -ribbons would become metallic at a certain critical thickness. Diffuse reflectance UV-Vis spectroscopy measurements revealed a reduction in the measured band gap energy (E_g) for the as-grown *type **A*** Li_3N fibers (E_g = 2.05 eV) as compared to bulk Li_3N (E_g = 2.13 eV) (Supplementary Materials; S12). Although the fibers are significantly thicker (by several orders of magnitude) than a single unit cell of Li_3N, for example, the experimental E_g values would support the premise from the DFT calculations that a reduction in fiber thickness (diameter) leads to a decrease in E_g. The decrease in the band gap energy in anisotropic nanostructured semiconductors has been previously attributed to the strain involved in the folding of the molecular sheets to yield wires or tubes (*26*). LDA calculations showed that the band gap in graphene and hexagonal BN hetero-bilayers could be tuned by application of biaxial strain by direct comparison between the biaxially strained and unstrained states of these materials (*37*). Furthermore, Seo *et al.* reported a decrease in E_g with respect to the bulk for GaN nanowires (NWs) of 25 nm in diameter synthesised by CVD using iron as a catalyst (*38*). Evidence from X-ray diffraction and Raman spectroscopy explained the GaN band gap narrowing in terms of biaxial compressive stresses in the inward radial direction and induced tensile uniaxial stresses in the growth direction of the NWs. A red-shift in photoluminescence data was also reported for GaN NWs coated with layers of boron carbonitride. These effects were again rationalised in terms of tensile strain (*39*).

Raman spectra from nanostructured Li_3N (fibers *type **A*** and *type **B***) and bulk Li_3N showed one prominent peak at *ca.* 580 cm^{-1}, attributable to the only Raman active mode of Li_3N, *i.e.* E_{2g} (Supplementary Materials; S13). This phonon mode corresponds to the displacement of the Li(2) and N atoms along the *ab* plane in Li_3N (*40*) and is consistent with group theory predictions and spectra of bulk Li_3N reported by Chandrasekhar *et al*. (*40*,*41*,*42*)**.** We found that the E_{2g} mode band was blue-shifted (by *ca*. 5 cm^{-1}) with respect to the bulk for both type ***A*** and type ***B*** fibers. Raman spectra of microcrystals of structurally-related graphite and BN (*43,44*) and of BN multi-walled and single-walled nanotubes (MWNTs, SWNTs) (*45,46*) also revealed that the E_{2g} band broadens and shifts to higher frequency as particle size decreases. This evidence was further

supported by *ab-initio* calculations on BN SWNTs, which attributed the blue shift in the E_{2g} mode (of 5 cm^{-1}) to a shortening of the sp^2 bonds with respect to the bulk (*45*). Therefore, the blue-shift of the E_{2g} band in the Li_3N fibers can be rationalised by the formation of nanostructures in which compression of the $[Li_2N]$ layers shortens the Li(2)-N bond. The additional bands observed at *ca.* 500 cm^{-1} and 700 cm^{-1} in both bulk and nanoscale Li_3N samples were assigned to the acoustic (*A*) and optical phonon (*O*) modes 2 TA (z, K), 2 TO(A) and 2 LA(A) (T= transverse, L = longitudinal) by direct comparison with the second-order Raman spectra of Li_3N (*47*). A band corresponding to the second-order phonon mode was also observed at 350 cm^{-1} (2 LA (M, K)) (*47*). The presence of these modes is attributed to the resonant conditions established when using laser irradiation, *i.e.* at 2.33 eV (*48*).

The hydrogen storage properties of the nanostructured Li_3N material were tested volumetrically using bespoke differential pressure analysis (DPA) equipment (*49*). For reference, these results were compared against data collected for bulk Li_3N. The initial H_2 uptake for the nano-Li_3N material was found to be lower (8.9 wt%) than for the sample of bulk Li_3N (10.5 wt%); the latter uptake is typical for pristine bulk material and close to the theoretical capacity, which corresponds to the two-step reaction mechanism that follows below (equation 2) (4):

$$Li_3N + 2\ H_2 \leftrightarrow Li_2NH + LiH + H_2 \leftrightarrow LiNH_2 + 2\ LiH \qquad (2)$$

One might postulate, given our earlier observations from TEM experiments, that the reduction in initial gravimetric capacity in the nanofibers is a result of surface hydrolysis ("passivation"). This is also reflected in the kinetics of the hydrogen uptake. There is a three-fold increase in the rate of hydrogen sorption for the nanoscaled Li_3N with respect to the bulk in the first cycle (Fig. 6). In subsequent cycles, the kinetics improved dramatically and were accompanied by an improved hydrogen capacity (an additional 1-2 wt% H_2) compared to the bulk material (Supplementary Materials; Table S6). Importantly, the microstructure of the dehydrogenated nitride is retained through cycling (from imide to amide and *vice versa*) and hence the (de)hydrogenation process is pseudomorphic and reversible (Supplementary Materials; S14). The enhanced hydrogen sorption kinetics and reversibility on cycling can thus be rationalised in terms of increased surface area and superior Li^+ (and by inference H^+) diffusion in the nanostructured Li-N-H materials.

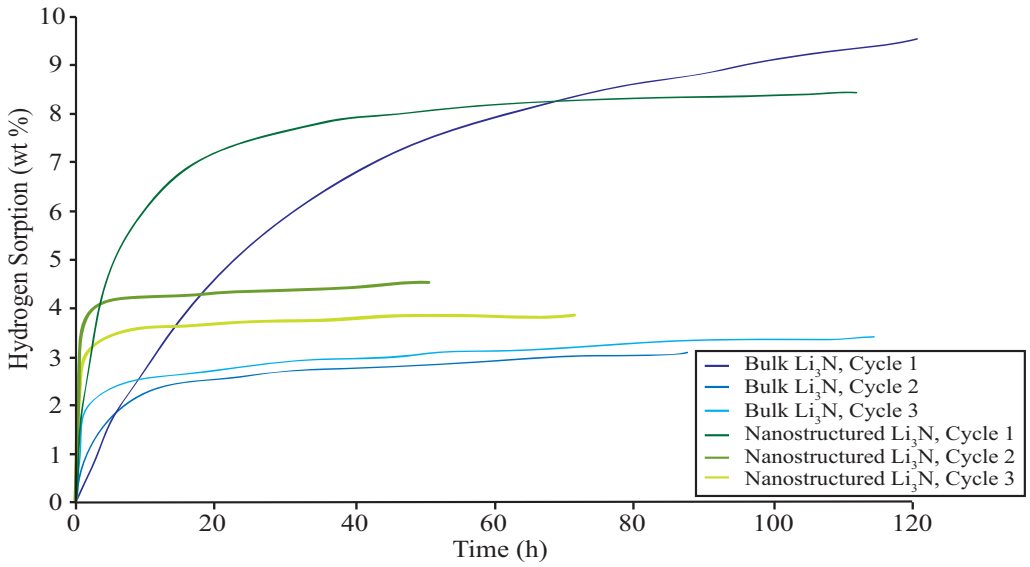


Fig. 6. Cycled hydrogen uptake of nanostructured (green) and bulk (blue) lithium nitride as a function of time measured using a differential pressure volumetric method at 200 °C under 10 bar of hydrogen pressure. Dehydrogenation was also performed at 200 °C.

In summary new low dimensional (1D and 2D) Li_3N nanostructured materials can be formed at reduced pressure and elevated temperature by analogy to similarly structured sp^2-like layered solids such as graphite and boron nitride. Nanofiber and nanosheet morphologies can be tuned *via* the preparative conditions and as with carbon and IFs, electronic and optical properties appear scalable with size and shape. Moreover, formation of 1D and 2D variants of Li_3N has important consequences for storage and transport of Li^+ and H_2 (H^+) which lead to demonstrable improvements in Li^+ ion diffusion and H_2 storage properties compared to the bulk material.

Acknowledgements

Supplementary Materials:

Materials and Methods:

Any Additional Author notes:

References and Notes:

(*1*) Y. H. Hu, Y. Huo, Fast and exothermic reaction of CO_2 and Li_3N into C-N-containing solid materials. *J. Phys. Chem. A* **115,** 11678-11681 (2011).

(*2*) L. Duan, Q. Liu, Y. Li, Y. Gao, G. Zhang *et al*., Thermally decomposable lithium nitride as an electron injection material for highly efficient and stable OLEDs. *J. Phys. Chem. C* **113**, 13386-13390 (2009).

(*3*) F. P. Baldwin, E. J. Blanchard, P. E. Koenig, *J. Org. Chem.* **30**, 671-673 (1965).

(*4*) P. Chen, Z. Xiong, J. Luo, J. Lin, K. L. Tan, Interaction of hydrogen with metal nitrides and imides. *Nature* **420**, 302-304 (2002).

(*5*) B. A. Boukamp, R. A. Huggins, Fast ionic conductivity in lithium nitride. *Mater. Res. Bull.* **13**, 23-32 (1978).

(*6*) U. Von Alpen, M. F. Bell, Impedance measurements on lithium nitride (Li_3N) single crystals. *J. Electroanal. Chem.* **99**, 85-92 (1979).

(*7*) Y. Inaguma, C. Liquan, M. Itoh, T. Nakamura, T. Uchida *et al.,* High ionic conductivity in lithium lanthanum titanate. *Solid State Comm.* **86**, 689-693 (1993).

(*8*) J. Kuwano, A. R. West, New lithium (1+) ion conductors in the system, lithium germanate-lithium vanadate (Li_4GeO_4-Li_3VO_4). *Mat. Res. Bull*. **15**, 1661-1667 (1980).

(*9*) F. Mizuno, A. Hayashi, K. Tadanaga, M. Tatsumisago, New, highly ion-conductive crystals precipitated from Li_2S-P_2S_5 glasses. *Adv. Mater.* **17,** 918-921 (2005).

(*10*) T. Shodai, S. Okada, S. Tobishima, J. Yamaki, Anode performance of a new layered nitride $Li_{3-x}Co_xN$ (x= 0.2-0.6). *J. Power Sources* **68**, 515-518 (1997); M. Nishijima, T. Kagohashi, Y. Takeda, M. Imanishi, O. Yamamoto, Electrochemical studies of a new anode material, $Li_{3-x}M_xN$ (M= Co, Ni, Cu). *J. Power Sources* **68**, 510-514 (1997).

(*11*) J. L. Rowsell, V. Pralong, L. F. Nazar, Layered lithium iron nitride: a promising anode material for Li-ion batteries. *J. Am. Chem. Soc.* **123**, 8598-8599 (2001).

(*12*) Z. Stoeva, R. Gomez, A. G. Gordon, M. Allan, D. H. Gregory *et al.*, Fast lithium ion diffusion in the ternary layered nitridometalate LiNiN. *J. Am. Chem. Soc.* **126**, 4066-4067 (2004). *J. Am. Chem. Soc.* **129**, 1912-1920 (2007).

(*13*) Z. Stoeva, B. Jäger, R. Gomez, S. Messaoudi, M. B. Yahia *et al.*, Crystal chemistry and electronic structure of the metallic lithium ion conductor, LiNiN. *J. Am. Chem. Soc.* **129**, 1912-1920 (2007).

(*14*) J. Cabana, Z. Stoeva, J. T. Titman, D. H. Gregory, M. R. Palacín, Towards new negative electrode materials for Li-ion batteries: electrochemical properties of LiNiN. *Chem. Mater.* **20**, 1676-1678 (2008).

(*15*) N.-S. Choi, Z. Chen, S. A. Freunberger, X. Ji, Y.- K. Sun *et al,.* Challenges facing lithium batteries and electrical double-layer capacitors. *Angew. Chem. Int. Ed.* **51**, 9994-10024 (2012).

(*16*) H. Schulz, K. H. Thiemann, Defect structure of the ionic conductor lithium nitride (Li_3N). *Acta Cryst. A***35**, 309-314 (1979).

(*17*) P. F. Adams, P. Hubberstey, R. J. Pulham, Review of the solubility of nonmetals in liquid lithium. *J. Less-Common Met.* **42**, 1-11 (1975).

(*18*) H. Kimura, M. Asano, K. Kubo, Vaporization of solid lithium nitride. *J. Nucl. Mater.* **91**, 200-204 (1980).

(*19*) E. A. Stach, P. J. Pauzauskie, T. Kuykendall, J. Goldberger, H. Rongrui *et al*., Watching GaN nanowires grow, *Nano Lett.* **3**, 867-869 (2003).

(*20*) G. W. Sears, A growth mechanism for mercury whiskers. *Acta Metall.* **3**, 361-366 (1955).

(*21*) G. W. Sears, A mechanism of whisker growth. *Acta Metall.* **3** 367-369 (1955).

(*22*) Z. R. Dai, Z. W. Pan, Z. L. Wang, Gallium oxide nanoribbons and nanosheets. *J. Phys. Chem. B*, **106**, 902-904 (2002).

(*23*) Z. A. Munir, A. W. Searcy, Activation energy for the sublimation of gallium nitride. *J. Chem. Phys.* **42**, 4223-4228 (1965)

(*24*) D. D. Koleske, A. E. Wickenden, R. L. Henry, J. C. Culbertson, M. E. Twigg, GaN decomposition in H_2 and N_2 at MOVPE temperature and pressures. *J. Cryst. Growth* **223**, 466-483 (2001).

(*25*) Z. J. Li, X. L. Chen, H. J. Li, Q. Y. Tu, Z. Yang *et al.,* Synthesis and Raman scattering of GaN nanorings, nanoribbons and nanowires. *Appl. Phys. A-Mater.* **72**, 629-632 (2001).

(*26*) R. Tenne, Inorganic nanotubes and fullerene-like materials. *Chem. Eur. J.* **8**, 5296-5304 (2002).

(*27*) R. Tenne, G. Seifert, Recent progress in the study of inorganic nanotubes and fullerene-like structures. *Annu. Rev. Mater. Res.* **39**, 387-413 (2009).

(*28*) N. M. Rodriguez, A. Chambers, R. T. K. Baker, Catalytic engineering of carbon nanostructures. *Langmuir*, **11**, 3862-3866 (1995).

(*29*) G. Che, B. B. Lakshmi, C. R. Martin, E. R. Fisher, Chemical vapor deposition based synthesis of carbon nanotubes and nanofibers using a template method. *Chem. Mater.* **10**, 260-267 (1998).

(*30*) R. Ma, Y. Bando, T. Sato, D. Golberg, H. Zhu *et al.,* Synthesis of boron nitride nanofibers and measurement of their hydrogen uptake capacity, *Appl. Phys. Lett*. **81**, 5225-5227, (2002).

(*31*) Y. Qiu, J. Yu, J. Rafique, J. Yin, X. Bai *et al.,* Large-scale production of aligned long boron nitride nanofibers by multijet/multicollector electrospinning, *J. Phys. Chem. C* **113**, 11228-11234 (2009).

(*32*) K. Differt, R. Messer, NMR spectra of Li and N in single-crystals of Li_3N - discussion of ionic nature. *J Phys C Solid State* **13**, 717–724 (1980).

(*33*) R. Messer, H. Birli, K. Differt, NMR Study of diffusion in Li_3N. *J. Phys. C Solid State* **14**, 2731–2746 (1981).

(*34*) Z. Stoeva, R. Gomez, D. H. Gregory, G. B. Hix, J. J. Titman, Evolution of structure, transport properties and magnetism in ternary lithium nitridometalates $Li_{3-x-y}M_xN$, M = Co, Ni, Cu. *Dalton Trans.* 3093–3097 (2004).

(*35*) S. Wu, S. S. Neo, Z. Dong, F. Boey, P. Wu, Tunable Ionic and Electronic Conduction of Lithium Nitride via Phosphorus and Arsenic Substitution: A First-Principles Study. *J. Phys. Chem. C.* **114***,* 16706–16709 (2010).

(*36*) Y. Huo and Y. H. Hu, UV-visible absorption spectrum determination of optical energy gaps of α and β lithium nitrides, *J. Phys. Chem. Solids* **73**, 999-1002 (2012).

(*37*) H. Behera, G. Mukhopadhyay, Strain-tuneable band gap in grapheme/h-BN hetero-bilayer. *J. Phys. Chem. Solids* **73**, 818-821 (2012).

(*38*) H. W. Seo, S. Y. Bae, J. Park, H. Yang, K. S. Park, S. Kim, Strained gallium nitride nanowires. *J. Chem. Phys*. **116**, 9492-9500 (2002).

(*39*) H. W. Seo, S. Y. Bae, J. Park, H. Yang, B. Kim, Direct synthesis of gallium nitride nanowires coated with boron carbonitride layers. *J. Phys. Chem. B* **107**, 6739-6742 (2003).

(*40*) H. R. Chandrasekhar, G. Bhattacharya, R. Migoni, H. Bilz, Infrared and Raman spectra and lattice dynamics of the superionic conductor lithium nitride (Li_3N). *Phys. Rev. B* **17**, 884-893 (1978).

(*41*) E. Zintl, G. Brauer, Constitution of lithium nitride. *Z. Elecktrochem*. **41**, 102-107 (1935).

(*42*) H. R. Chandrasekhar, G. Bhattacharya, R. Migoni, H. Bilz, Phonon spectra and lattice dynamics of lithium nitride. *Solid State Comm.* **22**, 681-684 (1977).

(*43*) R. J. Nemanich, S. A. Solin, First- and second-order Raman scattering from finite-size crystals of graphite. *Phys. Rev. B* **20**, 392-401 (1979).

(*44*) R. J. Nemanich, S. A. Solin , R. M. Martin, Light scattering study of boron nitride microcrystals. *Phys. Rev. B* **23**, 6348-6356 (1981).

(*45*) R. Arenal, A. C. Ferrari, S. Reich, L. Wirtz, J.-Y. Mevellec *et al.,* Raman Spectroscopy of single-wall boron nitride nanotubes. *Nano Lett.* **6**, 1812-1816 (2006).

(*46*) S. K. Singhal, A. K. Srivastava, A. K. Gupta, Z. G. Chen, Synthesis of boron nitride nanotubes by an oxide-assisted chemical method. *J. Nanopart. Res.* **12**, 2405-2413 (2010).

(*47*) W. Kress, H. Grimm, W. Press, J. Lefebvre, Lattice vibrations in lithium nitride, Li_3N. *Phys. Rev. B* **22**, 4620-4625 (1980).

(*48*) D. Nesheva, Raman scattering from semiconductor nanoparticles and superlattices. *J. Optoelectron. Adv. M.***7**, 185-192 (2005).

(*49*) J. M. Blackman, J. W. Patrick, C. P. Snape, *Proceedings of the 3rd International Conference on Sustainable Energy Technologies*. (2004).